Evolution of stratospheric ozone in the mid-latitudes in connection with the abundances of halogen compounds

Prijitha Gopalapillai

UNIVERSITY OF PIERRE AND MARIE CURIE - PARIS VI
Doctoral school of the Environmental Sciences / ED129

P H D T H E S I S

prepared at the laboratory CNRS/LATMOS
to obtain the degree of

Doctor of Philosophy
(Specialisation : **Physics**)

publicly presented and defended
by

GOPALAPILLAI Prijitha
(Prijitha J. Nair)

on
09 March 2012

Evolution of stratospheric ozone in the mid-latitudes in connection with the abundances of halogen compounds

The Jury

Dr. Nathalie Huret	LPCE/CNRS, Orléans, France	Referee
Dr. Philippe Ricaud	Météo-France/CNRS, Toulouse, France	Referee
Pr. François Ravetta	LATMOS/CNRS, Paris, France	President
Dr. Philippe Keckhut	LATMOS/CNRS, Guyancourt, France	Invited Examiner
Dr. Chantal Claud	LMD/CNRS, Palaiseau, France	Examiner
Dr. Corinne Vigouroux	IASB - BIRA, Brussels, Belgium	Examiner
Dr. Sophie Godin-Beekmann	LATMOS/CNRS, Paris, France	Thesis Supervisor

Contents

Acknowledgements

I would like to express my sincere gratitude to Dr. Sophie Godin-Beekmann for providing an opportunity and making available adequate funding to carry out my thesis under her supervision. She was inspiring and the routine discussions with her were thought-provoking. I appreciate her immense patience that helped me to develop a keen interest in the topic. Her generosity in giving full freedom to write articles is to be remembered. I also acknowledge her for spending her valuable time on critical reviews of my articles and comments on the thesis manuscript.

I am deeply conscious of my indebtedness to Dr. Jayanarayanan Kuttippurath (LATMOS), whose scientific guidance and moral support were crucial for developing my dissertation, scholarly writing and thinking skills and collegiate attitude. I greatly appreciate his comments on my manuscript and the scientific discussions with him. I also thank him for helping the extraction of Aura MLS data and his assistance in making the multiple regression model and heat flux data for the trend studies.

I wish to thank Dr. Philippe Keckhut (LATMOS) and Dr. Chantal Claud (LMD) for being a part of my thesis committee. I greatly appreciate the fruitful discussions I had with them during the course of my thesis and their comments on the thesis manuscript. Their encouragements will always be remembered.

I owe sincere thanks to Dr. Nathalie Huret (LPCE, Orléans) and Dr. Philippe Ricaud (Météo-France, Toulouse) for their critical review of my thesis and their encouraging thesis evaluation reports. Also, I thank Dr. Corinne Vigouroux (BIRA, Belgium) for her presence and comments during my thesis defence. I would like to convey my acknowledgment to Prof. François Ravetta (LATMOS) for being the President of the jury of my thesis defence committee.

This thesis makes use of ozone measurements from a number of instruments. The principal investigators of all those were very kind in providing relevant information to analyse the data. I wish to thank Dr. Florence Goutail (LATMOS), Dr. Gérard Ancellet (LATMOS), Dr. Andrea Pazmiño (LATMOS), Dr. Lucien Froidevaux (JPL, USA), Dr. Larry Flynn (NOAA, USA), Dr. Irina Petropavlovskikh (CIRES, USA), Dr. Wolfgang Steinbrecht (DWD, Germany), Dr. Hans Claude (DWD, Germany), Dr. Anne van Gijsel (RNMI, The Netherlands), Dr. Thierry Leblanc (JPL, USA), Dr. Jean-Christopher Lambert (BIRA, Belgium), Dr. Daan Hubert (BIRA, Belgium), Dr. Tetsuro Uekubo (JMA, Japan), Dr. Toshifumi Fujimoto (JMA, Japan) and Dr. Alan Thomas (NIWA, New Zealand).

I thank Dr. Danièle Hauser and Dr. Alain Hauchecorne, the directors of CNRS/LATMOS, for their hearty welcome to the laboratory to pursue my Ph.D. I also express my gratitude to Mrs. Laurence Touchon, the secretary of my Doctoral School, for helping me in all administrative matters related to the Doctoral School.

I would like to thank Mrs. Cathy Boonne (IPSL) for her timely help with the data and for maintaining ETHER data cluster. I thank Mr. Philippe Weill, the system administrator of the LATMOS, for all his assistance with my computers. I also remember Mrs. Michèle Moreau, Mrs. Maryse Grenier, Mrs. Evelyne Quinsac and Mrs. Valérie Fleury, the former and current secretaries of LATMOS for their help with the administrative formalities. I wish to thank Dr. Slimane Bekki (group head) and Dr. Marion Marchand (LATMOS) for their unconditional support and encouragement during the difficult phase of my thesis tenure.

I take this opportunity to express my sincere gratitude to those who pray for my well-being. I must single out the help, encouragement, and moral support I received from the parents of my husband (Mr. K. R. S. Nair and Mrs. M. Balamani Amma), my parents (Late Mr. K. S. Gopala Pillai and Mrs. P. Renukadevi Amma), brother (Mr. Praveen G.), sister (Mrs. Preethisree G.), brother-in-law (Mr. Arun Kumar S. Nair), and sister-in-law (Mrs. Priya A. Nair). With great respect and affection, I remember the efforts of my beloved, who brought me to this position. Besides this, several people have knowingly and unknowingly helped me in the successful completion of this study. Finally, I really thank the extreme power that activates my life and controls my existence.

This thesis was supported by a funding from the GEOMON (Global Earth Observation and Monitoring of the atmosphere) European project.

Acronym

ACE-FTS	:	Atmospheric Chemistry Experiment-Fourier Transform Spectrometer
AER	:	Aerosol
AK	:	Averaging Kernel
AO	:	Arctic Oscillation
BP	:	Bass and Paur
BD	:	Brewer-Dobson
BDM	:	Brion-Daumont-Malicet
Br	:	Bromine
CCM	:	Chemistry Climate Model
CCMVal	:	Chemistry Climate Model Validation
CF	:	Correction Factor
CFC	:	Chlorofluorocarbon
CH_4	:	Methane
Cl	:	Chlorine
ClO	:	Chlorine monoxide
CIRA	:	COSPAR International Reference Atmosphere
CO_2	:	Carbon dioxide
CTM	:	Chemical Transport Model
DIAL	:	Differential Absorption Lidar
DOAS	:	Differential Optical Absorption Spectroscopy
DU	:	Dobson Unit
ECC	:	Electrochemical Concentration Cell
EESC	:	Equivalent Effective Stratospheric Chlorine
ENSCI	:	Environmental Science Corporation
ENVISAT	:	Environmental Satellite
EP flux	:	Eliassen-Palm flux
ERBS	:	Earth Radiation Budget Satellite
FTIR	:	Fourier Transform Infrared
GHG	:	Greenhouse gas
GOME	:	Global Ozone Monitoring Experiment
GOMOS	:	Global Ozone Monitoring by Occultation of Stars
H	:	Hydrogen
HALOE	:	Halogen occultation Experiment
HFX	:	Eddy heat flux
HIRDLS	:	High Resolution Dynamics Limb Sounder
HNO3	:	Nitric Acid
H_2O	:	water vapour
H_2SO_4	:	Sulfuric Acid
IASI	:	Infrared Atmospheric Sounding Interferometer
IR	:	InfraRed
LIDAR	:	Light Detection And Ranging
MetOp	:	Meteorological Operational
MLS	:	Microwave Limb Sounder
MLO	:	Mauna Loa Observatory
MOHp	:	Meteorological Observatory Hohenpeissenberg
MSU	:	Microwave Sounding Unit
NAO	:	Northern Atlantic Oscillation
NASA	:	National Aeronautics and Space Administration

NAT	:	Nitric Acid Trihydrate
NCEP	:	National Center for Environmental Prediction
NDACC	:	Network for the Detection of Stratospheric Change
NH	:	Northern Hemisphere
NO	:	Nitrogen Oxide
NO_2	:	Nitrous Oxide
NOAA	:	National Oceanic and Atmospheric Administration
O	:	Oxygen
ODS	:	Ozone Depleting Substance
OH	:	Hydroxyl
OHP	:	Haute-Provence Observatory
OMI	:	Ozone Monitoring Instrument
OSIRIS	:	Optical Spectrograph InfraRed Imager System
ppb	:	Parts per billion
ppm	:	Parts per million
ppt	:	Parts per trillion
PSC	:	Polar Stratospheric Cloud
PW	:	Piecewise
PWLT	:	Piecewise linear trend
QBO	:	Quasi Biennial Oscillation
REPROBUS	:	Reactive processes ruling the ozone budget in the stratosphere
SAGE	:	Stratospheric Aerosol and Gas Experiment
SAOZ	:	Système d'Analyse par Observation Zénithale
SBUV	:	Solar Backscatter UltraViolet
SCIAMACHY	:	SCanning Imaging Absorption spectroMeter for Atmospheric CHartographY
SFX	:	Solar flux
SFX	:	Solar flux unit
SMR	:	Sub-millimetre Radiometer
SO_2	:	Sulfur Dioxide
SH	:	Southern Hemisphere
SPARC	:	Stratospheric Processes And their Role in Climate
STS	:	Supercooled Ternary Solutions
SPC	:	Science Pump Corporation
TMF	:	Table Mountain Facility
TOMS	:	Total Ozone Mapping Spectrometer
UARS	:	Upper Atmosphere Research Satellite
UV	:	Ultraviolet
VMR	:	Volume Mixing Ratio
V_{PSC}	:	Volume of PSC
WMO	:	World Meteorological Organisation

PUBLICATIONS

Peer-Reviewed

(1) **Nair, P. J.**, Godin-Beekmann, S., Pazmiño, A., Hauchecorne, A., Ancellet, G., Petropavlovskikh, I., Flynn, L. E., and Froidevaux, L.: Coherence of long-term stratospheric ozone vertical distribution time series used for the study of ozone recovery at a northern mid-latitude station, Atmos. Chem. Phys., 11, 4957–4975, doi:10.5194/acp-11-4957-2011, 2011.

(2) **Nair, P. J.**, Godin-Beekmann, S., Froidevaux, L., Flynn, L. E., Zawodny, J. M., Russell III, J. M., Pazmiño, A., Ancellet, G., Steinbrecht, W., Claude, H., Leblanc, T., McDermid, S., van Gijsel, J. A. E., Johnson, B., Thomas, A., Hubert, D., Lambert, J.-C., Nakane, H., and D. P. J. Swart: Relative drifts and stability of satellite and ground-based stratospheric ozone profiles at NDACC lidar stations, Atmos. Meas. Tech., 5, 1301–1318, doi:10.5194/amt-5-1301-2012, 2012.

(3) Godin-Beekmann, S., and **Nair, P. J.**: Sensitivity of stratospheric ozone lidar measurements to a change in ozone absorption cross-sections, J. Quant Spectrosc Radiat Transfer, doi:10.1016/j.jqsrt.2012.03.002, 2012.

In preparation

(4) **Nair, P. J.** et al.: Trends and variability in the vertical distribution of stratospheric ozone at Observatoire de Haute-Provence (OHP).

(5) Griesfeller A., Godin-Beekmann S., Petropavlovskikh, I., **Nair, P. J.**, Griesfeller J., Evans, R. D., and Pazmiño, A.: Comparison of long-term stratospheric ozone time series from lidar and Umkehr measurements at Observatoire de Haute-Provence (OHP), 44° N, 6° E.

Conference Abstracts

(6) **Nair, P. J.**, Godin-Beekmann, S., Froidevaux, L., Flynn, L. E., Ancellet, G., Steinbrecht, W., Claude, H., Nakane, H., Leblanc, T., McDermid, S., Swart, D. P. J., van Gijsel, J. A. E., and Thomas, A.: Relative drifts of stratospheric ozone measurements at NDACC lidar stations, Geophysical Research Abstracts, European Geosciences Union (EGU) General Assembly, 13, EGU2011-10825, 2011.

(7) **Nair, P. J.**, Godin-Beekmann, S. and Pazmiño, A.: Coherence of long-term stratospheric ozone time series for the study of ozone recovery in the northern mid-latitudes, Geophysical Research Abstracts, European Geosciences Union (EGU) General Assembly, 12, EGU2010-5519, 2010.

(8) Godin-Beekmann, S., **Nair, P. J.**, Froidevaux, L., Flynn, L. E., Ancellet, G., Steinbrecht, W., Claude, H., Nakane, H., Leblanc, T., McDermid, S., Swart, D. P. J., van Gijsel, J. A. E., and Thomas, A.: Relative drifts of stratospheric ozone measurements at NDACC lidar stations, NDACC symposium, 7–10 November 2011.

(9) Godin-Beekmann, S. and **Nair, P. J.**: Short term and long-term evolution of stratospheric ozone at a northern mid-latitude station, NDACC symposium, 7–10 November 2011.

(10) Griesfeller, A., Godin-Beekmann, S., **Nair, P. J.**, Goutail, F., Hendrick, F., Ionov, D., Pazmiño, A., Petropavlovskikh, I., Pommereau, J.-P., van Roozendael, M.: Long-term time series of ozone at Observatoire de Haute-provence (OHP), 44°N, 6°E, Geophysical Research Abstracts, European Geosciences Union (EGU) General Assembly, 11, EGU2009-9262, 2009.

Reports

(11) Scientific Assessment of Ozone Depletion 2010: Stratospheric Ozone and Surface Ultraviolet Radiation edited by Anne Douglass and Vitali Fioletov. (**Contributed**)

(12) Godin-Beekmann, S., **Nair, P. J.**, NDACC lidar and satellite measurement teams: What NDACC ozone lidars are telling us about long-term satellite measurements, ISPARC/IO3C/WMO-IGACO Workshop on Past changes in the Vertical Distribution of Ozone, Geneva, 25–27 January 2011.

(13) Godin-Beekmann, S. and **Nair, P. J.**: The effect of change of BP to DBM ozone absorption cross-sections on lidar measurements, IO3C-WMO-IGACO-O3/UV, Meeting on ozone absorption cross-section, Geneva, 23–25 March 2010.

(14) Godin-Beekmann, S., and **Nair, P. J.**: Sensitivity of stratospheric ozone lidar measurements on ozone cross-section, http://igaco-o3.fmi.fi/ACSO, 2010.

Abstract

This thesis addresses the issue of the long-term evolution of stratospheric ozone in relation to the halogen loading. To that aim, long-term records of satellite and ground-based (GB) ozone profile measurements at six lidar stations, of the Network for the Detection of Stratospheric Change, are examined to find the bias and drift in the measurements. The stratospheric ozone trends are then estimated from the ozone profile and total column measurements using the Equivalent Effective Stratospheric Chlorine time series and two linear trend functions (before and after 1997) called as piecewise linear trends (PWLTs), to account for the change in the trends of ozone depleting substances, at Northern mid-latitude stations. The analysis uses GB measurements from lidar, Umkehr, ozonesondes and the Dobson and SAOZ spectrometers, and satellite observations from SBUV(/2), SAGE II, HALOE, UARS MLS, Aura MLS and GOMOS. First of all, a sensitivity analysis is performed to diagnose the effect of using different ozone absorption cross-section data sets (Bass and Paur and Brion-Daumont-Malicet) on the retrieved lidar ozone profiles. The relative ozone differences computed using those two cross-section data are less than $\pm 1\%$ from 10 to 35 km at all latitudes, except a -1.5% deviation at 15 km in the tropics. Above 35 km, the deviations increase with a maximum of 1.7% in the tropics and a minimum of 1.4% in the high latitudes. The stability of various GB and satellite ozone profile time series is then evaluated by comparing with the ozone lidar data for each station. All ozone profile measurement techniques show their best agreement ($\pm 3\%$) with lidars in the 20–40 km altitude range and the estimated drifts are less than $\pm 0.3\%\mathrm{yr}^{-1}$ at all stations. Comparatively large biases and drifts are computed below 20 and above 40 km. A combined time series of the relative differences of SAGE II, HALOE and Aura MLS with respect to the lidar measurements at the six lidar sites is constructed to obtain long-term data sets from 1985 to 2010. The relative drifts derived from these combined data of $\sim$27 years are very small, within $\pm 0.2\%\mathrm{yr}^{-1}$. Then, stratospheric ozone trends are estimated at Meteorological Observatory Hohenpeissenberg (MOHp) using Dobson, and at Haute-Provence Observatory (OHP) using Dobson and SAOZ total column measurements and various GB and satellite ozone profiles. For that a multiple regression model is developed using different explanatory variables such as Quasi Biennial Oscillation (QBO), North Atlantic Oscillation (NAO), solar flux, eddy heat flux, aerosols and trend. The PWLTs computed from the ozone column at OHP and MOHp show significant negative ($-1.4 \pm 0.29\,\mathrm{DU\,yr}^{-1}$) and positive ($0.55 \pm 0.29\,\mathrm{DU\,yr}^{-1}$) values before and after 1997, respectively, indicating a clear signal of ozone recovery at these latitudes after 1996. Vertical distribution of ozone trends based on PWLT model, estimated using the all instrument average at OHP exhibit about $-0.5 \pm 0.1\,\%\,\mathrm{yr}^{-1}$ in the 16–22 km range and about $-0.8 \pm 0.2\,\%\,\mathrm{yr}^{-1}$ in the 38–45 km region before 1997. Significant positive trends (0.2 ± 0.05–$0.3 \pm 0.1\,\%\,\mathrm{yr}^{-1}$) are estimated in the 15–45 km altitude region after 1996. These significant ozone profile trends in the respective periods corroborate those derived from the ozone total column and hence, provide signs of ozone recovery in the northern mid-latitudes. The trends based on both PW and EESC regressions are similar and significant before 1997 while they differ slightly after 1996, with the largest value in the PW regression. In addition, the most recent increase in ozone after 1996 is due to the increase in QBO and planetary wave drive. For instance, QBO, NAO and heat flux contribute about 20–26 DU to the large total ozone anomaly of 25–30 DU in the winter/spring months in 2010. Therefore, this thesis presents some new and interesting results on the mid-latitude stratospheric ozone recovery.

Résumé

Cette thèse a pour objet l'étude de l'évolution à long terme de l'ozone stratosphérique, en liaison avec la variation dde l'abondance des composés halogénés dans la moyenne atmosphère. Dans ce but, les longues séries de mesures sol et satellitaires de la distribution verticale d'ozone obtenues depuis les années 1980 sont évaluées dans six stations du Network for the Detection of Atmospheric Composition Changes (NDACC - réseau international de surveillance de la composition atmosphérique), pour déterminer les biais et dérives éventuelles entre les mesures. Les tendances d'ozone stratosphérique sont ensuite évaluées dans deux stations de moyenne latitude de l'hémisphère nord à l'aide d'un modèle statistique utilisant deux types d'indicateurs pour représenter l'évolution des substances destructrices d'ozone dans la stratosphère: (1) l'Equivalent Effective Stratospheric Chlorine (EESC - paramètre quantifiant l'effet des composés chlorés et bromés stratosphériques sur l'ozone) et (2) deux fonctions linéaires avec changement de pente en 1997. L'étude de tendance est effectuée pour les mesures du contenu intégré d'ozone dans les deux stations et les mesures de distribution verticale à l'Observatoire de Haute-Provence. L'étude utilise les mesures sol d'ozone obtenues par lidar (profil d'ozone), spectromètre Dobson (contenu intégré et profil d'ozone par la méthode Umkehr), ozonosondage (profil d'ozone) et spectromètre UV-Visible SAOZ (contenu intégré). Les observations satellitaires utilisées proviennent des instruments SBUV(/2), SAGE II, HALOE, UARS MLS, Aura MLS et GOMOS. Tout d'abord une étude de la sensibilité des mesures lidar aux sections efficaces d'ozone utilisées dans l'algorithme de restitution est effectuée. La différence relative d'ozone obtenue à partir des mesures restituées à l'aide de différents jeux de données de section efficace reconnues par les instances internationales, est inférieure à ±1% entre 10 et 35 km à toutes les latitudes (à l'exception de -1.5 % à 15 km aux tropiques). Au-dessus de 35 km, l'écart s'accroit, avec un maximum à 45 km de 1.7 % aux tropiques et un minimum de 1.4 % aux hautes latitudes. La stabilité des différentes séries de mesures satellitaires et sol de la distribution verticale d'ozone est ensuite évaluée à partir de la comparaison avec les mesures lidar dans les six stations NDACC considérées au cours de la thèse. Le meilleur accord (±3%) entre les mesures issues des différentes techniques et les mesures lidar est obtenu entre 20 et 40 km. Dans ce domaine d'altitude, la dérive entre les différentes mesures est inférieure à $\pm 0.3\%\mathrm{yr}^{-1}$. Des dérives et des biais comparativement plus importants sont calculés en dessous de 20 km et au-dessus de 40 km. Par ailleurs, la stabilité à plus long terme des mesures d'ozone est étudiée à partir de séries temporelles combinant les différences relatives entre les mesures lidar et les mesures SAGE II et HALOE d'une part avec les différences relatives entre les mesures lidar et les les mesures Aura MLS d'autre part. Les dérives estimées à partir de ces séries composites couvrant 27 années de mesure sont très faibles, de l'ordre de $\pm 0.2\%\mathrm{yr}^{-1}$. Enfin les tendances évolutives du contenu intégré d'ozone sont évaluées à l'Observatoire Météorologique de Hohenpeissenberg (MOHp - Allemagne) à partir des mesures du spectromètre Dobson et à l'Observatoire de Haute-Provence (OHP - France) à partir des mesures des spectromètres Dobson et SAOZ. A l'OHP, les tendances de la distribution verticale d'ozone sont calculées à partir des mesures obtenues par différentes techniques de mesures, sol et satellitaires. Pour ce faire, un modèle de régression multilinéaire est développé, fondé sur l'utilisation de différentes variables telles que l'oscillation quasi-biennale (QBO), l'oscillation Nord-Atlantique (NAO), le flux solaire, le flux de chaleur turbulent, l'épaisseur optique des aérosols stratosphériques et les tendances à long terme. L'estimation des tendances calculées à partir des mesures de contenu intégré d'ozone dans les deux stations fournit des valeurs significatives, de l'ordre de $-1.4 \pm 0.29\,\mathrm{DUyr}^{-1}$) et $0.55 \pm 0.29\,\mathrm{DUyr}^{-1}$ respectivement avant et après 1997. Les valeurs

positives de la tendance après 1997, significatives pour un intervalle de confiance de 95 %, montrent clairement un début de rétablissement de l'ozone stratosphérique à ces latitudes. Concernant la distribution verticale d'ozone, les tendances calculées à partir de la moyenne des différentes séries de données à l'OHP montrent des valeurs maximales en valeur absolue de l'ordre de $-0.5 \pm 0.1\,\%\mathrm{yr}^{-1}$ entre 16 et 22 km et de $-0.8 \pm 0.2\,\%\mathrm{yr}^{-1}$ entre 38 et 45 km avant 1997. Des tendances positives significatives (0.2 ± 0.05–$0.3 \pm 0.1\,\%\mathrm{yr}^{-1}$) sont évaluées entre 15 et 45 km après 1996. Ces tendances significatives du profil vertical d'ozone avant et après 1997 corroborent les résultats obtenus à partir du contenu intégré d'ozone et confirment le début de rétablissement de l'ozone stratosphérique. Par ailleurs, dans les deux cas (contenu intégré d'ozone et distribution verticale), les tendances post-1997 restituées par le modèle utilisant les fonctions linéaires sont plus élevées que celles issues du modèle utilisant l'EESC, indiquant ainsi que d'autres paramètres contribuent à l'augmentation du contenu en ozone. Enfin, il a été constaté que les contenus intégrés élevés d'ozone observés ces dernières années étaient liés à l'influence de la QBO et des processus dynamiques. Ainsi la QBO, la NAO et le flux de chaleur turbulent expliquent environ 80 % de l'importante anomalie positive de 25 - 30 DU mesurée entre février et avril 2010.

Preface

Since the discovery of the Antarctic ozone hole in 1985 (Farman et al., 1985), several additional ground-based (GB) and satellite sensors have been employed globally for intense and constant monitoring of stratospheric ozone in the framework of World Meteorological Organisation - Global Atmosphere Watch (WMO–GAW) programme. The identification of the role of chlorofluorocarbons in ozone loss process leads to drafting the Montreal Protocol and related amendments for limiting the production of such ozone depleting substances (ODSs) (WMO, 1992). It resulted in the reduction of atmospheric concentration of ODSs (Mäder et al., 2010) and (Jones et al., 2011). Recently, ODSs has decreased to such an extent that the ozone shows stabilisation from 1997 onwards in the lower (WMO, 2011) and upper stratosphere (Steinbrecht et al., 2006) of the mid-latitudes.

Since, several factors affect the long-term evolution of ozone, it is important to assess the real reason for changes in ozone to identify the effects of reduction in ODSs on ozone and thus, to assess the effectiveness of the Montreal Protocol. To address this issue, highly stable ozone measurements spanning over several decades are necessary. Satellite measurements are usually prone to degradation at the end of their life span (WMO, 2007). All long-term satellites that started in late 1970s and early 1990s (SAGE and HALOE) have stopped measurements in the mid-2000s. Even though new satellites have been launched since the early 2000s (ODIN, ENVISAT, Aura and MetOp), their observation records are too short to be used for ozone trend studies. In addition, some measurements are yet to be thoroughly validated for such kind of analysis.

The Network for the Detection of Atmospheric Composition Change (NDACC), another international network, which relies on worldwide measurements from GB stations using various instruments was established in 1991. It was designed initially for the simultaneous monitoring of various atmospheric parameters that play a key role in the stratospheric ozone depletion, with the primary aim of validating satellite measurements. Since any significant drift in the data produces inaccurate trends, a careful evaluation of these data is inevitable. As the main goal of this thesis is the assessment of ozone trends, a stability analysis of the ozone measurements is necessary. Therefore, we first analyse the stability various GB (lidars, ozonesondes, Umkehr, Dobson and SAOZ) and space-based (SBUV(/2), SAGE II, HALOE, UARS MLS, Aura MLS and GOMOS) measurements at the NDACC lidar sites. Then, these measurements are used for the estimation of stratospheric ozone trends.

Chapter 1 presents an overview of the general features of stratospheric chemistry and dynamics to follow the discussions presented in this thesis. The formation, transport, destruction and recovery of ozone in the stratosphere are reviewed in this chapter.

Since ozone lidar measurements are integral part of this study, a detailed description of lidar characteristics, data retrieval of ozone lidar and the general features of different lidars are given in Chapter 2. Moreover, a sensitivity test is performed to find out the differences in retrieving ozone number density when using different ozone absorption cross-sections and meteorological data, with the aim of improving ozone lidar algorithm.

The next step is to assess the quality of these ozone lidar measurements for validating other GB and satellite data sets. To this end, we have performed the comparison of all available GB and satellite data at OHP. A thorough statistical analysis is carried out to find any bias or drift in the ozone measurements of the GB and satellite data records at this mid-latitude station and the results are presented in Chapter 3.

This analysis is further extended to all mid-latitude and subtropical lidar stations in Chapter 4. Several statistical analyses are carried out for the accurate evaluation of relative drifts. This chapter also assesses the possibility of extending the terminated satellite data

with the new satellite measurements (for e.g., SAGE II/HALOE and Aura MLS) to obtain a long-term data set spanning over several decades for ozone trend studies.

Since the ultimate goal of this thesis is to diagnose the trends in stratospheric ozone, these well validated and bias corrected data sets from GB and satellite instruments are used for the computation of ozone trends and the results are given in Chapter 5. A regression model using various explanatory variables is developed for this purpose and is applied to the GB and satellite data for the discussion of the derived trends. Further, response of ozone at different latitudes and seasons with respect to several explanatory variables are also investigated here.

Finally, Chapter 6 concludes with the main findings from the three years of study.

List of Figures

List of Tables

Chapter 1

Introduction

Contents

This thesis discusses the evolution of stratospheric ozone measured from various ground and space-based observations over the middle and subtropical NDACC (Network for the Detection of Atmospheric Composition Change) lidar (Light Detection And Ranging) stations. Therefore, a brief introduction of the chemical and dynamical processes that affect the distribution of ozone in the stratosphere is presented in this chapter, to follow the later sections and discussions on the ozone evolution. Section 1.1 describes different layers of the atmosphere and the temperature distribution. A detailed description of stratospheric chemistry and dynamics involved in the production, distribution and destruction of stratospheric ozone is given in Section 1.2. The chemical and dynamical processes associated with the rapid destruction of ozone is discussed in Section 1.3 followed by the measurements of the stratospheric ozone destruction in Section 1.4. Section 1.5 presents a review of stratospheric ozone column and profile trends and described the different stages of ozone evolution. Then, a link between ozone and climate is discussed in Section 1.7. Finally, Section 1.8 concludes the general description and presents the objectives of the study.

1.1 Vertical structure of the atmosphere

The atmosphere is divided into different layers from the ground to 100 km based on the distribution of temperature. Figure 1.1 illustrates a schematic representation of various layers in the atmosphere, namely the troposphere, stratosphere, mesosphere and thermosphere. Each layer is distinct with respect to its temperature distribution. The tropopause separates troposphere and stratosphere, stratopause divides stratosphere and mesosphere

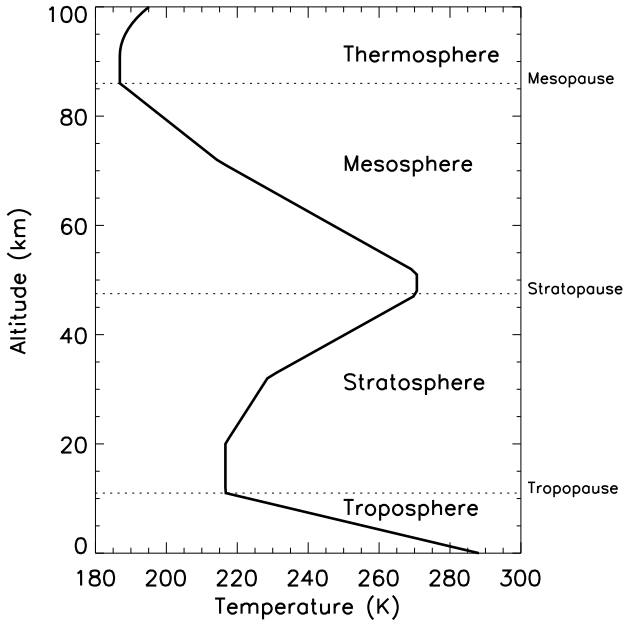

Figure 1.1: Schematic representation of the thermal structure of the atmospheric temperature based on the US Standard Atmosphere (1976).

and mesopause is the boundary between mesosphere and thermosphere. The temperature decreases with altitude in the troposphere and the tropopause decreases in altitude from the tropics to the poles and varies with respect to seasons. On average, it ranges between 8 km in the polar latitudes, 15 km in the mid-latitudes and 17 km in the tropics. The tropopause varies from ∼7 km in winter to ∼9 km in summer in the poles, from ∼12 km in winter to ∼18 km in summer in the mid-latitudes and from ∼15 km in winter to ∼20 km in summer in the tropics. All weather phenomena (e.g. clouds, rains etc.) take place in the troposphere. The region above tropopause to about 50 km is called the stratosphere, where temperature increases with height and is the focus of the present study. So the regions above the stratopause are not discussed here. The region above the tropopause until ∼110 km is termed as the middle atmosphere (Andrews et al., 1987).

1.2 Stratospheric ozone

Ozone, made up of three oxygen atoms is a minor constituent (0.000004 %) in the atmosphere. The ozone was first identified in the laboratory by Christian Fredrich Schönbein in 1840 and the presence of ozone in the air was first detected by André Houzeau in 1858 (Brasseur, 2008). Since then, routine research has been going on to measure the atmospheric concentration of ozone. Studies revealed that most of the ozone is confined to the stratosphere. Maximum ozone concentration and mixing ratio are found near 22 and 35 km respectively, depending on latitude and season. Ozone absorbs the harmful ultraviolet radiation (UV), particularly UV-B (280–315 nm) and UV-C (100–280 nm), and thus acting as a heat source responsible for the temperature positive gradient in the stratosphere. This is the only gas in the atmosphere that absorbs UV-B radiation and hence, it is considered as a vital atmospheric constituent that helps to keep life on the Earth.

Stratospheric ozone can be measured as both vertical profile and total column. General form of the measured quantities are volume mixing ratio (VMR) in parts per million by volume (ppmv), number density in molecules/ cm^3, partial pressure in mPa and Dobson Unit in DU, depending on the characteristics of the measuring instrument. Total column is

equivalent to the thickness of the ozone layer at standard temperature (0°C) and pressure (1013.25 mb). It is about 3 mm or 300 DU (8×10^{22} molecules/ m^2) for a column containing the global mean amount of ozone (Andrews et al., 1987), where 1 DU=10^{-2} mm and 1 DU=2.69×10^{16} molecules/ cm^2.

The mathematical formulations of the units are :

$$1\,DU = \frac{dA \times 1\,O3 \times 10^{14} \times V}{N_A}$$

$$1\,molecules/cm^3 = \frac{1\,VMR}{T \times 1.38 \times 10^{-19}}$$

$$1\,molecules/cm^3 = \frac{1PP}{1.38 \times 10^{-14}}$$

where mm is millimeter, dA is difference in altitude in meter (m), O3 is ozone in molecules/m^3, V is volume of ideal gas at standard temperature and pressure ($22.4\,m^3/kmol$), N_A is Avogadro's Number (6.022×10^{26} /kmol), VMR in ppmv, P is pressure in hPa, T is temperature in Kelvin (K) and PP is ozone partial pressure in milli-Pascal (mPa).

1.2.1 Stratospheric chemistry

The stratospheric ozone chemistry involves both production and natural destruction of ozone. In the stratosphere, these processes are dominated by photochemical reactions. A photochemical model for the vertical distribution of ozone in the stratosphere was first formulated by Chapman, known as the Chapman mechanism (Chapman, 1930). According to Chapman reactions, ozone is produced by the photodissociation of oxygen molecule (O_2) by UV-radiation. That is,

$$O_2 + h\nu \rightarrow O + O \qquad \lambda \leq 242\,nm \tag{1.1}$$

$$O + O_2 + M \rightarrow O_3 + M \tag{1.2}$$

where M is an inert air molecule stabilizing the reaction by removing excess energy.
The photochemical production of ozone is balanced by its loss through the photolytic process.

$$O_3 + h\nu \rightarrow O_2 + O(^3P) \qquad \lambda \leq 1100\,nm \tag{1.3}$$

$$O_3 + h\nu \rightarrow O_2 + O(^1D) \qquad \lambda \leq 320\,nm \tag{1.4}$$

$$O + O_3 \rightarrow 2O_2 \tag{1.5}$$

$$O + O + M \rightarrow O_2 + M \tag{1.6}$$

However, Chapman's ozone chemistry was not sufficient to explain the actual amount of ozone present in the stratosphere, which is lower than that predicted in Chapman mechanism. Later, it is reported that the stratospheric ozone was destroyed not solely by atomic oxygen, but several catalytic mechanisms are also involved in the natural ozone removal process, i.e.,

$$X + O_3 \rightarrow XO + O_2 \tag{1.7}$$

$$XO + O \rightarrow X + O_2 \tag{1.8}$$

$$Net : O + O_3 \rightarrow 2O_2 \tag{1.9}$$

where X is a catalyst, which is not consumed in the process. The catalysts are hydrogen (H), hydroxyl radical (OH), nitrogen oxide (NO), chlorine (Cl) and bromine (Br).

The catalytic reactions caused for the destruction of ozone are:
a) Hydrogen catalytic cycle : Bates and Nicolet (1950) discovered that the oxidation of water vapour produces OH, which plays a critical role in destructing ozone as a direct reactant or helps other ozone destruction reactions.

$$H_2O + O(^1D) \rightarrow 2OH \tag{1.10}$$
$$O + OH \rightarrow O_2 + H \tag{1.11}$$
$$H + O_2 + M \rightarrow HO_2 + M \tag{1.12}$$
$$O + HO_2 \rightarrow O_2 + OH \tag{1.13}$$
$$Net : O + O + M \rightarrow O_2 + M \tag{1.14}$$
$$OH + O_3 \rightarrow HO_2 + O_2 \tag{1.15}$$
$$HO_2 + O_3 \rightarrow OH + 2O_2 \tag{1.16}$$
$$Net : 2O_3 \rightarrow 3O_2 \tag{1.17}$$

b) Nitrogen catalytic cycle : The reaction with nitrogen oxides could represent a significant sink for ozone in the stratosphere (Crutzen, 1971) .

$$NO + O_3 \rightarrow NO_2 + O_2 \tag{1.18}$$
$$O + NO_2 \rightarrow NO + O_2 \tag{1.19}$$
$$Net : O + O_3 \rightarrow 2O_2 \tag{1.20}$$

c) Chlorine catalytic cycle : Stolarski and Cicerone (1974); Molina and Rowland (1974) pointed out that the rising atmospheric concentrations of chlorofluoromethanes produces a significant amount of Cl in the stratosphere. It undergoes a catalytic reaction that destructs ozone.

$$Cl + O_3 \rightarrow ClO + O_2 \tag{1.21}$$
$$ClO + O \rightarrow Cl + O_2 \tag{1.22}$$
$$Net : O + O_3 \rightarrow 2O_2 \tag{1.23}$$

The reaction 1.22 is faster than the reaction 1.19. So reaction 1.22 is more efficient in destroying ozone.

The destruction rate of ozone by different catalytic cycles varies depending on altitude and latitude. Figure 1.2 illustrates the relative contribution of different reactions in destroying ozone at various latitudes and altitudes. The Figure shows that the NO_X cycle is dominant in the middle stratosphere and amounts to >50 % at all latitudes. The contribution of HO_X cycle is the largest (50–90 %) in the lower and upper stratosphere without any latitudinal difference. The Cl cycle plays an important role in 20–30 and 35–45 km, contributing to about 30 % while Br cycle provides its maximum (20–50 %) in the lower stratosphere at high latitudes in the southern hemisphere (SH) and ∼10 % in the lower stratosphere of the equator and in the northern hemisphere (NH).

So ozone equilibrium is a consequence of creation and destruction processes. The photochemical production of ozone is favourable in the 200–242 nm range, the wavelength that can penetrate up to the lower stratosphere. Since UV radiation is highest in the tropics, maximum ozone is produced there, with the expected maximum in summer and minimum

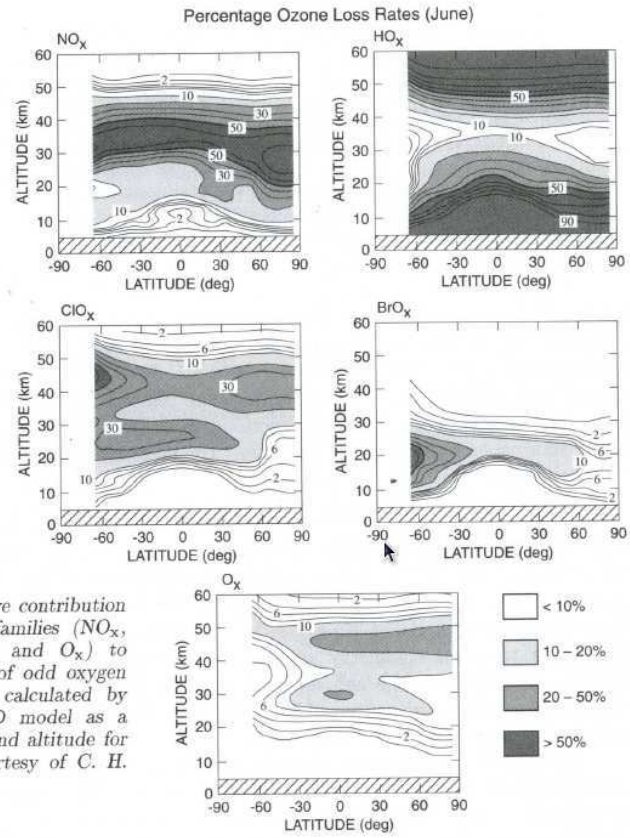

Figure 14.8. *Relative contribution of various chemical families (NO_x, HO_x, ClO_x, BrO_x, and O_x) to the destruction rate of odd oxygen in the stratosphere, calculated by the NASA/GSFC 2D model as a function of latitude and altitude for June conditions (courtesy of C. H. Jackman, NASA).*

Figure 1.2: Vertical distribution of the relative contribution of various reaction cycles in depleting ozone at various latitudes (from Brasseur et al., 1999).

in winter. Nevertheless, the observed behaviour is very different from this theoretical framework since most ozone is found in the mid to high latitudes with the highest levels in spring and the lowest in autumn while the lowest values are located in the tropics, as shown in Fig. 1.3.

Hence, it is clear that although ozone is produced from the photochemical reactions, its global distribution in the atmosphere is driven by atmospheric motions transporting ozone from its source region in the tropics to the high latitudes. These processes are described in the following section.

1.2.2 Dynamical processes

The discrepancy between the photochemical theory and observations in the distribution of ozone can be explained by the transport processes in the atmosphere. The transport of ozone from the tropical source regions to the middle and high latitudes is mainly responsible for the observed high ozone amounts in those regions. The transport processes are sensitive to temperature and pressure. Because of the high solar radiation in the tropical regions, the air warms, converges and rises through the tropical upwelling and creates a low pressure system in the equator. When it reaches upper part of the troposphere (10–15 km), it is forced to turn and moves horizontally toward the north and south poles. A portion of the air cools and sinks at about 30°N/S, resulting in a high pressure system in the subtropics.

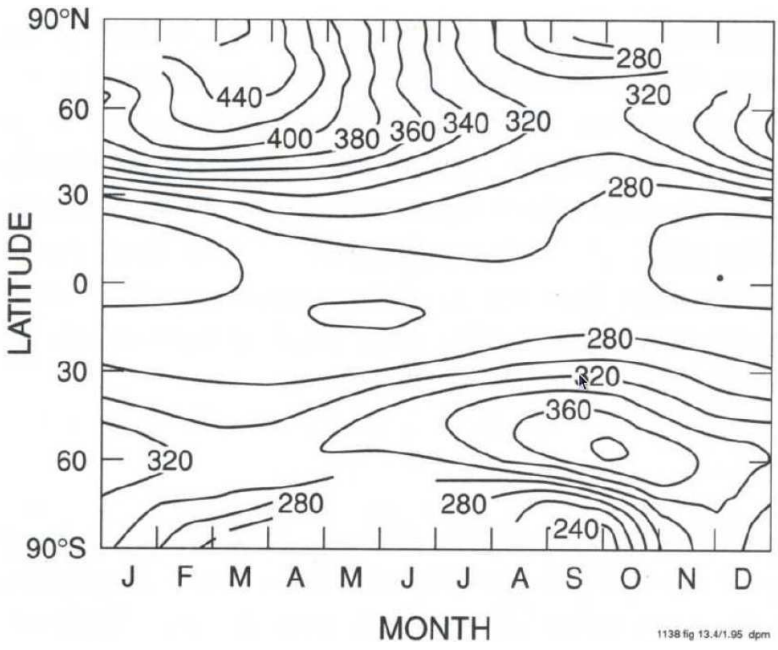

Figure 1.3: Monthly mean ozone total column abundance in DU from the TOMS observations averaged in 1979–1986 as function of latitude and season (from Brasseur et al., 1999).

Because of this pressure gradient (the subtropical high and equatorial low), air close to the surface moves from the subtropics to the equator. This circulation pattern of air is known as Hadley cell. The portion of air moving from the subtropics to the equator is deflected towards the west from east by the Coriolis force and is called tropical easterlies. The other portion of air close to the tropopause moving from the subtropics to the poles produces westerlies.

Air parcels from the troposphere enters the stratosphere in the tropics, moves towards the winter pole over a period of years and returns to the troposphere in the extratropics. This vertical transport controlled by the large-scale diabatic circulation is referred to as the Brewer-Dobson (BD) circulation in honour of the eminent atmospheric scientists, Brewer and Dobson. Because, using this mean meridional circulation Brewer explained the observed low water vapour mixing ratios in the stratosphere (Brewer, 1949) and Dobson pointed out the observed high ozone concentration in the polar lower stratosphere (Dobson, 1956). Schematic outline of the BD circulation is shown in Fig. 1.4. BD circulation consists of two meridional cells in each hemisphere with rising motion in the tropics, poleward flow at mid-latitudes and sinking motion in the polar regions. The summer stratosphere is characterised by the mean easterly flow while the winter stratosphere by mean westerly flow. During winter, the tropospheric wave disturbances propagate upward into the stratosphere, where they break and dissipate due to wave breaking processes (Haynes, 2005). This dissipation leads to a drag acting in the opposite direction to the westerly flow. Since the Earth is rotating, the Coriolis force, which is maximum in the poles, balances this drag and produces a poleward motion.

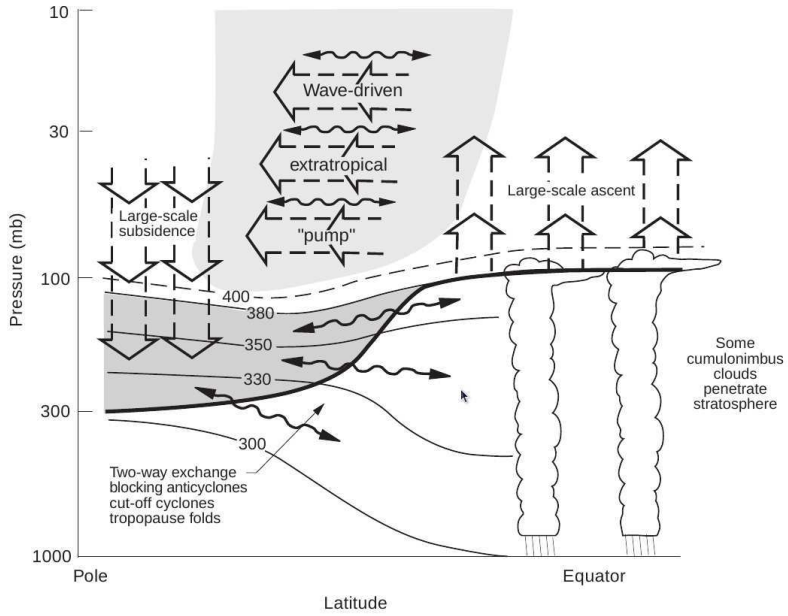

Figure 1.4: Schematic representation of the stratospheric circulation (from Holton et al., 1995).

1.3 Ozone depletion issue

Apart from the natural destruction of ozone, as mentioned in Sect. 1.2.1, the stratospheric ozone depletion is further enhanced by the higher levels of Cl and Br containing compounds emitted by the human activities. These halogen source gases of anthropogenic origin controlled under the Montreal Protocol are referred to as ozone depleting substances (ODSs). They include chlorofluorocarbons (CFCs), hydrochlorofluorocarbons, (HCFCs), brominated CFCs (halons), carbon tetrachloride (CCl_4), methyl chloroform (CH_3CCl_3) and methyl bromide (CH_3Br) (WMO, 2007, 2011). These emissions accumulate in the troposphere and are transported to the stratosphere, where they convert to reactive halogen gases by UV radiation and increases the ozone depletion. The degradation of ODSs in the stratosphere releases Cl and Br atoms, which are readily combined to form inorganic Cl (Cl_y) and inorganic Br (Br_y) compounds. Since CFCs and halons are more stable and are not decomposed in the troposphere, their use leads to an increase in the concentration of Cl and Br in the stratosphere. The most abundant Cl_y reservoirs are HCl and $ClONO_2$ and Br_y reservoirs are HBr and $BrONO_2$. These reservoirs are transformed to active Cl or Br and thus deplete stratospheric ozone. The studies (Daniel et al., 1999; Sinnhuber et al., 2009) reveal that the potential for ozone depletion by Br is significantly larger (∼40–100) than that by Cl as the Br_y reservoirs are less stable than their Cl_y counterparts.

1.3.1 Antarctic ozone loss

In 1985, a path-breaking study by Farman et al. (1985) announced a dramatic loss of ozone column in spring at the Halley-Bay station, in the Antarctic. It was later confirmed by satellite measurements and in other Antarctic regions too. The ozone profile measurements by ozone sounding (Chubachi, 1984) revealed that the loss was severe in the 12–21 km altitude range. A complete loss of ozone (saturation of ozone loss) at this altitude region was observed since early 1990s too. This ozone layer having less than 220 DU was termed

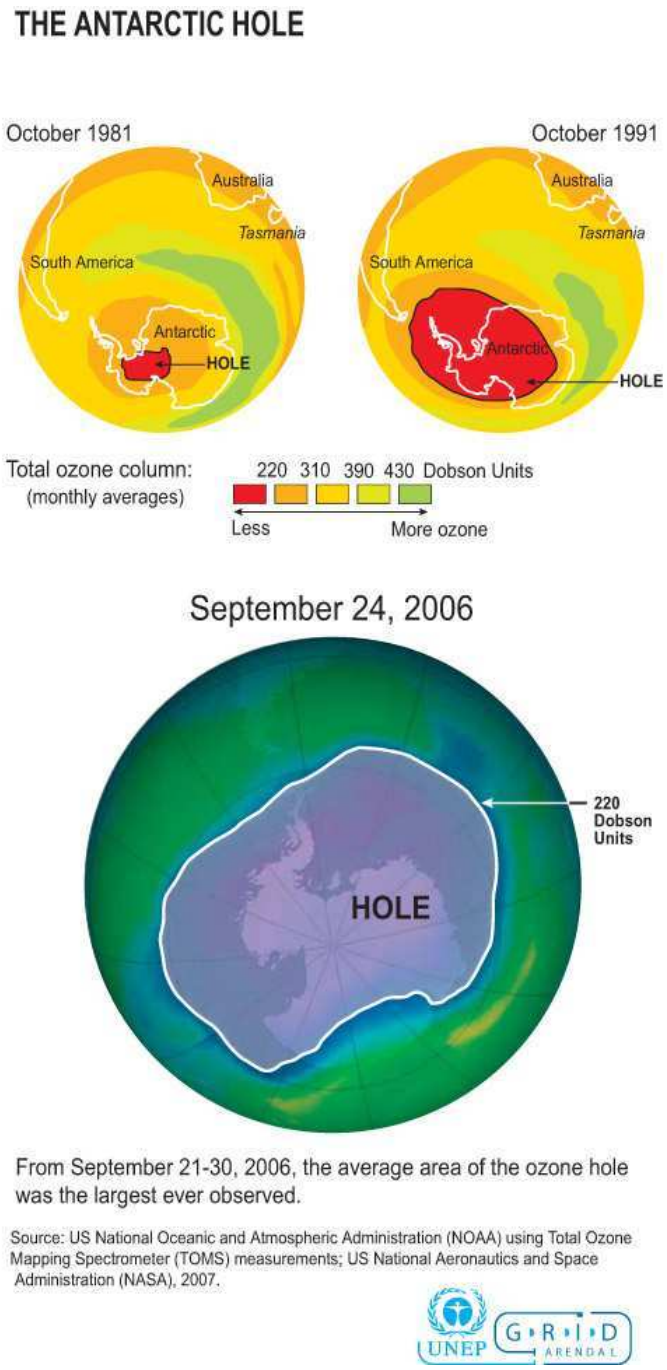

Figure 1.5: An illustration of the Antarctic ozone hole in 2006 (source : NASA).

as the Antarctic ozone hole. Figure 1.5 demonstrates the Antarctic ozone hole in 2006, the largest one (∼56 %) ever observed in the Antarctic stratosphere, in comparison with that in 1981. The ozone loss chemistry, described previously, was not sufficient to explain very rapid loss in the Antarctic. Because in the low light conditions the concentration of oxygen atoms (O) is very low. Therefore, the reactions requiring O were no longer effective there. Several theories including dynamics and chemistry were put forward for explaining this ozone loss in the polar lower stratosphere.

Figure 1.6 shows different steps leading to the depletion of ozone in the Antarctic. First, chemically active clouds in the stratosphere called polar stratospheric clouds (PSCs) are formed inside the extremely persistent Antarctic polar vortex during very cold condition, when temperature reaches below 195 K. Second, heterogeneous reactions occur on the surfaces of PSCs releasing active Cl_2 from its reservoirs (Solomon et al., 1986) and produces HNO_3 from NO and NO_2. The removal of NO and NO_2 reduces the possibility to reform $ClONO_2$ or $BrONO_2$. Third, Cl_2 undergoes photolysis and produces Cl when sunlight returns. Fourth, ozone destruction occurs through catalytic reactions with Cl. First and second processes need darkness while third and fourth steps occur in the presence of sunlight. A detailed description of these processes are given below.

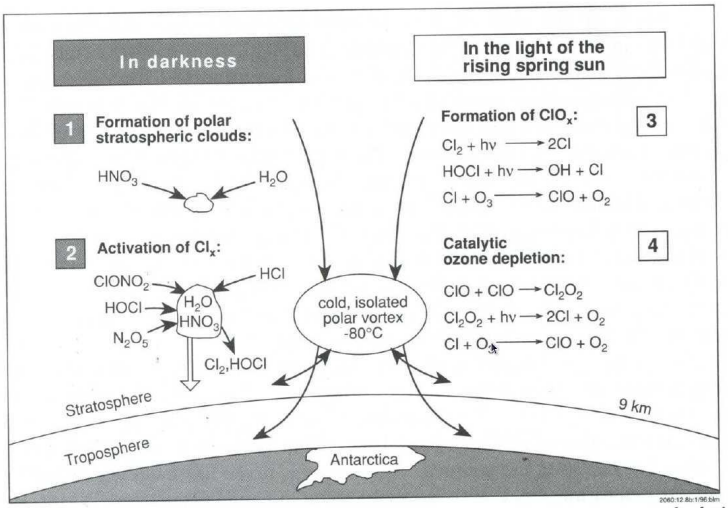

Figure 1.6: Schematic diagram showing various chemical and dynamical processes involved in the destruction of ozone in the Antarctic polar vortex (source : Brasseur et al., 1999).

Several cycles not involving oxygen atoms were proposed after the discovery of ozone hole for explaining the chemical polar ozone loss. One mechanism involves Br radicals, as reported by McElroy et al. (1986).

$$BrO + ClO \rightarrow Br + Cl + O_2 \quad (1.24)$$
$$BrO + ClO \rightarrow BrCl + O_2 \quad (1.25)$$
$$BrCl + h\nu \rightarrow Cl + Br \quad (1.26)$$
$$Cl + O_3 \rightarrow ClO + O_2 \quad (1.27)$$
$$Br + O_3 \rightarrow BrO + O_2 \quad (1.28)$$
$$Net : 2O_3 \rightarrow 3O_2 \quad (1.29)$$

Another catalytic cycle found to be important for the ozone destruction in the Antarctic lower stratosphere is the one involved with chlorine monoxide (ClO) dimer proposed by Molina and Molina (1987). High amount of ClO triggers a new catalytic reaction involving a self reaction of ClO, which is caused for the significant ozone loss.

$$ClO + ClO + M \rightarrow Cl_2O_2 + M \quad (1.30)$$
$$Cl_2O_2 + h\nu \rightarrow Cl + ClO_2 \quad (1.31)$$
$$ClO_2 + M \rightarrow Cl + O_2 + M \quad (1.32)$$
$$2[Cl + O_3 \rightarrow ClO + O_2] \quad (1.33)$$
$$Net : 2O_3 \rightarrow 3O_2 \quad (1.34)$$

The net reaction in the two cases is the destruction of two ozone molecules forming three oxygen molecules. Studies have shown that contribution of the chemical cycles ClO_X and BrO_X to the ozone loss is about 40–45 and 35–40 %, respectively in June–mid-October (Marchand et al., 2005; Kuttippurath et al., 2010). These reactions occur in the presence of visible light only. So ozone destruction due to these reactions takes place in the winter/spring, when sunlight returns to the polar stratosphere. During the term, late winter/early spring, the UV radiations are weak and hence, ozone production does not happen. Hence, if sufficient amount of ClO is generated in the atmosphere, these reactions can explain most of the ozone loss found over Antarctica. Large amount of ClO has been originated from the reactions taking place on the PSCs and are described below.

Figure 1.7: Schematic view of PSC in the Antarctic stratosphere (source : NASA).

1.3.1.1 PSCs and heterogeneous chemistry

Normally, the stratosphere is very dry and cloudless even though a thin layer of aerosol (liquid-phase binary H_2SO_4/H_2O droplets) is present in the lower stratosphere. But during polar night, when temperatures reach below 195 K in 15–25 km the background aerosols take up HNO_3 and H_2O and evolve into ternary $HNO_3/H_2SO_4/H_2O$ droplets, referred to as PSCs (Carslaw et al., 1994). Figure 1.7 shows a photograph of the PSCs in the Antarctic stratosphere. PSCs are classified into three types, Type Ia, Type Ib and Type II, according to their physical state or optical properties and chemical composition. This classification is based on air-borne lidar measurements (lidar backscatter and depolarisation ratios for PSCs) as the instrument is sensitive to the state of polarisation of the backscattered light

(Browell et al., 1990; Felton et al., 2007). Type Ia PSCs are made up of crystals of nitric acid trihydrate [NAT - (HNO_3. $3H_2O$)] and Type Ib consists of supercooled ternary solutions (STS) of $HNO_3/H_2SO_4/H_2O$. Type II PSCs are frozen water ice non-spherical crystalline particles. During austral winter heterogeneous reactions occur on the surface of PSC particles and convert the reservoir species such as $ClONO_2$ and $BrONO_2$ into more active species. The principal heterogeneous reactions are given below.

$$HCl(s) + ClONO_2(g) \rightarrow HNO_3(s) + Cl_2 \quad (1.35)$$
$$BrONO_2(g) + H_2O(l) \rightarrow HNO_3(g) + HOBr(g) \quad (1.36)$$
$$HCl(s) + BrONO_2(g) \rightarrow HNO_3(g) + BrCl(g) \quad (1.37)$$
$$HCl(l) + HOBr(g) \rightarrow H_2O(l) + BrCl(g) \quad (1.38)$$

Other heterogeneous reactions occurring on the surfaces of PSCs releasing Cl_2 are

$$ClONO_2(g) + H_2O(s) \rightarrow HNO_3(s) + HOCl(g) \quad (1.39)$$
$$HCl(s) + HOCl(g) \rightarrow H_2O(s) + Cl_2(g) \quad (1.40)$$

Another heterogeneous reaction releasing photolytically active Cl_2 by the photolysis of $ClNO_2$ is

$$N_2O_5(g) + HCl(s) \rightarrow ClNO_2(g) + HNO_3(s) \quad (1.41)$$

However, for the production of Cl atoms sunlight is required. When the sun starts to shine on the polar stratosphere at the beginning of austral spring, Cl_2 is photolysed to Cl, that enters into catalytic destruction of ozone. This is the reason why ozone is depleted in spring, when sunlight returns. Thus, above reactions accumulate the ClO concentration in the polar lower stratosphere, which then initiate the ozone destruction cycle (Reactions 1.30–1.34).

1.3.2 Arctic ozone loss

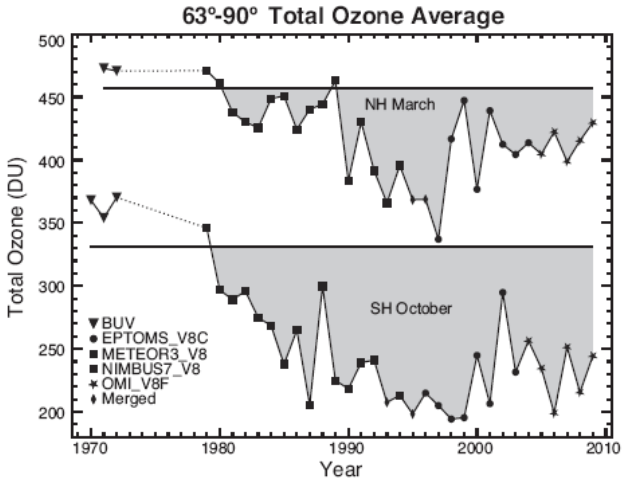

Figure 1.8: Total ozone average in March and October in the northern and southern hemispheres, respectively. The horizontal Gray lines are the average total ozone prior to 1983 in March (NH) and October (SH) and the symbols represent the satellite data in different years.

The ozone depletion was observed in the Arctic also, but not as large as in the Antarctic (Hofmann et al., 1989). The reasons outlined above for the Antarctic ozone depletion are applicable in the Arctic too. Figure 1.8 shows the differences in the total ozone averaged between 63–90° latitudes in both hemispheres. It is clear that the springtime total ozone in the NH is always larger than that in the SH. The Arctic stratosphere is warmer than the Antarctic stratosphere and thus the formation of PSCs is less frequent. The Arctic vortex is less stable because of the land mass and associated stronger wave activities in the NH. As a result, the Arctic polar vortex tends to mix with the surrounding air and does not attain complete isolation and very low temperatures. Also, wintertime transport of ozone from the tropics to the north pole is stronger. All these factors limit the Arctic ozone depletion. A diagram showing arctic ozone loss in 2011 can be found in Fig. 1.9. The ozone loss estimated from SAOZ (Système d'Analyse par Observation Zénithale) ozone total column observations by using the passive tracer method shows a range of values between 5–7 % in the warm Arctic winters and 25–30 % in the very cold Arctic winters. However, during the Arctic winter 2011 Hurwitz et al. (2011), a record ozone loss of about 2.4 ppmv at a broader altitude range of about 450–500 K or a total column loss of about 140 DU are estimated (Manney et al., 2011; Hurwitz et al., 2011; Kuttippurath et al., 2012).

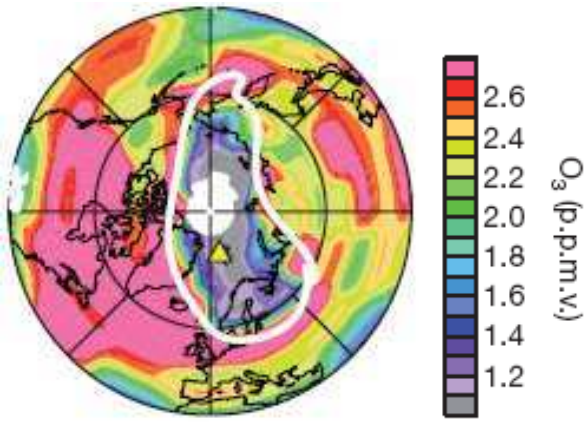

Figure 1.9: Arctic ozone loss in mid-March 2011 at an altitude of ∼20 km (Taken from Manney et al., 2011).

1.3.3 Mid-latitude ozone loss

By the discovery of springtime polar ozone depletion linked to the heterogeneous reactions on the cloud surfaces, ozone amount in other latitudes were also analysed carefully and significant ozone loss over mid-latitudes were found (WMO, 1992), although not so large as in the polar regions. In the mid-latitudes also, gas phase and heterogeneous chemistry as well as the dynamical processes are tied with the ozone reduction. Regarding chemical processes, the ClO_X gas phase catalytic cycle (Reactions 1.21–1.23) is most effective in depleting ozone in the upper stratosphere (35–45 km). The heterogeneous reactions occurring on the sulfate aerosols (Tolbert, 1996) are the main source of ozone depletion in the lower stratosphere (Hofmann and Solomon, 1989) following major volcanic eruptions. The most important heterogeneous reaction occurring on sulfate aerosols is the hydrolysis of N_2O_5 to a stable HNO_3.

$$N_2O_5(g) + H_2O(aerosol) \quad \rightarrow \quad 2HNO_3(g) \tag{1.42}$$

This hydrolysis of N_2O_5 reduces the amount of NO_X in the lower stratosphere and hence the impact of NO_X catalytic cycle on ozone destruction (Fahey et al., 1993). In contrast, formation of $ClONO_2$ is also decreased by the reduction of NO_X, which indirectly enhances the ClO_X and HO_X catalytic ozone destruction cycles (Brasseur et al., 1999). Another heterogeneous reaction predominant in the colder conditions of the mid-latitude stratosphere is Reaction 1.39. This reaction provides a path to produce Cl_2 from an active HOCl (Reaction 1.40). Another most efficient ozone loss cycle in the lower stratosphere is the BrO–ClO cycle (Reactions 1.24–1.29) (Daniel et al., 1999).

The dynamical processes also strongly influence mid-latitude ozone. They include the advection of polar air activated within the vortex mixed with the mid-latitude air and the spreading of ozone depleted air from the polar vortex to the mid-latitudes in spring, referred to as the dilution (Andersen and Knudsen, 2006). That is, when vortex breakup the filaments of ozone poor air move to the low latitudes and dilute the ozone concentration in the mid-latitudes, as demonstrated in Fig. 1.4. Hadjinicolaou and Pyle (2004) also pointed out that maximum ozone depletion in the mid-latitudes coincides with the date of polar vortex breakdown and the abundance of ozone depleted polar air in the mid-latitudes. The ozone loss in the mid-latitudes thus depends on the strength and persistence of the polar vortex and severity of ozone loss.

1.4 Equivalent Effective Stratospheric Chlorine

As seen in Sect. 1.3, Cl_y and Br_y originated from the CFCs and halons are the main cause for the stratospheric ozone depletion. The quantification of the combined impact of Cl_y and Br_y to destroy ozone is defined as the Equivalent Effective Stratospheric Chlorine (EESC).

$$EESC = Cl_y + \alpha Br_y \tag{1.43}$$

where α is the weighting factor that accounts for the greater effectiveness of Br in destructing ozone compared to that of Cl on a per-atom basis. It varies with latitude, altitude and time.

As described in Sect. 1.3, even though the amount of Br_y compounds is less than that of Cl_y, the Br catalytic cycle is more efficient in destroying ozone eventhough PSC surface is not required for the activation of Br catalytic cycle. In order to account for this, Br_y contribution is scaled by a factor α (WMO, 2007). The value of column α varies in a range from 50 to 130 from the equator to the poles depending on season. The global annual mean value of α is about 66. In the mid-latitudes, α is estimated to be about 60 in the lower stratosphere and 5 in the upper stratosphere (Sinnhuber et al., 2009).

Stratospheric EESC at different regions is calculated from the surface measurements of tropospheric ODS abundances and taking into account for the transit times (or ages) and conversion of Cl_y and Br_y. The extent of degradation of ODSs in the stratosphere is described by considering the mean stratospheric age of an air parcel (Newman et al., 2007). The mean age of air in the lower stratosphere is ∼3 years in the mid-latitudes and ∼5.5 years in the polar latitudes (Waugh and Hall, 2002; Newman et al., 2006). Therefore, EESC values are directly linked with the ODS emissions in the atmosphere. The discovery of the cause of polar ozone depletion led to the implementation of the Montreal Protocol in 1987 for controlling the vast emission of human-produced CFCs. Studies by Rinsland et al. (2003) and Lary et al. (2007) reported that levels of Cl and Br radicals are decreasing from the past decade onwards, which is clear from the EESC values too.

Figure 1.10 illustrates the values of EESC in ppt (top panel) and % (bottom panel) as a function of time in the mid-latitude and polar stratosphere. Even if the pattern of EESC is

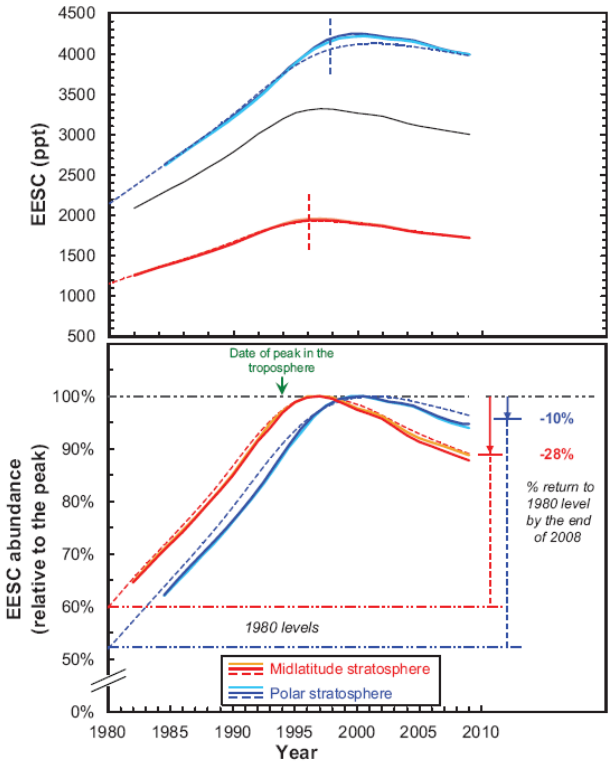

Figure 1.10: A diagram showing the evolution of stratospheric EESC in ppt (top panel) and in % (bottom panel) in the mid-latitude and polar stratosphere.

same, its growth and declining amount varies at different regions, i.e., in the mid-latitudes, the EESC values are smaller than those in the polar latitudes. Because, in the mid-latitudes the amount of inorganic halogen is lower while in the polar stratosphere, as air ages ODSs photochemically decompose so that a higher fraction of inorganic halogen is available. From the Figure, it is obvious that the EESC values increased from the 1980s and showed its peak value in 1996 and 2000 in the mid and polar latitudes, respectively and started to slowly decrease afterwards. This difference in the EESC peak year at different latitude regimes is due to the difference in the transit time or mean stratospheric age of air.

1.5 Present state of the ozone layer

1.5.1 Ozone total column measurements

The analysis of ozone measurements revealed a significant reduction in ozone total column at all latitudes. For example, a study by Stolarski et al. (2006) found negative ozone trends of -3.7 ± 0.5 DU/decade in 1978–1996 using TOMS-SBUV merged data in the latitude band of 60°S–60°N. Similarly, Fioletov et al. (2002) reported statistically significant ozone trends varying from about -0.5 to -3 %/decade from 20° to 60° latitudes in both hemispheres in 1979–2002. Recent evaluation of stratospheric ozone total column observations shows that total ozone was no longer decreasing and remains in a constant level since the mid or late 1990s (WMO, 2011). Figure 1.11 shows the total ozone deviations for different latitude bands (60°S–60°N, 90°S–90°N, 35°N–60°N and 35°S–60°S). From the figure, it is clear that the total ozone was decreasing and showed a minimum value in the mid 1990s followed by an increase, which is stabilised afterwards.

Because of the non-linearity in the evolution of ODSs after the mid-1990s, ozone trends

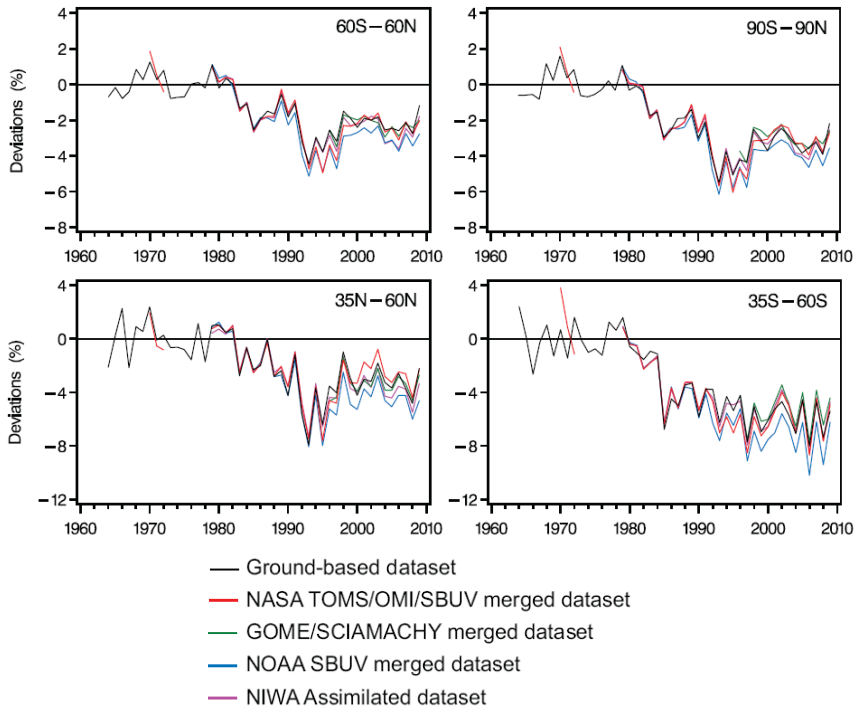

Figure 1.11: The deseasonalised total ozone deviations in 1964–2009 for the latitude bands (60°S–60°N, 90°S–90°N, 35°N–60°N and 35°S–60°S) estimated from different data sets. The zero line indicates the pre-1980 level (Taken from WMO, 2011).

were estimated using piecewise linear trend (PWLT) model in which different linear fits before and after a turning point are used and EESC time series (more detailed discussion can be found in Chapter 5). Vyushin et al. (2007) analysed ozone trends in such a way (using piecewise linear and EESC time series) from 60°S to 60°N in 1979–1995 and 1996–2008 and is shown in Fig. 1.12. The Figure shows that the PWLTs and EESC based trends in 1979–1995 (top panel) are similar in the SH while they vary slightly in the NH. The trends derived from the PWLT and EESC fits in 1996–2008 (bottom panel) differ only slightly in the SH, but largely in the NH. This discrepancy between the PWLTs and EESC based trends in the latter period can be explained using the residual circulation (Dhomse et al., 2006; Harris et al., 2008). These studies showed that the residual circulation is the cause of the recent increase in the northern hemispheric total ozone. In addition, Yang et al. (2006) found that the observed rapid increase in the ozone total column is driven by the the changes in atmospheric transport in the lowermost stratosphere. Vigouroux et al. (2008) showed significant positive trends of $2.8 \pm 2.2\,\%$/decade in Europe from the FTIR measurements. Similarly, Yang et al. (2009) evaluated a significant positive trend of $1.24\,\%$/decade in 1996–2007 from SBUV (Solar Backscatter UltraViolet) measurements averaged in 50°S–50°N.

1.5.2 Ozone vertical profile

As for the ozone total column observations, a significant decrease of upper stratospheric ozone in the 1979–1995 period was also reported in the mid-latitudes (SPARC, 1998; WMO, 2007). For instance, Randel et al. (1999) found statistically significant trends of −7 to

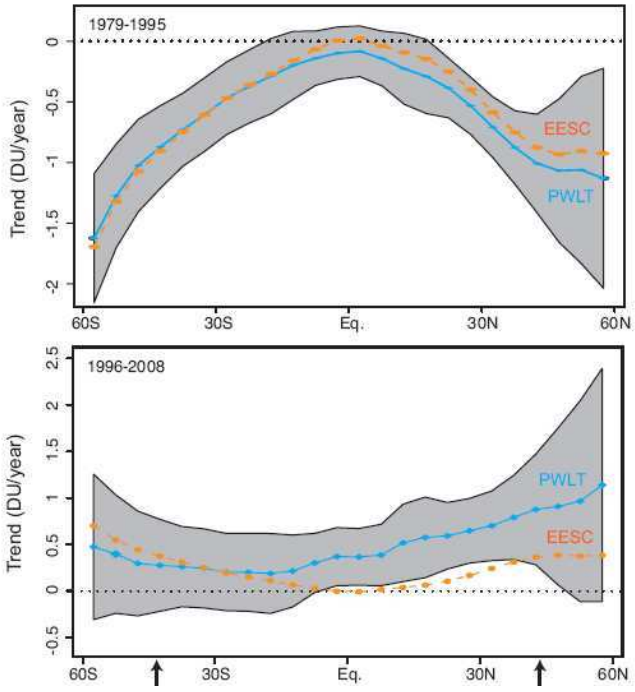

Figure 1.12: Ozone total column trends in 1979–1995 (top panel) and 1996–2008 (bottom panel) at all latitudes (Taken from WMO, 2011).

−8 %/decade at 15 and 40 km in 1979–1996 from SAGE (Stratospheric Aerosol and Gas Experiment) I/II, SBUV(/2), Umkehr and ozonesonde measurements in the northern mid-latitudes. A study by Li et al. (2002) confirmed these values, and led to estimates of about −8 and −10 %/decade in the upper stratosphere of the northern and southern mid-latitudes respectively, using SAGE I/II measurements in the same period. Logan et al. (1999) found −10 %/decade at ∼17 km by analysing sonde measurements. A similar trend ($\sim -0.8\,\%\,\mathrm{yr}^{-1}$), in the upper stratosphere (∼40 km), was also estimated by Newchurch et al. (2000) from SAGE I/II, SBUV(/2) and Umkehr measurements.

Steinbrecht et al. (2006) estimated ozone trends of about −6, −8 and −4.5 %/decade in the northern and southern mid-latitude sites and at subtropical station respectively before 1997 and a change in trend of about 7, 11 and 7 %/decade at the respective latitude regimes from the average of various ground-based and satellite ozone profile measurements. Statistical analyses using SAGE I/II and HALOE (Halogen Occultation Experiment) measurements indicate a decrease in the stratospheric ozone loss at 35–45 km since 1997 and shows signs of ozone recovery in the extra polar regions (Newchurch et al., 2003). The analysis over Tsukuba showed a significant trend of −6.0 %/decade at 30–40 km from lidar and SAGE II observations for the period 1988–1997 and a statistically insignificant trend of −0.8 %/decade after 1998 (Tatarov et al., 2009). Further, the Umkehr measurements at Belsk estimated a trend of 3 to 5 %/decade in 1996–2007 (Krzyścin and Rajewska-Wiech, 2009). The study by Jones et al. (2009), using ozone measurements from SBUV/2, HALOE, SMR, OSIRIS and SCIAMACHY, also revealed a significant trend of −7.2 %/decade in 1979–1997 and an insignificant trend of 1% /decade in 1997–2008 in the two mid-latitudes and about −4.1±0.6 and −0.5±1.5 %/decade for the respective periods in the tropics at 35–45 km. The levelling off of ozone in the last decade reported by the above-said works is also

confirmed by Steinbrecht et al. (2009), who utilised a series of satellite and ground-based observations for the analysis.

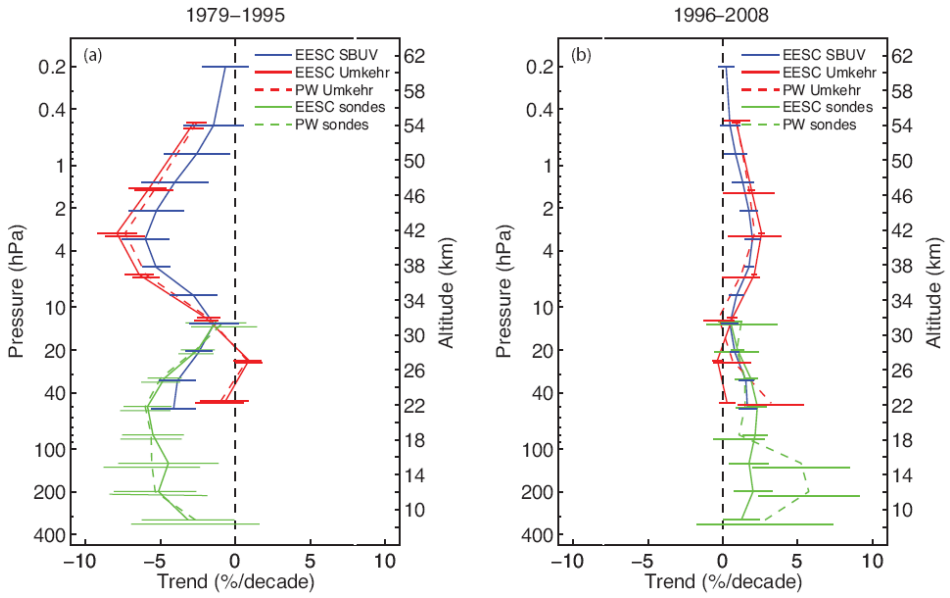

Figure 1.13: Vertical profile of ozone trends estimated from ozonesondes, Umkehr and SBUV(/2) measurements using regression made with Quasi Biennial Oscillation (QBO), solar cycle and EESC curve and converted to %/decade in 1979–1995 (left panel) and 1996–2008 (right panel) (Adapted from WMO, 2011).

Figure 1.13 represents the ozone trends in the northern mid-latitudes estimated from ozonesondes, Umkehr and SBUV(/2) for the two periods in 1979–1995 and 1996–2008 depending on the value of EESC. SBUV(/2) trends were derived from the 40–50°N zonal mean data, Umkehr trends were computed from the average ozone anomalies at Belsk, Arosa, Haute-Provence Observatory (OHP) and Boulder and the ozonesonde trends were the average of ozone trends from nine northern mid-latitude stations. In the middle and upper stratosphere, the observed decline in ozone loss is consistent with the levelling off of the ODS abundances (WMO, 2011).

1.6 Ozone recovery : different stages of ozone evolution

The satellite and ground-based observations showed a clear decrease in ozone before the mid-1990s, a stabilisation and an increase afterwards. Figure 1.14 presents the temporal evolution of ozone showing the past, present and future ozone levels between 60°S and 60°N in 1960–2100. Because of the successful implementation of the Montreal Protocol and its amendments, the observations showed a slowing of stratospheric ozone decline and is considered as the first stage of ozone evolution. This first stage of ozone evolution is already revealed in several studies, referred in Sect. 1.5. The second stage of ozone evolution is considered as the onset of increase in ozone due to the reduction in ODSs. Since the mid-1990s, the decline of ozone has completely stopped in the considered latitude regimes and the ozone levels start to stabilise. More recently, the ozone levels show a slight increase reflecting the second stage of ozone evolution. Now the main issue is to identify whether this increase in ozone is related to the ODS decrease or not.

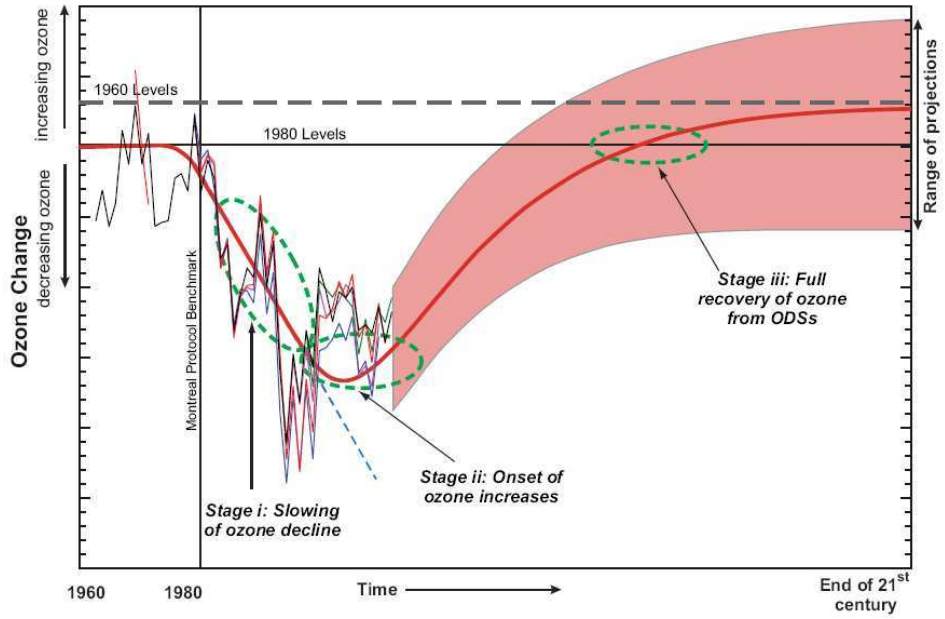

Figure 1.14: Schematic picture showing the evolution of ozone column between 60°S and 60°N in 1960–2100. The red curve shows the ozone observed to date and projected to future and the shaded region represents the simulation results of the ozone level for the future. The green circles denote different stages of ozone evolution (courtesy : WMO, 2011).

1.7 Ozone and climate

Variations in climate is caused by several parameters in which greenhouse gases (GHGs) are the most important ones. The GHGs absorb the outgoing thermal infrared (IR) radiations from the surface and thus warm the troposphere. In addition, they emit IR radiations out to space, thus cooling the stratosphere. Therefore, a change of GHG concentration warms the troposphere and cools the stratosphere (Ramaswamy et al., 2006). The most important GHGs are carbon dioxide (CO_2), water vapour (H_2O), ozone, methane (CH_4), nitrous oxide (N_2O) and ODSs. Among the GHGs, CO_2 and H_2O play important roles in the climate change in which H_2O is more powerful and more prevalent than CO_2 in the atmosphere. Because, in the presence of ODSs, the stratosphereic H_2O, enhances ozone loss and thus slow down the ozone recovery due to the reduction in ODSs (WMO, 2011).

The increased emission of CO_2 and H_2O cools the middle and upper polar stratosphere by about 2 K /dec from the late 1970s (Shepherd, 2008). The balloon-borne stratospheric H_2O measurements over Boulder showed an increase from 0.44±0.13 ppmv at 16–18 km to 0.07±0.07 ppmv at 24–26 km in 1980–1989 and increased by an average of 0.57±0.25 ppmv in 1990–2000. The H_2O decreased by an average of 0.35±0.04 ppmv in 2001–2005 and increased by an average of 0.49±0.17 ppmv in 2006–2010 (Hurst et al., 2011).

Change in stratospheric ozone affects climate through radiative effects and the resulting temperature and circulation changes. For instance, ozone depletion due to the increase in ODSs cools the lower and upper stratosphere. Because of the ozone depletion, the lower stratosphere cools by about 1 K /dec, as computed from the Microwave Sounding Unit (MSU) measurements. This cooling in the tropical lower stratosphere affects the BD circulation (Thompson and Solomon, 2009). Even if the stratospheric ozone depletion is not the principal cause of the climate change, the aspects of ozone loss and climate change

cannot be isolated.

In the same way as the change in ozone impacts climate, the variations of climate affect ozone in addition to the changes due to atmospheric ODS concentrations and other factors. Indeed, production and loss of ozone are dependent on temperature, chemical composition and circulation, which are affected by climate change. The additional stratospheric cooling can lead to the persistence of PSCs for a longer period and thus, enhances winter polar ozone depletion in the lower stratosphere (WMO, 2007, 2011). Further, climate change can alter the strength of the BD circulation and hence the distribution of ozone in the stratosphere. So changes in ozone and climate are two important factors that cannot be separated.

1.8 Conclusions

The WMO (2007, 2011) reports conclude that the stratospheric ozone depletion has stopped completely in the mid-latitudes and ozone level is stabilised. An onset of ozone recovery has already been detected in the mid-latitudes even though the polar regions are still in a state of approaching to the onset of recovery. Therefore, accurate estimation of ozone trends requires highly stable and long-standing ozone measurements. The aforementioned facts indicate the necessity of the analyses of ozone trends with new or additional data sets and also warrant to diagnose the validity of current ozone measurements to detect ozone recovery due to the recent decrease in halogen abundances. Here is the importance of our study, as we use highly resolved ozone lidar profiles in conjunction with well-validated six different satellite observations in addition to the available ozonesonde measurements. Apart from the profile measurements, a good cluster of ozone total column observations are also used to diagnose the long-term ozone trends. This thesis mainly focuses on dynamical, teleconnection and anthropogenic parameters to distinguish the cause of ozone recovery and how much increase can be attributed from the decrease in ODS abundance.

Chapter 2

Ozone lidar measurements

Contents

This thesis mainly deals with the estimation of stratospheric ozone trends. Before estimating trends a thorough analysis on the quality, consistency and stability of the data is essential for improving the accuracy in the estimated trends. The consistency of the data is checked considering ozone lidar measurement as the reference, assuming that it is stable. That means, majority of the work is based on the lidar measurements and hence, a detailed discussion of lidar instrument and its features are necessary. So this chapter deals with a brief description of lidar and the general characteristics of ozone lidar measurements, its retrieval, precision and the error analysis in Sects. 2.1 and 2.2 respectively. In the following section, the OHP ozone lidar system and the retrieval algorithm is presented in detail. Since all lidar stations use a similar technique for measuring ozone, the general principle of the measurement and retrieving algorithms are similar even if there are slight differences. Even though a special focus is given to OHP lidar, some important features of other station lidars are also described in Sect. 2.4. We have also performed some sensitivity tests using different absorption cross-sections and temperature and are discussed in Sect. 2.5. Application of their sensitivity analysis to OHP ozone lidar is described in Sect. 2.6. The final section summarises the main findings from the study.

2.1 LIDAR

Lidar is an active remote sensing instrument operating in the optical range of 100–1000 nm. It emits laser pulses of specific wavelengths into the atmosphere, which interact with the atmospheric particles and molecules and a small part of the radiation is reflected back by those objects. This backscattered radiation is collected by a telescope and transmitted to the detector, generally a photomultiplier tube, where it is converted to electrical current that is analysed by an electronic acquisition system. Lidar measures different atmospheric parameters like temperature, wind speed, densities of clouds, and the concentration of aerosols, ozone, water vapour, methane, nitrous oxide, sulfur dioxide, etc. The use of laser makes the lidar an active instrument, where the time delay between emission and return of the radiation can be measured precisely, yielding a very high vertical resolution. Depending on the desired species to be measured it uses various light matter interactions such as Rayleigh, Mie elastic scattering, Raman inelastic scattering, absorption and fluorescence.

The simplified lidar equation for a monochromatic laser pulse emission at wavelength λ considering elastic scattering is

$$N(\lambda, z) = N_e(\lambda) A \frac{\Delta z}{z^2} \beta(\lambda, z) \exp -2\tau(\lambda, z) \tag{2.1}$$

where $N(\lambda, z)$ is the number of photons backscattered during the integrating time Δt from the atmospheric layer situated at an altitude z in m (meter), $N_e(\lambda)$ is the number of photons emitted by the laser, A is the surface area of the collector (telescope) in m^2, Δz in m is the initial vertical resolution corresponding to $c\Delta t/2$, $\beta(\lambda, z)$ is the total atmospheric backscatter coefficient (Rayleigh and Mie) in m^{-1}, and $\tau(\lambda, z)$ is the atmospheric optical depth. $\tau(\lambda, z)$ depends on various parameters and is given by

$$\tau(\lambda, z) = \int_0^z [\alpha_m(\lambda, z') + \alpha_p(\lambda, z') + \sigma_c(\lambda) n_c(z') + \sum_e \sigma_e(\lambda) n_e(z')] \, dz' \tag{2.2}$$

where $\alpha_m(\lambda, z')$ and $\alpha_p(\lambda, z')$ are the molecular (Rayleigh) and particle (Mie) extinction coefficients respectively. $\sigma_c(\lambda)$ and $n_c(z')$ are the absorption cross-section coefficient and the concentration of the measured species, respectively, and $\sigma_e(\lambda)$ and $n_e(z')$ are the absorption cross-section coefficient and the concentration of other trace gases, respectively.

From equations 2.1 and 2.2, the optical thickness due to absorption by the measured species can be derived as

$$\begin{aligned} \tau_c(\lambda, z) = \frac{1}{2} \left[-\ln N(\lambda, z) z^2 + \ln N_e(\lambda) A \Delta z + \ln \beta(\lambda, z) \right] - \\ \int_0^z [\alpha_m(\lambda, z') + \alpha_p(\lambda, z') + \sum_e \sigma_e(\lambda) n_e(z')] \, dz' \end{aligned} \tag{2.3}$$

Since our species of interest is ozone, the differential absorption method employed for measuring atmospheric ozone measurements is described in detail in the following section.

2.2 Ozone DIAL system

Ozone lidar measurements are performed using the DIAL (Differential Absorption Lidar) technique. It requires the simultaneous emission of two laser beams at different wavelengths characterised by different absorption cross-sections. That is, one being in the region of high

absorption, specific to the measured parameter, and the other one being less absorbed, considered as the reference wavelength. In the case of ozone, spectral range is chosen in the UV region (200–400 nm), where its absorption is most efficient. The choice of wavelength pair differs depending on the altitude range of the measurement. For example, in the troposphere a strong UV absorption is needed to detect small ozone VMRs while in the stratosphere the radiations must reach the stratosphere and measure the high ozone concentration. Additionally, in the upper stratosphere the simultaneous measurement of low ozone number density and the decrease in atmospheric number density which provides the backscatter radiation have to be considered.

The tropospheric ozone measurements are performed using various wavelengths ranging between 266 and 316 nm wavelengths. For stratospheric ozone measurements the absorbed wavelength is selected at 308 nm, generated from a Xenon Chloride (XeCl) excimer laser. Different techniques are available for obtaining the non-absorbed wavelength and depending on the method it varies from 351 to 355 nm. The XeF laser provides the wavelength at 351 nm, first Stokes radiation by stimulated Raman scattering in a cell filled with hydrogen generates 353 nm and the third harmonic of a Nd:YAG (Neodymium-doped Yttrium Aluminum Garnet) laser gives light at 355 nm. Another important requirement for the ozone lidar measurement is the presence of clear sky since the laser radiation is rapidly absorbed by clouds and only cirrus can be tolerated for accurate stratospheric ozone measurements.

2.2.1 Retrieval

Now we need to retrieve ozone number density from the detected lidar signal as described in Eq. 2.1. For that we use the following procedure, as described in Godin (1987). The ozone number density $n_{o3}(z)$ is retrieved at an altitude z from the lidar signals as (Godin et al., 1989)

$$n_{o3}(z) = \frac{-1}{2\Delta\sigma_{o_3}(z)} \frac{d}{dz} ln \left(\frac{P(\lambda_1, z) - P_{b1}}{P(\lambda_2, z) - P_{b2}} \right) + \delta n_{o3}(z) \tag{2.4}$$

where $P(\lambda_1, z)$ and $P(\lambda_2, z)$ are the number of photons detected at wavelengths λ_1 (absorbed) and λ_2 (non-absorbed) respectively, P_{b1} and P_{b2} are the background radiation at wavelengths λ_1 and λ_2 respectively and $\Delta\sigma_{o_3}(z)$ represents the differential ozone absorption cross-section $(\sigma_{o_3}(\lambda_1, z) - \sigma_{o_3}(\lambda_2, z))$. $\delta n_{o3}(z)$ is the correction term considering the absorption by other atmospheric constituents, Rayleigh and Mie differential extinction and scattering, and can be expressed as

$$\delta n_{o3}(z) = \frac{1}{\Delta\sigma_{o_3}(z)} \left[\frac{1}{2} \frac{d}{dz} ln \frac{\beta(\lambda_1, z)}{\beta(\lambda_2, z)} - \Delta\alpha_m(z) - \Delta\alpha_p(z) - \sum_e \Delta\sigma_e n_e(z) \right] \tag{2.5}$$

where $\frac{1}{\Delta\sigma_{o_3}(z)} \left[\frac{1}{2} \frac{d}{dz} ln \frac{\beta(\lambda_1, z)}{\beta(\lambda_2, z)} \right]$ is the differential atmospheric scattering with $\beta(\lambda, z)$ as the sum of Rayleigh and Mie backscatter coefficients. $\Delta\alpha_m(z)$ is the difference between Rayleigh extinction coefficients and $\Delta\alpha_m(z)/\Delta\sigma_{o_3}(z)$ is the differential Rayleigh extinction. Similarly, $\Delta\alpha_p(z)$ is the difference between Mie extinction coefficients and $\Delta\alpha_p(z)/\Delta\sigma_{o_3}(z)$ is the differential Mie extinction. $\sum_e \Delta\sigma_e n_e(z)/\Delta\sigma_{O_3}(z)$ is the differential absorption extinction by other atmospheric constituents.

Hence ozone number density can be deduced from the difference in slope of the logarithm of the returned lidar signals. There is no need of instrument calibration with this technique as it does not require any instrumental constant for ozone retrieval and hence, it is a self-calibrated technique. The laser wavelengths used for the ozone measurements are chosen such that the term δn_{o3} is less than 10% of the derived ozone (n_{o3}).

2.2.2 Precision

The precision of the retrieved ozone number density is defined by the statistical error in the detection process because the signals detected by photomultipliers follow the Poisson statistics. So the statistical error in ozone is calculated from the Poisson statistics as

$$\varepsilon_s(z) = \frac{1}{2n_{o3}(z)\Delta\sigma_{o3}(z)\Delta z}\sqrt{\sum_{i,j}\frac{c_j^2 P_{i,j}}{N_i(P_{i,j}-P_{bi})^2}} \tag{2.6}$$

where $\varepsilon_s(z)$ is the statistical error, Δz is the initial vertical resolution of the acquisition system, $P_{i,j}$ is the lidar signal at wavelength λ_i from altitude z_j, c_j are the coefficients of the derivative filter used to differentiate the signals and P_{bi} and N_i are the background radiation and the number of laser shots at wavelength λ_i, respectively.

Statistical error is larger in the upper stratosphere due to the rapid decrease in the signal-to-noise ratio, and so, the vertical resolution of the measurement is degraded to reduce the error. So the final statistical error depends on various factors such as experimental system characteristics, the duration of the measurement (T_a), the final vertical resolution (Δz_f), the telescope area (A) and the laser power (P_o) and are linked through the relation

$$\varepsilon_s(z) \propto (A\Delta z_f^3 P_o T_a)^{-1/2} \tag{2.7}$$

Commonly, low pass filters differing in number of points with respect to altitude is used to derive the vertical resolution of the measurements (Godin et al., 1999). i.e., the vertical resolution is estimated from the cut off frequency of the numerical filter that varies with the number of points used. Hence, the vertical resolution of the DIAL stratospheric ozone measurements varies from several hundred meters in the lower stratosphere to several kilometers in the upper stratosphere.

2.2.3 Error analysis

The accuracy of the DIAL ozone measurement depends on the accuracy of the ozone absorption cross-section, the estimation of δn_{o3}, the laser line width and on linearity of the acquisition device (Godin-Beekmann et al., 2003). The laser line width introduces a small error of $\pm 0.8\%$, which can be reduced to less than $\pm 0.2\%$ by monitoring laser spectral emission. The term δn_{o3} corresponds to less than 10% of the measured ozone. The ozone absorption cross-section and the evaluation of Rayleigh extinction term in δn_{o3} depend on the temperature profile. So the accuracy of ozone measurements in turn depends on the pressure and temperature (P/T) profiles used for the ozone retrieval.

Interferences of other minor constituents on the ozone absorption also induces some errors to the ozone retrieval. The main trace gases influencing the ozone absorption in the 300–350 nm range are SO_2 and NO_2 because of their similar absorption cross-sections as that of ozone. However, SO_2 does not interfere much the stratospheric ozone if there is no massive ejection from any process such as volcanic eruption. In the case of high stratospheric aerosol loading conditions ozone measurements could be perturbed by the presence of SO_2, but do not last for more than 40 days as its life time is about 30–40 days. In the same way, NO_2 also causes errors to the ozone measurements and is estimated to be of 0.4% at 25–30 km.

The most important error source associated with the ozone measurement in the lower stratosphere is the presence of volcanic aerosols. Under high aerosol loading conditions, aerosols at the volcanic cloud altitude perturb the ozone profile locally and the correspond-

ing error is expressed as

$$\varepsilon_a(z) = -\frac{1}{\Delta\sigma_{o3}(z)}\left(\frac{1}{2}\frac{d}{dz}\ln\frac{\beta(\lambda_1,z)}{\beta(\lambda_2,z)} - \Delta\alpha_p(z)\right) \tag{2.8}$$

So $\varepsilon_a(z)$ is related to the spectral variation of atmospheric backscatter and extinction coefficients. In the presence of aerosols $\varepsilon_a(z)$ is dominated by the backscatter term, directly linked to the aerosol profile. In the case of very strong aerosol loading, this term can exceed 100% in the layers affected by aerosol. This problem is solved by detecting additional lidar signals corresponding to the first Stokes vibrational Raman scattering by atmospheric nitrogen of the laser beams. The Raman wavelengths corresponding to 308 and 355 nm are 331.8 and 386.7 nm respectively. These wavelengths allow an ozone profile to be observed, much less perturbed by the presence of volcanic aerosols (McGee et al., 1993). The ozone number density from the lidar signals received at the Raman wavelengths λ_1^R and λ_2^R can be determined as

$$n_{o3}^R(z) = -\frac{1}{\Delta\sigma_{o3}^R(z)}\frac{d}{dz}ln\left(\frac{P(\lambda_1^R,z) - P_{b1}^R}{P(\lambda_2^R,z) - P_{b2}^R}\right) + \delta n_{o3}^R(z) \tag{2.9}$$

where $\Delta\sigma_{o3}^R(z) = \sigma_{o3}(\lambda_1,z) - \sigma_{o3}(\lambda_2,z) + \sigma_{o3}(\lambda_1^R,z) - \sigma_{o3}(\lambda_2^R,z)$, $P(\lambda_i^R,z)$ and P_{bi}^R are the lidar and background signals received at Raman wavelength λ_i^R, respectively and the correction term $\delta n_{o3}^R(z)$ is given as

$$\delta n_{o3}^R(z) = -\frac{\alpha(\lambda_1,z) - \alpha(\lambda_2,z) + \alpha(\lambda_1^R,z) - \alpha(\lambda_2^R,z)}{\Delta\sigma_{o3}^R(z)} - \sum_e \frac{\Delta\sigma_e^R}{\Delta\sigma_{o3}^R(z)} n_e(z) \tag{2.10}$$

where $\Delta\sigma_e^R = \sigma_e(\lambda_1) - \sigma_e(\lambda_2) + \sigma_e(\lambda_1^R) - \sigma_e(\lambda_2^R)$

The advantage of this method is the removal of aerosol contribution to the backscatter component and its disadvantage is the loss of accuracy of ozone measurement due to smaller Raman scattering efficiency and hence, the measurement based on Raman signals is not possible above 30 km. The error on the Raman ozone profile linked to the aerosol extinction is found to be less than 5%.

2.3 The ozone lidar system at OHP

The ozone lidar system at OHP (43.93° N, 5.71° E) uses DIAL technique for measuring stratospheric ozone since 1986. Since then, various improvements have been made in the experimental set-up among which the most important one is the implementation of a new optical and electronic detector in 1993. The schematic picture of OHP ozone lidar system is shown in Fig. 2.1 and a detailed description of the new experimental set-up is discussed in the following sections.

2.3.1 Transmitter

The lidar system includes a Lambda Physik EMG 200 excimer laser for the ozone absorbed laser radiation at 308 nm and the third harmonic of a continuum Nd:YAG laser for the reference wavelength at 355 nm. Excimer laser operates at 100 Hz and the output energy is 200 mJ/pulse. The Nd:YAG laser operates at 50 Hz and its output energy is adapted to provide a return signal equivalent to the on-line signal at 40 km altitude, which results in an emitted pulse energy of ∼60 mJ. Additionally, two beam expanders are used to reduce the divergence of both lasers to 0.2 and 0.1 mrad at 308 and 355 nm respectively.

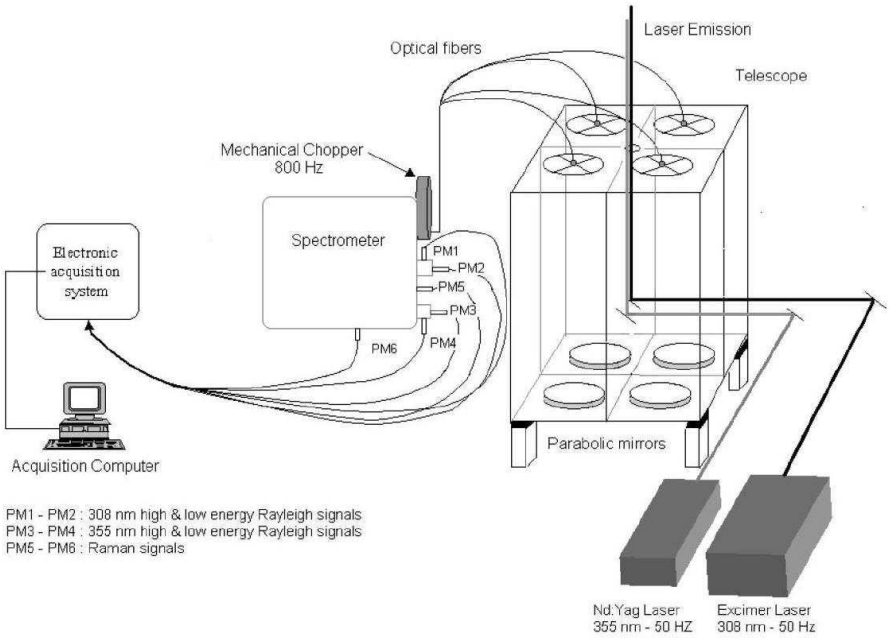

Figure 2.1: Schematic view of the OHP lidar system (Reproduced from Godin-Beekmann et al., 2003).

2.3.2 Optical receiver

The back scattered radiations of the emitted laser pulses is collected by an optical receiver consisting of four Newtonian telescopes having F/3 mirrors of 0.53 m diameter. These mirrors collect a fraction of the backscattered light that is transmitted to the optical analysing device through the optical fibers mounted on the focal plane of the mirrors, which can be moved vertically for focusing and horizontally for the alignment. As the transmission of the emitted laser beams is in the center of the mirrors, the system can be considered as quasi-coaxial. The optical device includes the imaging optics, a mechanical chopper and a spectrometer. The chopper consists of a 40 W cooled motor, rotating at 24000 rpm in primary vacuum.

The spectrometer comprises a collimated mirror for the incoming light, a holographic grating having 3600 grooves/mm providing a dispersion of $0.3\,\mathrm{nm\,mm^{-1}}$ with an efficiency of 52%. The spectrometer separates the backscattered radiations into the emitted laser beams at 308 and 355 nm (Rayleigh signals) and at 331.8 and 386.7 nm (Raman signals). To account for the high dynamic range of the lidar signals the elastically scattered Rayleigh signals are separated into a high and low energy channels so that the lidar set up consists of 6 optical channels.

2.3.3 Detection and acquisition

The 6 optical channels are detected by bialkali Hamamatsu photomultiplier tubes (PMTs), characterised by a quantum efficiency of ∼20% in the 300–400 nm spectral range. The PMT provides current pulses when photons strike the photocathode. They are amplified by a 250 MHz bandwidth amplifier resulting in its broadening up to 5 ns and the current signals are converted to voltage signals. In addition to the chopper, electronic gating of the PMT is used for the high energy Rayleigh signal detection that reduces the signal-induced noise

in these channels.

These signals are then directed to the acquisition system that uses photon counting method to process the electronic lidar signals. For that, high speed counters (250 MHz) operated with 1024 time gates of 1μs corresponding to a sampling vertical resolution of 150 m are used. Each channel is equipped with two counters in parallel to avoid the dead time between two memory bins. The overlap between the pulses of finite duration restricts the linearity of the counter, which mostly affects the Rayleigh signals. It is managed by the use of two optical channels for Rayleigh signals. All these processes are controlled by a computer program and the master clock is set at 800 Hz and is provided by a mechanical chopper or a quartz crystal. The trigger of the counter is set by the laser light pulse, which is detected by a fast photodiode and converted to a transistor-transistor-logic signal. The six counting channels are transferred simultaneously to the computer with the acquisition time of 1024 μs. The data are averaged over 1000 shots corresponding to a temporal resolution of 200 s.

2.3.4 Ozone retrieval algorithm

The retrieval algorithm is generally based on the differential lidar equation formalism. First, to increase the signal-to-noise ratio, the lidar signals are time averaged during the measurement period (3–4 h in general), taken as the temporal resolution of the measurement. Then, a certain number of corrections such as background correction and dead time correction are applied to the averaged signals. The former term is related to the estimation of background light using linear or polynomial regression in the 80–150 km altitude range, where the lidar signal is negligible. The latter term is linked with the saturation of photon counting used for the signal acquisition in the lower ranges. In addition to the differentiation, a low pass filter is used in the DIAL technique to account for the rapid decrease of signal-to-noise ratio in the higher altitudes (above 40 km). Generally, the ozone number density is computed from the difference in the derivative of the logarithm of each lidar signal fitted to a straight line, or to a second order polynomial or to higher order polynomials. At OHP, the second order polynomial fit is used to derive the ozone number density (Godin et al., 1999).

The Rayleigh high and low energy and Raman signals optimise the accuracy of the ozone profile in the upper, middle-low and lower stratosphere respectively. In background aerosol loading conditions, the low energy Rayleigh signals provide more vertically resolved profiles than the Raman signals in the lower stratosphere, but the use of these signals in the lowermost stratosphere is prevented by the saturation of the photon counters. Hence, a correction called pulse pile-up correction is applied to correct for this saturation. The equation used to compute the true photon count rate from the observed count rate is

$$P_c = 1 + [(1 - x)P_r - 1] \exp(-xP_r) \tag{2.11}$$

where P_c is the observed photon count rate, P_r is the true count rate and $x = 1/P_{max}$ with P_{max} is the maximum observed count rate.

For high energy Rayleigh signals, x is adjusted for each wavelength in order to obtain the best agreement between the slopes of both low and high energy Rayleigh signals. For the low energy Rayleigh signals, Raman signal is used by computing reference Rayleigh slopes from the Raman slopes, the derived Raman ozone profile and the Rayleigh extinction correction. So the final ozone profile is retrieved by combining the slopes of low and high energy Rayleigh signals at first and then by combining the Raman and the composite Rayleigh ozone profiles. The altitude range, where both profiles are combined depends on the aerosol content. It is around 14–15 km in the case of background aerosol conditions while

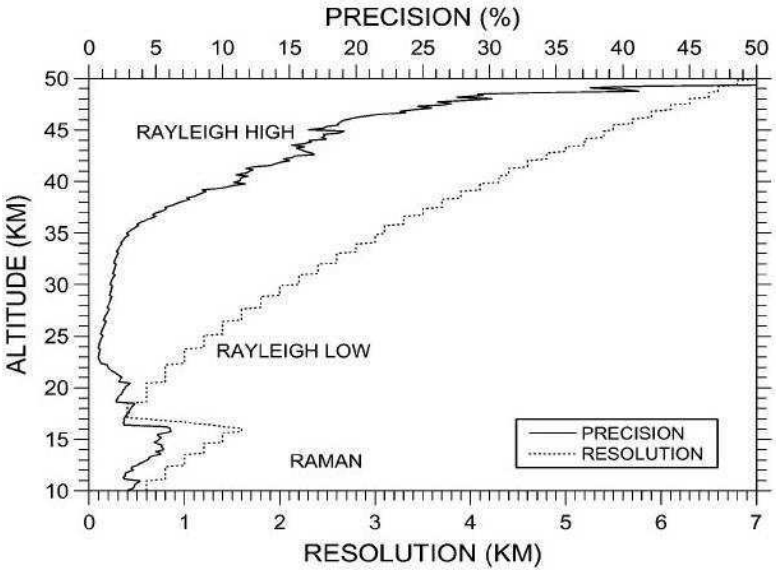

Figure 2.2: The precision and vertical resolution of OHP ozone lidar measurement (Reproduced from Godin-Beekmann et al., 2003).

high energy Rayleigh channels are used from 18 to 22 km. At the end, both Raman and composite Rayleigh profiles are corrected from the Rayleigh extinction using the pressure-temperature profiles obtained from nearby radio soundings performed in Nîmes in the lower stratosphere and the COSPAR International Reference Atmosphere 1985 (CIRA-85) model in the upper stratosphere.

2.3.5 Features of OHP lidar measurements

The optical receiver installed in 1993 enabled the ozone lidar system to measure in the lowermost stratosphere even in the presence of volcanic aerosols. The simultaneous acquisition of all lidar signals improved the observational capacity in terms of temporal resolution and accuracy. Thus, the average number of measurements per year increased from ∼40 in 1986–1993 to ∼110 from 1994 onwards, with a maximum of 190 in 1997. The typical duration of an ozone measurement in the whole stratosphere with the present DIAL system at OHP is 4 hours. The precision and vertical resolution of ozone measurement is shown in Fig. 2.2. The precision ranges from about 5% below 20 km to more than 20% above 45 km. The vertical resolution ranges from 0.5 km at 20 km to about 2 km at 30 km, and it increases to ∼4.5 km at 45 km. The average accuracy ranges from ∼5% below 20 km to more than 10% above 45 km and the best accuracy of 3% is found in the 20–45 km altitude range (Godin-Beekmann et al., 2003). The altitude range of each profile varies depending on the presence of clouds in the lower stratosphere and varied signal-to-noise ratio in the upper stratosphere. The profiles are cut when 80% statistical error is reached.

2.4 Features of other NDACC lidar measurements

The NDACC lidar stations considered in the study include the lidars from Meteorological Observatory Hohenpeissenberg (MOHp: 47.8°N, 11°E), Tsukuba (36°N, 140°E), Table Mountain Facility (TMF: 34.5°N, 117.7°W), Mauna Loa Observatory (MLO: 9.5°N, 155.6°W) and Lauder (45°S, 169.7°E). All lidar stations use DIAL method for measuring stratospheric ozone with 308 nm as the ozone absorption wavelength. The main difference among the lidars is in the selection of reference wavelength. Most lidar stations use

355 nm as the reference wavelength except MOHp and Lauder lidar, which use 353 nm over the whole period and, TMF and MLO lidars used this configuration until 2000 and then changed to 355 nm (Leblanc and McDermid, 2000). Other differences among the lidars are in the receiving system and the number of channels used to detect the lidar signal in order to increase their dynamical range. At Tsukuba (Tatarov et al., 2009) and Lauder (Brinksma et al., 2000), 6 channels (4 Rayleigh and 2 Raman) are used to measure ozone. However, only 2 receiving channels (Rayleigh) are used at MOHp (Steinbrecht et al., 2009a) and, 8 channels at TMF (4 at 308, 332 nm; 4 at 355, 387 nm) and MLO (3 at 308, 332 nm; 5 at 355, 387 nm). The precision of lidar ozone measurements decreases generally from 1% up to 30 km, 2–5% at 40 km and to 5–25% at 50 km.

2.5 Sensitivity tests

2.5.1 Ozone absorption cross-section

Absorption cross-section is a measure of the probability of a molecule to absorb photon at a particular wavelength. It is proportional to the intensity of absorption or emission between the two energy levels and is expressed in cm^2/molecule. The absorption cross-section of a substance can be determined from the Beer-Lambert law as

$$I(\lambda) = I_0(\lambda) \exp(-\sigma(\lambda) N l) \tag{2.12}$$

where I_0 and I are intensities, in W/m^2, of the incident and transmitted light, respectively, $\sigma(\lambda)$ is the absorption cross-section in cm^2, N is the number density of absorbing particles in molecules/cm^3 and l is the cell optical path in cm or the distance the light travels through the material.
There are different groups performing experiments for the determination of ozone cross-sections. Most commonly used cross-sections are the Bass and Paur (BP) and Brion-Daumont-Malicet (BDM) cross-sections. The BP cross-sections are measured over 230–350 nm wavelength range for temperatures 203, 223, 246, 273, 276 and 280 K based on the assumption that the ozone cross-section at 253.65 nm mercury line is temperature independent (Bass and Paur, 1984). BDM ozone cross-sections are provided at 218, 223, 243, 273 and 295 K in the spectral range 195–345 nm except for the measurements at 273 K which are limited to 300–345 nm (Daumont et al., 1992). BDM cross-sections at 295 K are now available in the 345–830 nm wavelength range too (Brion et al., 1998).

2.5.2 Temperature and wavelength dependence of cross-section

Figure 2.3 shows the spectral variations of BDM (top) and BP (bottom) ozone cross sections with wavelengths, in the Hartley (200–310 nm) and Huggins (310–345 nm) bands, at different temperatures. The wavelength ranges used for the DIAL ozone measurements in the troposphere and stratosphere are also shown on the Figure. It is clear that the cross-section decreases as wavelength increases. That is, ozone cross-section at 355 nm is less than that at 308 nm. The cross-sections at different temperatures show a strong continuity and are identical until 310 nm, indicating a weak temperature dependence in the Hartley band. Above 310 nm or in the region of Huggins bands, the cross-section varies with temperature. In the 305–315 nm range, temperature dependence is almost linear and ∼15% difference is observed between the cross-sections at 218 and 295 K. However, above 315 nm the temperature effect becomes prominent and increases progressively as wavelength increases, where the difference in cross-section at the extreme temperatures reaches more than 50%. The features are the same for BP too.

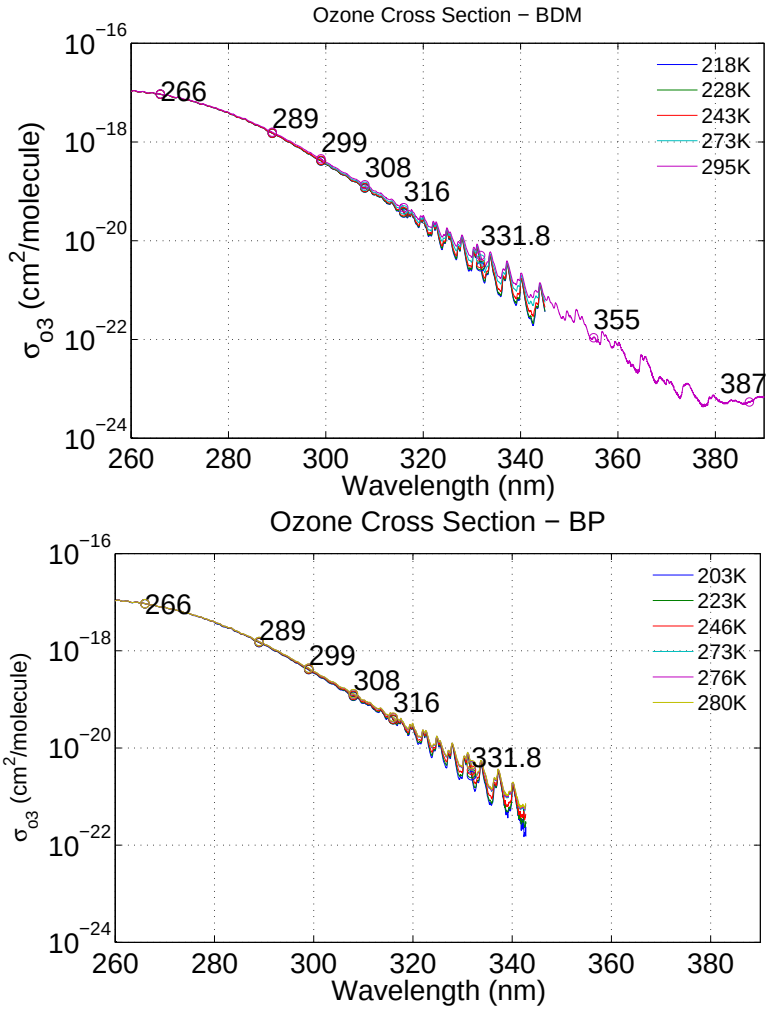

Figure 2.3: Spectral variation of the temperature dependence of ozone cross-section from BDM (top) and BP (bottom). The wavelengths used for the DIAL ozone measurements in the troposphere and stratosphere are also marked.

2.5.3 Comparison between BP and BDM cross-sections

A sensitivity study is performed to find out the differences in the derived ozone number density using BP or BDM ozone absorption cross-sections. We have seen that the ozone cross section decreases largely as wavelength increases, i.e. the ozone cross-section in the non-absorbed wavelength regions (355 and 387 nm) is about 3 orders of magnitude less than that in the absorbed wavelength regions. The emission range of the XeCl excimer laser is between 307.9 and 308.2 nm. However, the variations in the ozone cross-sections over this range is very small. Because of these reasons, the ozone absorbed Rayleigh wavelength at 308 nm and the corresponding Raman wavelength at 331.8 nm are used for the present sensitivity analysis.

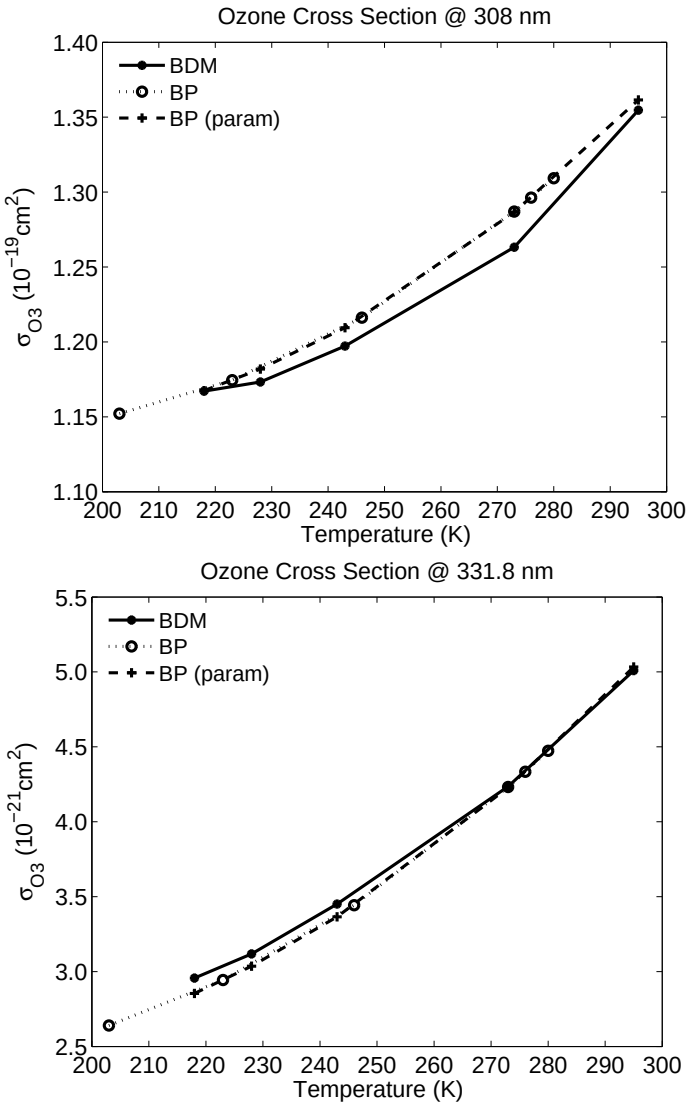

Figure 2.4: Variation of ozone absorption cross-sections (BDM, original BP and the parameterised BP) with respect to temperature, at 308 (top) and 331.8 nm (bottom).

BP and BDM ozone cross-sections are available at different temperatures. So for comparison BDM temperatures are taken as the reference and BP cross-sections at BP temper-

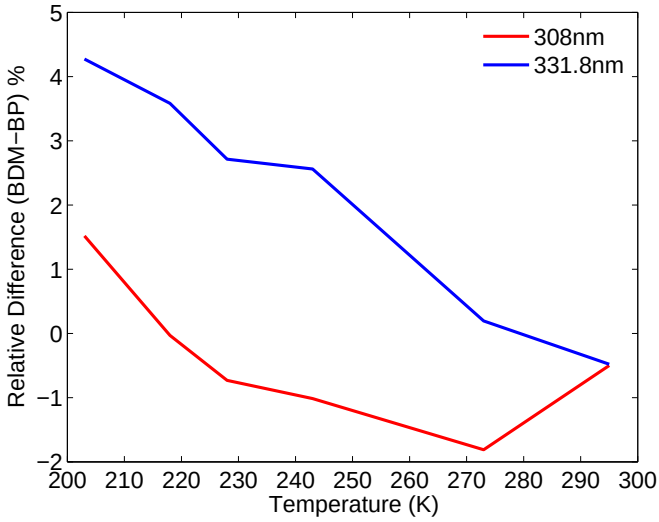

Figure 2.5: Relative deviations between BP and BDM ozone cross sections at 308 and 331.8 nm with respect to temperature.

atures are converted to the BDM temperatures by performing a second order polynomial parameterisation as proposed in (Bass and Paur, 1984)

$$\sigma_{o3} = c_0 + c_1\theta + c_2\theta^2 \tag{2.13}$$

where θ is the BDM temperature in $^{\circ}C$ and c_0, c_1 and c_2 are the quadratic coefficients computed from all the available spectra (archived from the ACSO website: http://igaco-o3.fmi.fi/ACSO/).

Figure 2.4 presents the ozone absorption cross sectional differences among BDM, BP (at BP temperatures) and the parameterised BP (at BDM temperatures) with respect to temperature, at 308 (top panel) and 331.8 nm (bottom panel). The BP cross-section at 203 K is also included in the parameterised BP cross-section because in the stratosphere temperatures can reach below 218 K particularly in the tropics above tropopause. From the Figure it is clear that the BP ozone cross-sections are always larger than the BDM cross-sections at 308 nm while they are lower than the BDM cross-sections at 331.8 nm until 273 K and are slightly higher above this temperature. Also, the ozone absorption cross-section is more variable with temperature at 331.8 nm than at 308 nm. To better understand the difference between BP and BDM cross-sections, the relative difference between them is calculated at 308 and 331.8 nm and is shown in Fig. 2.5. It shows a large difference between the wavelengths. The relative differences at 308 nm is always negative and do not exceed $\pm 1.8\%$, while the differences at 331.8 nm are larger and positive at 203–273 K with values ranging from 4.2 to 0.4% respectively, and negative (-0.4%) at 295 K.

2.5.4 Comparison between BP and BDM ozone number densities

The ozone number density is inversely proportional to the ozone cross-section. To find out the effect of change in cross-section to the derived number density, relative differences in ozone from the BP and BDM cross-sections are calculated using the following equation

$$\Delta n_{o3} = \frac{\Delta\sigma_{o3}^{BP}}{\Delta\sigma_{o3}^{BDM}} - 1 \tag{2.14}$$

Because of the very small ozone cross-section at 355 nm, the Rayleigh (308 nm) and the combined Rayleigh-Raman (308+331.8 nm) wavelengths are taken into account for the comparison. Figure 2.6 displays the relative difference in ozone retrieved using BP and BDM

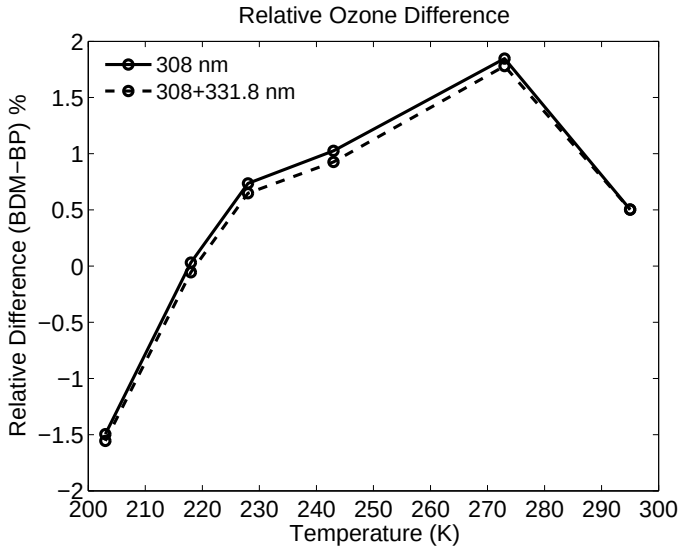

Figure 2.6: Relative differences of ozone number densities derived from the BP and BDM cross-sections at Rayleigh (308 nm) and combined Rayleigh-Raman (308+331.8 nm) wavelengths.

ozone cross-sections for the measurements at 308 and 308+331.8 nm wavelengths in the range 200–300 K. Since the BDM cross-sections are not available at 203 K, a polynomial fit is applied to the BDM data to extrapolate to the lowest BP temperature (203 K). The differences are nearly the same at the two DIAL retrievals. It is clear from Fig. 2.4 that the ozone cross-sections at 331.8 nm is 2 orders of magnitude less than that at 308 nm. So the combined Rayleigh-Raman cross-section is predominant by the Rayleigh cross-sections. The differences increase from −1.6% at 203 K to 1.8% at 273 K and decrease to 0.5% at 295 K.

2.5.5 Temperature dependence of ozone retrieval

The effect of change in cross-section on the derived ozone number densities is evaluated at various latitudes and at different altitudes using temperature data from CIRA-85 atmospheric model (Godin-Beekmann and Nair, 2012). The analysis is performed at the 65, 45 and 20° latitudes on both hemispheres, representing the locations of NDACC lidar stations. The BP and BDM cross-sections at BDM temperatures and at 203 K are interpolated to the CIRA temperatures (at different altitudes) in each month for those latitudes. The CIRA temperatures are less than 203 K below 25 km in the tropics (20°N&S) and below 20 km in the mid-latitudes (45°N&S). In such case the lowest temperature is taken as 203 K.

The relative difference between the ozone number densities computed from the two cross-sections at 308 nm is calculated at all altitudes and at different latitudes for 12 months. Then, the annual mean of the differences is estimated as in the following equation and is presented in Fig. 2.7. The same is calculated at 308+331.8 nm also, but the differences are nearly the same as at 308 nm. So the discussion is made only for the classical Rayleigh signals.

$$\overline{\Delta n_{o3}(z)} = \frac{\sum_{m=1}^{12} \frac{n_{o3}^{BDM}(z,m) - n_{o3}^{BP}(z,m)}{n_{o3}^{BP}(z,m)}}{12} \tag{2.15}$$

where $n_{o3}^{BP}(z,m)$ and $n_{o3}^{BDM}(z,m)$ are the BP and BDM ozone number densities, z is altitude and

m is the month.

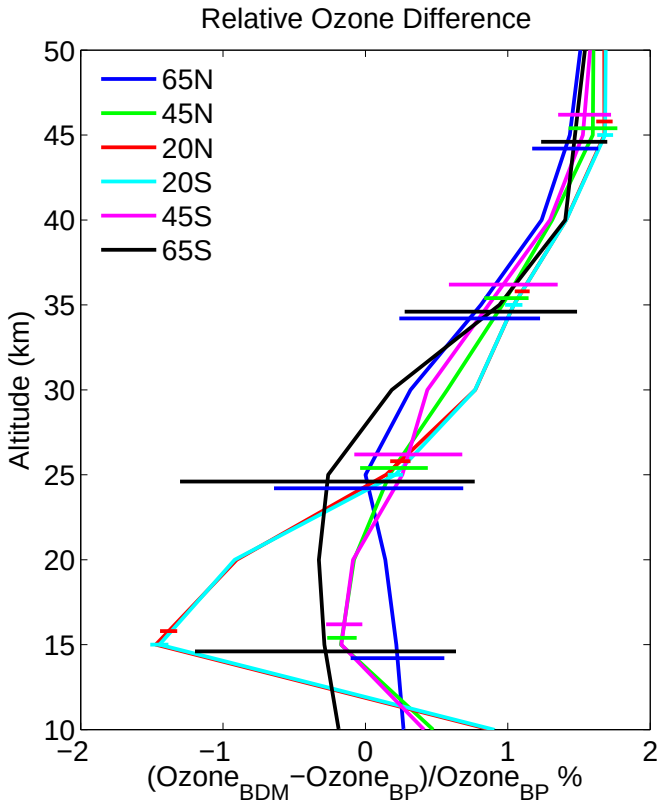

Figure 2.7: Vertical distribution of the annual mean of retrieved ozone from BP and BDM cross-sections at different latitudes. The error bars represent one sigma standard deviation.

The Figure shows that the differences in ozone between both cross-sections are relatively small and do not exceed ±2%. The deviations are less than ±1% below 35 km at all latitudes except in the tropics at 15 km. However, above 35 km the differences are slightly higher and positive with a maximum of 1.8% in the tropics at 45 km. The difference in ozone number density due to the change in cross-section is increasing with respect to altitude or temperature. That is, the differences are larger in the upper stratosphere than in the lower stratosphere. Large discrepancies are observed below 35 km, with the largest in the tropics and smallest in the mid-latitudes. The higher deviations in the tropics around 15–20 km are due to the very low temperatures observed in the lowermost stratosphere in the tropics.

2.6 OHP lidar ozone retrieval using NCEP data

We have already found that the temperature has a great influence on the cross-section and hence on the ozone number density. So it is necessary to check the effect of temperature on the OHP ozone lidar. The ozone cross-section used in the OHP ozone lidar algorithm has been calculated using radiosonde data in the lower stratosphere and CIRA climatology (Randel et al., 2003) in the upper stratosphere. But it has been reported that the CIRA climatology has a warm bias of 5–10 K in the stratosphere (SPARC, 2002). So to account

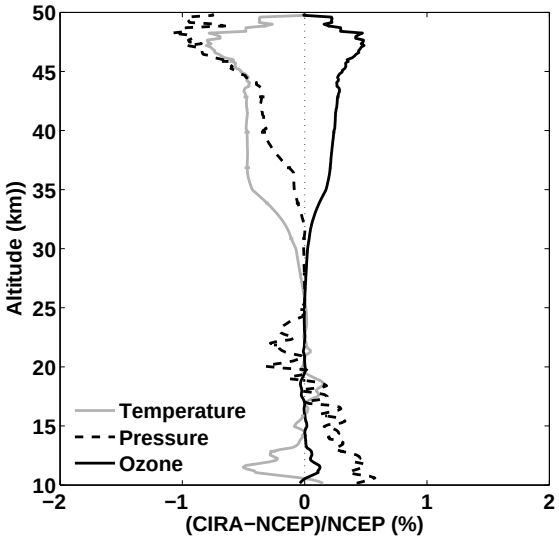

Figure 2.8: The relative difference between the old (radiosonde+CIRA) and the new (NCEP) retrievals for ozone, temperature and pressure. Error bars represent twice the standard error.

for this temperature effect on the cross-sections, the OHP ozone lidar measurements are recalculated using pressure and temperature profiles from NCEP (National Center for Environmental Prediction) and using BP ozone cross-sections. The DIAL ozone measurements can easily be recomputed from the raw data. For that, BP cross-sections are calculated for lidar and NCEP temperatures (NCEP data are interpolated to the lidar altitudes) using a polynomial parameterisation and the number density is derived as

$$n_{o3ncp}(z) = \frac{\sigma_{lid}(z)}{\sigma_{ncp}(z)} n_{o3lid}(z) \tag{2.16}$$

where $\sigma_{lid}(z)$ and $\sigma_{ncp}(z)$ are the BP cross-sections at lidar and NCEP temperatures, $n_{o3lid}(z)$ is the original lidar ozone number density at altitude z.

The relative difference between the retrieved ozone using the old (radiosonde and CIRA) and the new (NCEP) data is calculated. Figure 2.8 shows the average deviation over the period (1985–2010). The mean difference in ozone is within ±0.05% below 30 km and is less than 0.5% above 30 km. Similarly, the mean difference in temperature between the old and new retrievals is within ±0.5% below 30 km and less than −1.2% above 30 km. The same difference is found for pressure too.

In the same manner, the OHP ozone lidar measurements are recalculated using the NCEP data and the BDM ozone cross-sections. The difference in ozone retrieved from the BP and BDM ozone cross-sections are also evaluated for the OHP ozone lidar retrievals. Figure 2.9 presents the mean difference in ozone, retrieved using the two cross-sections, over the period (1985–2010). It is found to be within ±0.08% in 10–50 km. Since the difference in ozone from the two cross-sections is very small, the present work uses the ozone number density derived from BP cross-sections.

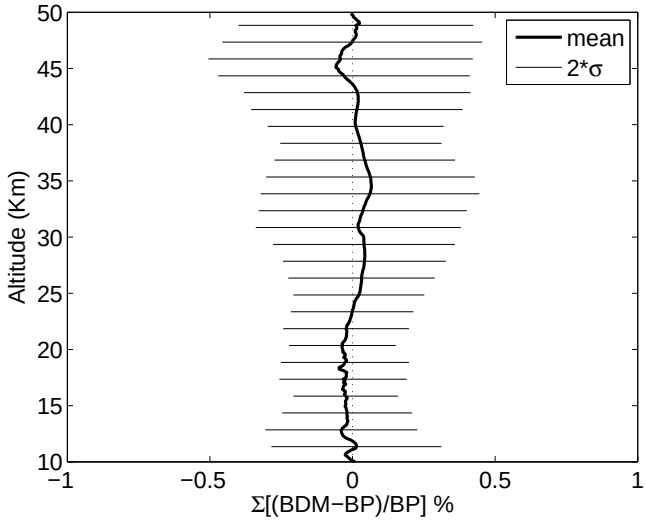

Figure 2.9: The vertical distribution of average difference in ozone measurements estimated using BP and BDM ozone cross-sections at OHP.

2.7 Summary

This chapter describes the general characteristics of ozone lidar measurement technique, retrieval, accuracy and precision of the retrieved ozone profiles. Additionally, within the frame of this thesis, we have performed some important sensitivity analyses to diagnose the effect of using different ozone absorption cross-sections and various meteorological data on the retrieved ozone profiles. The main results from these studies are presented here.

We used the BP and BDM cross-sections to find out the effect of temperature on ozone cross-sections. The analysis implies that the BP cross-sections are always larger than that of BDM at Rayleigh wavelength (308 nm) at 218–295 K. While at Raman wavelength (331.8 nm) BP cross-sections are lower, same and higher than the BDM ones at temperatures below 273, at 273 and at 295 K respectively. The relative differences between BP and BDM ozone cross-sections also show a large difference between 308 and 331.8 nm at 218–273 K, and is nearly zero at 295 K. In the 218–273 K range the differences are all negative at 308 nm, differing from -0.03 to -1.8%, and positive at 331.8 nm varying from 3.6 to 0.2%. The differences in the ozone number densities from two cross-sections are analysed to find out the effect of change in cross-sections on the derived number density. The relative ozone differences computed from the BP and BDM cross-sections at Rayleigh and combined Rayleigh-Raman (308+331.8 nm) wavelengths are very small and are within ±2%. The differences increase from -1.6 to 1.8% from 203 to 273 K and reduce to 0.5% at 295 K.

The temperature dependence of ozone concentration is studied using CIRA-85 atmospheric model at 6 different latitudes from the tropics to high latitudes, to match the locations of NDACC lidar stations. The relative ozone differences of the two cross sections are less than ±1% below 35 km at all latitudes, except -1.5% deviation at 15 km in the tropics. Above 35 km the deviations increase until 45 km with the maximum of 1.7% in the tropics and minimum of 1.4% in the high latitudes. So the difference in ozone number density due to the change in cross-sections is larger in the upper stratosphere than in the lower stratosphere.

To account for the temperature dependence of ozone absorption cross-section, the OHP ozone lidar time series in 1985–2010, which have been retrieved using radiosonde and CIRA model, are recalculated using pressure and temperature profiles from NCEP making use of

both the BP and BDM ozone cross-sections. These recalculated lidar data are further used for the whole analysis performed in the thesis. With BP cross-sections, an average ozone difference of 0.5% is observed above 30 km between the old (radiosonde+CIRA) and new (NCEP) retrievals. Below 30 km the differences are less than ±0.05%. The mean difference in temperature and pressure between old and new retrievals is found to be less than ±0.5% below 30 km and less than -1.2% above 30 km. The average relative difference in OHP ozone lidar from the BP and BDM cross-section over the period (1985–2010) is found to be within ±0.08% in 10–50 km.

Chapter 3

Stability of ozone measurements at OHP

Contents

This chapter deals with the evaluation of the coherence of ground-based and satellite measurements of the ozone vertical distribution above OHP to diagnose the signature of ozone recovery in the northern mid-latitudes. The consistency is evaluated by the intercomparison of collocated ozone profiles from various instruments with the ozone lidar measurements, as lidar provides a long-term data record of ozone from 1985 to 2010. Both the ozone partial columns and profile measurements, having very low and high vertical resolutions, retrieved using entirely different techniques are used for the comparisons. The compared data include the ground-based Umkehr and ozonesonde measurements performed

at OHP and the satellite instruments like, SBUV(/2), SAGE II, HALOE, MLS (Microwave Limb Sounder) on board UARS (Upper Atmosphere Research Satellite) and Aura satellites and GOMOS (Global Ozone Monitoring by Occultation of Stars). A short description of these data are given in Sect. 3.1. The method of analysis is presented in Sect. 3.2. The average biases and the time series of the relative differences are described in Sects. 3.3 and 3.4 respectively. The relative drifts deduced for both the long and short-term data sets from the comparison with lidar are discussed in Sect. 3.5.

3.1 Ozone Measurements

3.1.1 Umkehr

Umkehr observations at OHP are performed using an automated Dobson spectrophotometer, measuring the ratio of transmitted zenith sky radiance at a wavelength pair in the UV (311.5 and 332.5 nm), with the former strongly and the latter weakly absorbed by ozone. The general procedure of the Umkehr ozone retrieval is that the ozone measurements are partitioned into 10 Umkehr layers which are divided into equal log pressure vertical intervals between ∼1013 and ∼1 hPa. It is assumed that the pressure at the top of an Umkehr layer is half of the pressure at the adjacent bottom layer. However, layer 1 is a double layer containing information of layers 0 and 1 (1013–250 hPa). Based on averaging kernels (AKs), Umkehr has independent ozone information in layers 4–8 while other layers are inter-dependent and are combined to 4^- (layers 0, 1, 2, 3) and 8^+ (layer 8 and above) to provide useful information. We use ozone profiles retrieved with the UMK04 algorithm (Petropavlovskikh et al., 2005). The vertical resolution of UMK04 is ∼10 km and the estimated accuracy is better than 10 % for layers 4–8 (64–2 hPa) (WMO, 2007). The UMK04 algorithm was designed to produce ozone profiles optimised for monthly averaged long-term trends. Although the Umkehr ozone profiles tend to have biases relative to other measurements, the data are useful for studies of the long-term ozone evolution.

It should be noted that Umkehr ozone retrievals are influenced by the out-of-band (OOB) stray light of the Dobson instrument. The stray light is defined as extraneous light that enters the slit due to incomplete rejection of the light outside of the core-defined band-pass. Evans et al. (2009) noted that the OOB contribution is dependent on the total ozone and solar zenith angle. Evans et al. (2009) developed a method to reduce the OOB contribution to the Umkehr retrievals. This OOB correction to Umkehr measurements prior to the retrieval reduces the noise in the retrieved data (Petropavlovskikh et al., 2009). So in our study we used both the original and the stray light corrected Umkehr data.

3.1.2 Ozonesondes

Ozonesonde measurements are characterised by a higher vertical resolution (∼0.2 km) compared to other measurements. The main ozonesonde types are Brewer-Mast (BM) (Brewer and Milford, 1960), Electrochemical Concentration Cell (ECC) (Komhyr, 1969) and Japanese ozonesonde (KC). The measurement principle of sondes is that ambient air is pumped into a chamber containing a potassium iodide (KI) solution, where it gets oxidised by ozone and a current is produced. In the Japanese KC sondes, the concentration of potassium bromide (KBr) is higher than that of KI and it plays an auxiliary role for the above reaction. The amount of ozone in the air sample can be derived from the measurement of the electron flow together with the air volume flow rate delivered by the sonde pump.

Generally, correction factor (CF) is used to screen the sonde profiles (Tiao et al., 1986). It is the ratio of total ozone provided by a nearby column measuring instrument to the sum

of total ozone integrated up to the burst level of sonde measurements and a residual total ozone value evaluated above that level (Logan et al., 1999). The profiles having CF of 0.8–1.2 for ECC and KC and 0.9–1.2 for BM sondes are considered of good quality (SPARC, 1998) and are selected in this study. ECC sonde measurements have an uncertainty of about ±5–10% and provide accurate measurements up to ∼32 km (Smit et al., 2007). Ozonesoundings performed at MOHp, OHP, Tateno, Hilo and Lauder are considered here.

Recent studies have analysed the differences in ozone measurements from various types of sondes (Johnson et al., 2002; Smit et al., 2007; Deshler et al., 2008; Stübi et al., 2008). These studies report that ENSCI-Z ECC sondes overestimate ozone by ∼5 % below 20 km and 5–10 % above 20 km as compared to SPC-6A ECC sondes, when both operate with 1 % KI full buffer cathode solution. The decrease in pump efficiency at reduced pressures is corrected by a pump CF that increases with the decrease in air pressure. It affects predominantly the upper part of the ozone profile. In the middle stratosphere, the measured uncertainties are larger due to inconsistent pump efficiency and increase in cathode sensor solution concentration by evaporation. In general, sonde profiles are good up to ∼32 km with an accuracy of about ±5–10 % (Smit et al., 2007).

At OHP, the ozone soundings were performed by BM sondes from 1985 to 1991 and afterwards by ECC sondes, using the standard 1 % KI cathode sensor solution. In order to avoid inhomogeneity due to different ozone sensors we consider ozone observations from ECC sondes in 1991–2009 only. During the period the ozonesonde system at OHP has experienced a number of changes. For instance, ECC sondes manufactured by Science Pump Corporation (SPC-5A) were flown from January 1991 to March 1997. In March 1997, they were replaced by 1Z series ECC sondes of Environmental Science Corporation (ENSCI) and are still in use. The acquisition system was also changed, for which the ECC sondes coupled with the Vaisala RS80 radiosondes by a TMAX interface were used until 2007. Ozone values were derived using the concept designed by KFA Julich (Ancellet and Beekmann, 1997) in 1995–2003 and the "strato" program (Vömel et al., 2002) in 2004–2007. Since 2007 Modem M2K2DC radiosondes coupled to ENSCI-Z ECC sondes by OZAMP Modem interface board have been used. At OHP, Dobson spectrophotometer is used to calculate the normalisation factor until 2007 and SAOZ afterwards. The residual ozone column is computed from the measured ozone at the last altitude and the relative ozone altitude variation based on a monthly ozone climatology derived from the stratospheric ozone lidar data from 22 to 35 km and MAP85 (Middle Atmosphere Program 1985) above 35 km (Ancellet and Beekmann, 1997).

3.1.3 SBUV(/2)

The first generation of SBUV(/2) instruments was launched on the NASA (National Aeronautics and Space Administration) NIMBUS-7 satellite and the second on the NOAA (National Oceanic and Atmospheric Administration) −9, 11, 14, 16, 17, 18 and 19 satellites. The instruments make use of the nadir viewing technique for measuring ozone profiles from the backscattered UV radiation (250–340 nm). The ozone values are derived from the ratio of the observed backscattered spectral radiance to the incoming solar spectral irradiance (Bhartia et al., 1996). The instruments provide a continuous record of stratospheric ozone measurements from November 1978 to December 2007. The vertical resolution of version (V) 8 data is 6 km near 3 hPa which is degraded to ∼8 km near 50 hPa and the horizontal resolution is 200 km (Bhartia et al., 2004). The latitudinal coverage of the measurements is 80° S–80° N and the long-term calibration accuracy is ∼3 % (DeLand et al., 2004). SBUV(/2) measures about 35 000 profiles per month (McLinden et al., 2009). The data are provided both in VMRs on 15 pressure levels and in DU on 13 pressure layers.

We use V 8 ozone column profiles from NIMBUS-7 (01 January 1985–30 November 1988), NOAA-11 (01 December 1988–31 March 1995 and 15 July 1997–02 October 2000), NOAA POST-92 (01 April 1995–14 July 1997), NOAA-16 (03 October 2000 –31 December 2002) and NOAA-17 (01 January 2003–31 December 2007).

3.1.4 SAGE II

SAGE II, an instrument aboard Earth Radiation Budget Satellite (ERBS), has provided long-term observations of ozone from 1984 to 2005. It uses the solar occultation technique for measuring limb transmittance in seven channels between 385 and 1020 nm during each sunrise and sunset. From these transmittance measurements, vertical profiles of ozone, nitrogen dioxide, aerosol extinction and water vapour were derived by the inversion method using the onion-peeling approach (Wang et al., 2002). It observes up to 15 sunrise and 15 sunset events each day, and the consecutive measurements are separated by 24.5° in longitude and in small latitude bands. The 57° inclination of the ERBS orbit allows a spatial coverage from approximately 80° S to 80° N and sampling takes about a month to progress from one latitudinal extreme to the other. The SAGE II observations were temporarily interrupted from July to October 2000 by an instrument failure. After November 2000, SAGE II measured only one per orbit, either sunrise or sunset. The vertical range of the ozone profiles is 10–50 km with a vertical resolution of ∼1 km and a horizontal resolution of 200 km. The ozone measurements have an accuracy of ∼5 % at 20–45 km and 5–10 % at 15–20 km. The ozone number density profiles retrieved in geometric altitudes and processed by the V 6.2 algorithm (Wang et al., 2006) for the period 1985–2005 are used in this work.

3.1.5 HALOE

HALOE on the UARS satellite was put into orbit in September 1991, and operated for 15 years, until 2005. This is another solar occultation instrument, measuring limb transmittances of ozone, HCl, HF, CH_4, H_2O, NO, NO_2, aerosol extinction and temperature at 4 IR wavelengths (Russell et al., 1993). The limb transmittances from the 9.6 μm ozone band are used to retrieve ozone vertical profiles. The ozone profiles are derived from the ratio of solar intensity measured as a function of tangent height to the exo-atmospheric signal and are inverted by applying the onion-peeling procedure. It performs approximately 30 observations per day from both sunrise and sunset in small latitude bands separated by 24° in longitude. The latitudinal coverage of the measurements is 80° S–80° N over the course of one year. The vertical range of the ozone profiles is 15–60 km with a vertical resolution of ∼2 km and a horizontal resolution of 500 km. Accuracy of the measured profiles is about 10 % at 30–64 km and ∼30 % at 15 km (Brühl et al., 1996). Ozone VMR profiles from V 19 for 1991–2005 are used for the comparison.

3.1.6 GOMOS

GOMOS on board the Environmental Satellite (ENVISAT) employs the stellar occultation technique for measuring ozone in UV, visible and near IR wavelength ranges (250–950 nm). Measurements are retrieved using the Tikhonov regularisation method (Kyrölä et al., 2010). The payload was placed in orbit in 2002 and is observing the atmosphere with a global coverage. It executes about 100 000 occultations per year. The altitude range of dark limb profiles is 15–100 km with a vertical resolution ranging from 2 km below 30 km to 3 km above 40 km, and a horizontal resolution of 300 km. The estimated accuracy of the ozone profiles varies with the visual magnitude and the temperature of the star being focused at.

It is less than 5 % at 25–60 km for a star with temperature higher than 10 000 K and visual magnitude up to 2. Below 25 km the accuracy is independent of star temperature and is 3 and 10 % for stars with visual magnitudes 0 and 2 respectively. The instrument was off-line in the beginning of 2005 due to an instrument anomaly resulting in a data gap in 2005. Ozone profiles retrieved on dark limb are of better quality than on bright limb because of the perturbations from background light (Hauchecorne et al., 2010). We use dark limb profiles retrieved with the V 5 algorithm from 2002 to 2009 for this study.

3.1.7 MLS

MLS was launched on UARS in 1991 and its successor aboard Aura in 2004. These instruments measure thermal emissions from rotational lines of the measured species through the limb of the atmosphere. The 57° inclination of the UARS orbit allowed MLS to observe from 34° on one side of the equator to 80° on the other. UARS performs a 180° yaw manoeuvre at ∼36 day intervals allowing it to switch the viewing geometry between northern and southern high latitudes. Because of instrumental deterioration, the number of operational days per year decreased gradually from late 1991 to 1993. It reached about 50 % of the initial number in 1994 and became very small from 1995 onwards, largely because of spacecraft power-sharing constraints. The profiles retrieved from the 205 GHz ozone line have a vertical range of 15–60 km with a resolution of ∼3–4 km, and the horizontal (along-track) resolution is 300 km. The estimated accuracy of a single profile is 6 % at 21–60 km and 15 % at 16–20 km (Livesey et al., 2003). Its successor, Aura MLS, has a better spatial coverage and horizontal and vertical resolutions. The latitudinal coverage of the measurements is 82° S–82° N on a daily basis and it provides about 3500 profiles per day. Ozone measurements retrieved from the 240 GHz ozone line have a vertical range of 12–73 km with a vertical resolution of 2–3 km, below 65 km. The horizontal resolution is ∼200 km and the accuracy is about 5–10 % between 16 and 60 km (Froidevaux et al., 2008). The ozone VMRs of UARS MLS V 5 in 1991–1999 and Aura MLS V 2.2 and V 3.3 in 2004–2010 are used for the analysis.

3.2 Methodology

3.2.1 Data screening

The data are screened with respect to the uncertainties of the measurements, instrumental artifacts and recommendations provided by the validation references. A common error source that influences most data (except microwave) is the presence of aerosols. Almost all ground and space-based instruments, except ozonesondes, are affected by the high aerosol loading produced from the volcanic eruptions El Chichón (1983) and Mount Pinatubo (1991). Since our study starts in 1985, the El Chichón volcanic eruption is not considered. However, the measurements affected by the aerosols from Mount Pinatubo eruption are treated with special care.

Lidar observations below 25 km are almost excluded for the period 1991–1993 because of aerosol contamination due to Mount Pinatubo volcanic eruption (Guirlet et al., 2000). Umkehr measurements are highly sensitive to aerosols and thus the data from June 1991 to June 1993, affected by the Mount Pinatubo eruption, are omitted from the analysis as suggested by SPARC (1998). Since SAGE II measurements are also very much affected by aerosol loading, the filters proposed in SPARC (1998) (see Table 2.2 of SPARC, 1998) are adopted. Since filtering is based on the pressure levels, complete removal of SAGE II data is not needed and the filtering criteria is different in different latitude bands. For example,

in the mid-latitudes, the ozone measurements from June 1991 to January 1992 are removed below 14 hPa (below ∼30 km). Similarly, data from February 1992 to June 1992, July 1992 to January 1993, February 1993 to June 1993 and July 1993 to January 1994 are eliminated below 32, 46, 68 and 100 hPa respectively.

Product error flags are used as another screening criterion considered in our study. Ozone profiles with flag 0 for GOMOS (from the meta data) and 0, 10, 100 and 110 for SBUV(/2) (recommended in V 8 data quality) are selected for the analysis. As described earlier, CF is used to screen and correct the ozonesonde profiles. It has been reported that the ECC ozonesondes having CF between 0.8 and 1.2 are of good quality (SPARC, 1998) and are considered here. Aura MLS profiles are screened as per the criteria given by Froidevaux et al. (2008). For example, ozone profiles with convergence <1.8 and quality >0.4, and temperature and geopotential height fields with convergence <1.2 and quality >0.6 are considered. Additionally, MLS data having negative precision are also eliminated from the analysis. Moreover, negative values of ozone are excluded from the analysis for all measurement techniques.

3.2.2 Coincidence criteria

The main objective of the study is to check the consistency of different ozone measurements. It is done by comparing the collocated profiles of various ozone observations with respect to the ozone lidar. The instruments considered for the analysis use entirely different measurement and retrieval techniques, and have different viewing geometry. So the criteria applied for finding coincidences differ in accordance with the measurement characteristics to achieve reasonable sampling to derive a meaningful statistics.

Generally, the horizontal resolution of the satellite observations is about 100 times larger than the vertical resolution. Also the zonal variation of ozone is less compared to the meridional one. So the collocation criteria is relaxed longitudinally and tightened latitudinally. That is, the spatial criteria used for extracting SBUV(/2) and UARS MLS is ±2.5° latitude and ±5° longitude with respect to the location of OHP. Nonetheless, for Aura MLS, coincidences are determined within the ±2° latitude and longitude bands as it provides more collocated profiles with the lidar within the prescribed area. The occultation measurements (SAGE II, HALOE and GOMOS) provide comparatively less sampling, so a spatial criterion of ±5° latitude and ±10° longitude is considered for them. In the same way, a temporal restriction is also applied for finding the coincidences. The profiles measured within ±12 h with respect to the measurement time of lidar is used for the comparisons. Also, Umkehr and satellite measurements yield more than one coincidence a day. In that case, the closest one in latitude and time is used.

The spatial and temporal criteria and the number of matching events obtained for each data set with lidar are listed in Table 3.1. Comparison periods depend on the time overlap between the measurements from lidar and other instruments. The number of observations in each month averaged over the period and the total number of observations in each year retrieved from various data sets (satellite measurements are extracted around the OHP station using the spatial criteria given in Table 3.1) are shown in Fig. 3.1. As is evident in the Figure (top panel), the number of ozonesonde measurements does not vary seasonally whereas it does for the other data sets. The maximum number of observations for lidar and Umkehr are found in winter and summer respectively. Among the satellite observations, SAGE II and HALOE provide comparatively fewer observations, with a maximum in winter and autumn. From the bottom panel it is clear that the number of lidar measurements increased from 1994 onwards. Umkehr provided more profiles at the beginning of the observation period, with a maximum of 320 in 1989. Since ozonesondes are launched usually

Table 3.1: Statistics of the comparison study: selection criteria in latitude (Lat) and longitude (Lon) applied for the satellite measurements with respect to OHP (43.93° N, 5.71° E), time period (Year) and the maximum number of coincident profiles obtained seasonally [Winter (January, February, and March – JFM), Spring (April, May, and June – AMJ), Summer (July, August, and September – JAS), and Autumn (October, November, and December – OND)] and over the coincident periods (N) with the time difference of ±12 h.

Instrument	ΔLat (N)	ΔLon (E)	Period (Year)	Winter (JFM)	Spring (AMJ)	Summer (JAS)	Autumn (OND)	Total N
SBUV(/2)	±2.5	±5	1985–2007	227	201	225	173	826
SAGE II	±5	±10	1985–2005	88	20	20	85	213
HALOE	±5	±10	1991–2005	69	4	11	62	146
UARS MLS	±2.5	±5	1991–1999	53	26	39	32	150
GOMOS	±2.5	±10	2002–2009	46	31	28	38	143
Aura MLS	±2	±2	2004–2009	55	42	45	49	191
ozonesondes			1991–2009	102	91	89	65	347
Umkehr			1985–2007	204	177	203	178	762

once a week, the number of measurements are fewer and are about 50 per year on average. SAGE II observations show degradation after 1999, while HALOE provided almost constant measurements throughout the period (e.g. Remsberg, 2009), with a slightly higher number in 1992–1994. SBUV(/2) and Aura MLS have more profiles throughout the period. As already mentioned, a gradual decrease in the number of observations with time is found for UARS MLS.

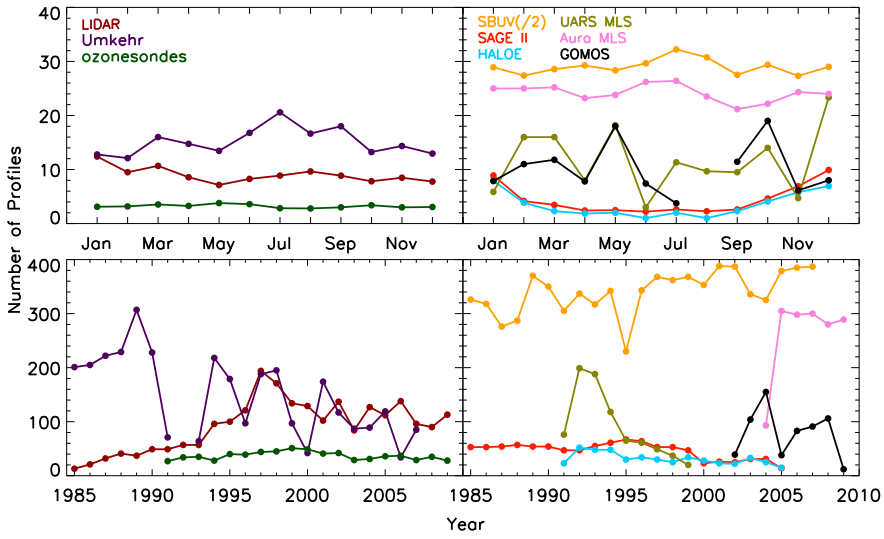

Figure 3.1: Average number of observations in each month over the respective period (top panel) and the total number of observations per year (bottom panel) of various data sets. Left: ground-based measurements at OHP. Right: satellite observations extracted around OHP.

3.2.3 Data conversion

The method of analysis differs slightly for each measurement technique depending on the altitude grid of the data. The lidar ozone retrievals are in number density (moleculescm^{-3}) on

geometric height (km) with a sampling resolution of 150 m. Therefore, except for SBUV(/2) and Umkehr ozone column observations, measurements from other techniques are converted to ozone number density to compare with the ozone lidar.

Ozonesonde measurements in partial pressure (mPa) are converted to number density, using temperature data from sonde measurements, and are compared to that of lidar by interpolating both data sets onto 0.15 km altitude grids. Since Umkehr measurements are in DU, the lidar profile is converted to DU and partial ozone columns are calculated above the pressure levels from NCEP data corresponding to lidar altitudes. The resulting partial columns are interpolated to 61 Umkehr pressure levels and the consecutive values are subtracted to obtain the ozone profile in quarter Umkehr layers (Petropavlovskikh et al., 2005). The ozone lidar values at pressure levels within the standard Umkehr layers are then added to get ozone column at standard Umkehr layers, given in Table 3.2 (This is method is provided by Irina Petropavlovskikh). As Umkehr has very low vertical resolution, lidar profiles are smoothed using Umkehr AKs and a priori (Griesfeller et al., 2012); but this did not make a significant difference to the annual average even though some differences are observed in the seasonally averaged data, especially in winter and autumn with maximum difference of 3.6 and 2.6% respectively. So in this study we compared the lidar data without AK smoothing.

The vertical resolutions of the occultation measurements are similar to that of the lidar. Hence, the satellite and lidar profiles are interpolated to 1 km grid, the standard vertical resolution of the occultation measurements to get the same vertical window for comparison. HALOE ozone values measured in VMRs are converted to number density using temperature and pressure from HALOE data. Similarly, the ozone VMR profiles from MLS measurements are converted to number density using the corresponding MLS temperature and pressure. Geopotential heights are taken as the geometric altitudes for MLS as the difference between them is very small in the studied altitudes (∼0.04 and 0.33 km at 15 and 45 km respectively). So it hardly affects the derived ozone values even in steep gradient regions. Comparison with both UARS and Aura MLS sensors is performed on their original lower resolution altitude grids. For that, the higher resolution lidar profile is integrated (trapezoidal integration) vertically within the ±1.5 km altitude band with respect to the MLS altitudes. Then both data are interpolated onto an average altitude grid calculated for the periods of MLS data.

SBUV(/2) has a very low vertical resolution compared to that of lidar. So comparison between them is performed in two ways, by convolving lidar data with SBUV(/2) AKs and without convolution of lidar data, using ozone in DU since SBUV(/2) a priori data are provided in DU. The lidar profile is first converted to DU and partial columns are added above each pressure level with respect to lidar altitudes. The resulting values are then interpolated to the pressure levels of the SBUV(/2) ozone AKs in the former comparison (with convolution of ozone lidar), or to the pressure levels of SBUV(/2) ozone column in the latter comparison (without convolution of lidar) and the adjacent layers are then subtracted to obtain partial ozone column in each layer. The convolution of lidar profiles with the AKs is made using the Eq. 3.3, obtained by the optimal estimation method (Rodgers, 1976) and is given below.

By the optimal estimation method, the smoothing errors associated with the retrieved profiles can be written as

$$x - x_a = (AK - I)(x - x_a) \tag{3.1}$$

where x is the retrieved value, x_a is the a prioiri information, AK is averaging kernel and I is the identity matrix.

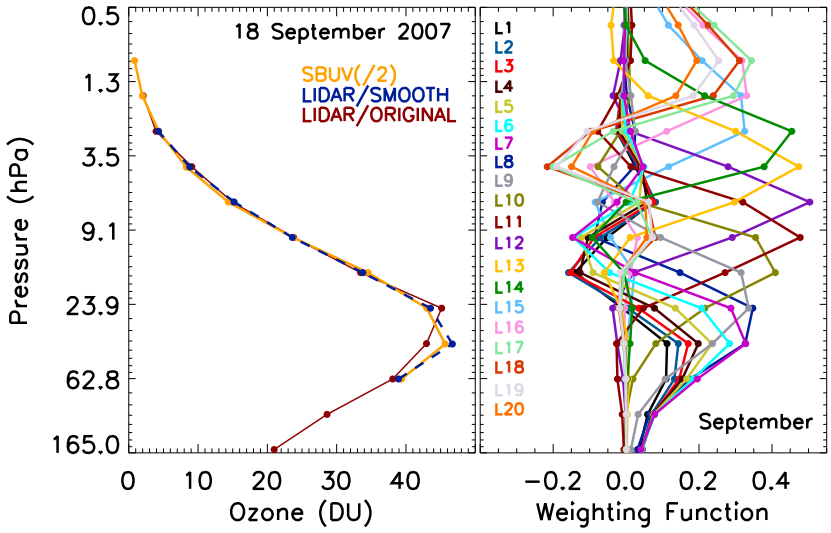

Figure 3.2: Left: comparison of lidar measurements, both original and convolved using SBUV(/2) AKs and SBUV(/2) profile on 18 September 2007 at OHP. Right: SBUV(/2) AKs used for convolving lidar data.

Then, the convolution is performed as

$$x_s = x_a + AK(x - x_a) \tag{3.2}$$

From this, we get the equation for convolving the high resolution profiles to compare with the low resolution profiles and is

$$L_S(i) = \sum_{i,j} \left[\frac{AK(i,j) \times (L_O(j) - A(j))}{A(j)} \right] \times A(i) + A(i) \tag{3.3}$$

where L_S = Smoothed ozone lidar in i-th pressure level, L_O = Lidar ozone in j-th pressure level, AK = averaging kernel matrix, and A = SBUV(/2) a priori in i and j pressure levels.

Figure 3.2 shows an example of the SBUV(/2) and lidar profile and the lidar profile convolved using SBUV(/2) ozone AKs for 18 September 2007 in the left panel and SBUV(/2) AKs in September above OHP, used for smoothing the lidar profile, in the right panel. As illustrated in the Figure, the original lidar data differs from SBUV(/2) below 23.9 hPa, but the smoothing with AK reduces this difference. The smoothing is done if the lidar data reach the pressure levels where SBUV(/2) weighting functions are greater than 0.2.

In order to compare all measurements in a common scale, geometric altitudes are preferred. Therefore, geometric altitudes corresponding to Umkehr and SBUV(/2) mid-pressure levels are computed from the lidar profiles and are averaged over the comparison period (1985–2007). The pressure levels and the corresponding geometric altitudes of SBUV(/2) and Umkehr are given in Table 3.2.

3.2.4 Data analysis

The average bias and relative drift of different long and short-term data are analysed with respect to the ozone lidar measurements in order to ensure the consistency and the stability of OHP ozone lidar.

Table 3.2: SBUV(/2) pressure levels corresponding to ozone column measurements, the Umkehr pressure layers and the approximate altitudes corresponding to the mid-pressure levels used in the study.

SBUV Layer	Pressure limits (hPa)	Mid-Pre. (hPa)	Altitude (km)
2	63.9-40	51.95	21
3	40-25.1	32.55	24
4	25.1-15.8	20.45	27
5	15.8-10	15.23	30
6	10-6.3	58.15	33
7	6.3-4	5.15	37
8	4-2.51	3.25	40
9	2.51-1.58	2.04	43

Umkehr Layer	Pressure limits (hPa)	Mid-Pre. (hPa)	Altitude (km)
4	63-32	48	21
5	32-16	24	25
6	16-8	12	30
7	8-4	6	35
8	4-2	3	40

3.2.4.1 Relative difference and mean bias

The comparison is performed by finding the relative ozone difference between the compared data sets, which is computed as

$$\Delta O_{3L}(i,j) = \frac{Meas(i,j) - lidar(i,j)}{lidar(i,j)} \times 100\,\% \tag{3.4}$$

where $i =$ coincident day, $j =$ altitude or pressure and "Meas" denotes the compared instruments Umkehr, ozonesondes, SBUV(/2), SAGE II, HALOE, MLS and GOMOS.
The mean bias of each measurement technique is then calculated by averaging the relative differences over the respective coincident periods with the lidar.

$$\overline{\Delta O_{3L}(j)} = \frac{\sum_i \Delta O_{3L}(i,j)}{N(j)} \tag{3.5}$$

The standard error of the bias is determined as

$$\sigma_N(j) = \frac{\sigma(j)}{\sqrt{N(j)}} \tag{3.6}$$

where $\sigma(j)$ is the standard deviation of the relative differences and N is the total number of profiles.
We have also analysed the data for each season and the analysis takes Winter as January, February and March (JFM), Spring as April, May and June (AMJ), Summer as July, August and September (JAS), and Autumn as October, November and December (OND).

3.2.4.2 Slope and its standard deviation

The time evolution of the differences is analysed to find out whether the comparisons show any temporal changes or drifts in the ozone measurements with time. So drifts in the measurements are found from the estimation of slopes from the monthly averaged difference time series using simple linear regression. We considered the derived drift as significant if the slope is greater than twice the standard deviation of the slope (95% confidence interval). That means the error estimation is an important aspect of the drift analysis. Therefore, the selection of the best error estimator is crucial in determining the stability of the data, and we performed a sensitivity test to find out the best way for evaluating the uncertainty of the slope. We used four different methods to calculate the standard deviation and are

described below.
Firstly, we assume a straight line model, $y = a + bx$ and chi square merit function (χ^2) is calculated to see how well the model agrees with the data. Then, the standard deviation (σ_1) is estimated as (Press et al., 1989)

$$\sigma_1(j) = \frac{\sqrt{\frac{\chi^2(j)}{N(j)-2}}}{\sqrt{\sum_{i=1}^{N(j)} (x_i - \overline{x})^2}} \tag{3.7}$$

where $\chi^2(j) = \sum_{i=1}^{N(j)} (y_i - a - bx_i)^2$, N = number of months, x = month, y = monthly relative difference, a = y-intercept, b = slope, and j = altitude or pressure level.
Secondly, the equation given by Frederick (1984) is used for finding the standard deviation (σ_2),

$$\sigma_2(j) = \frac{\sigma_y(j)\sqrt{\frac{1+\phi}{1-\phi}}}{\sqrt{\sum_{i=1}^{N(j)} (x_i - \overline{x})^2}} \tag{3.8}$$

where $\sigma_y(j)$ = standard deviation of the relative differences and ϕ is the autocorrelation of the error (ε) and is calculated as (from Hauchecorne et al., 1991)

$$\phi = \frac{\sum_{j,k=1}^{N-1} \varepsilon(j,k)\varepsilon(j,k+1)}{\sum_{j,k=1}^{N-1} \frac{\varepsilon(j,k)^2 + \varepsilon(j,k+1)^2}{2}} \tag{3.9}$$

Finally, the method adopted by Weatherhead et al. (1998) is used for computing the standard deviation (σ_3) for n years.

$$\sigma_3(j) = \frac{\sigma_y(j)\sqrt{\frac{1+\phi}{1-\phi}}}{n^{\frac{3}{2}}} \tag{3.10}$$

The standard deviations obtained from these equations and the equation chosen for the further analyses are discussed in Sect. 3.5.1.

3.3 Vertical distribution of mean bias

The vertical distribution of average relative deviations in each season and over the period of each data set are shown in Fig. 3.3, for the long-term (top panel) and short-term (bottom panel) data sets. In general, comparisons of various observations with the lidar measurements exhibit smaller differences, within ±5%, at 20–40 km and somewhat higher differences outside this range. Below 20 km the atmospheric variability is larger and the accuracy and precision of ozone measurements are lower. Above 40 km, we have seen that the signal-to-noise ratio and precision of lidar measurements are lower. This larger uncertainty of lidar profiles induces relatively larger deviations above 40 km. This is also reflected in the comparison between mean and median. Both give similar results at 20–40 km while the median deviates from the mean below 20 and above 40 km.

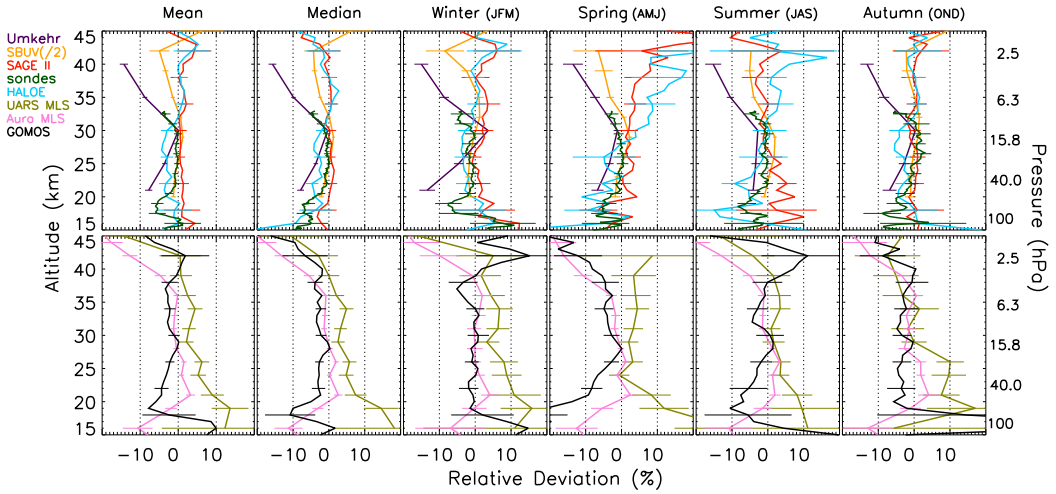

Figure 3.3: Vertical distribution of average relative differences of the coincident ozone measurements of various observations with lidar. Top panel: instruments with more than 10 years of data. Bottom panel: instruments with less than 10 years of data. The dotted vertical lines represent −10, 0, and 10 % and the error bars correspond to twice the standard error. Approximate pressure levels corresponding to the geometric altitudes are also shown on the right axes.

3.3.1 Long-term data sets

On average, SAGE II, SBUV(/2) and ozonesondes provide similar results up to 30 km even though ozonesondes show a bias of about −6% around 17–19 km, which will be discussed in detail in Sect. 3.4.2. Up to 30 km, HALOE yields larger negative deviations compared to SAGE II, consistent with the results of Nazaryan et al. (2007) and Froidevaux et al. (2008), who also noted lower HALOE ozone values as compared to SAGE II at these altitudes. Above 30 km, SAGE II and HALOE exhibit positive deviations while SBUV(/2) gives mostly negative deviations. SAGE II shows an excellent agreement of ±1% with the lidar in the 17–41 km range. Ozonesondes and SBUV(/2) also provide ±1% difference at 20–30 km. Umkehr stands out with slightly larger negative deviations. The best agreement is found at 16–8 hPa with near zero bias.

To find out which instrument agrees best with the lidar, root mean square (RMS) difference is evaluated vertically from the average biases as

$$RMS = \sqrt{\frac{\sum_{j=1}^{n}\left(\overline{\Delta O_3(j)}\right)^2}{n}} \tag{3.11}$$

where n is the number of altitudes. The altitude levels are 15–45 km for SAGE II and HALOE; 15–33 km for ozonesondes; 20–45 km for SBUV(/2) and 20–40 km for Umkehr . In terms of RMS, SAGE II and Umkehr provide the lowest (2.1%) and the highest (8.4%) value respectively. HALOE, SBUV(/2) and ozonesondes give RMS value of 2.7, 3 and 2.5% respectively.

Seasonally, the differences are smaller in absolute scales in autumn and winter for all measurements except for Umkehr at 63–32 and 4–2 hPa, and for SBUV(/2) around 40 km in winter. Larger biases are observed for SAGE II and HALOE in spring and summer. This is due to their limited sampling in the northern mid-latitudes during these seasons. For example, only one profile among the 4 coincidences of HALOE with lidar in spring reached up to 45 km. Hence, the relative differences over the period are mainly weighted by

the winter and autumn sampling for HALOE and SAGE II. Ozonesondes do not show any seasonal dependence, whereas Umkehr shows a positive deviation at 16–8 hPa in winter.

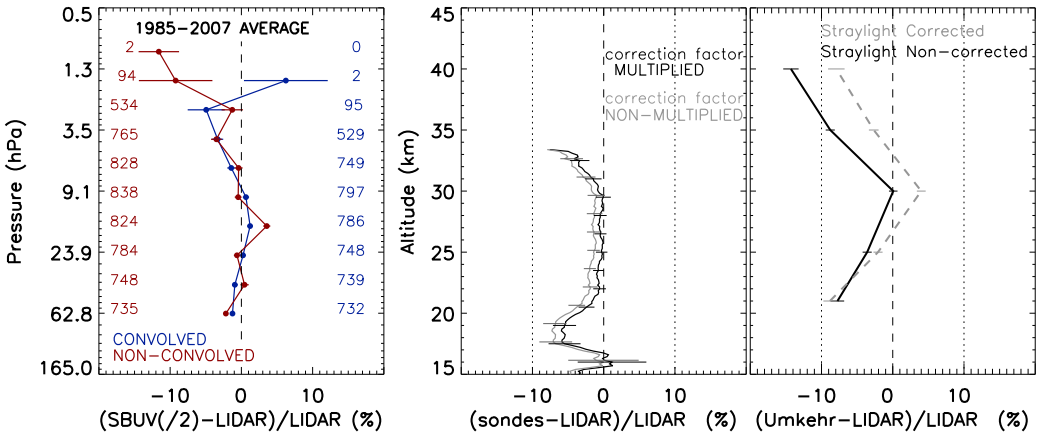

Figure 3.4: Left: Average bias between SBUV(/2) and lidar (with and without convolution using AKs and a priori). The number of analysed profiles with and without convolution are also provided in respective colours. Middle: Average relative deviation of ozone from lidar and ozonesondes, with and without multiplying by correction factor. Right: Average bias from the comparison of lidar with the original and stray light corrected Umkehr. The error bars represent twice the standard error. The dashed line represents 0 % and the dotted lines represent -10 and 10%.

In addition to these results, the differences achieved from the two kinds of comparisons for SBUV(/2), ozonesondes and Umkehr are also presented in Fig. 3.4. The left panel shows the average bias obtained for the comparison between SBUV(/2) and lidar, both convolved and non-convolved, over the period (1985–2007). It is evident that the average bias with the convolved lidar is smoother than that with the non-convolved lidar. The error bars below 2.51 hPa are very small because of the large number of coincident profiles between the convolved and non-convolved lidar. The results are quite similar except at 2.51 and 1.58 hPa. This difference can be due to the low number of matching events with the convolved lidar, because of the selection criterion using the SBUV(/2) weighting functions as discussed in Sect. 3.2.3. i.e. the smoothing reduces the number of coincident profiles particularly in the upper range.

For ozonesondes, we investigated the impact of multiplying sonde profiles with the CF (as noted in Sect. 3.1.2). The average deviation computed with and without multiplying by the CF for the period 1991–2009 are shown in Fig. 3.4 (middle panel). The multiplication by CF yields smaller differences in the 15–33 km range and the differences are very close to zero around 16 km and in 21–31 km. These results show that the quality of the sonde profiles, as evaluated by the lidar measurements, is improved when the CF is applied.

Similarly, the relative difference between the stray light corrected Umkehr (as described in Sect. 3.1.1) and the ozone lidar is calculated and is compared with that between the original Umkehr and lidar. The result is shown in the right panel of Fig. 3.4. Both data show a similar bias at 20 km and non-corrected Umkehr data exhibit smaller bias (nearly 0%) at 30 km. However, the stray light correction to the Umkehr data reduced the biases to a large extent, by about 6%, at 8–4 (∼35 km) and 4–2 hPa (∼40 km).

3.3.2 Short-term data sets

Figure 3.3 (lower panel) shows the average relative differences calculated for the short-term data in their respective periods. Aura MLS shows small variations, within ±2% at 19–38 km, and it systematically underestimates ozone lidar below 20 and above 38 km. Compared to Aura MLS, UARS MLS exhibits slightly higher bias, with positive differences at 16–40 km throughout the period except in autumn above 28 km. Livesey et al. (2003) compared UARS MLS ozone with SAGE II, ozonesondes and lidar data, and found positive deviations in most cases, matching our results. A small positive bias is estimated for Aura MLS in the lower stratosphere when compared with SAGE II, HALOE (Froidevaux et al., 2008) and ozonesondes (Jiang et al., 2007). In contrast, in agreement with our results, the comparison of Aura MLS with the ground-based microwave radiometer (Boyd et al., 2007) and lidar (Jiang et al., 2007) data do not exhibit a positive bias in the lower stratosphere.

GOMOS observations show smaller biases with lidar measurements at 28–40 km when averaged over the period. Below 28 km, negative differences are found down to 18 km and positive ones in the range 15–17 km. Above 40 km, lidar overestimates ozone as compared to GOMOS. Seasonal differences in winter and autumn are very similar to the whole period averages except above 40 km in winter. In spring, the negative bias of GOMOS data is more pronounced in the lower and upper stratosphere. In summer, discrepancies are larger but the comparison is performed on very few collocated measurements, 28 in total over the period. In order to check our results with those of other studies, we compared lidar and GOMOS ozone using a spatial criterion of 800 km and a temporal criterion of ±20 h, similar to the criteria set in Gijsel et al. (2009), which yielded very similar results.

3.4 Temporal evolution

Relative differences with respect to time are analysed for each measurement technique at reference altitudes 18, 21, 25, 30, 35 and 40 km by averaging ozone over a range of ±2 km, with respect to the reference altitudes, in order to provide relatively smooth time series of ozone measurements and also to homogenise different data sets for the comparisons. Monthly average results are shown with black dots and daily values are with Grey dots in the background. The monthly average data show smaller differences than the daily ones and hence the analysis focuses on the former. In general, monthly deviations are larger if there is only one or a small number of collocated events.

3.4.1 Comparison of Umkehr with lidar

Figure 3.5 presents the comparison of Umkehr ozone, both the original (left panel) and the stray light corrected (right panel) with that of lidar for 1985–2007. The comparison is based on Umkehr pressure layers instead of geometric altitudes. Both comparisons show similar results at 63–32 hPa (∼21 km), 32–16 hPa (∼25 km) and at 16–8 hPa (∼30 km) and the differences are larger prior to 1994 in the two comparisons. The analysis presents its best agreement at 32–16 and 16–8 hPa until 2005, where deviations are within ±5%. At 63–32 hPa and 8–4 hPa (∼35 km), the relative differences are around ±10% and slightly larger at 4–2 hPa (∼40 km). At 8–4 and 4–2 hPa the comparison with the original Umkehr ozone shows large negative biases. This higher negative differences is likely be due to the lower ozone values of Umkehr caused by the internal scattered light problems of the Dobson spectrometer. It is mostly rectified by applying a stray light correction to the Umkehr data as seen in the right panel.

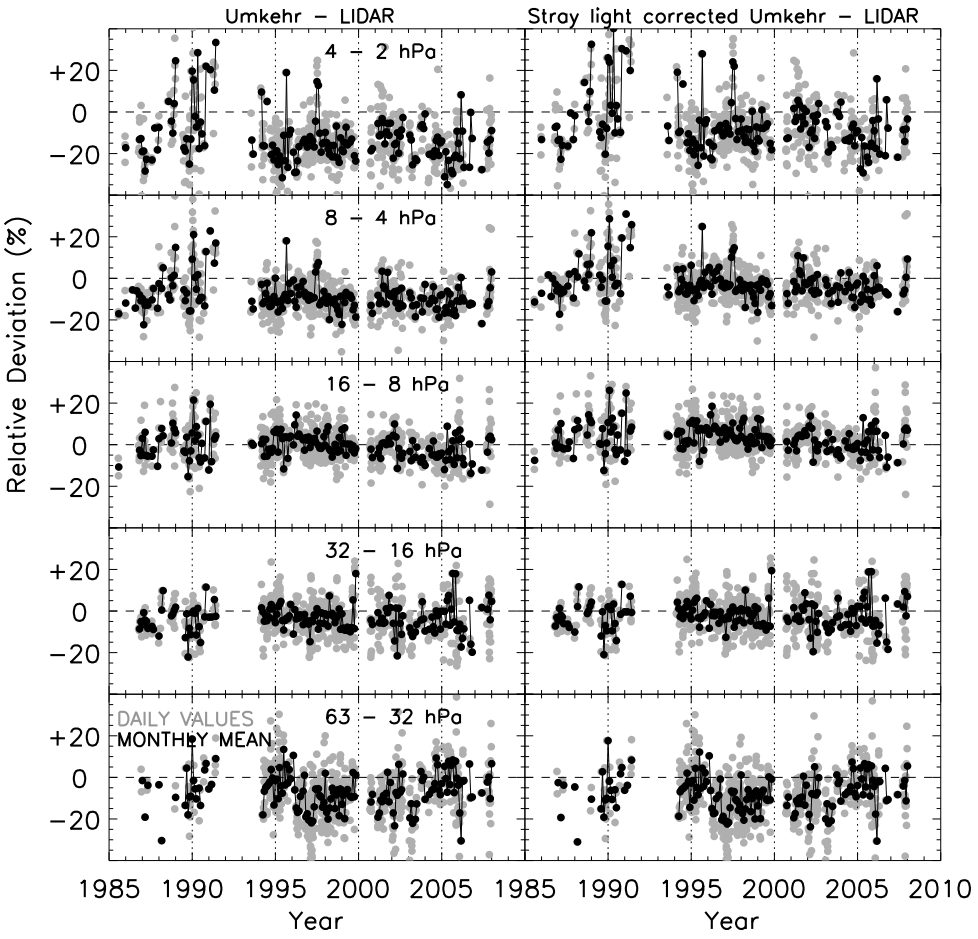

Figure 3.5: Comparison of lidar with the original (left panel) and stray light corrected (right panel) Umkehr ozone. The Grey and black circles represent the daily and monthly averaged differences respectively. The dashed horizontal lines represent 0 % and the dotted vertical lines represent year 1990, 1995, 2000, and 2005.

3.4.2 Comparison of ozonesondes with lidar

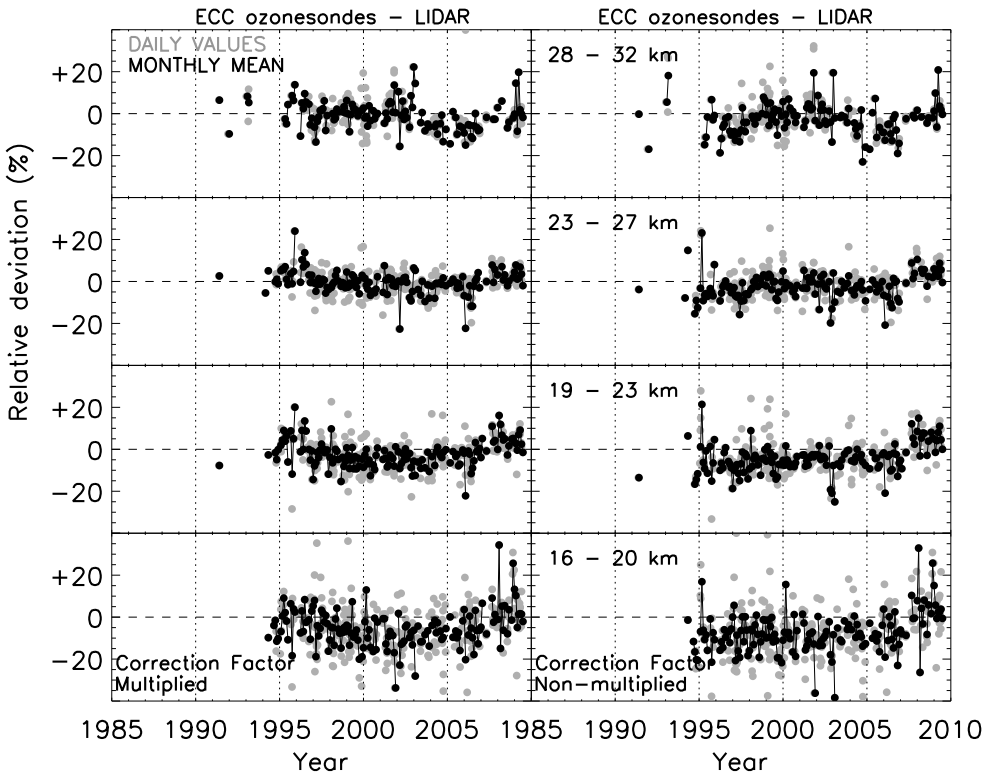

Figure 3.6: Same as Fig. 3.5, but for ozonesondes, multiplied by CF (left panel) and without multiplying by CF (right panel).

Figure 3.6 displays the relative differences between ozonesondes and lidar data in 1991–2009. The left panel shows the comparison made by multiplying CF to the sonde profiles. For understanding the effect of multiplying correction factor, we analysed the sonde profiles without multiplying using correction factor, which is shown in the right panel. The comparison made by the multiplication of CF shows small deviations than that without the multiplication of CF and a good agreement of ±5% is found at 19–23, 23–27 and 28–32 km. All altitudes exhibit a similar behaviour in that the differences decrease until 1997 and stabilises afterwards up to 2006, and then starts to increase. The decrease in 1997 is not observed in the right panel, which indicates that this change can be due to a relatively higher value of the CF in 1995–1997, which on multiplication with the ozone gives rise to high ozone values. However, the positive bias after 2007 is found in the two comparisons. So it could be in part due to the change in ozone receiving system from Vaisala to Modem or from the differences originated from the changes in the systems and methods used for deriving the ozone as described in Sect. 3.1.2. These results pinpoint the need of a homogenised data for ozone trend evaluation.

In terms of altitudes, the comparison shows slight negative biases at 16–20 and 19–23 km compared to other altitudes. The average lidar ozone is about 4.6% larger than that of sondes in the 16–23 km range, which is similar to the results of Godin-Beekmann et al. (2003), who compared average ozone lidar concentration to that of sondes at 450–

500 K (∼16–20 km) in 1994–2000. Additionally, a similar insignificant bias was noted when ozone lidar was compared to ECC sondes and SAGE II ozone at 16–19 km in 1985–2000 too (Godin-Beekmann et al., 2004). Further, Nardi et al. (2008) show comparatively larger negative bias around 100 hPa, when OHP ozone lidar was compared to HIRDLS (High Resolution Dynamics Limb Sounder) ozone and are not significant.

3.4.3 Comparison of SAGE II and HALOE with lidar

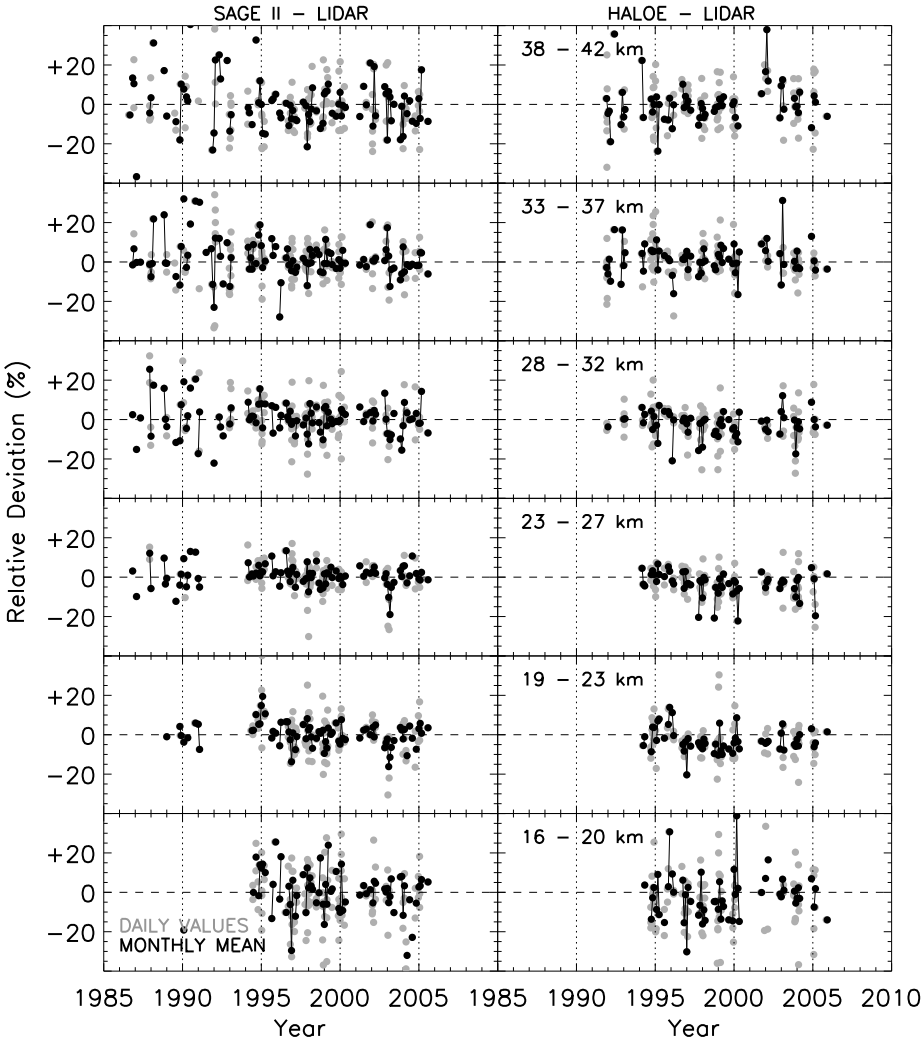

Figure 3.7: Same as Fig. 3.5, but for SAGE II (left panel) and HALOE (right panel) with lidar.

Figure 3.7 (left panel) represents the comparison of SAGE II with ozone lidar in 1985–2005. The best agreement between the data sets is seen at 19–23 and 23–27 km, where deviations are less than ±5%. At 28–32 and 33–37 km the differences are within ±10% and, at 16–20 and 38–42 km they exceed ±10%. The differences are in general larger prior to 1994 because of the lower quality of lidar data and the fewer number of matching events.

Figure 3.7 (right panel) shows the relative deviations of HALOE against ozone lidar

from 1991 to 2005. The deviations are mostly within ±5% at all altitudes while they exceed ±10% at 16–20 and 38–42 km. HALOE provided fewer collocations when compared to other longer data sets. Not even a single matching event is obtained in the lower stratosphere before 1994 after filtering the data following the Mount Pinatubo volcanic eruption.

3.4.4 Comparison of SBUV(/2) with lidar

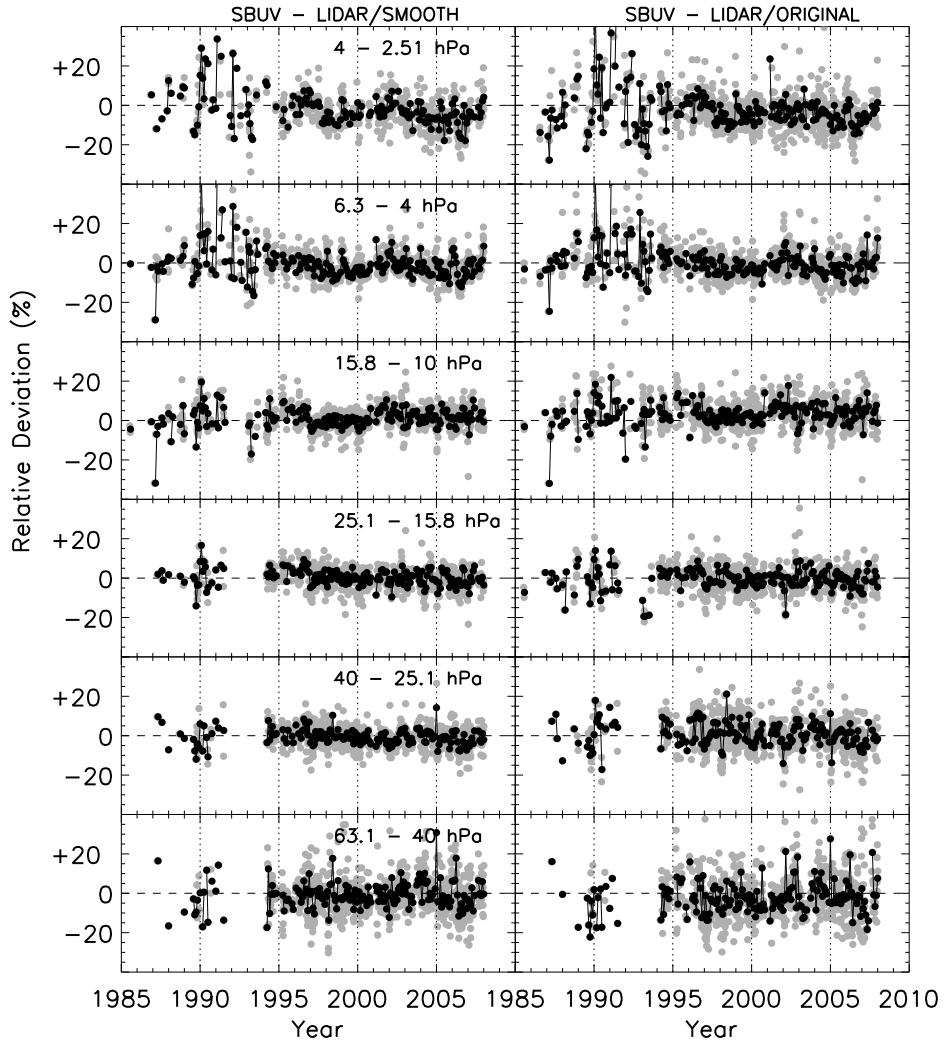

Figure 3.8: Same as Fig. 3.5, but for SBUV(/2) with lidar, both convolved using SBUV(/2) AKs (left panel) and the non-convolved (right panel).

Figure 3.8 (left panel) displays the time series of comparison between SBUV(/2) and convolved ozone lidar in 1985–2007 and the right panel shows the same but with the non-convolved lidar. It is clear that the AK smoothing results in a comparatively lower biases and are less noisy too on a day to day basis. An excellent agreement within ±4% is found at 40–25.1 hPa (∼23 km) and 25.1–15.8 hPa (∼26 km). At 15.8–10 hPa (∼29 km) and 6.3–4 hPa (∼35 km) the differences lie within ±5 and ±10% respectively, except for a few points

prior to 1994. At these altitudes the deviations decrease from 1995 to 1997 followed by an increase until 2003, and again a decrease afterwards. A similar result is also shown by Terao and Logan (2007) when SBUV(/2) data are compared with ozonesondes. A sudden increase, from -0.2 to 6%, is observed at 15.8–10 hPa in 2000–2001 and also at 6.3–4 and 4–2.51 hPa (∼39 km) to a lesser extent.

To closely examine the increase in 2001 found at 15.8–10 hPa, SBUV(/2) ozone column profiles were compared to all OHP Umkehr data and SAGE II measurements extracted above OHP. To perform the comparisons, the Umkehr ozone columns were interpolated to SBUV(/2) pressure levels and, SAGE II ozone number density profiles are analysed as discussed previously for SBUV(/2)-lidar (non-convolved) comparison. Relative differences were determined at the SBUV(/2) pressure levels as

$$\Delta O_{3_{SBUV}}(i,j) = \frac{Meas(i,j) - SBUV(/2)(i,j)}{SBUV(/2)(i,j)} \times 100\% \tag{3.12}$$

where i = coincident day, j = pressure, and "Meas" represents Umkehr, lidar and SAGE II.

The compared results were smoothed by 3-month running average and are presented in Fig. 3.9. Relative differences of SBUV(/2) with SAGE II and lidar show similar behaviour, whereas Umkehr gives negative differences consistently. In 2001–2002, all data sets exhibit larger negative deviations compared to other years. In this study, we use SBUV/NOAA–16 data from October 2000 to December 2002. The aforesaid deviations can be due to the comparatively larger ozone values of SBUV/NOAA–16 as discussed in Nazaryan and McCormick (2005), who compared SBUV/2 with SAGE II, in Fioletov et al. (2006), who analysed SBUV(/2) with Umkehr, SAGE II and ozonesondes, and in Nazaryan et al. (2007), who compared SBUV/2 with HALOE. It should be noted, however, that the Dobson instrument at OHP was struck by lightning in 1999 and 2002, and these events have affected the quality of Umkehr data thereafter.

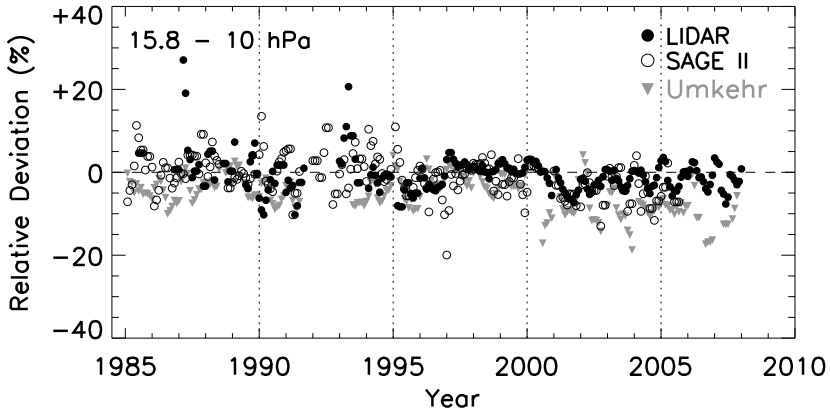

Figure 3.9: Monthly averaged differences of SBUV(/2) with lidar, SAGE II and Umkehr at 15.8–10 hPa. The dashed line represents 0 % and the dotted lines represent year 1990, 1995, 2000, and 2005. Data are smoothed by 3 month running mean.

3.4.5 Comparison of MLS and GOMOS with lidar

Figure 3.10 shows the comparison of ozone lidar with the shorter data sets MLS (left panel) and GOMOS (right panel). UARS MLS shows its best agreement with the lidar in 23–27 and 28–32 km with differences of ±10%. Differences are somewhat higher at other altitudes.

As the valid pressure range of UARS MLS is 100–0.22 hPa, we obtained only a few number of matching events at 16–20 km. Aura MLS produced smaller differences (±5%) at all altitudes except at 16–20 and 38–42 km where differences reach ±10%. GOMOS exhibits small deviations of ±5% from 2002 to 2005 at all altitudes. After 2005, the differences are a little higher, of the order of ±10% at 23–27, 28–32, 33–37 and 38–42 km and about ±15% at 16–20 and 19–23 km. This higher differences after 2005 can be due to the degradation of GOMOS data caused by the increase of the detector noise Tamminen et al. (2010).

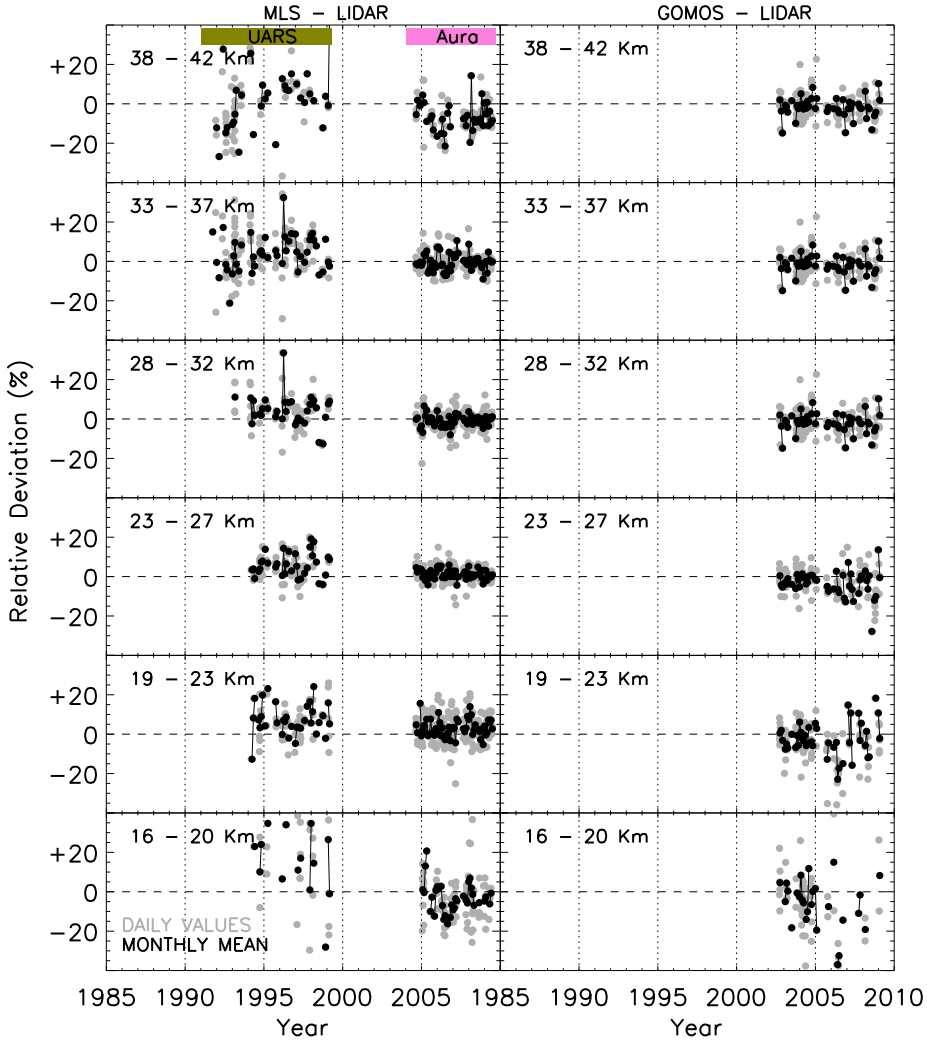

Figure 3.10: Same as Fig. 3.5, but for MLS on UARS and Aura satellites (left panel) and GOMOS (right panel). The period of observations of UARS MLS and Aura MLS are shown with respective colour shades, as for Fig. 3.1.

3.5 Drift in ozone differences

In order to evaluate possible drifts between various data sets and the lidar observations, a simple linear regression was computed from the monthly averaged time series of ozone

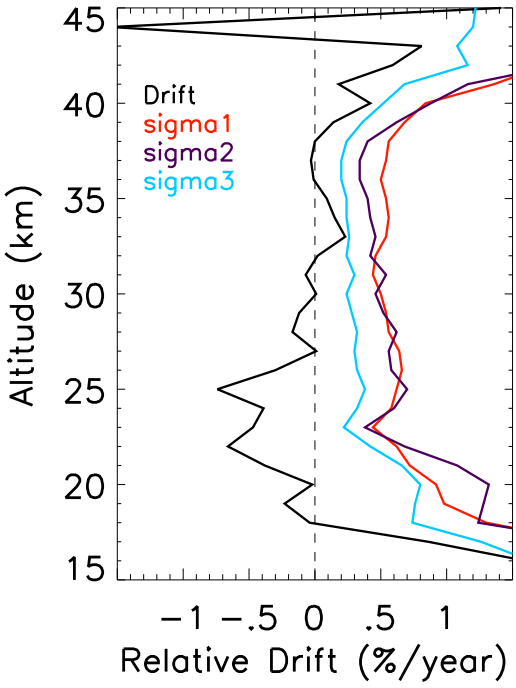

Figure 3.11: The relative drift and twice the standard deviations estimated from the Eqs. 3.7, 3.8 and 3.10 which are denoted as σ_1, σ_2 and σ_3 respectively, for the comparison of HALOE with lidar.

relative differences. Although some time series show non-linear variation as a function of time (e.g. in the case of SBUV(/2) at 15.8–10 hPa or ozone soundings), linear regression provides a simple way to check the drifts in various observational records.

3.5.1 Sensitivity of standard deviations

As stated earlier, different methods are available to find out the standard deviation of the slope. So in order to find out the best one, we took the commonly used Eqs. 3.7, 3.8 and 3.10 and are applied to the time series of the monthly averaged relative differences. Figure 3.11 shows an example of the relative drift and the standard deviations calculated from those equations for the comparison of HALOE with lidar. We can see that Eqs. 3.7 and 3.8 show only slight differences. In contrast, Eq. 3.10 yields smaller values, which could be due to the fact that it considers regular time sampling, which is not the case for the studied data set. So in our study we took Eq. 3.7 since it is well documented and widely used. The chosen standard deviation is then applied to all data sets for finding the significant drifts and are described in the following section.

3.5.2 Significance of the drifts in terms of the chosen standard deviation

Due to the reduced sampling of lidar measurements in the earlier period, the number of coincidences is smaller prior to 1994. After 1994 the number of lidar profiles increased due to the upgrade of the experimental set up and improved observational capacity at OHP. Therefore, linear regressions are evaluated over the respective period of each data set in 1985–2009 and 1994–2009. The starting (e.g. 1985 or 1994) and ending (2009) year of the analyses depend on the availability of the observations. Results of both calculations for the long-term data are displayed separately in Fig. 3.12 (left and middle panels). As

shown in the Figure, no striking difference is found by separating both periods, except for SAGE II and Umkehr above 35 km, with smaller drifts in 1994–2009. Also SAGE II exhibits larger drifts at 18–20 km in 1994–2005 as compared to that in 1985–2005. As for the average biases, the slopes are generally larger below 20 and above 40 km and are less than $\pm 0.5\%\,\mathrm{yr}^{-1}$ in the 20–40 km range. The drifts estimated for the specific altitudes are summarised in Table 3.3.

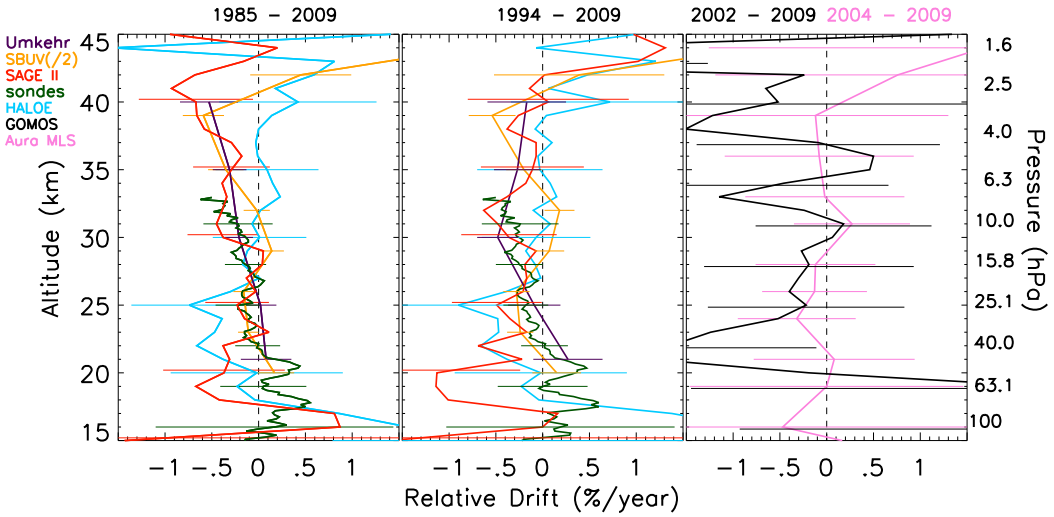

Figure 3.12: Vertical distribution of the slopes calculated from monthly mean of the relative differences of long-term (left and middle panels) and short-term (right panel) data sets with lidar data. The slopes are estimated in two periods, in 1985–2009 and 1994–2009, for the long-term data. The beginning (e.g. 1985, 1994, 2002 and 2004) and ending (2009) year of the analyses depend on the availability of the respective observations during the period. The dashed vertical line represents $0\,\%\,\mathrm{yr}^{-1}$ and the error bars represent twice the standard deviation of the slope. Approximate pressure levels corresponding to the geometric altitudes are also shown on the right axis.

In the case of SBUV(/2), a significant drift of $\sim \pm 0.2\%\,\mathrm{yr}^{-1}$ with respect to lidar is estimated at 25.1–15.8 and 6.3–4 hPa in 1985–2007 and at 40–25.1, 25.1–15.8 and 15.8–10 hPa in 1994–2007. At 6.3–4 hPa, larger deviations are found in the early 1990s, which could explain the significant slope calculated over the period. The shifts found at this pressure level and at 15.8–10 hPa in 2001 (Fig. 3.8) point out the inadequacy of using a simple linear regression over successive SBUV(/2) records at some pressure levels. SAGE II exhibits a significant slope of $-0.59\%\,\mathrm{yr}^{-1}$ at 19–23 km in 1994–2005 due to positive differences in 1994–1996 followed by negative ones in 2004–2005. Umkehr observations also show significant drift of $-0.3\%\,\mathrm{yr}^{-1}$ with respect to lidar at 16–8 and 8–4 hPa in 1985–2007 and 1994–2007. At 4–2 hPa, a relative drift of $-0.53\%\,\mathrm{yr}^{-1}$ is detected in 1985–2007. At these levels the relative differences have higher positive values at the beginning of the periods and higher negative values at the end of the period, which result in significant slopes over these periods. HALOE shows somewhat larger slopes than other measurement records at 20–25 km, but due to larger error bars the relative drifts are not significant.

A significant slope of $-0.33\%\,\mathrm{yr}^{-1}$ is estimated for ozonesonde - lidar comparison at 30 km in both periods, which can be due to the reduced accuracy of ozonesonde data at this altitude. The slopes are less than $\pm 0.6\%\,\mathrm{yr}^{-1}$ at 15–33 km in these periods. Further, relative drifts were also estimated for two other periods (1994–2001 and 2002–2009) to test the negative deviations found at 16–20 km in 1994–2006. Negative and positive slopes

were computed from 16 to 29 km in 1994–2001 and 2002–2009 respectively, but were less than $\pm 1.5\%\,\mathrm{yr}^{-1}$ at 21–33 km in both periods. At 16–20 km, the slopes were more negative in 1994–2001 and more positive in 2002–2009, with maximum of -3.1 and $2.8\%\,\mathrm{yr}^{-1}$ respectively.

Our drift estimates are in generally good agreement with those found in other studies. In this work, SBUV(/2)–lidar, Umkehr–lidar, sondes–lidar, SAGE II–lidar, HALOE–lidar, GOMOS-lidar and Aura MLS-lidar comparisons provide slopes generally less than $\pm 0.5\%\,\mathrm{yr}^{-1}$ in the 20–40 km range and are larger beyond this range. The study by Nazaryan and McCormick (2005) mentions slopes of less than 0.5 and $3\%\,\mathrm{yr}^{-1}$ for the time series of SAGE II with SBUV/2 data sets NOAA-11 and NOAA-16 respectively, in the 20–50 km range. Similarly, the slopes of HALOE with NOAA-11 and NOAA-16 are less than 1 and $2\%\,\mathrm{yr}^{-1}$ respectively (Nazaryan et al., 2007), consistent with our results. Cunnold et al. (2000) also studied instrumental drifts for different measurement techniques. They show SBUV-SAGE II slopes of less than $\pm 0.5\%\,\mathrm{yr}^{-1}$ at 20–40 km and around $1.5\%\,\mathrm{yr}^{-1}$ at 45 km in the 1984–1989 period at northern mid-latitudes. In 1989–1994, SBUV/2-SAGE II slopes are around $1\%\,\mathrm{yr}^{-1}$ at 25–45 km and are very small at 20 km. UARS MLS-SAGE and UARS MLS-HALOE provide slopes of around $\pm 1\%\,\mathrm{yr}^{-1}$ at 25–45 km in 1991–1996. Similarly, our results are similar to those found in SPARC (1998), for lidar–SAGE II comparison at OHP.

The drifts of the short-term data sets GOMOS and Aura MLS are also estimated with respect to lidar measurements in 2002–2009 and 2004–2009, respectively, and are shown in Fig. 3.12 (right panel). GOMOS shows small drifts less than $\pm 1\%\,\mathrm{yr}^{-1}$ between 24 and 37 km and of about ± 1.6 to $\pm 6\%\,\mathrm{yr}^{-1}$ outside this range. Aura MLS exhibits smaller drifts than those of GOMOS, ranging from ± 0.01 to $\pm 0.7\%\,\mathrm{yr}^{-1}$ at 15–42 km. As mentioned in Sect. 4.1.2, the degradation of the GOMOS data after 2005 could play a role in contributing large drifts. GOMOS provides relatively fewer number of coincidences with the lidar and that results in high variability in the monthly averages, and hence, larger drifts on a short period. The estimated drifts are not significant for Aura MLS at any altitude, whereas significant drifts of the order of -1.86, -1.67 and $-6\%\,\mathrm{yr}^{-1}$ are estimated for GOMOS at 21, 22 and 43 km respectively.

Thus, our analyses of the long-term evolution and drifts of ozone for various techniques are in good agreement with ozone trend studies for the northern mid-latitudes, although no other works evaluates drifts for more than 15 years using a variety of measurements, as performed in this study. Also, the short-term data with relative drifts comparable to those of the long-term data can be considered as an asset for their use in future ozone trend studies.

Table 3.3: The slope (S) and twice its standard deviation (σ) deduced from the monthly averages of the relative differences (%) at selected altitude levels for the periods 1985–2009 (S_{8509}) and 1994–2009 (S_{9409}). The two periods are chosen because of the upgradation of OHP lidar in 1993. Umkehr and SBUV(/2) are given on pressure levels.

Instrument	$S_{8509} \pm 2\sigma$ (% yr^{-1})	$S_{9409} \pm 2\sigma$ (% yr^{-1})	$S_{8509} \pm 2\sigma$ (% yr^{-1})	$S_{9409} \pm 2\sigma$ (% yr^{-1})	$S_{8509} \pm 2\sigma$ (% yr^{-1})	$S_{9409} \pm 2\sigma$ (% yr^{-1})	$S_{8509} \pm 2\sigma$ (% yr^{-1})	$S_{9409} \pm 2\sigma$ (% yr^{-1})	$S_{8509} \pm 2\sigma$ (% yr^{-1})	$S_{9409} \pm 2\sigma$ (% yr^{-1})	$S_{8509} \pm 2\sigma$ (% yr^{-1})	$S_{9409} \pm 2\sigma$ (% yr^{-1})
	16–20 km		19–23 km		23–27 km		28–32 km		33–37 km		38–42 km	
SAGE II	-0.42 ± 0.77	-0.74 ± 0.80	-0.31 ± 0.32	-0.59 ± 0.43	-0.10 ± 0.23	-0.29 ± 0.33	-0.18 ± 0.32	-0.32 ± 0.42	-0.33 ± 0.36	-0.22 ± 0.49	-0.51 ± 0.54	-0.01 ± 0.69
HALOE	0.26 ± 0.97	0.26 ± 0.97	-0.25 ± 0.49	-0.25 ± 0.49	-0.47 ± 0.49	-0.47 ± 0.49	-0.10 ± 0.45	-0.08 ± 0.50	0.08 ± 0.49	0.05 ± 0.59	0.31 ± 0.66	0.46 ± 0.75
ozonesondes	0.25 ± 0.34	0.25 ± 0.34	0.15 ± 0.24	0.13 ± 0.24	-0.21 ± 0.21	-0.20 ± 0.21	-0.33 ± 0.28	-0.33 ± 0.30				
	63.1–40 hPa		40–25.1 hPa		25.1–15.8 hPa		15.8–10 hPa		6.31–4 hPa		4–2.51 hPa	
SBUV(/2)	0.17 ± 0.21	0.15 ± 0.26	-0.11 ± 0.12	-0.24 ± 0.14	-0.16 ± 0.11	-0.28 ± 0.15	-0.02 ± 0.14	0.18 ± 0.16	-0.35 ± 0.19	-0.19 ± 0.19	0.45 ± 0.54	0.39 ± 0.91
			63–32 hPa		32–16 hPa		16–8 hPa		8–4 hPa		4–2 hPa	
Umkehr			0.08 ± 0.27	0.27 ± 0.37	0.02 ± 0.17	-0.09 ± 0.28	-0.21 ± 0.15	-0.48 ± 0.22	-0.31 ± 0.18	-0.27 ± 0.25	-0.53 ± 0.32	-0.17 ± 0.42

3.6 Summary

The homogeneity of various observational records of the stratospheric ozone vertical distribution at OHP is analysed by comparing lidar measurements with ECC ozonesondes and Umkehr measurements at OHP and with SBUV(/2), SAGE II, HALOE, UARS MLS, Aura MLS and GOMOS satellite observations, extracted above the station. The comparison of collocated ozone measurements helps to quantify the errors associated with each measurement system. The comparisons show generally the best agreement in the 20–40 km altitude range with average deviations within ±5%. The differences are larger below 20 km due to large atmospheric variability and also because of the lower accuracy and precision of the satellite measurements and above 40 km, because of the lower precision of ozone lidar measurements. Umkehr data show larger negative deviations as compared to other measurements, especially at 63–32 and 4–2 hPa. SBUV(/2) observations display a shift around 2001 at 15.8–10 hPa and to a lesser extent at 6.3–4 and 4–2.51 hPa. SAGE II and HALOE provide relatively less sampling at OHP in spring and summer. The best agreement with the lidar data is found for SAGE II with an RMS difference of 2.1% in the 15–45 km range, as compared to the other long-term data sets. The temporal evolution of ozonesondes–lidar comparison shows differences originated from the changes in the ozone receiving system, ozone column data used for normalising the sonde profiles and from the ozone deriving methods. Hence, a homogenised data are needed for the better evaluation of ozone trends. Shorter observational records such as UARS MLS, Aura MLS and GOMOS were also analysed to check their measurement consistency. UARS MLS displays positive biases and are relatively larger compared to Aura MLS. Aura MLS shows good agreement with the lidar at 20–40 km, but negative deviations above 40 km, with GOMOS also showing such a tendency during some seasons. GOMOS compares well with the lidar at 28–40 km.

Linear regressions were computed on the monthly average difference data sets in order to detect possible drifts with respect to the lidar measurements. Collectively, drifts are generally within $\pm 0.5\%\,\mathrm{yr}^{-1}$ at 20–40 km in both analysed periods (1985–2009 and 1994–2009), and are generally not significant at the 2σ level. Aura MLS yields very small and non-significant drifts (± 0.01–$0.7\%\,\mathrm{yr}^{-1}$) at 15–42 km with the lidar, comparable to those of the long-term data sets. Hence, the tested observational records should generally allow for analyses of the long-term evolution.

Chapter 4

Stability of ozone observations over NDACC lidar stations

Contents

To understand the long-term ozone changes or the ozone recovery due to ODS changes, a set of stable ozone measurements spanning over a few decades are necessary. In the case of ozone profile measuring instruments, it is difficult to homogenise different data sets because of the varied vertical resolutions and the differences in retrieving data, particularly in the lower stratosphere, where most instruments provide less accurate measurements. Furthermore, the lack of highly resolved ozone vertical observations over several decades is another issue because SAGE II and HALOE stopped their service in 2005. Also these data sets show degradation from 2000 onwards and the succeeding satellites were operational since 2002 only. To this end, no studies have assessed the validity of a combined time series of terminated and new satellite measurements and no studies have performed the evaluation of stratospheric ozone trends using such a long-term combined data set.

Based on these aspects, this chapter in line with the previous chapter assesses the stability of ozone lidar measurements at various NDACC lidar stations by comparing the lidar measurements with available ozonesondes and satellite measurements at the station. The focus is made on the ozone lidars, which are having more than 10 years of continuous observations. Apart from the lidar and satellite ozone comparisons, various satellite-satellite ozone comparisons are also performed to discuss the relative drifts and stability of the lidar measurements.

This chapter is organised in the following way: The data description of ozonesondes at different stations is followed by the methodology used for the analyses in Sect. 4.2.

Sect. 4.3 and 4.4 discuss the average biases, the stability evaluation of ozone measurements using relative drifts respectively. The temporal evolution of the combination of older and newer satellite data sets and the drifts derived from the combined data are presented in Sect. 4.5. Section 4.6 summarises the main findings from the study.

4.1 Ozonesonde measurements

In addition to the data sets described in Chapter 3, ozonesonde measurements performed at MOHp, Tateno, Hilo and Lauder are also utilised here. BM sondes manufactured by the Mast Keystone Corporation, have been used at MOHp since 1967 (Steinbrecht et al., 1998). They employ a bubbler consisting of an electrochemical cell filled with 0.1% buffered KI solution in which cathode and anode wires are immersed in. The accuracy of BM sondes is better than 5% in the stratosphere. The radiosonde type has been changed from VIZ to Vaisala RS80 in 1996. Ozone profiles (1987–2011) normalised by a total column data are used in this study.

The KC type ozonesondes, manufactured by Meisei Electric Company, are used at Tateno (hereafter termed as Tsukuba ozonesondes) from 1968 to November 2009 and ECC sondes afterwards. The KC68, KC79 and KC96 were used in 1968–1979, 1979–1997 and from mid-1997 to 2009, respectively. They are based on a carbon-iodine ozone sensor, an electrochemical cell containing platinum gauze as cathode and carbon as anode immersed in an aqueous neutral KI/KBr solution (Fujimoto et al., 1996). In 1979, the double-chambered electrochemical cell is modified to a single cell. The KC sondes are normalised to a total column data and are used here for the period 1988–2009.

ECC sondes made by SPC-4A, 5A and 6A and ENSCI 1Z and 2Z models have been used for measuring ozone at Hilo in 1991–2010. These are connected to Vaisala RS-80-15 type radiosondes using the interface boards En-Sci V2C for all 2Z sondes, TMAX for all 5A, 6A and 1Z sondes and an analog data system for 4A sondes. The data acquisition is made using the Strato version (V) 7.2 program. The cathode sensor solution has been switched from 1% KI buffered to 2% KI unbuffered in 1998 and is again changed to 1% KI buffered in 2005. The integrated ozone column is compared to that of Dobson, but normalisation is not performed (McPeters et al., 1999). In our analysis the correction factor is calculated from the ratio of the Dobson ozone column to the sonde ozone column provided in the data files. Hereafter, Hilo ozonesondes are referred to as the ozonesondes at MLO.

At Lauder, ECC ozonesondes with 1% KI cathode solution concentration have been flown from 1986 to 1996 and using 0.5% KI from 1996 to the present. SPC-4A, 5A and 6A series of sondes were used in 1986–1989, 1990–1994 and 1995–1996, respectively, followed by ENSCI-1Z. The VIZ radiosonde was used until 1989 and then Vaisala RS80, coupled with a TMAX interface. Here ozonesonde data are not normalised with a total ozone column data, but the data from the sondes containing 1% solution are multiplied by 0.9743 to make them on the Dobson column measurement on the BP scale because the BP cross sections affect the Dobson data on which ozonesonde calibrations are based (Bodeker et al., 1998). Corrections are applied to the ozonesonde values above 200 hPa to account for pump efficiency degradation. The integrated ozone profile is compared to the total column of ozone measured by Dobson spectrophotometer at Lauder and the uncertainty is typically less than 5%. Ozonesonde measurements from 1986 to 2009 are analysed here.

Table 4.1: Various NDACC lidar stations, their locations and the period of observations of lidar and the analysis period of ozonesondes used in this study are given. The satellite data sets utilised for the study and their observational periods are also noted.

Station	Location		Period	
	Lat	Lon	Lidar	ozonesondes
MOHp	47.8 N	11.0 E	1987–2011	1987–2011
OHP	43.9 N	5.7 E	1985–2010	1991–2010
Tsukuba	36.0 N	140.0 E	1988–2010	1988–2009
TMF	34.5 N	117.7 W	1988–2011	-
MLO	19.5 N	155.6 W	1993–2011	1993–2010
Lauder	45.0 S	169.7 E	1994–2011	1994–2009

Instrument	Period
SBUV(/2)	1984–2007
SAGE II	1984–2005
HALOE	1991–2005
UARS MLS	1991–1999
Aura MLS	2004–2011

4.2 Data analysis

The average bias and relative drift of different long and short-term data sets are analysed with respect to the ozone lidar measurements in order to evaluate their consistency and stability. The lidar stations, the respective locations and other observations considered for the analysis are listed in Table 4.1. The spatial criteria used for extracting satellite data at all stations are the same as used for the extraction above OHP, as described in Chapter 3 except that Aura MLS has been extracted in $\pm 2.5^\circ$ latitude and $\pm 5^\circ$ longitude bands with respect to the location of each station. The coincidence criteria is also the same as mentioned in Chapter 3.

Figure 4.1 displays the total number of measurements of all observational techniques at the lidar stations and the number of coincidences obtained by all data sets from different comparisons. The panel (a) shows the total number of ozone profiles measured by each observation technique above the stations. Regarding the ground-based measurements, around 2000 lidar profiles are available at MOHp, OHP, TMF and MLO for the analysis. Tsukuba and Lauder lidar measured nearly 600 and 1000 profiles respectively. The number of sonde measurements are larger at MOHp ($\sim$3000) compared to those of OHP (870), MLO (860) and Lauder (1500).

Among the satellites, SBUV(/2) and Aura MLS provide the maximum number of measurements ($\sim$8000) during their observational period of 22 and 8 years respectively. They measure nearly the same number of profiles at all regions irrespective of latitudes. On the other hand, UARS MLS, SAGE II and HALOE show a clear latitudinal dependence with fewer observations by SAGE II and HALOE at all stations. SAGE II and HALOE take more observations above 40° latitude on both hemispheres (e.g. MOHp, OHP and Lauder) and less measurements at other stations. On the contrary, UARS MLS yield more profiles at stations situated below 37° latitude (e.g. Tsukuba, TMF and MLO) and less profiles at other stations. Generally, UARS MLS provides more measurements between 34°S to 34°N because of its yaw manoeuvres. The panel (b) of the Fig. 4.1 illustrates the total number of measurements when considering only one measurement per day.

The analysis is performed using the coincident ozone profiles of various data sets. Coincidences are determined using spatial grids similar to those applied for the data extraction mentioned previously, with a time difference of ± 12 h. In order to get a clear idea about the bias and drift of various time series, four different types of comparisons are performed at each station. First various data sets are compared to the lidar measurements and then the same data sets including the lidar ones are compared to each long-term satellite record (e.g. SBUV(/2), SAGE II and HALOE). Comparison with respect to MLS as reference is not considered due to its relatively shorter time period. The number of collocations ob-

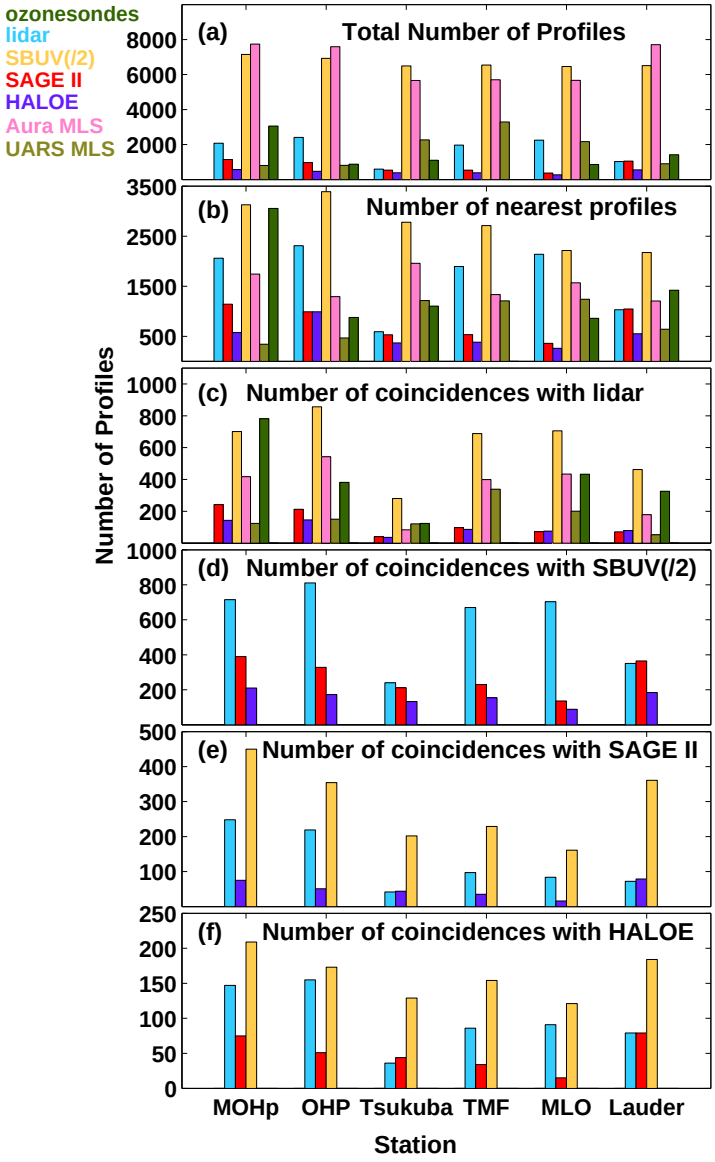

Figure 4.1: Total number of profiles of all data sets at various stations (panel (a), the total number of profiles considering one measurement per day (panel (b), the total number of coincidences of different observations with lidar (panel (c) and the total number of coincidences of the long-term measurements with SBUV(/2) (panel (d), SAGE II (panel (e) and HALOE (panel (f).

tained for each data from these comparisons are presented in the lower panels of Fig. 4.1. The panel (c) shows the total number of coincidences of all measurement techniques with respect to the ozone lidar. Among the lidars, the Tsukuba lidar provides the fewest coincidences due to its comparatively lower measurement frequency. Compared to the stations above 40° N/S, Lauder lidar provides fewer collocations since it has started operation in 1994, about 8 years after the MOHp and OHP lidars. The panels (d), (e) and (f) of Fig. 4.1 display the number of collocated profiles of the long-term measurements with respect to SBUV(/2), SAGE II and HALOE, respectively. As expected HALOE and SBUV(/2) provide the lowest and the highest number of collocated profiles, respectively with respect to all other measurement techniques.

4.2.1 Relative difference and mean bias

In order to quantify the bias of various data records with respect to lidar, the difference time series are computed. As the observing period of lidars is different for various stations, the period of comparisons also differ. The comparison periods of ozonesondes depends on the availability of both lidar and sonde data at the station. In the case of comparison with the lidar, the difference between collocated measurements are computed as in Eq. 3.4. The mean bias and the standard error are calculated as in Eq. 3.5 and Eq. 3.6, respectively.

The estimation of drifts of satellite data requires an evaluation of the stability of the reference measurements, the lidars, in this study. The stability of lidar data is analysed by comparing lidar ozone with SBUV(/2), SAGE II, HALOE and ozonesondes as references and by estimating their relative drifts. To compare the drift of lidar measurements with those of other long-term data, SBUV(/2), SAGE II and HALOE data are compared with each other (taking each of them as the reference) in a similar way. For instance, the comparison with SBUV(/2) as the reference is performed as

$$\Delta O_{3B}(i,j) = \frac{Meas(i,j) - SBUV(/2)(i,j)}{SBUV(/2)(i,j)} \times 100\% \tag{4.1}$$

with 'Meas' as lidar, SAGE II and HALOE.
The same procedure is repeated for the comparisons with respect to SAGE II and HALOE. i.e.,

$$\Delta O_{3S}(i,j) = \frac{Meas(i,j) - SAGE\ II(i,j)}{SAGE\ II(i,j)} \times 100\% \tag{4.2}$$

where 'Meas' is lidar, SBUV(/2) and HALOE and

$$\Delta O_{3H}(i,j) = \frac{Meas(i,j) - HALOE(i,j)}{HALOE(i,j)} \times 100\% \tag{4.3}$$

where 'Meas' is lidar, SBUV(/2) and SAGE II.

4.2.2 Data conversion

Data conversion and the method used for the analysis are also the same as discussed in Chapter 3. However, there are significant improvements in the analysis presented in this chapter to find the relative difference, bias and drifts. One of the important change is in the comparison of Aura MLS with the lidar measurements above 30 km. Because above 30 km the lidar and MLS have similar vertical resolution and so the comparison is done by interpolating lidar data to MLS altitudes in this region, which reduces the large bias found in the upper stratosphere.

Table 4.2: The RMS values estimated in 20–40 km from the average bias of each measurement technique at various stations.

Instrument	MOHp	OHP	Tsukuba	TMF	MLO	Lauder	AVG
SBUV(/2)	2.90	2.33	4.66	3.43	3.72	2.72	3.29
SAGE II	2.30	1.07	3.56	3.38	3.31	2.36	2.66
HALOE	3.02	2.44	2.30	2.53	2.29	1.90	2.41
UARS MLS	4.21	5.15	3.57	1.01	1.37	6.51	3.63
Aura MLS	1.41	1.24	4.17	2.84	3.89	1.99	2.59

Another main change is that we have used NCEP data for converting ozone lidar number densities to ozone partial columns for comparing with SBUV(/2). It showed a slightly large drift in the comparison between SBUV(/2) and lidar above 30 km. In a similar study McLinden et al. (2009) also referred to an anomalous temperature trend above 30–35 km for the comparison between SBUV(/2) and SAGE II. Therefore, in this study we took temperature and pressure data from Arletty (Hauchecorne, 1998), an atmospheric model that makes use of the ECMWF (European Centre for Medium Range Weather Forecasts) meteorological analysis (operational data) and MSIS90 climate model for deriving atmosphere profiles, to convert ozone number density from lidars and SAGE II or VMR from HALOE to partial column for the comparison with SBUV(/2). Arletty uses ECMWF data up to 30 km and MSIS90 above 30 km in 1979–1998 and from 1999 onwards ECMWF data are used until 45 km. Even if the comparisons are performed on pressure levels, the results are presented on geometric altitudes for the comparison with other measurement techniques too. For that, the approximate altitudes corresponding to the SBUV(/2) mid-pressure levels are calculated using the Arletty data.

4.3 Average biases: comparison with lidar measurements

Figure 4.2 displays the vertical distribution of average relative differences between coincidences of different observations and lidar measurements for the various stations. The consistency of ozone measurements can easily be judged from these mean differences. Different measurements show generally a very small bias with the lidar data, within ±3% in 20–40 km, except UARS MLS at OHP and Lauder. A very consistent behaviour in the relative differences is shown by all observations at TMF above 21 km except SBUV(/2) between 30 and 40 km. At MLO also all observations display a similar bias. The root mean square (RMS) of mean biases in the 20–40 km altitude range is calculated, as described in Chapter 3 for all measurements to see which instrument agrees best with the lidar. From the average of the RMS values at all stations, it is found that among the satellite measurements, HALOE yields the lowest (2.41%) and UARS MLS the highest (3.63%). The estimated RMS values for each instrument at all stations and the average RMS of each measurement technique is provided in Table 4.2. The average of the RMS values of all observations at each station shows the smallest value (2.45%) at OHP and the largest value (3.65%) at Tsukuba.

Generally, the differences are larger in the upper stratosphere (above 40 km) compared to those in the middle stratosphere (20–40 km), but are less than those observed in the lower stratosphere (below 20 km). Yet they do not exceed ±7% in most cases. These large biases above 40 km are likely due to the relatively lower precision of the ozone lidar above

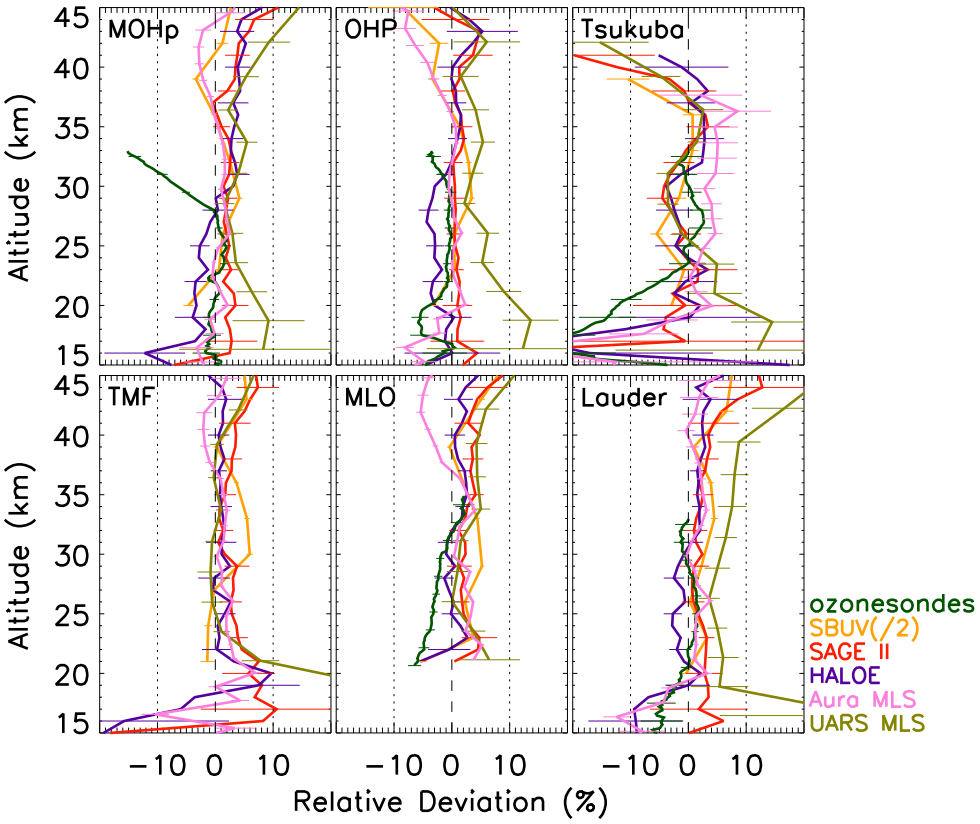

Figure 4.2: Vertical distribution of the average relative differences of the coincident ozone profiles of different datasets with various lidar measurements $\left[\Sigma\left(100 \times \frac{Meas-lidar}{lidar}\right)\right]$. The dashed and dotted vertical lines represent 0 and ±10% respectively and the error bars correspond twice the standard error.

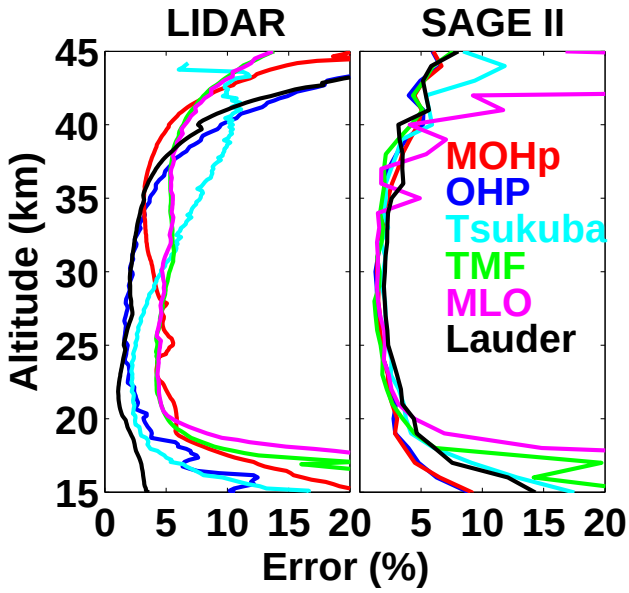

Figure 4.3: The vertical distribution of the average error of ozone lidar and SAGE II data at various stations.

40 km. Smaller biases are observed with respect to TMF lidar measurements, which implies that these are less noisy in the upper stratosphere. Figure 4.3 shows the uncertainties of the lidar and SAGE II ozone measurements at different stations, provided in the data files, averaged over the respective periods. It is clear that below 20 km both instruments exhibit large measurement uncertainty except Lauder lidar, which yields only 3 %. Also, ozone lidar measurements provide larger error above 40 km compared to that of SAGE II.

Comparatively larger differences observed below 18 km are mostly due to the large ozone variability in the lower stratosphere. It is noted that the tropopause varies from ∼10 to ∼15 km depending on the season at MOHp, OHP and Lauder, and from ∼12 km in winter to ∼18 km in summer at Tsukuba and TMF, whereas it is located between 16 and 20 km at MLO. Because of the elevated tropopause in all seasons, the analysis excludes the measurements below 21 km at MLO. Near the tropopause the ozone variability is largest, which can be the reason for the observed large differences for all measurements below 18 km at Tsukuba and TMF. Besides, as in our analysis, Jiang et al. (2007) also showed some high bias for Aura MLS with the OHP, TMF and MLO lidars in the lower stratosphere. In addition, it is a more difficult region to retrieve ozone from satellite measurements.

Large deviations are found at Tsukuba particularly in 15–17 and 40–42 km, as seen in Tatarov et al. (2009). These are possibly due to the fewer coincidences with Tsukuba ozone lidar measurements. The large positive deviations found for UARS MLS below 20 km at all stations can be due to the poorer retrieval of UARS MLS in this altitude range. This positive bias near to 100 hPa was also found in the comparison between SAGE II and UARS MLS in all latitudes (Livesey et al., 2003). Aura MLS shows very small deviations above 20 km even though a slight negative bias of ∼5% is found at OHP and MLO above 38 km. This negative difference above 38 km (3–1.46 hPa) was already shown in Jiang et al. (2007) for the comparison with lidar measurements at MLO and in Boyd et al. (2007) for the comparison with microwave radiometer (MWR) at MLO. At MLO, it could be due to the MLS temperature data used for the conversion of MLS ozone VMR to number density. The

differences of SAGE II and Aura MLS with the MWR show positive deviations in the upper stratosphere at Lauder (Boyd et al., 2007), which is same as obtained in our comparison for SAGE II and Aura MLS with the Lauder lidar.

4.3.1 Correction factor

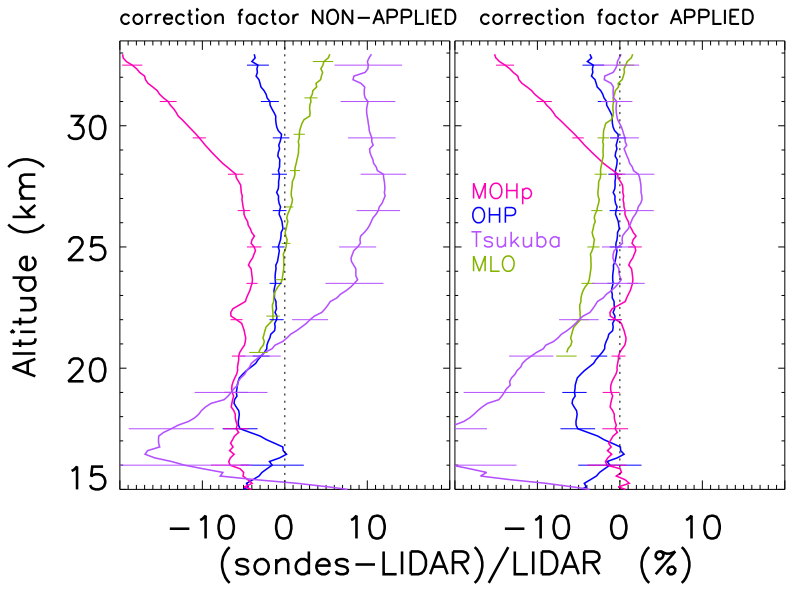

Figure 4.4: The average bias of sonde measurements, without (left panel) and with (right panel) multiplying the profiles by the CF, obtained for the comparison with lidar at MOHp, OHP, Tsukuba and MLO. The dotted vertical line represents 0% and the error bars correspond twice the standard error.

As mentioned in Sect. 3.1.2, CF is used to screen the sonde profiles in our analysis also and to compare the average bias and drift. This procedure is used for the ozonesonde data at MOHp, OHP, Tsukuba and MLO in our study. Here, we investigate the sensitivity of average bias and drift with respect to the lidar to the use of CF. Therefore, the normalised BM and KC sonde profiles are divided by the CF to remove the scaling. Figure 4.4 shows the average biases obtained for the comparison between lidar and non-normalised (left panel) and normalised (right panel) sondes. The non-normalised BM (at MOHp), KC (at Tsukuba) and ECC (at OHP) sondes provide larger bias compared to the normalised sondes. However, the non-normalised ECC sondes at MLO yield smaller bias than that of the normalised sondes. The non-normalised sondes consistently underestimate ozone at all altitudes at MOHp and OHP. Nevertheless, the non-normalised KC sondes at Tsukuba overestimate ozone above 22 km and underestimate below 19 km, whereas the normalised KC sondes show comparatively larger negative bias below 22 km. In general, multiplication of the CF reduces the bias except at MLO. Besides, the differences between these comparisons, in terms of CF, are not as large for ECC sondes as compared to the BM and KC sondes. In addition, the ozonesondes at MOHp show slightly large bias above 29 km in both cases, which is largely due to the inadequate correction of decreasing pump efficiency in the low pressure regions (Steinbrecht et al., 1998, 2009a).

4.4 Relative drifts

Monthly mean difference time series of the compared data sets are used to evaluate drifts in the ozone measurements because they are less noisy compared to the daily variations and hence, the influence of outliers can be reduced from the drift estimation. A simple linear regression is applied to these time series and drifts are derived from the slope value of the regressions.

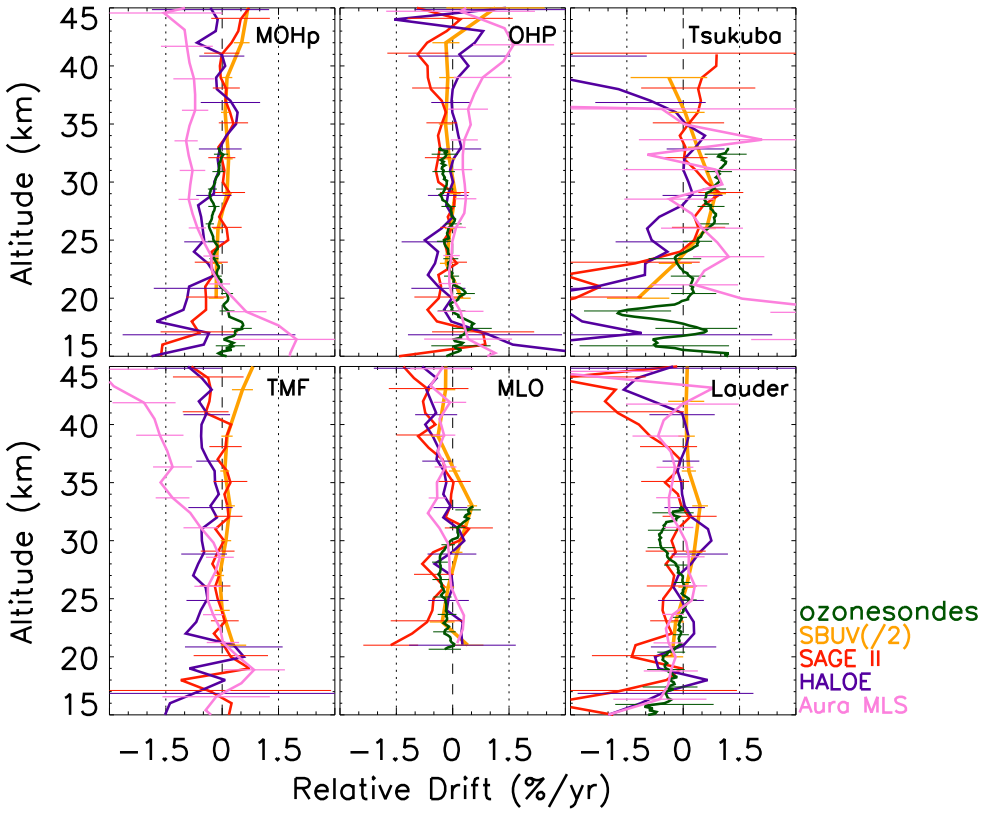

Figure 4.5: Vertical distribution of the slopes evaluated from the monthly averaged difference time series of all observations with the lidar measurements at various regions $\left(100 \times \frac{Meas-lidar}{lidar}\right)$. The error bars represent twice the standard deviation of the slope. The dashed vertical line represents $0\%\,\mathrm{yr}^{-1}$ and the dotted vertical lines represent $\pm 1.5\%\,\mathrm{yr}^{-1}$.

4.4.1 Comparison with ozone lidar as reference

Lidars are used as a reference for Fig. 4.5, where drifts are estimated for the data set samples from SBUV(/2), SAGE II, HALOE, Aura MLS and ozonesondes. UARS MLS is excluded from the drift estimation since it is not considered as good for trend studies because of the change of instrument set-up in 1997 due to the failure of one radiometer for the independent P/T retrievals. Generally, the relative drifts are less than $\pm 0.3\%\mathrm{yr}^{-1}$ at 20–40 km and most of them are insignificant. However, some significant drifts are observed for SAGE II in 22, 38–41 km at OHP and in 20–22,25, 38 and 39 km at MLO. Similarly HALOE shows significant drifts in 15, 22–23 and 25 km at OHP, in 22–24 and 37–40 km at TMF and in 37, 40 and 42 km at MLO. SBUV(/2) exhibits statistically significant drifts in 33 and 43 km at

TMF and in 33 and 39 km at MLO. As we have seen for the biases, drifts are larger below 20 and above 40 km. Among the long-term measurements, SBUV(/2) and ozonesondes provide the smallest drift with respect to all lidars. Aura MLS also exhibits comparable drifts as that of SAGE II and HALOE even if it has only 8 years of measurements. Aura MLS drifts are significant at some altitudes at MOHp, TMF and MLO. The average of the RMS values of the drifts calculated in the 20–40 km altitude range shows the smallest value ($0.27\%\mathrm{yr}^{-1}$) for SBUV(/2) and the largest ($1.36\%\mathrm{yr}^{-1}$) for Aura MLS. The station average of the RMS values of all measurement techniques provide the lowest value ($0.29\%\mathrm{yr}^{-1}$) at OHP and the highest ($2.27\%\mathrm{yr}^{-1}$) at Tsukuba.

Aura MLS shows relatively larger negative drifts at MOHp and TMF above 30 km. In order to understand these negative drifts, we analysed the deseasonalised raw ozone time series (i.e., by considering all observations irrespective of the coincident profiles) from various observations including Aura MLS and lidar, at MOHp and TMF. From the deseasonalised ozone time series, it is observed that MOHp lidar ozone increases from 2007 onwards above 30 km and TMF lidar shows high ozone values in 2008 and 2009 above 30 km compared to all other measurements, which results in significant negative drifts.

Note that the drift in the measurement differences may not entirely be due to the measurement uncertainties of the comparison data sets, as the reference data can also contribute to it. Therefore, accurate diagnosis of the stability of the reference data is a prerequisite in drift studies and hence, the stability of lidar time series is evaluated in the following section.

4.4.2 Comparison of lidar with SBUV(/2), SAGE II and HALOE as references

The stability of ozone lidar measurements is checked by analysing their drifts in comparison with other long-term data sets such as SBUV(/2), SAGE II and HALOE as references and the estimated drifts are shown in panels a, b and c of Fig. 4.6 respectively. It is almost similar to Fig. 4.5 with the change in reference data. This method is adopted to find the differences in the drifts for the change of reference data too. Generally, all lidars exhibit very small drifts (within $\pm 0.2\%\,\mathrm{yr}^{-1}$) with SBUV(/2) and some of these are significant at MOHp (in 30–34 and 39–45 km), Tsukuba (in 25–33 km), TMF (in 32–34 and 41–45 km) and MLO (in 30–34 and 39–41 km). The drifts with SAGE II and HALOE are slightly larger compared to that with SBUV(/2), but most of them are not significant except the ones with SAGE II at MLO at some altitudes. The RMS of the drifts of lidar in the 20-40 km altitude region, averaged over the stations excluding Tsukuba is about 0.16, 0.34 and $0.42\%\,\mathrm{yr}^{-1}$ with respect to SBUV(/2), SAGE II and HALOE respectively. So the lidars can be taken as a reliable reference for drift evaluation of satellite and other ground-based measurements. To corroborate these results, the drifts of other long-term measurements SBUV(/2), SAGE II and HALOE are estimated in a similar manner and are described in the following section.

4.4.3 Comparison of SBUV(/2), SAGE II and HALOE

As mentioned earlier, the relative drifts of SBUV(/2), SAGE II and HALOE are evaluated by comparing them to each other. Figure 4.7 (a) shows the relative drifts of HALOE at various stations with SAGE II as reference. This comparison shows drifts maximum of about $\pm 0.2\%\,\mathrm{yr}^{-1}$ at MOHp and Lauder and $\pm 0.4\%\,\mathrm{yr}^{-1}$ at OHP and Tsukuba. At TMF, it is more or less scattered and is less than $\pm 0.5\%\,\mathrm{yr}^{-1}$ except at 21–22 and 29–34 km. At MLO also the drifts are more scattered and slightly larger. At MLO, the coincidences are

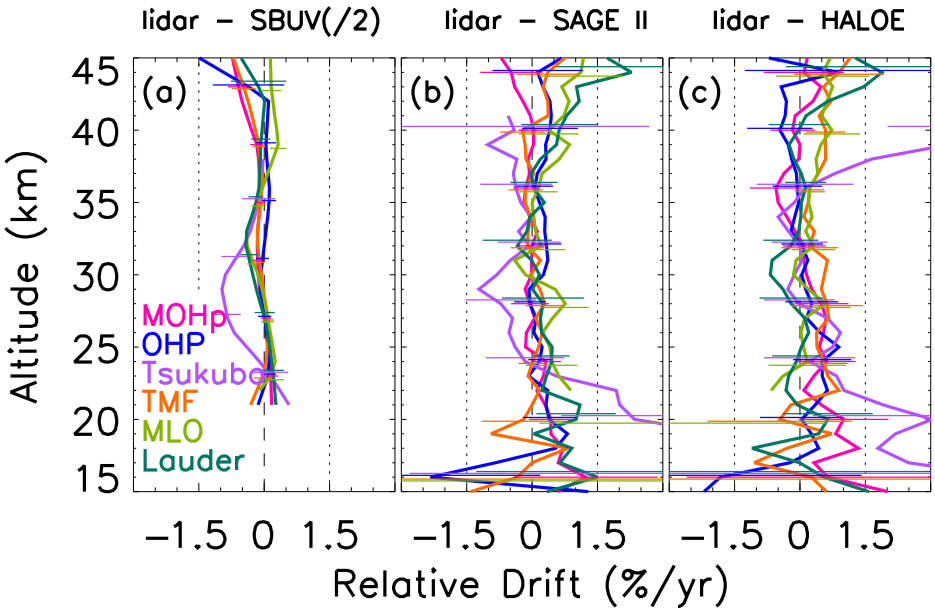

Figure 4.6: The drifts of various lidars for the comparison with SBUV(/2), SAGE II and HALOE as references $\left(100 \times \frac{lidar-ref}{ref}\right)$. The error bars correspond the 95% confidence interval of the slope.

available in 1999–2003 only. This is the reason for the estimated large drifts at MLO. The HALOE - SAGE II drifts are compatible with the no-drift hypothesis, but the uncertainty is too large to detect small drifts. At MLO, the coincidences are available in 1999–2003 only. This is the reason for the estimated large drifts at MLO.

Figure 4.7 (b) and (c) represent the relative drifts of SBUV(/2) with SAGE II and HALOE as references respectively. The relative drifts of SBUV(/2) from both comparisons are very small and most of them are close to zero irrespective of the stations. SBUV(/2)–SAGE II comparison yields smaller drifts than those between SBUV(/2) and HALOE. The former comparison yields around $\pm 0.1\%\,\mathrm{yr}^{-1}$ in 20–44 km while the latter leads to about $\pm 0.2\%\,\mathrm{yr}^{-1}$ at 21–25, 30–42 km and $\sim 0.5\%\,\mathrm{yr}^{-1}$ at 45 km at all stations. The importance is that even if the drifts are very small, some of these are significant particularly in the upper and middle stratosphere. For example, SBUV(/2)–HALOE drifts are significant at MOHp (in 28 and 31 km), OHP (in 21, 27, 30 and 40 km), Tsukuba (at 26, 29, 43 km), TMF (at 28, 31, 41 and 44 km), MLO (at 26, 29, 41 and 44 km) and at Lauder (at 27 km). These results are very similar to those mentioned in Nazaryan and McCormick (2005) and Nazaryan et al. (2007), who compared SBUV/2 (NOAA-11,16) with SAGE II and HALOE respectively in the latitude bands 50–40 S, 10–20 N, 30–40 N and 40–50 N. In the same manner, Cunnold et al. (2000) calculated drifts between SBUV and SAGE and found very small drifts of $\pm 0.5\%\,\mathrm{yr}^{-1}$ in the tropical and mid-latitude regions.

From Figs. 4.6 and 4.7, it is obvious that the comparison between SBUV(/2) and all other long-term measurements provides near-zero drifts (or no drifts) at all stations and at all altitudes. Here, the comparison is performed using partial ozone columns on SBUV(/2) pressure levels, which reduces the ozone variability. Moreover, the coincidences between SBUV(/2) and other measurements provide a continuous time series (or the coincidences are available in all months considered over the time period) and also the number of coincidence are large. These reasons contribute to the smaller drifts.

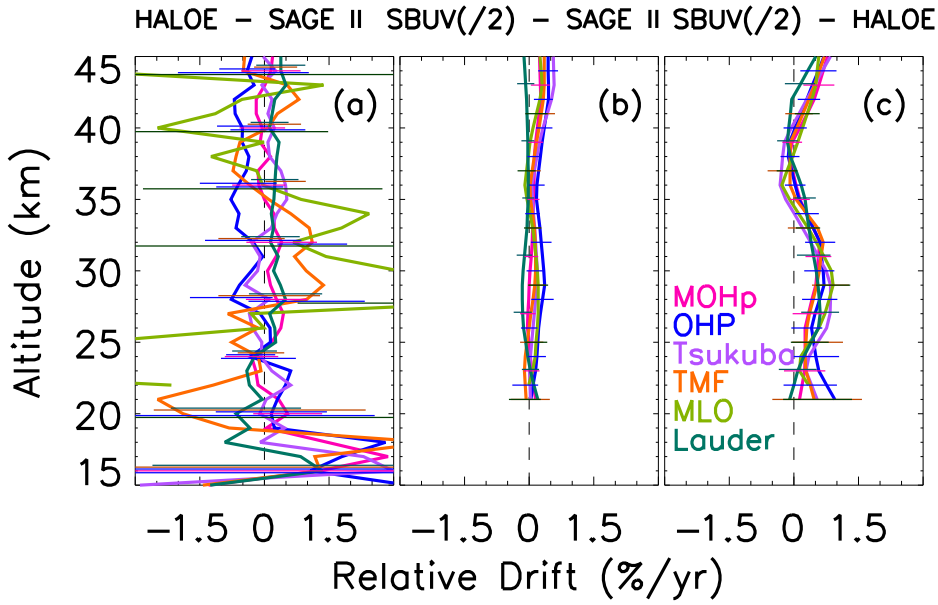

Figure 4.7: a) The drifts of HALOE in comparison with SAGE II as reference (see Eq. 4.2) at various stations. b) The drifts of SBUV(/2) with SAGE II as reference (see Eq. 4.2). c) Same as (b), but with HALOE as reference (see Eq. 4.3). The error bars represent twice the standard deviation of the slope.

From all the comparisons, it is clear that only the comparison between SAGE II and HALOE shows relatively larger, but insignificant drifts (Fig. 4.7(a)). However, even if the comparison between SAGE II and HALOE produces larger drifts with each other, their comparison with SBUV(/2) and lidar yields very small or near zero drifts. It means that the comparison of similar techniques having a low measurement frequency does not provide an accurate drift estimation from the difference time series. Therefore, the large drift obtained for the comparison between SAGE II and HALOE does not imply that these measurements are unstable for the long-term study. From these estimations, it is inferred that we cannot reach a conclusion on whether measurements are stable or unstable only by comparing two data sets with relatively fewer coincidences in comparison to the other data sets.

4.4.4 Average of the drifts of long-term measurements

In order to summarise or to compare globally the magnitude of the drifts of different measurement techniques obtained from various comparisons, the average drifts are computed for each data set at each station and are presented in Fig. 4.8. For example, the drift of the lidar shown at each station is the average of its drifts (shown in Fig. 4.6) obtained from the comparisons with SBUV(/2) (Eq. 4.1), SAGE II (Eq. 4.2) and HALOE (Eq. 4.3) as references. Similarly, the mean drift of SBUV(/2) is the average of the drifts obtained from the comparisons with lidar (Eq. 3.4), SAGE II (Eq. 4.2) and HALOE (Eq. 4.3) as references and similarly for SAGE II and HALOE. In a similar way, the standard deviation corresponding to the mean drift of each measurement technique is computed by averaging the standard deviations of each drift obtained from different comparisons. It is just a way to represent the standard deviation and does not show the significance of the drift.

Generally, as found in the previous comparisons, all data sets show small drifts of around

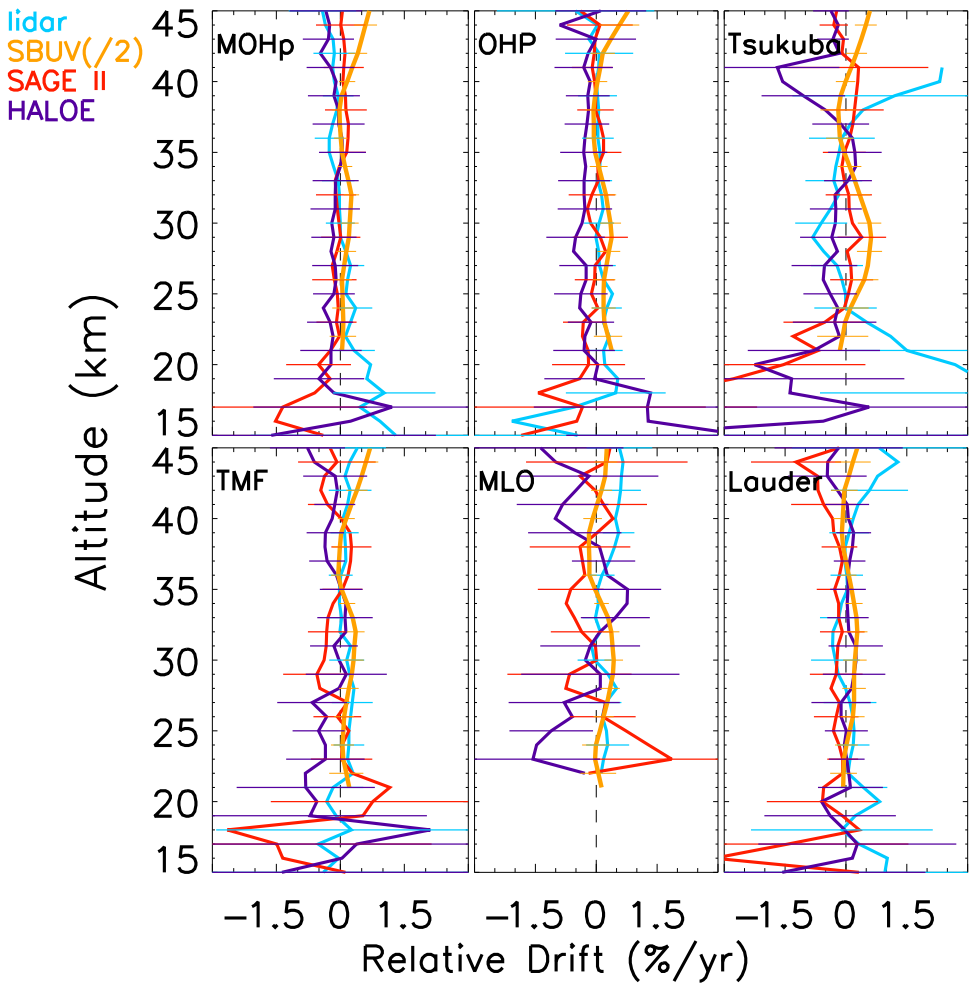

Figure 4.8: The mean drifts estimated for the long-term observations with respect to other long-term measurements as references. The error bars represent twice the average of the standard deviations of the slopes obtained from different comparisons.

$\pm 0.2\%\,\mathrm{yr}^{-1}$ at 18–45 km and the measurements are stable too. Below 18 km the drifts are larger as expected. In this altitude range, the large ozone variability near the tropopause play a pivotal role in deciding the magnitude of the differences. Among the long-term data sets, lidar and SBUV(/2) yield very small drifts at all stations. Also, the drifts of SBUV(/2) are similar at various stations. SAGE II and HALOE also provide small drifts at all stations except at MLO, where slightly large drifts, but not $>1\%\,\mathrm{yr}^{-1}$ are observed because of the lack of coincidences in most years. Among the lidars, only Tsukuba lidar exhibits comparatively large drifts below 25 and above 37 km. The behaviour of long-term satellite data are almost similar at different latitudes.

4.5 Combined data: SAGE II, HALOE and Aura MLS

4.5.1 Time series

It is obvious (from Fig. 4.5) that the 8 year data record of Aura MLS yields comparable drifts as of the long-term measurements at all regions. So Aura MLS is a strong candidate for extending terminated observations such as SAGE II and HALOE. Therefore, in this study we assess the possibility of using Aura MLS as a successor of SAGE II and HALOE for ozone trend studies in the low and mid-latitude regions. The combined data sets are computed from the relative differences between the lidar data and SAGE II or HALOE measurements until August 2004, and Aura MLS observations from September 2004 to the end of the respective coincident periods. Before combining data sets of entirely different observational techniques, a correction of bias with respect to lidar measurements needs to be applied. For this, the average biases over the coincident periods of SAGE II, HALOE and Aura MLS, with respect to lidar data, are removed from the corresponding time series of relative differences at each station. Because of the differences in vertical resolutions of SAGE II, HALOE and Aura MLS, the combined data sets are made available at specific reference altitudes (18, 21, 25, 30, 35 and 40 km). The relative differences at these altitudes are calculated by averaging ozone number density within ± 2 km of the altitudes (e.g. 18 ± 2 km). The drifts are also determined from these combined data and are discussed in Sect. 4.5.2.

Figure 4.9 shows the bias corrected combined time series at MOHp (left panel), OHP (middle panel) and Tsukuba (right panel). At MOHp and OHP, small differences (± 5–7%) are observed for SAGE II and HALOE in 19–23, 23–27, 28–32 and 33–37 km. Aura MLS shows very small deviations of less than $\pm 5\%$ in these altitudes at both stations. At 16–20 and 38–42 km, differences are relatively larger ($\pm 10\%$) for SAGE II and HALOE and are less than $\pm 7\%$ for Aura MLS. Even if the Tsukuba time series is characterised by relatively fewer data and large discontinuities, smaller differences are observed. At MOHp, a decreasing tendency is observed in the relative differences of Aura MLS from 28–32 km onwards because of the increase in ozone lidar data after 2007, as discussed in Sect. 4.4.1. In addition, a clear seasonal difference is also seen for the comparison with Aura MLS at 38–42 km showing positive deviation in winter indicating that the Aura MLS ozone is slightly higher than that of MOHp lidar in that season.

Figure 4.10 displays the bias corrected combined time series at TMF (left panel), MLO (middle panel) and Lauder (right panel). At MLO, the relative differences are less than $\pm 5\%$. In the tropics, the ozone variability is very small compared to that of high latitudes, which explains the smaller differences at MLO. At TMF and Lauder, Aura MLS shows differences of $\pm 5\%$ at all altitudes except at 16–20 km, and SAGE II and HALOE exhibit about $\pm 10\%$ deviation except at 16–20 km, where the differences exceed $\pm 20\%$. At TMF, Aura MLS exhibits negative deviations in 2008 and 2009 from 28–32 km onwards, which can

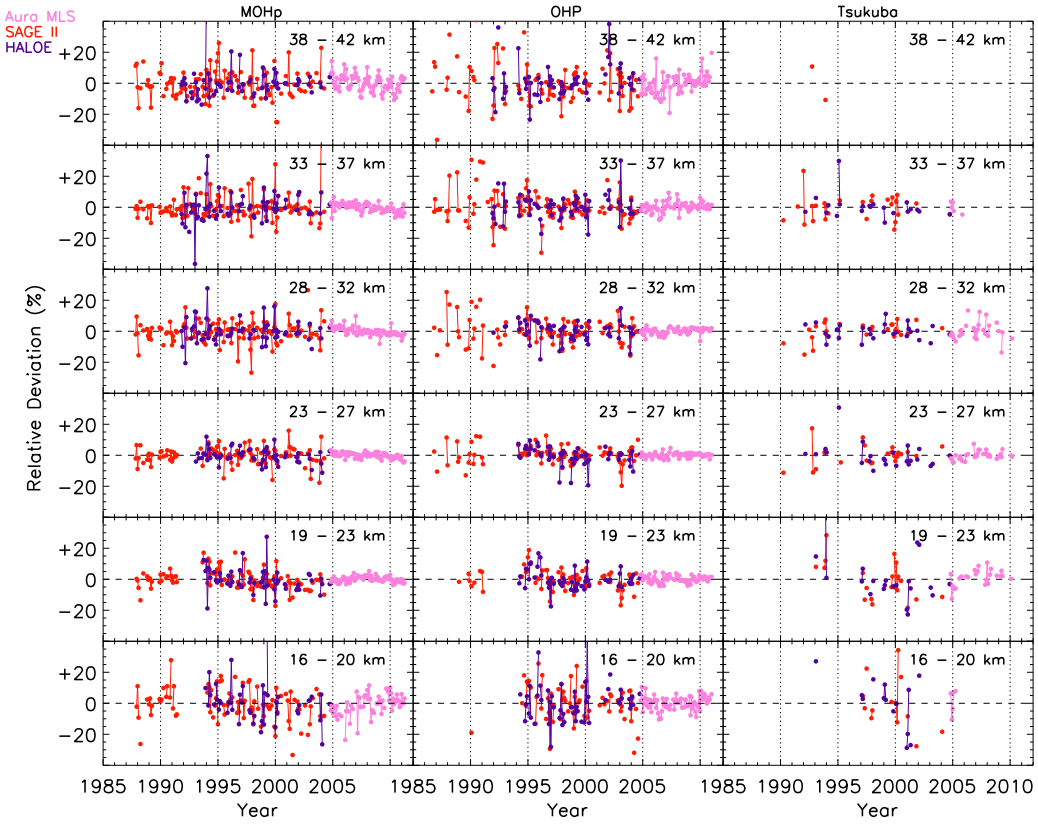

Figure 4.9: Temporal evolution of the bias removed monthly averages of the relative differences of SAGE II, HALOE and Aura MLS with ozone lidar at MOHp (left panel) , OHP (middle panel) and Tsukuba (right panel). The dashed horizontal line represents 0%.

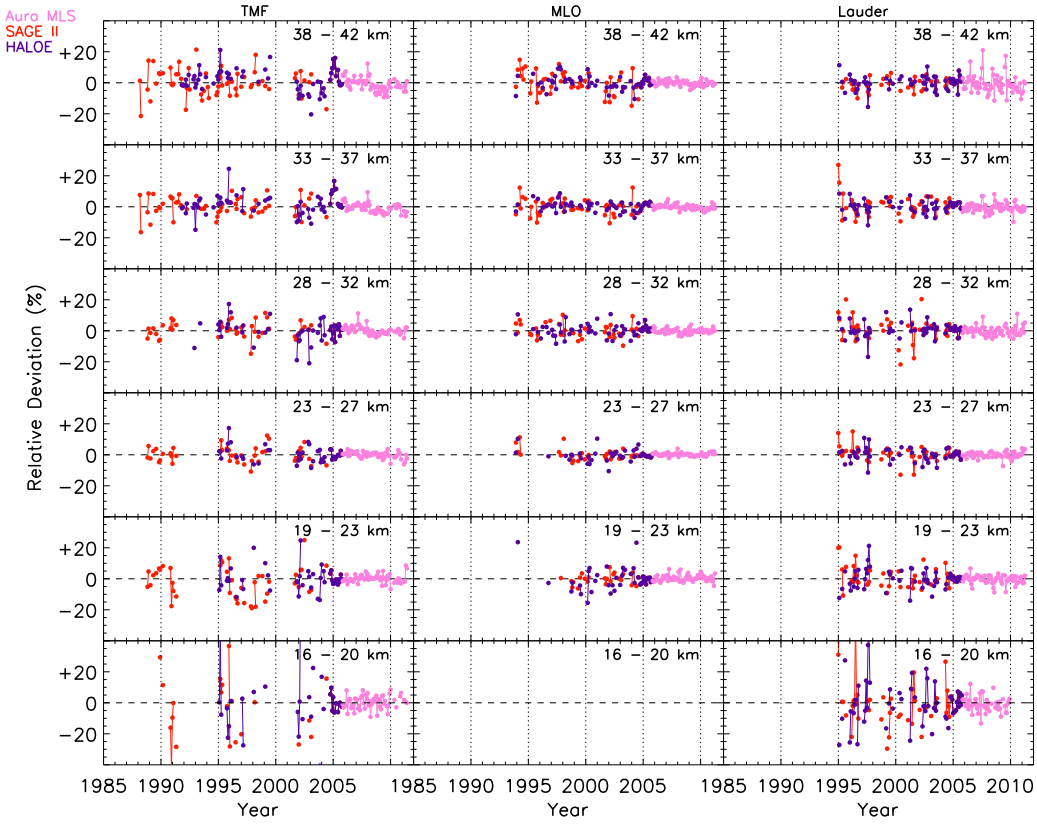

Figure 4.10: Same as Fig. 4.9, but at TMF (left panel), MLO (middle panel) and Lauder (right panel).

be due to higher ozone lidar data during the period as compared to other measurements, as mentioned in Sect. 4.4.1.

4.5.2 Relative drifts of the combined time series

Figure 4.11 presents the relative drifts estimated from the combined time series (as shown in Figures 4.9 and 4.10) of SAGE II and Aura MLS (left panel), and HALOE and Aura MLS (right panel) at various stations. The drifts are generally within $\pm 0.2\%\text{yr}^{-1}$. However, SAGE II/Aura MLS drift at Lauder shows around $\pm 0.2\%\text{yr}^{-1}$ at 21, 25, 30 and 35 km and around ± 0.3 and $\pm 0.48\%\text{yr}^{-1}$ at 18 and 40 km respectively. These large values are due to the fact that the first two measurements in the beginning of the period show slightly larger difference for SAGE II versus lidar as shown in Fig. 4.10. The removal of those two measurements results in a very small drift of less than $\pm 0.2\%\text{yr}^{-1}$ over the whole range (shown as dashed lines with the same color as given for Lauder in the left panel of Fig. 4.11). At Tsukuba, drifts are relatively larger at some altitudes compared to that at other stations. Generally, the combined data show insignificantly small drifts. It indicates that the combination of these satellite observations provides a potential long-term data set for the evaluation of long-term ozone trends in the stratosphere.

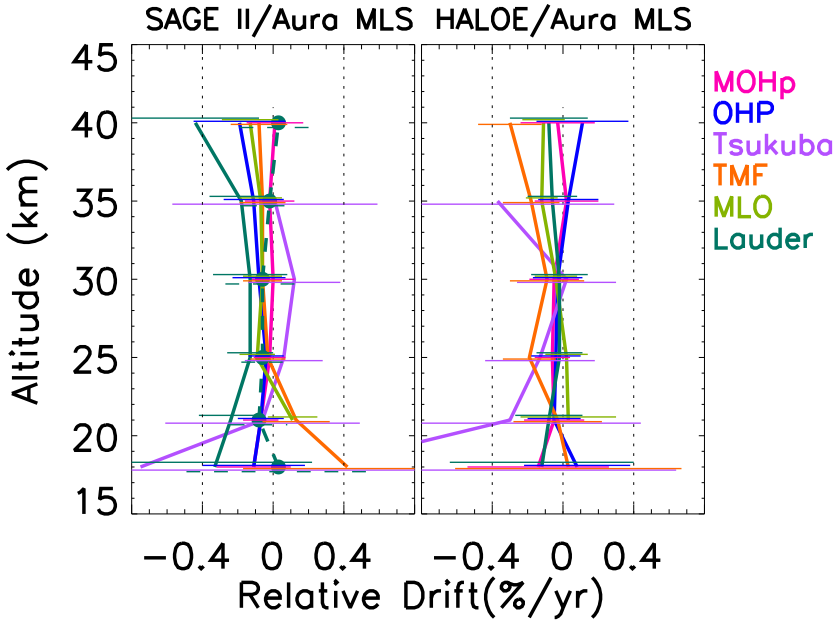

Figure 4.11: The drifts evaluated from the combined time series of SAGE II/Aura MLS (left) and HALOE/Aura MLS (right) at various stations. The dashed line in the left panel represents the drift of SAGE II/Aura MLS at Lauder estimated after removing the first two measurements. The error bars represent twice the standard deviation of the slope. The dotted vertical lines represent 0 and $\pm 0.4\%\,\text{yr}^{-1}$.

4.6 Summary

An extensive analysis of stratospheric ozone measurements at different NDACC lidar stations (MOHp, OHP, Tsukuba, TMF, MLO and Lauder) is performed in this study.

The diagnosis is done by comparing various long and short-term satellite observations of SBUV(/2), SAGE II, HALOE, UARS MLS and Aura MLS as well as ozonesonde measurements at the respective stations.

The relative difference (or bias) of all measurement techniques is found by comparing them with respect to lidar measurements in their respective coincident periods. All measurement techniques (satellites and sondes) agree well with all lidars, with average biases of less than ±3%, in the 20–40 km range. In order to detect ozone trends on the order of a few %/decade, stability of long-term measurements is essential. This is particularly important for long-term ground-based and satellite sensors, which may be subject to some degradation during their life time. Therefore, in this study we examine the stability of each measuring system by investigating the magnitude of the drifts. This is attained first by comparing all measurements with respect to lidars, which yields drifts of less than $\pm 0.3\%\mathrm{yr}^{-1}$ at 20–40 km for all observations. Aura MLS with 8 years of observation also shows drifts that are comparable to those from the long-term data sets at all stations. Below 20 and above 40 km relative differences and drifts are larger, mostly due to discontinuity in the time series, smaller ozone values and lower uncertainty of ozone observations in these altitude regions. In addition, in the lower stratosphere larger atmospheric variability at the mid-latitude stations and a higher tropopause at the tropical station also contribute to the observed large biases and drifts.

A successful evaluation of biases and drifts depends on the stability of the reference data and hence the drifts of ozone lidar measurements with respect to the longer data sets SBUV(/2), SAGE II and HALOE are estimated. The relative drifts of lidar are nearly zero at most altitudes. Similarly, the drifts of SBUV(/2), SAGE II and HALOE are estimated by comparing them with each other. Comparison between SAGE II and HALOE shows drifts with maximum of ± 0.2–$0.4\%\mathrm{yr}^{-1}$ in 20–45 km whereas the comparison of SBUV(/2) with lidar, SAGE II and HALOE produces near zero drifts. Because of successive instruments, SBUV(/2) provides daily global measurements over the whole period with a large number of collocated profiles, and thus a very accurate evaluation of drift of the data is performed. So a sufficient number of continuous profiles is an important factor for deducing accurate drifts with meaningful statistics. The averages of the drifts of long-term measurements obtained from various comparisons are within $\pm 0.2\%\mathrm{yr}^{-1}$ in 20–45 km. Therefore, the long-term measurements considered here are stable at the respective latitude bands.

As the various ozone measurement techniques yield consistent results, it is useful to combine different ozone measurements to establish a long-term data set for further analyses and trend studies. Hence, a bias-corrected combined time series is constructed using the relative differences of SAGE II and HALOE, with respect to lidar data, with that of Aura MLS and the relative drifts are estimated. It shows drifts of $\pm 0.1\%\mathrm{yr}^{-1}$ at most altitudes for all the considered latitude bands. So the combination of the older data sets, SAGE II and HALOE, with Aura MLS is shown to be very suitable for the estimation of long-term ozone trends.

Chapter 5

Stratospheric ozone evolution in the northern mid-latitudes

Contents

The role of ozone depleting substances in global ozone negative trends called for a tight check on the vast uncontrolled emissions of related trace gases into the atmosphere, which led to the constitution of the Montreal Protocol. About two decades of the emission controlled scenario did help to reduce the level of stratospheric ODSs such as CFCs and halons. The ODS emission has stopped from 1996 onwards in the developed countries and from 2010 onwards in other countries. Stratospheric ozone abundances change in response to decrease of ODSs (WMO, 2007), i.e., stratospheric ozone showed a slowing of ozone decline attributable to ODS changes. Several studies (Newchurch et al., 2003;

Reinsel et al., 2002) also showed that stratospheric ozone has stopped to decline and the ozone levels are stabilised since 1995, indicating signs of the first stage of stratospheric ozone recovery in the upper stratosphere. Some other studies (Steinbrecht et al., 2006; Zanis et al., 2006; Jones et al., 2009; Tatarov et al., 2009) showed significant negative ozone trend before the mid-1990s and insignificant positive trend afterwards, in the upper stratosphere. As a result of continued decrease in ODSs, ozone is expected to increase as time progresses. The analysis using zonal average data shows that the ozone total column measurements in the northern mid-latitudes are stabilised from the mid-1990s onwards (Reinsel et al., 2005; Dhomse et al., 2006; Harris et al., 2008; Vyushin et al., 2007). A major part of the stratospheric ozone resides in the lower and middle stratosphere, where a significant decline of about -10%/decade has been observed (Logan et al., 1999) by analysing sonde measurements in 1970–1996 and a stabilisation afterwards (WMO, 2011). Therefore, the goal of this study is to investigate ozone trends in the mid-latitudes in an ozone recovery perspective and thus to assess the effectiveness of the Montreal Protocol and its amendments.

The drift in the ozone profile measurements at different NDACC lidar stations is analysed in Chapters 3 and 4. Thus, we have a well validated ozone data sets from the ground-based and satellite instruments for a better evaluation of stratospheric ozone trend. This chapter uses those data sets for estimating stratospheric ozone trends at two northern mid-latitude stations, OHP and MOHp, using multiple regression analysis. Ozone total column measurements and ozone vertical profiles are used to estimate ozone trends and to study the interannual variations of ozone with respect to different explanatory variables.

This chapter is organised in the following way: Section 5.1 presents various explanatory parameters and their importance in the study. The multiple regression model and method of regressing data are detailed in Sect. 5.2. The description of ozone total column measurements: evolution, anomaly and the estimation of drifts in Sect. 5.3 is followed by the application of multiple regression to the Dobson and SAOZ column data at OHP and MOHp in Sects. 5.4 and 5.5 respectively. Section 5.6 discusses the evolution, anomaly and the multiple regression analysis of vertically resolved ozone profiles at OHP. Then, a link between the contribution of proxies on ozone vertical distribution and that to the ozone total column measurements is briefly described in Sect. 5.7. A summary of the important results is presented in Sect. 5.8.

5.1 Explanatory variables

Generally, ozone changes are influenced by the natural and anthropogenic variations. This can be explained statistically by using different explanatory variables (proxies) or predictors associated with those natural and anthropogenic changes. A number of possible proxies are made available to diagnose the variations in ozone connected to the day-to-day, seasonal and periodical changes. Quasi Biennial Oscillation (QBO), solar flux and seasonal cycle are the widely used ones for studying ozone changes (Reinsel et al., 1994; Bojkov et al., 1990; Staehelin et al., 1998) as these proxies have a great influence on the interannual variability of ozone. Additionally, aerosol optical depth is used to describe the effect of volcanic aerosols on ozone. In the recent decade, several studies focused on dynamical and meteorological proxies to analyse ozone changes related to the residual circulation and climate change. For instance, statistical analysis by Reinsel et al. (2005) showed a substantial influence of dynamical proxies such as Arctic Oscillation (AO) and Eliassen-Palm flux (EP flux) on the total ozone increase in the latitude bands above 40°. The increase in the northern hemispheric total ozone is partly explained by eddy heat flux, another proxy describing the

planetary wave drive (Dhomse et al., 2006; Harris et al., 2008) and thus the BD circulation, as mentioned in Chapter 1. Also, Weber et al. (2011) showed the effect of BD circulation on the seasonal evolution of total ozone, using eddy heat flux. Similar to the dynamical proxies, teleconnection patterns such as North Atlantic Oscillation (NAO) and AO also have significant influence on ozone, particularly in the middle stratosphere (Weiss et al., 2001). Moreover, Steinbrecht et al. (2011) explained that the reason for the very high total ozone observed in the NH mid-latitude in 2010 was the occurrence of negative AO index and the easterly phase of QBO during the term. Recently, EESC has been used as a proxy to identify ozone trends associated with the changes in stratospheric halogen loading (Yang et al., 2006; Vyushin et al., 2007; Wohltmann et al., 2007; Kiesewetter et al., 2010). It is hard to select proxies that have more influence on ozone. In this aspect, Mäder et al. (2007) applied a stepwise backward elimination procedure to find the contribution of explanatory variables to the ozone variability. Their findings showed that QBO, EP-flux, aerosols and EESC have a noteworthy influence on the NH mid-latitude ozone. Hence, in this study, we use proxies, those have a significant effect on the measured ozone in the northern mid-latitudes as shown by other studies and are EESC, QBO, solar flux (SFX), aerosols (AER), eddy heat flux (HFX) and NAO. Figure 5.1 displays the evolution of these proxies (except EESC, which is shown in Chapter 1, Fig. 1.10) during the study period.

5.1.1 Quasi Biennial Oscillation

QBO is a quasi-periodic oscillation of the equatorial zonal wind, expressed in m/s. It is characterised by alternating easterlies and westerlies those repeat at intervals varying from about 22 to 34 months, with an average period of about 28 months. These wind regimes originate at the top of the lower stratosphere and descend at a speed of about 1 km/month from 10 to 100 hPa until they dissipate at the tropical tropopause. The easterlies are specified with continuous downward motion and have amplitude, twice as strong as of the westerlies. The easterlies dominate at the top of the vertical domain while westerlies appear generally at the bottom layers. A general theory about the QBO is that Kelvin and Rossby-gravity waves produce westerly and easterly momentum for the oscillatuion, respectively (Baldwin et al., 2001; Lott et al., 2009).

To analyse the effect of QBO on ozone, monthly mean zonal wind components are calculated for the levels 70, 50, 40, 30, 20, 15 and 10 hPa from the radiosonde observations at equatorial stations Canton Island (3°S, 172°W) in January 1953–August 1967, Gan/Maldive Islands (1°S, 73°E) in September 1967–December 1975 and Singapore (1°N, 104°E) from January 1976 onwards (Andrews et al., 1987) in which Singapore zonal winds are used for this study. QBO has a great influence on the inter-annual variability of the tropical region and is also connected to ozone changes in the middle and polar latitudes (Baldwin et al., 2001). Since QBO is of equatorial origin, its effect on ozone in the extratropics is represented by an optimal lag relation (Bojkov et al., 1990), i.e., effect of QBO on ozone variations is in different phases at different latitudes. In our study, this phase shift with respect to latitude is accounted for by considering QBO indices at 10 and 30 hPa (hereafter QBO 10 and QBO 30, respectively), which are out of phase by $\sim \frac{\pi}{2}$ (Steinbrecht et al., 2003).

5.1.2 Solar flux

Solar variation originates from the change in the amount of radiation emitted by the sun and in its spectral distribution. The periodic component of these variations is termed as solar cycle. The formation of stratospheric ozone is initiated by UV radiation coming from

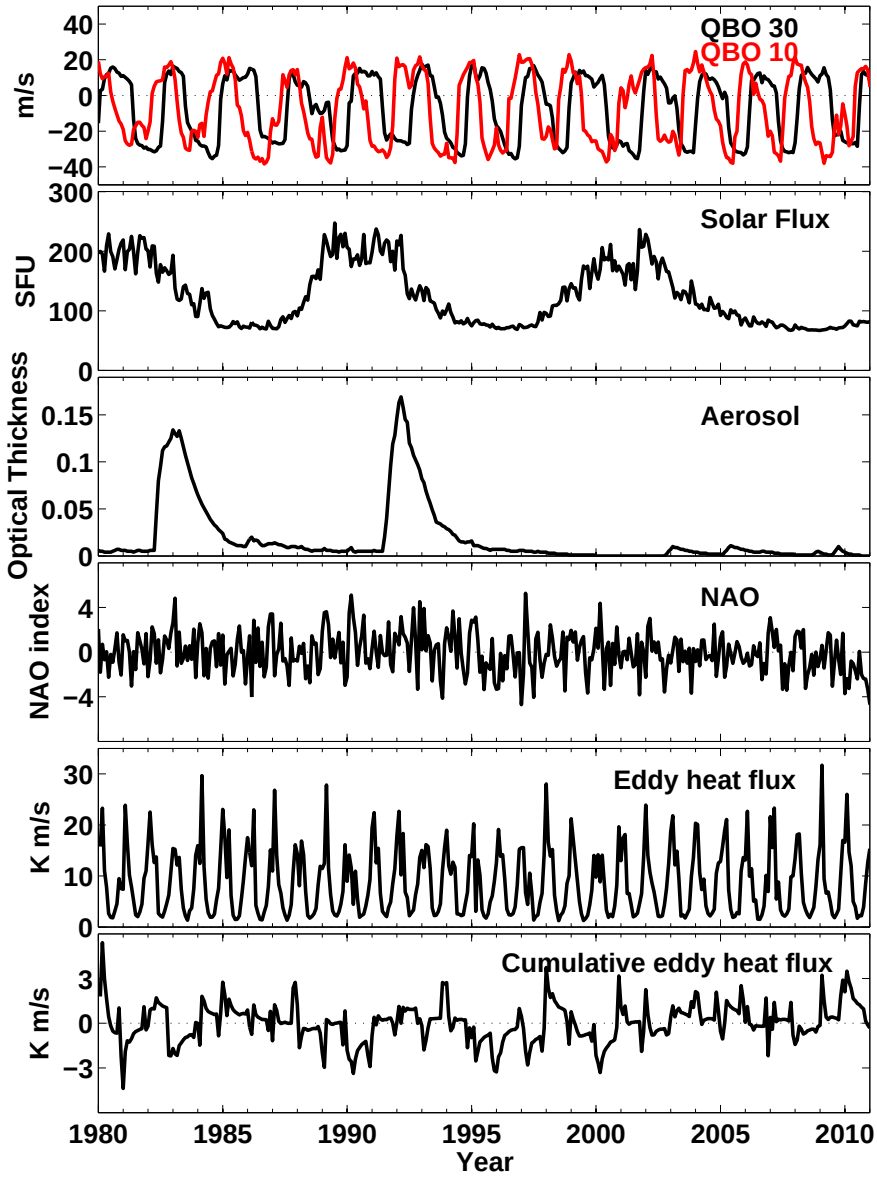

Figure 5.1: Time series of the monthly mean QBO at 10 and 30 hPa, solar flux, aerosol, NAO, eddy heat flux and the deseasonalised (monthly mean - mean over the period) cumulative eddy heat flux in 1980–2010.

the Sun. Therefore, an increase in the Sun's radiation output increases the amount of ozone. Different kinds of solar UV flux data are available to recognise the decadal variability of stratospheric ozone (Chandra et al., 1994). They include 27-day and 11-year solar cycles, solar UV variations at 205 nm and Mg II index. Generally, solar radiation changes at a wavelength 10.7 cm is used as a proxy to investigate the impact of 11-year solar cycle related variations of UV irradiance on ozone. It is a measure of the solar radio diffuse, non-radiative heating of the coronal plasma trapped by magnetic fields over active regions, and is an excellent indicator of overall solar activity levels (Tapping, 1987). It is expressed in solar flux unit ($1\,\mathrm{SFU} = 10^{-22} W m^{-2} H z^{-1}$). Statistical studies (McCormack and Hood, 1996; Hood, 1997) revealed that the upper stratospheric ozone in the mid-latitudes showed a significant response on the solar variations, with an increase of 4–6 % from the solar minimum to maximum. Similarly, Soukharev and Hood (2006) reported that the influence of solar flux variations on the lower stratospheric ozone is the main cause for the observed solar cycle variation in ozone total column at tropical latitudes. Monthly mean 10.7 cm solar flux observations made at Ottawa and Pentiction are used in the study (for e.g., Steinbrecht et al., 2011).

5.1.3 Aerosols

The volcanic eruptions can eject huge amounts of sulfur dioxide (SO_2) into the stratosphere, which are oxidised to form sulfuric acid (H_2SO_4) and condensed to form aerosols. These sulfate aerosols provide surfaces for heterogeneous reactions to occur, thus enhance ozone depletion when sufficient amount of chlorine is available. The El Chichón (1982) and Mount Pinatubo (1991) are the largest volcanic eruptions those have occurred in the recent decades. Following these volcanic eruptions, ozone has reduced significantly (SPARC, 1998). The volcanic aerosols also affect tropospheric and stratospheric temperatures and atmospheric circulation. They absorb IR radiations and warm the stratosphere (WMO, 2007). Also, they scatter the incoming solar radiations and thus decrease the surface temperature and cools the troposphere. The tropospheric cooling changes the atmospheric circulation as well as the interaction between troposphere and stratosphere. Volcanic aerosols, thus, can cause both chemical (as noted in Chapter 1) and dynamical effects responsible for the ozone changes. The monthly mean aerosol optical depth, a dimensionless quantity, at 550 nm (Sato et al., 1993) is used as a proxy in our model to account for the effect of aerosols emanated from the volcanic eruptions. Aerosol optical thickness (τ) is the degree to which aerosols affect the transmission of light by absorption or scattering at the specified wavelengths.

5.1.4 Eddy heat flux

Variations in planetary wave activity from the troposphere to stratosphere affect BD circulation, as discussed in Chapter 1, and eddy mixing that influences ozone transport (Randel et al., 2002). This planetary wave forcing is represented by the divergence of the Eliassen-Palm (EP) flux (Andrews et al., 1987). The vertical component of EP flux, termed as the eddy heat flux ($\overline{\nu' T'}$), is a good proxy for explaining ozone transport. It is the zonal average of the product of meridional wind and temperature departures (ν', T') from their respective zonal averages ($\overline{\nu}$, $\overline{T}$). It is expressed in K m/s. In our regression model, we use 100 hPa eddy heat flux, a measure of planetary wave drive into the stratosphere, calculated using ECMWF reanalyses, averaged over 45–75°N (Kuttippurath and Nikulin, 2012).

The transport and photochemical decay generally determine the fate of stratospheric ozone in the mid-latitudes. Since stratospheric ozone transport is higher in winter, more ozone is transported in the winter/spring season and this wintertime ozone anomaly per-

sists until the late autumn reflecting the absence of dynamical variability and presence of photochemical decay in the summer stratosphere (Fioletov and Shepherd, 2003). In late spring and summer, the total ozone change is controlled by the NO_X chemistry (for e.g., Kuttippurath et al., 2010). To account for the wintertime build up of ozone and its persistence in spring and summer, cumulative eddy heat flux (see the bottom panel in Fig. 5.1) is calculated for a given month by integrating the eddy heat flux from the preceding fall (October for the NH) to the month concerned. The cumulative eddy heat flux for October is considered as the monthly mean eddy heat flux in October itself.

5.1.5 North Atlantic Oscillation

The NAO is a large scale mode of natural climate variability affecting the NH atmosphere (Hurrell et al., 2003). This variability is expressed in the NAO index, a dimensionless quantity, measured as the difference between the normalised sea level pressure over Gibraltar (36°N) and Southwest Iceland (60°N). Its effect is strongest in winter and has two phases. Figure 5.2 shows the NAO index averaged for the winter season (DJFM). The NAO index is positive when there is a large pressure difference between the Gibraltar and Iceland (low pressure at Iceland and high pressure at Gibraltar). This results in increased westerlies and wet winters over Central Europe. In other words, during positive NAO phase, total ozone is reduced over Europe and increased over the North Atlantic region (Appenzeller et al., 2000). While negative NAO index indicates that there is only a small pressure difference between the Gibraltar and Iceland (weak Icelandic low and weak Gibraltar high pressure system) resulting in cold winters over Europe. This change in pressure gradient from one phase to another produces large-scale modulations of zonal and meridional heat and moisture transport, which results in change in surface temperature. Hurrell (1996) pointed out that the increased rate of surface warming of the NH and the cooling over the northwest Atlantic from the 1970s to the 1990s is linked with the more positive phase in NAO during the period. From the beginning of 2000s, it decreases and a more negative index is found in 2010 during the 190 year data record.

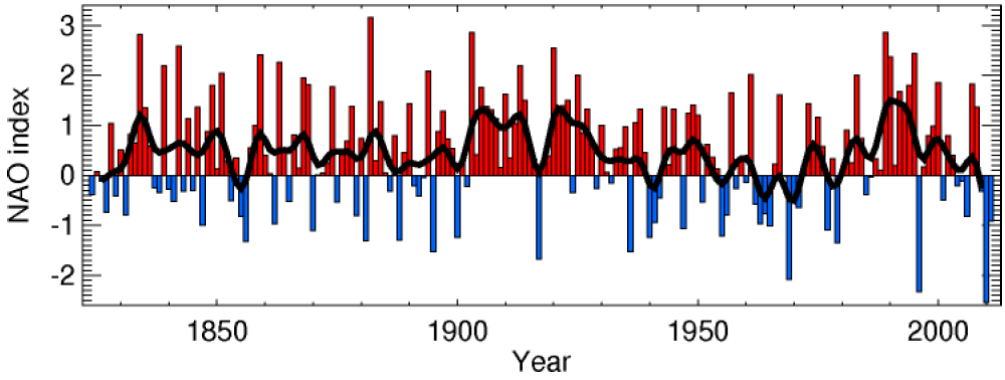

Figure 5.2: Time series of the NAO index averaged for the winter months from December to March with a 5 year moving average in black (taken from http://www.cru.uea.ac.uk/ timo/datapages/naoi.htm).

5.1.6 PWLT and EESC : Ozone trend estimation methods

Before EESC comes into picture, a linear function was used for determining the long-term trend of ozone due to ODSs. However, because of the successful implementation of the

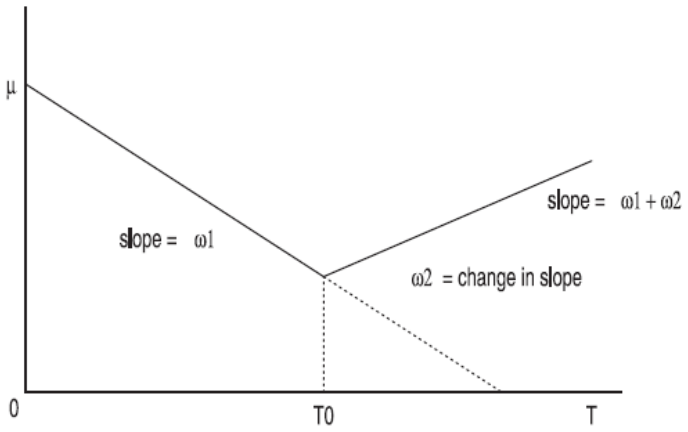

Figure 5.3: Demonstration of the PWLTs before the turnaround year (T0) and afterwards (Adapted from Reinsel et al., 2002).

Montreal Protocol, the amount of chlorine and bromine loading has stabilised and was reduced, as seen in Chapter 1. As a result, the anthropogenic destruction of ozone was decreased and ozone level was stabilised from the mid-1990s onwards. This change in the evolution of ozone has to be accounted for in the statistical models for the accurate estimation of ozone trends. Hence, a concept of evaluating piecewise linear trends (PWLTs) before and after a turnaround year considering time as a proxy has been incorporated in different trend analyses (Reinsel et al., 2002; Newchurch et al., 2003; Reinsel et al., 2005; Zanis et al., 2006). Such a statistical model assumes two different linear trend terms, from the beginning of the data record ($\omega 1$) and the change in trend at the turning point ($\omega 2$). Then, the overall trend estimate after the turnaround year is calculated as $\omega = \omega 1 + \omega 2$. Figure 5.3 illustrates the two linear trends as given in Reinsel et al. (2002).

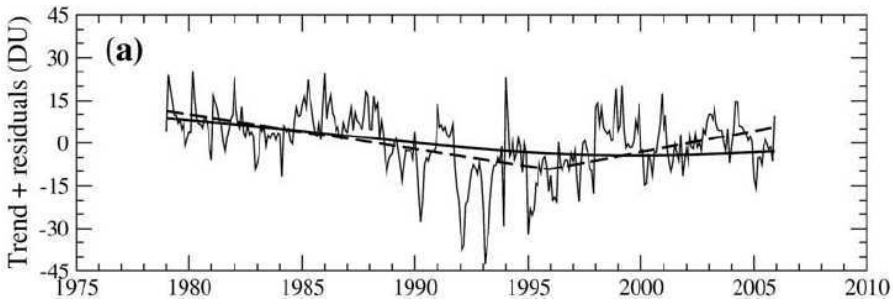

Figure 5.4: The residuals obtained by filtering out the seasonal cycle, QBO, solar flux along with the PWLT (dashed line) and EESC (solid line) fits using multiple regression analysis (Reproduced from Vyushin et al., 2007).

EESC is an important parameter that accounts for ODS abundances and their effectiveness in reducing ozone amount, as described in Chapter 1. Because of the change in temporal evolution of ODSs, EESC reached its peak value in the mid-1990s (around 1996) in the mid-latitudes and started to decrease slowly, afterwards (WMO, 2007). Therefore, EESC has two different linear trends depending on its peak year. The estimated trends in EESC are 0.86 ± 0.02 and -0.26 ± 0.01 ppb/decade for 1970–1996 and 1997–2010, respectively. It should be noted that the trend in the latter period is less than the trend

in the former period. Hence, EESC function is used to analyse ozone time series instead of linear or piecewise linear terms in several studies (Dhomse et al., 2006; Brunner et al., 2006; Stolarski et al., 2006; Wohltmann et al., 2007). The difference in the long-term ozone trends estimated using piecewise linear functions and EESC time series has been reported in Vyushin et al. (2007), and these two fits are displayed in Fig. 5.4. Therefore, EESC is also used as a proxy in our regression model to describe long-term trend in ozone, related to ODSs.

5.2 Multiple regression model and method

The evolution of monthly mean ozone in the northern mid-latitudes is analysed using a multiple regression model, similar to the models that have been widely used for several decades (Reinsel et al., 1994; Staehelin et al., 1998; Brunner et al., 2006). The model uses various explanatory parameters as discussed above. As stated before, we have adopted two different methodologies to assess the long-term variability of ozone in relation to the halogen loading for which, year 1997 is considered as the turnaround year as EESC decreases from July 1996 onwards. Hence, PWLTs are estimated before 1997 (hereafter pre-turnaround trend) and from 1997 to the end of the data record (hereafter post-turnaround trend). Secondly, the long-term stratospheric ozone trends are estimated using EESC function (WMO, 2011) instead of PWLT terms. The multiple regression model used for the estimation of trends in our study is expressed as follows, in the case of PWLT (this model is hereafter termed as the PW regression model).

$$Y(t) = M(t) + N(t) \tag{5.1}$$

where Y is the input data (deseasonalised ozone or ozone anomaly in our case), t corresponds to the month in the ozone time series over the period, M is the regression model and N is the residual.

$$\begin{aligned} M(t) = &\sum_{m=1}^{12} C_m^A \delta_{mt} A + \sum_{m=1}^{12} C_m^{LIN} \delta_{mt} T1(t) + \sum_{m=1}^{12} C_m^{CHG} \delta_{mt} T2(t) + \\ &\sum_{m=1}^{12} C_m^{Q30} \delta_{mt} Q30(t) + \sum_{m=1}^{12} C_m^{Q10} \delta_{mt} Q10(t) + \sum_{m=1}^{12} C_m^{SFX} \delta_{mt} SFX(t) + \\ &\sum_{m=1}^{12} C_m^{AER} \delta_{mt} AER(t) + \sum_{m=1}^{12} C_m^{HFX} \delta_{mt} HFX(t) + \sum_{m=1}^{12} C_m^{NAO} \delta_{mt} NAO(t) \end{aligned} \tag{5.2}$$

where m represents month (January, February,...., December), A is a constant, T1 is the time period considered for the analysis, T2 is the time period after 1996 (i.e., starting from January 1997 to the end of the data period), C_m^X represent monthly regression coefficients of each proxy (X), i.e., C_m^A are the monthly coefficients of the constant term, C_m^{LIN} are the monthly pre-turnaround trends, C_m^{CHG} are the change in linear trend, C_m^{Q30} and C_m^{Q10} are the QBO coefficients at 30 and 10 hPa respectively, C_m^{SFX} are the solar flux coefficients, C_m^{AER} are the aerosol coefficients, C_m^{HFX} are the cumulative eddy heat flux coefficients, and C_m^{NAO} are the NAO coefficients.

For the EESC regression model, PWLT terms $\left(\sum_{m=1}^{12} C_m^{LIN} \delta_{mt} T1(t) + \sum_{m=1}^{12} C_m^{CHG} \delta_{mt} T2(t) \right)$ are replaced by EESC as

$$\sum_{m=1}^{12} C_m^{EESC} \delta_{mt} EESC(t) \tag{5.3}$$

where C_m^{EESC} are the coefficients of EESC values.

The deseasonalised ozone is calculated by subtracting the monthly climatology (the long-term average of ozone for each month) from the monthly mean ozone values. The ozone anomaly in relative units is computed by dividing the deseasonalised ozone with the monthly climatology. In the regression model, monthly mean QBO, solar flux, aerosols, NAO, EESC and the deseasonalised (monthly mean - mean over the period) cumulative eddy heat flux (e.g., Brunner et al., 2006) are applied. For solar flux, average solar flux over the analysis period is subtracted from the corresponding monthly averages. All proxies are divided by the corresponding amplitude over the data period (difference between the maximum and minimum values) so that the regression coefficients have the same unit as that of Y. However, the time period for the PW regression model is retained as such so that the pre-turnaround and changes in linear trends are obtained in the unit of Y/year. The regression coefficients are determined using the linear least square method. The standard deviation of the regression coefficients is calculated using the equation provided in Press et al. (1989) as given below.
The matrix-vector representation of Eq. 5.1 can be written as

$$\overrightarrow{\mathbf{Y}} = \overrightarrow{\mathbf{a}}.\mathbf{A} + \overrightarrow{\mathbf{N}} \tag{5.4}$$

where $\overrightarrow{\mathbf{Y}}$ is the vector of ozone time series, $\overrightarrow{\mathbf{a}}$ is the vector of regression coefficients, $\mathbf{A}$ is the matrix of the proxies and $\overrightarrow{\mathbf{N}}$ is the vector of residuals.
The covariance matrix of regression coefficients ($\sigma^2_{\hat{a}}$) can be calculated using the generalised least square estimator as

$$\sigma^2_{\hat{a}} = (A^T A)^{-1} \times \frac{\chi^2}{Z - P} \tag{5.5}$$

where $\chi^2 = \sum_t \left(Y(t) - \sum_{k=1}^{P} C_k X_k(t) \right)^2$, Z is the number of data points and P is the number of fitted parameters.

Commonly, autocorrelation (ϕ) is made available to determine the error values of the regression coefficients (Weatherhead et al., 1998). Autocorrelation is defined as the correlation of a time series with its own past values. Here, ϕ is the cross-correlation of the residuals with a time lag of one instant. Since, we have applied multiple regression for each month, a time lag of one instant means a time lag of one year.

$$\phi = corr[N(t), N(t-1)] \tag{5.6}$$

It can also be calculated as in Eq. 3.9. Considering that the residuals are of first order autoregressive (AR(1)), i.e., $N(t) - \phi N(t-1) = \varepsilon$, the standard deviation of the regression coefficients can be redefined as

$$\sigma_{\hat{a}} = \sigma_{\hat{a}} \times \sqrt{\frac{1+\phi}{1-\phi}} \tag{5.7}$$

The goodness of the multiple regression model is generally evaluated using the coefficient of multiple determination, denoted as R^2, which is the ratio of sum of squares of the regression to the total sum of squares around the mean (Storch and Zwiers, 1999). It can have values between 0 and 1. If R^2 is 1, it means that the regression model could explain the observed variance completely. So for a model to be good, or to describe most of the

observed variations in ozone using the model, R^2 should be large.

$$R^2 = \frac{\sum_t \left[M(t) - \overline{Y}\right]^2}{\sum_t \left[Y(t) - \overline{Y}\right]^2} \tag{5.8}$$

where $\overline{Y}$ is the mean of the input data over the period.

Because of the use of monthly regression model, the model provides 12 regression coefficients corresponding to each month, for each proxy. Therefore, year-round pre-turnaround trend (C_{T1}) is estimated by averaging the monthly pre-turnaround trend coefficients (Reinsel et al., 1994). Similarly, change in annual trend (C_{T2}) is calculated from the corresponding monthly changes in trends. Then, the overall trend estimate or the post-turnaround trend (C_T) is computed as (Reinsel et al., 2002),

$$C_T = C_{T1} + C_{T2} \tag{5.9}$$

Corresponding standard deviations are calculated as

$$\sigma_T = \frac{\sqrt{\sum_{m=1}^{12} \left[\sigma_{T1_m}^2 + \sigma_{T2_m}^2 + 2 \times (\sigma_{T1T2_m})^2\right]^2}}{12} \tag{5.10}$$

$$\sigma_{T1} = \frac{\sqrt{\sum_{m=1}^{12} (\sigma_{T1_m})^2}}{12} \tag{5.11}$$

where σ_{T1_m} and σ_{T2_m} are the standard deviations of pre-turnaround and changes in monthly trends respectively, $(\sigma_{T1T2_m})^2$ is the covariance of C_m^{LIN} and C_m^{CHG}, σ_{T1} is the standard deviation of the year-round pre-turnaround trend and σ_T is the standard deviation of the year-round post-turnaround trend.

When EESC is used instead of PWLTs, the regression coefficient of EESC can be converted to pre-turnaround and post-turnaround trends by multiplying the average of the monthly regression coefficients of EESC with the trend in EESC for the two periods (Stolarski et al., 2006). In addition to the stratospheric ozone trends, the influence of each explanatory variable to the ozone variability is analysed in detail.

5.3 Ozone total column measurements

A number of ozone total column measuring instruments are available worldwide for the continuous monitoring of ozone from the ground and space. Most of the ground-based column measurements have a long life span. Among those, Dobson spectrometer is the first instrument used to measure ozone total column in DU and is named after its inventor G. M. B. Dobson, in 1924. The measurement principle is based on the differential absorption of solar light by ozone. It performs ozone observations by measuring the relative intensities of UV wavelengths emanating from the Sun, Moon or zenith sky (Dobson, 1980). These measurements are commonly used to validate data from other instruments and its measurement uncertainty is about 1–2%.

SAOZ is an ozone total column measuring instrument in the UV-Visible region. It observes sunlight scattered from the zenith sky in the 290–590 nm spectral range during

sunrise and sunset (Pommereau and Goutail, 1988). Ozone measurements are carried out in the Chappuis band (450–560 nm) and are retrieved using Differential Optical Absorption Spectroscopy (DOAS) method (for e.g. Hendrick et al., 2011). The advantage of SAOZ data is that it measures during twilight and in the visible range. Therefore, it can measure continuously up to 91° solar zenith angle throughout the polar circle in all weather conditions. Also, the ozone absorption cross-section correction due to the change in temperature is not required. The measurement uncertainty is of the order of 3%.

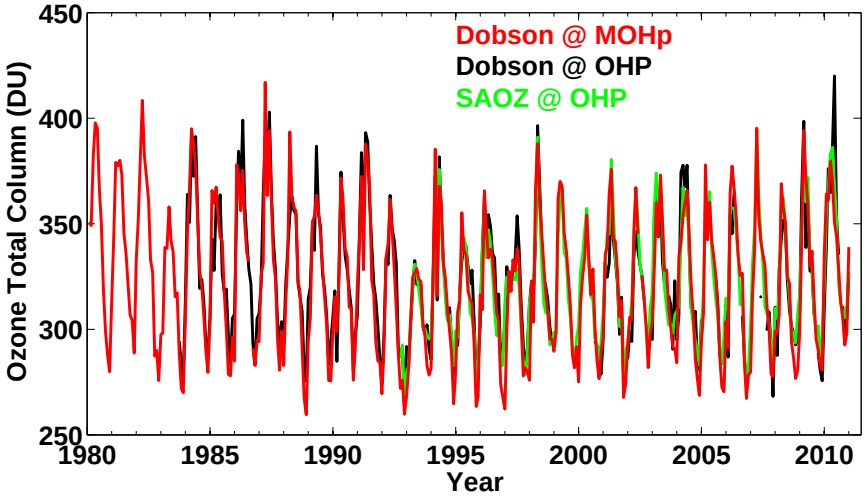

Figure 5.5: Temporal evolution of monthly mean ozone total column measurements from the Dobson spectrometer at MOHp in 1980–2010, Dobson and SAOZ spectrometers at OHP in 1983–2010 and 1992–2010 respectively.

5.3.1 Evolution of ozone total column

This study uses ozone total column measurements from the Dobson spectrometer at the northern mid-latitude stations MOHp and OHP and the SAOZ spectrometer at OHP. The temporal evolution of these ozone measurements are displayed in Fig. 5.5. The Dobson spectrometer at MOHp is in operation from 1968 onwards while that at OHP started measurements in 1983. The SAOZ spectrometer at OHP observes ozone from 1992 to the present. Therefore, we use Dobson ozone column data at MOHp in 1980–2010, Dobson measurements at OHP in 1983–2010 and SAOZ V2 data at OHP in 1992–2010. The evolution of ozone is similar in all three data sets showing similar seasonal variations. Maximum ozone value of about 420 DU for the whole period is found for OHP Dobson spectrometer in 2010.

5.3.2 Ozone anomaly

Figure 5.6 presents the monthly ozone anomaly of the ozone total column measurements from the Dobson spectrometers at MOHp and OHP and the SAOZ spectrometer at OHP. All data sets follow a similar pattern of ozone anomaly. The ozone anomaly decreases from the start of the data record to around 1995–1997 and shows a stabilisation afterwards followed by an increase in 2010. The largest positive ozone anomaly is found in 2010 as noted in Steinbrecht et al. (2011) and the largest negative ozone anomaly is found in

1990. From the Dobson ozone anomaly at MOHp, it is clear that aerosols from the Mount Pinatubo volcanic eruption were more effective in reducing ozone level than that from the El Chichón.

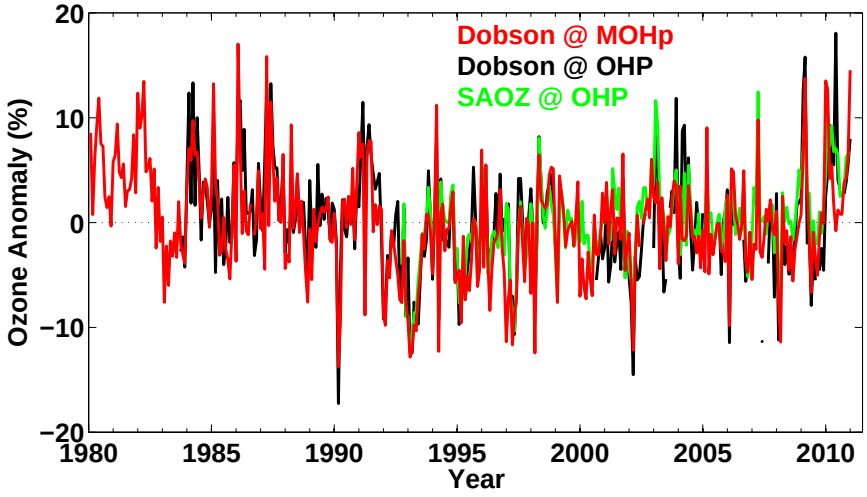

Figure 5.6: Temporal evolution of monthly mean ozone anomaly from the Dobson spectrometer at MOHp in 1980–2010, Dobson and SAOZ spectrometers at OHP in 1983–2010 and 1992–2010 respectively.

5.3.3 Comparison between Dobson and SAOZ at OHP: bias and drift

The Dobson and SAOZ ozone measurements at OHP are analysed to find out drift in the ozone time series. The relative difference of Dobson with respect to SAOZ is calculated for coincident days and the drift is estimated from the monthly mean of these relative differences. The computed differences are shown in Fig. 5.7. The deviations are very small, within $\pm 2\,\%$ in 1992–1999 and around $\pm 5\,\%$ in 2000–2010. The average bias over the period with twice the standard error is found to be $0.33 \pm 0.17\,\%$ and the estimated drift with 2σ uncertainty is $-0.12 \pm 0.12\,\%\mathrm{yr}^{-1}$.

5.4 Multiple regression analysis of ozone total column at OHP

The multiple regression method is applied to the 5 month running mean of the deseasonalised ozone total column measurements in DU. At OHP, the Dobson and SAOZ measurements are averaged to obtain a combined data set from 1983 to 2010. Figure 5.8 presents the regression of monthly mean deseasonalised ozone from the combined Dobson and SAOZ data for OHP. The deseasonalised ozone, the fitted PW regression model and residuals (Input data - Regressed data) are shown in the top panel of the Figure. It is noted that the regression model fits well with the deseasonalised ozone, showing a correlation of 0.82. Also, the model is good in the sense that the estimated R^2 is about 0.67, which implies that about 67% of the variance of total ozone column can be explained using the corresponding regressed data. In addition, the residuals show a negligible autocorrelation of $\sim$0.12 for a

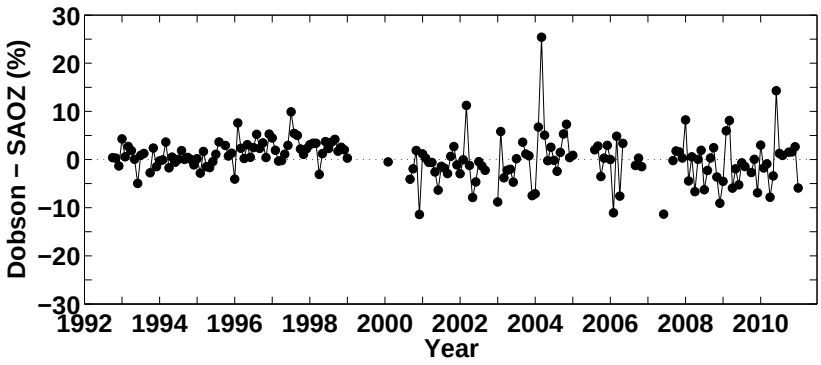

Figure 5.7: Time series of the relative differences of Dobson with respect to SAOZ ozone total column measurements at OHP.

lag of one instant, which means that the noise term is not autocorrelated and hence, the residual of the previous year does not have much influence on that of the current year.

The fitted signals due to explanatory parameters (e.g., $C_m^X \times X$) are displayed in the second to fourth panels of Fig. 5.8. It provides an evaluation of the overall contribution of various proxies to the evolution of total ozone. The highest contribution to total ozone variation arises from the combined effect of QBO 10 and QBO 30, which reaches about 24 DU from the easterly to the westerly phase, in March. The seasonal variation of QBO shows that its influence on total ozone is maximum in the winter/spring season ranging between 16 and 24 DU. The amplitude of the total ozone variation due to eddy heat flux is maximum in February and March with value of ∼17 DU. In January, April and May, it amounts to 11–14 DU. The contribution of NAO to total ozone amounts to 13 DU in the November–January period and is smaller in other seasons. Solar flux has a relatively lower contribution to total ozone variability with a maximum of 10 DU, from solar maximum to solar minimum, in summer. The aerosol terms associated with the Mount Pinatubo eruption explains about 24 DU decrease in total ozone in 1993. The PWLTs and the regression coefficients of various proxies along with twice the standard deviation of these estimates for the months March and September and average of all months are noted in Table 5.1.

Table 5.1: The piecewise linear trends before (C_{T1}) and after (C_T) 1997 and the regression coefficients of QBO 10, QBO 30, aerosol, solar flux, NAO and heat flux, estimated from the combined Dobson and SAOZ ozone total column measurements at OHP are shown for March, September and the average of all months. C_{T1} and C_T are given in DU/year, aerosol, NAO and heat flux are given in DU, QBO 10 and QBO 30 are expressed in DU/(m/s) and solar flux is in DU/(100 SFU). Twice the standard deviation of the trends and regression coefficients are given in the parentheses.

Month	C_{T1}	C_T	QBO 10	QBO 30	aerosol	solar flux	NAO	heat flux
March	-2.18(1.21)	1.28(1.27)	-0.22(0.20)	-0.24(0.27)	-25.03(24.88)	1.89(7.92)	-7.69(24.98)	21.46(26.48)
September	-0.57(0.66)	-0.14(0.64)	0.03(0.14)	0.08(0.12)	-12.33(15.32)	2.84(4.67)	-10.43(15.72)	31.83(33.21)
Average	-1.39(0.29)	0.55(0.30)	-0.06(0.05)	-0.06(0.06)	-15.84(6.56)	2.00(2.06)	-6.31(6.70)	18.61(9.52)

Variations of the proxies QBO, eddy heat flux, NAO and solar flux together explain most of the observed variations in ozone. For example, the large ozone values in 1986, 1987, 2009 and 2010 are caused by the easterly phase of QBO, large negative NAO index and large eddy heat flux. The decrease of ozone in 1990 and 2002 is well captured by the model and can be attributed to the westerly phase of QBO (∼8 DU), large positive values of NAO and

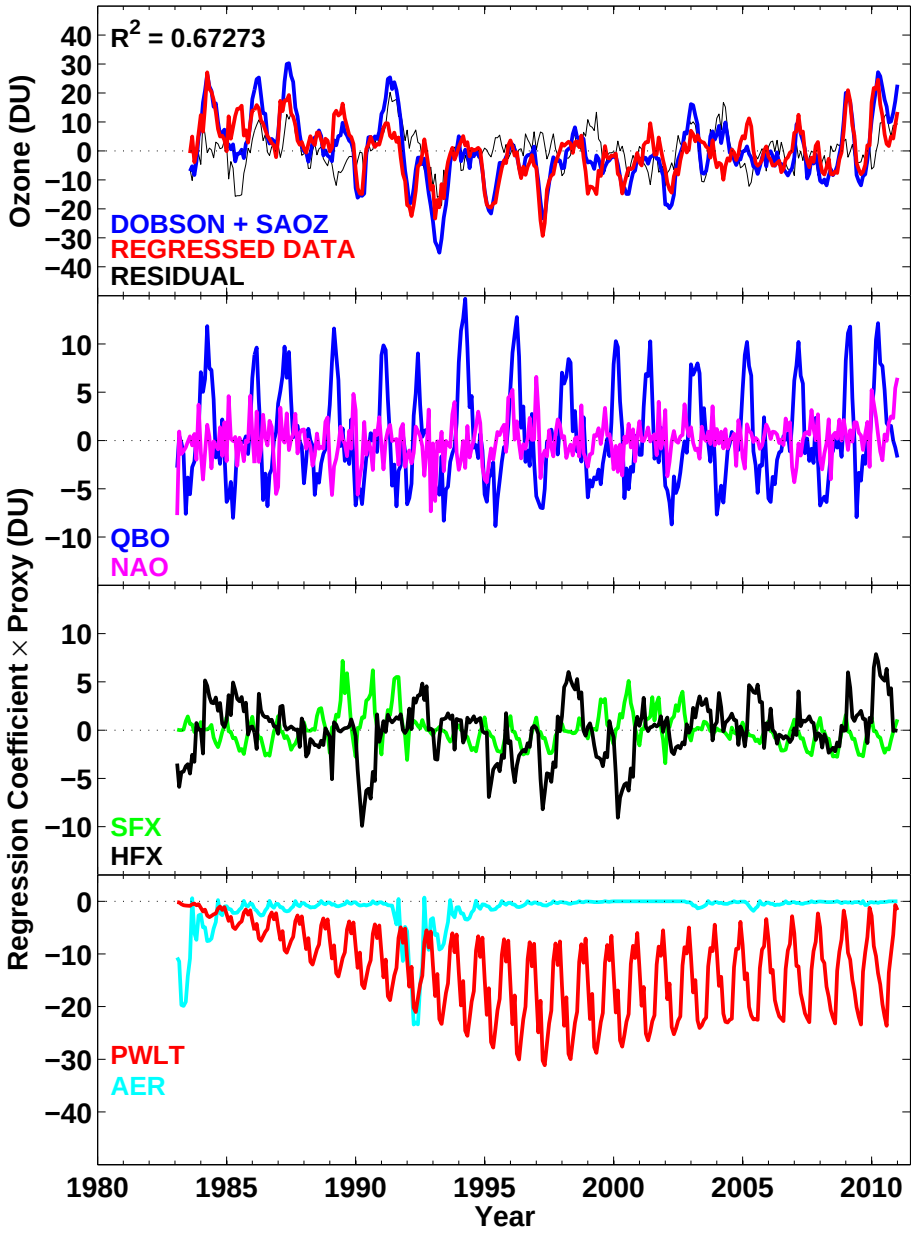

Figure 5.8: Regression plot of monthly mean deseasonalised ozone from the combined Dobson and SAOZ measurements at OHP, the PW regression model and the residual (top panel), contribution from the individual proxies QBO, NAO (second panel), solar flux, heat flux (third panel) and aerosols along with the piecewise linear trend (PWLT) fit (fourth panel).

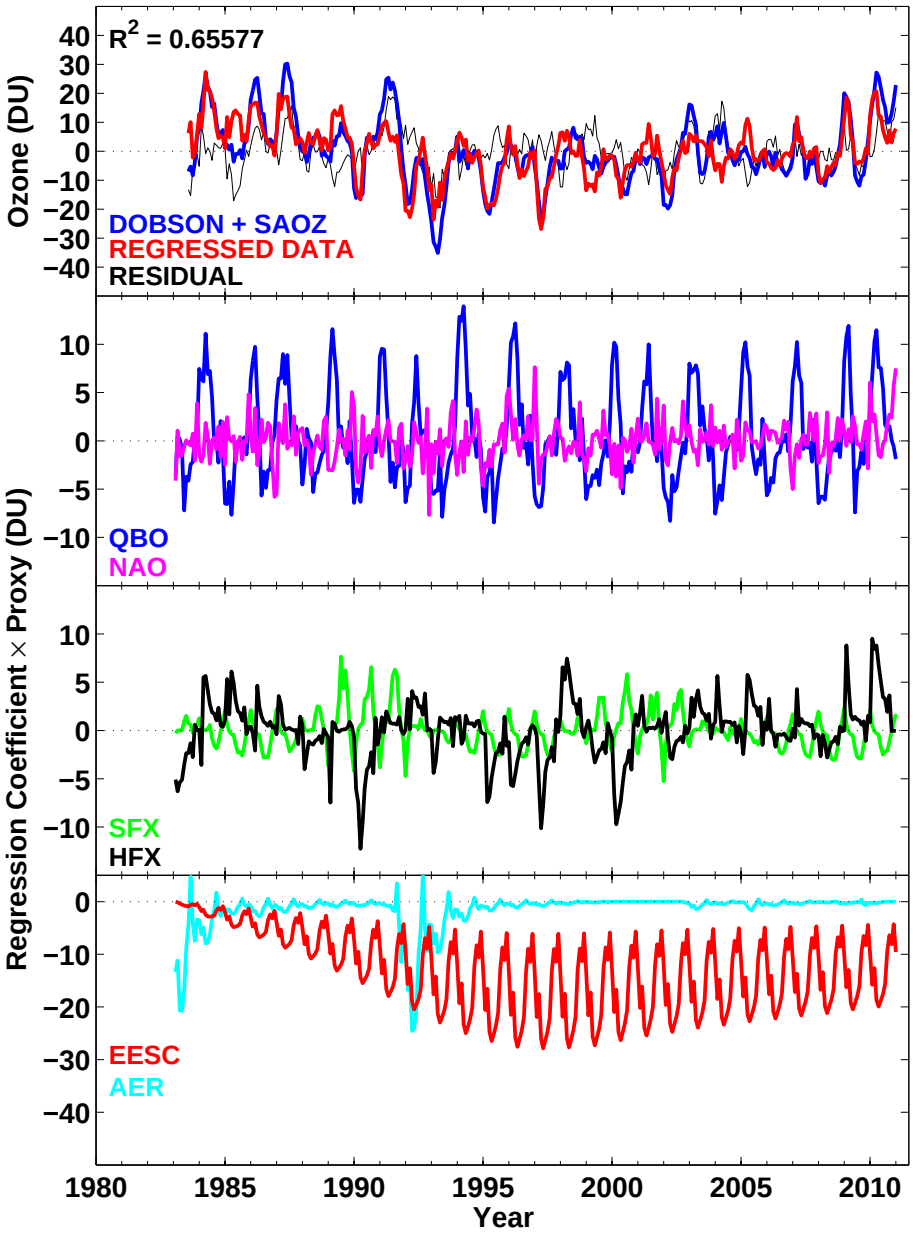

Figure 5.9: Same as Fig. 5.8, but using EESC regression model.

low eddy heat flux even if solar flux maximum should increase the ozone amount. On the contrary, a large reduction in ozone is observed during the 1995–1997 period. It could be due to the coincidence of solar minimum and low values of the eddy heat flux. Also, in 1995 and 1997 the westerly phase of QBO positively correlates with the positive NAO index. All these lead to large negative ozone anomaly during the period. Furthermore, the Arctic winter 1994/1995 was characterised by very low temperatures in winter/spring with very large volume of PSC (V_{PSC}) and the Arctic winter 1996/1997 was featured with very low temperature in spring with moderate amount of V_{PSC} (Rex et al., 1999). So, V_{PSC} could be added as a proxy (Weber et al., 2003; Wohltmann et al., 2007) in the regression model to study the influence of polar ozone loss on the mid-latitudes because the mid-latitudes are generally affected by the polar ozone loss through the dilution process after the breakdown of polar vortex, as discussed in Chapter 1. But Dhomse et al. (2006) remind that the V_{PSC} and heat flux are anticorrelated and so the heat flux itself could also explain the observed features in ozone. So, considering this anticorrelation between V_{PSC} and heat flux, it was decided not to include V_{PSC} in our regression model.

As for PW regression, EESC regression model is also analysed in detail to find out the differences between the two types of regression analysis. Figure 5.9 displays the result attained by performing EESC regression. It shows the same features as in Fig. 5.8 with R^2 estimate of 0.65 and a correlation of about 0.8. Contributions of solar flux, eddy heat flux and NAO are a bit larger when EESC is used as a proxy, though their patterns remain the same as for PW regression (see Fig. 5.8).

Table 5.2: The interannual variability of ozone total column measurements in DU, estimated for each month at OHP and MOHp.

Station	January	February	March	April	May	June	July	August	September	October	November	December
OHP	13.52	14.55	16.24	14.94	12.51	11.45	9.87	6.73	6.06	5.51	7.28	11.48
MOHp	15.83	15.94	16.13	14.59	12.90	10.75	8.98	7.02	6.68	7.73	10.2	15.05

5.4.1 Contribution of proxies to ozone variability

The effect of each proxy on the ozone total column measurements is evaluated, particularly for the specific years. Therefore, for making a general assessment, the interannual variability of ozone total column measurements (standard deviation of ozone) at OHP is investigated for each month and is provided in Table 5.2. To find out the influence of proxies on the variability of ozone, the variability of proxies is calculated for each month using both PW and EESC regressions. Variability is defined as twice the standard deviation of the fitted proxy time series, i.e., $C_m^X \times 2\sigma(X)$ (Steinbrecht et al., 2003). It is considered to be significant if the regression coefficient (C_m^X) of a proxy is greater than twice the standard deviation of that proxy [$2\sigma(C_m^X)$]. The positive values generally show positive correlation of the proxy and ozone data while negative values exhibit anticorrelation between them.

The variability in the combined Dobson and SAOZ ozone column measurements at OHP, analysed using both PW and EESC regression models are shown in Fig. 5.10 in the top and bottom panels respectively. The magenta colored markers show months, when proxies contribute significantly to the ozone variability. The ordinate represents the proxies in which Q10 and Q30 are the individual contributions of QBO 10 and QBO 30 respectively. In general, QBO 10 and QBO 30 exhibit an anticorrelation with ozone in November–May. QBO 30 is significant only in May, contributing to a maximum of about 8 DU in both

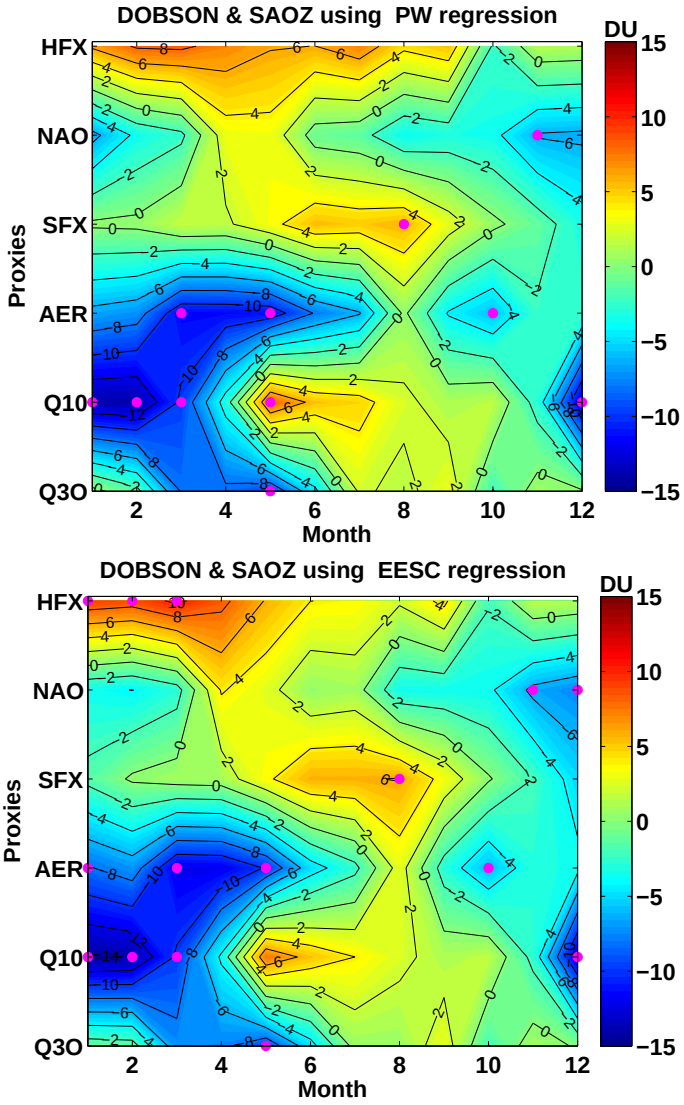

Figure 5.10: The influence of individual explanatory variables on the variability of combined Dobson and SAOZ ozone column data at OHP analysed using both PW (top panel) and EESC (bottom panel) regressions.

regressions while QBO 10 provides a significant contribution of about 12 DU to the ozone variability in winter and about 6 DU in spring. As expected, Mount Pinatubo volcanic aerosols show an anticorrelation with ozone in all months and explains about 10 DU of the ozone variability. Also, solar flux shows a significant variability of about 5 DU in summer, with a positive correlation with ozone. NAO provides a positive correlation with ozone in spring and negative correlation in other seasons and the variability is maximum of about 6 DU in November. The heat flux always shows positive correlation, but the contribution is not significant at 95% confidence level for PW regression while significant in winter for EESC regression, providing about 8 DU variability.

5.4.2 Trends in ozone total column

Ozone trends are calculated by removing the known influences of all explanatory variables from the ozone time series. Figure 5.11 displays the seasonal variations of the pre-turnaround and post-turnaround trends estimated based on PW regression. As expected, pre-turnaround trends are all negative and post-turnaround trends are positive except in the months July–September, where negative trends of the order of $-0.01\,\mathrm{DUyr}^{-1}$ are evaluated. In addition, a clear seasonality is observed in both trends with maximum in the winter/spring season. Maximum pre-turnaround trend is calculated in April and amounts to $-2.25 \pm 1.4\,\mathrm{DU\,yr}^{-1}$. Minimum is in September with about $-0.56 \pm 0.66\,\mathrm{DU\,yr}^{-1}$. Similarly, maximum post-turnaround trend is computed in March with value of $1.28 \pm 1.26\,\mathrm{DU\,yr}^{-1}$ and minimum in September, about $-0.14 \pm 0.32\,\mathrm{DU\,yr}^{-1}$. In our study, the uncertainty is provided with 95% significance level. A significant annual trend of $-1.4 \pm 0.29\,\mathrm{DU\,yr}^{-1}$ is estimated in 1983–1996 and a significant positive trend of $0.55 \pm 0.30\,\mathrm{DU\,yr}^{-1}$ is computed in 1997–2010.

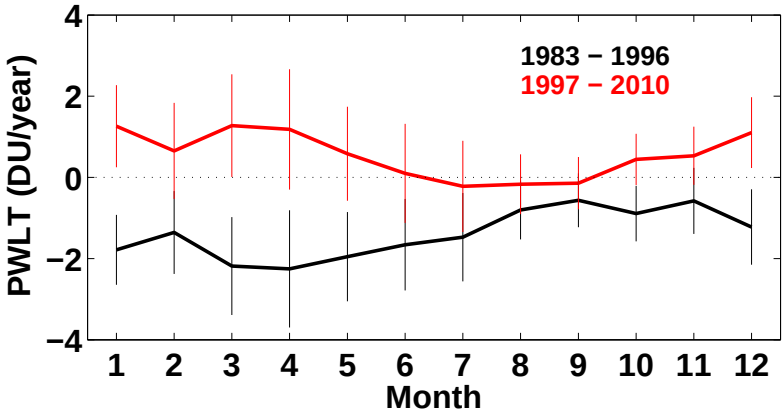

Figure 5.11: The monthly PWLTs derived from the combined Dobson and SAOZ ozone total column measurements at OHP. The black and red curves represent the pre-turnaround (prior to 1997) and post-turnaround trends (after 1996) respectively. The error bars correspond to twice the standard deviation of the trends.

In order to check the influences of ODSs in detail, the regression slopes of EESC are evaluated. The annual trends estimated from both regressions are shown in Table 5.3. The estimated trends using EESC are $-1.3 \pm 0.26\,\mathrm{DU\,yr}^{-1}$ in 1983–1996 and $0.34 \pm 0.08\,\mathrm{DU\,yr}^{-1}$ in 1997–2010. It should be noted that the PWLT prior to 1997 nearly coincides with the trend estimated using EESC function while the PWLT after 1996 is larger than that computed using EESC.

Table 5.3: The year-round pre-turnaround and post-turnaround trends, and twice the standard deviation estimated using both PW and EESC regressions for OHP and MOHp. Trends and standard deviations are shown in $DUyr^{-1}$.

Station	PWLTs		EESC based Trends	
	Pre-turnaround	Post-turnaround	Pre-turnaround	Post-turnaround
OHP	-1.4 ± 0.29	0.55 ± 0.29	-1.3 ± 0.26	0.39 ± 0.08
MOHp	-1.6 ± 0.19	0.81 ± 0.25	-1.5 ± 0.20	0.42 ± 0.06

5.5 Multiple regression analysis of ozone total column at MOHp

To compare the results obtained from the multiple regression analysis of ozone total column measurements at OHP, another NDACC station MOHp, very near to the latitude and longitude (see Chapter 2) of OHP is considered. The Dobson ozone column measurements at MOHp are analysed using PW and EESC multiple regression models and are displayed in Figs. 5.12 and 5.13, respectively. In both cases, the regression model fits well with the deseasonalised ozone yielding R^2 of 0.73 and 0.71, and correlations of 0.86 and 0.84, for the PW and EESC regressions respectively.

At MOHp, all proxies show a similar pattern as the ones at OHP, but with slightly larger values. For instance, the contribution of eddy heat flux to the total ozone change is about 23 DU in winter/spring at MOHp, which is larger by about 6 DU compared to OHP, indicating the increase in strength of the planetary wave drive with the increase in latitude. The amplitude of QBO variation of total ozone is maximum in winter/spring season with about 11–21 DU. In contrast to heat flux, the effect of QBO is found to be reduced a bit at MOHp compared to that at OHP, even if maximum contribution is nearly same at both stations. At MOHp, aerosol associated with Mount Pinatubo decreased ozone by about 30 DU, compared to the 24 DU decrease at OHP, while aerosols from the El Chichón volcanic eruption reduced total ozone by 24 DU at MOHp. Besides, the influences of NAO and solar flux are larger at MOHp compared to that at OHP. The contribution of NAO to the total ozone variation is maximum in winter with about 16–20 DU. Similarly, solar flux contributes its maximum in summer with values of 9–13 DU. As found in the previous works on this subject and from our analyses, it can be inferred that the effect of QBO decreases with respect to latitude, from the equator to the poles (Dhomse et al., 2006) whereas the effect of heat flux, solar flux, aerosols and NAO increases with the latitude (from OHP to MOHp in our study, even though the latitudinal difference between them is very small). Moreover, effect of QBO to the seasonal variation of total ozone is maximum during winter/spring in the extratropics and the effect of variation of eddy heat flux is maximum in winter/spring season, due to larger planetary wave activity. Similarly, the effect of NAO variation of total ozone is maximum in winter but solar flux shows maximum contribution in summer, as expected. Table 5.4 gives the estimated regression coefficients of all proxies along with twice the standard deviation of these estimates for March and September and for the average of all months.

The deseasonalised ozone and the regressed data at MOHp, follow more or less similar tendency as observed at OHP. For instance, the deseasonalised ozone is mostly negative during 1993–2002. In 1993, aerosols originating from the Mount Pinatubo volcanic eruption decrease ozone levels. In 1995–2002, the same reasons explained for the OHP station are applicable here too. In addition, effect of aerosols from the El Chichón volcanic eruption can be found by a steep ozone decrease in 1983. Similarly, ozone values are higher in some

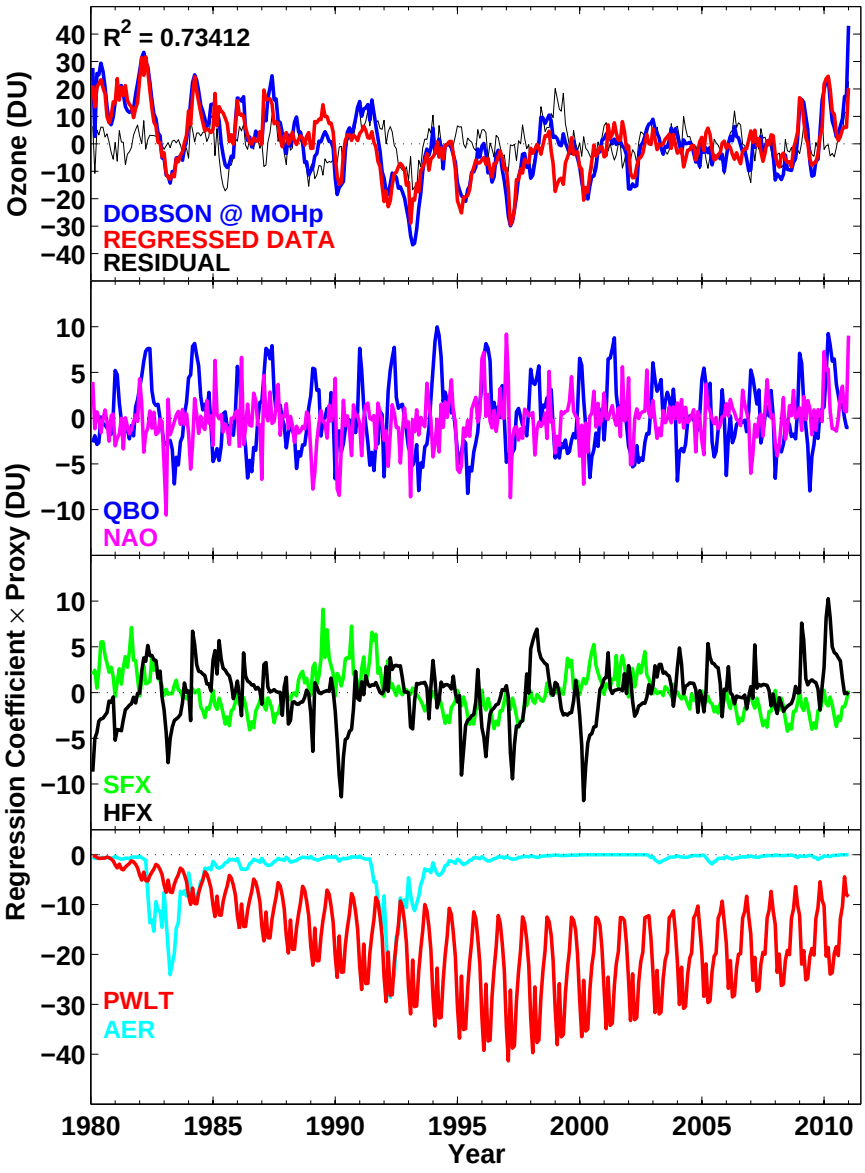

Figure 5.12: Same as Fig. 5.8, but for Dobson ozone column measurements at MOHp.

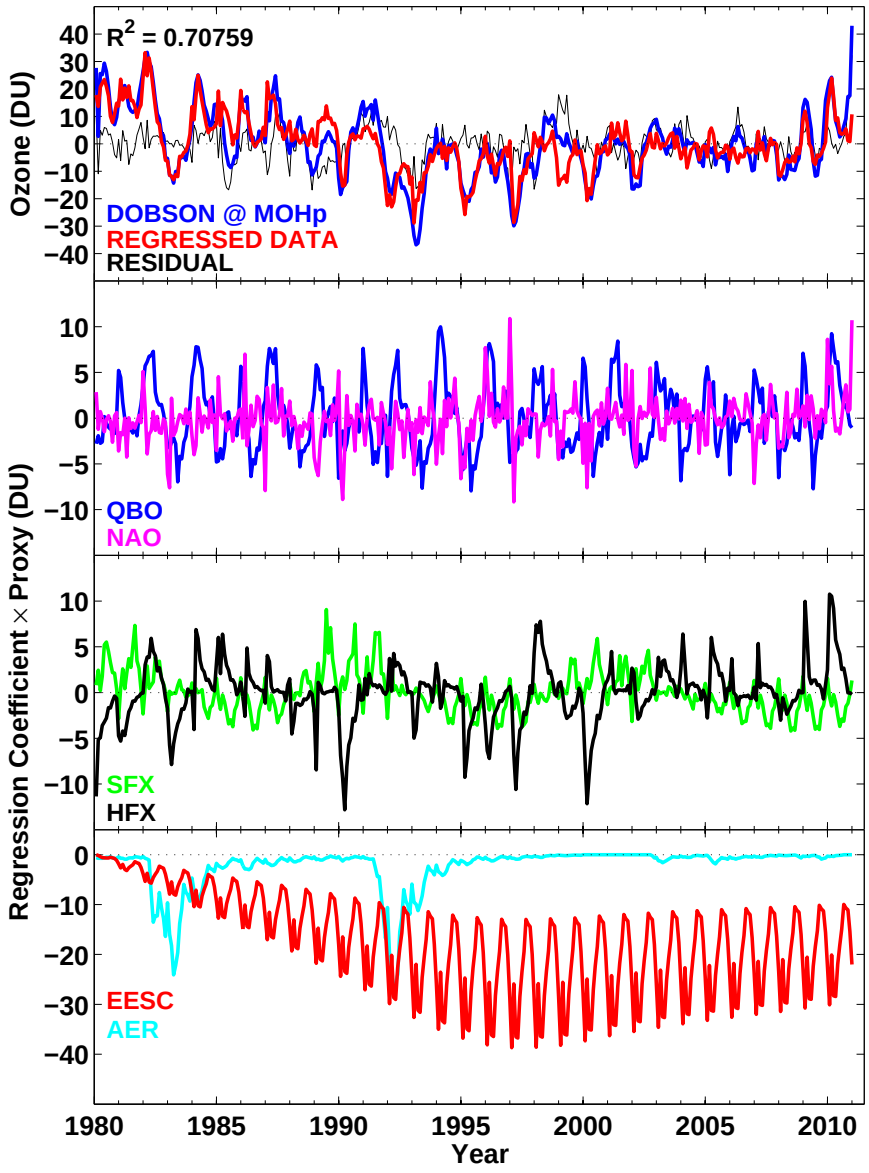

Figure 5.13: Same as Fig. 5.9, but for Dobson ozone column measurements at MOHp.

years like, 1986, 1987, 2009 and 2010 and the possible causes of this increase in ozone are explained earlier for OHP. A very recent study by Steinbrecht et al. (2011) reported that the unanticipated large value of ozone (∼340 DU) at MOHp in 2010 is due to the occurrence of easterly phase of QBO and an anomalously large negative AO index. However, our study reveals that large wave activity, indicated by the considerably large eddy heat flux contributes about 10–12 DU to the total ozone, in addition to the total contribution of about 15 DU from QBO and NAO together. It should be noted that heat flux is the largest in 2009 and 2010 for the whole data record of 31 years.

Table 5.4: Same as Table 5.1, but for Dobson ozone total column measurements at MOHp.

Month	C_{T1}	C_T	QBO 10	QBO 30	aerosol	solar flux	NAO	heat flux
March	-2.30(0.61)	1.14(0.88)	-0.06(0.13)	-0.24(0.18)	-30.56(13.63)	1.16(5.67)	-10.05(18.57)	27.79(19.93)
September	-0.82(0.53)	0.25(0.61)	0.08(0.13)	0.02(0.11)	-16.04(13.10)	3.63(4.12)	-14.63(15.20)	12.20(36.32)
Average	-1.57(0.20)	0.81(0.25)	0.01(0.05)	-0.09(0.05)	-21.03(4.73)	3.72(1.80)	-7.18(5.69)	17.76(8.13)

5.5.1 Contribution of proxies to ozone variability

As discussed in Sect. 5.4.1, the interannual variability of Dobson ozone total column measurements at MOHp is computed for each month and is presented in Table 5.2. Figure 5.14 displays the influence of various proxies on the variability of Dobson ozone column measurements at MOHp for PW (top panel) and EESC (bottom panel) regression. The contribution of QBO 30 is significant in February–May with a maximum of about 12 DU. QBO 10 shows a positive contribution of about 6 DU in May and July. The influence of aerosol is significant in all months, contributing about 12 DU ozone variability. Likewise, contribution of solar flux is significant in summer with a positive correlation and contributes about 7 DU to the ozone variability. Significant NAO contribution is anticorrelated with ozone with a maximum of 8 DU in January, August and September. The eddy heat flux yields significant contribution of about 10 DU to ozone variability in winter with a positive correlation.

5.5.2 Trends in ozone total column

The monthly and year-round ozone trends based on PW and EESC regressions are estimated using Dobson ozone measurements at MOHp to compare with that obtained from the Dobson and SAOZ data at OHP. Maximum pre-turnaround and post-turnaround PWLTs are computed in January with values of about $-2.4 \pm 0.57\,\mathrm{DU\,yr^{-1}}$ and $1.6 \pm 0.83\,\mathrm{DU\,yr^{-1}}$, respectively. Similarly, minimum pre-turnaround and post-turnaround PWLTs are evaluated in August of about $-0.73 \pm 0.42\,\mathrm{DU\,yr^{-1}}$ and $-0.03 \pm 0.54\,\mathrm{DU\,yr^{-1}}$, respectively. The PW regression yields year-round pre-turnaround trends of about $-1.5 \pm 0.19\,\mathrm{DU\,yr^{-1}}$ in 1980–1996 and $0.8 \pm 0.25\,\mathrm{DU\,yr^{-1}}$ in 1997–2010. Similarly, year-round trends based on EESC are of about $-1.5 \pm 0.20\,\mathrm{DU\,yr^{-1}}$ and $0.42 \pm 0.06\,\mathrm{DU\,yr^{-1}}$ in the corresponding periods. The estimated ozone trends using the PW and EESC time series are given in Table 5.3.

From the analysis, it can be inferred that linear trends evaluated from both PW and EESC fits before 1997 are the same. Nevertheless, the PWLT after 1996 is higher and nearly double than the EESC based trends, as mentioned in Sect. 5.4.2. In general, from these analyses, it is found that in the considered latitude regimes, the decrease in total ozone before 1997 is attributed to the increased ODS abundances while only 50% of the increase in total ozone after the turnaround year can be explained using the decreased amount of

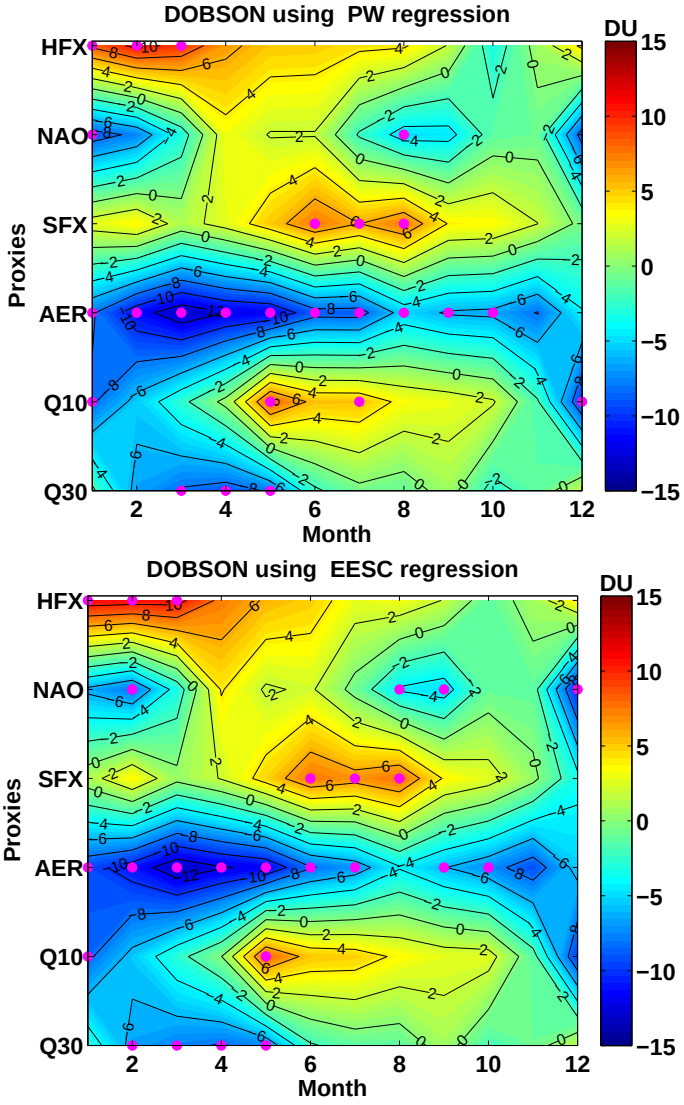

Figure 5.14: Same as Fig. 5.10, but for Dobson ozone column measurements at MOHp.

ODSs. A study by Vyushin et al. (2007), using zonal average data, found that the PWLTs are nearly 4 times greater than the ozone trends based on EESC fit in the northern mid-latitudes. It confirms the influence of dynamically driven variations in addition to the ODS decrease for the positive trend in ozone (WMO, 2011).

5.6 Vertically resolved ozone observations at OHP

5.6.1 Stratospheric ozone evolution

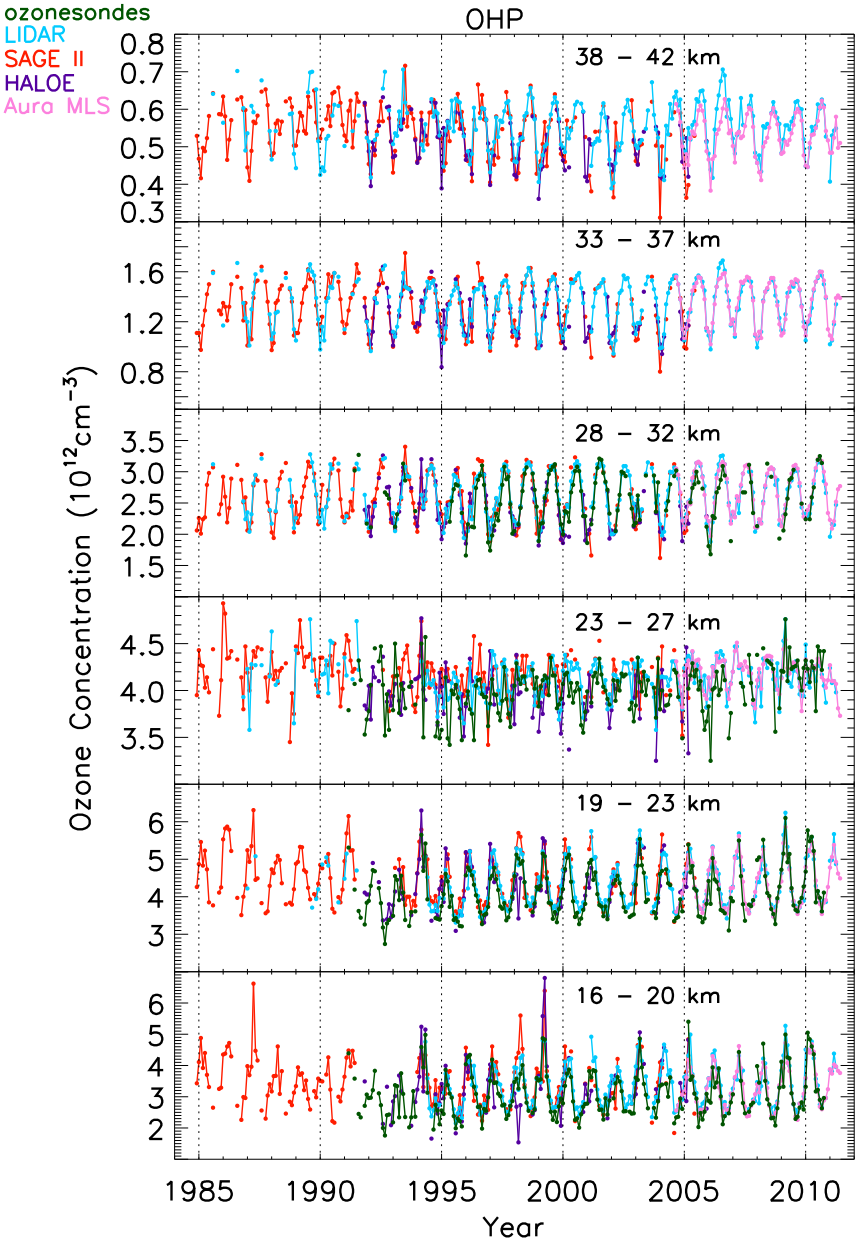

Figure 5.15: Temporal evolution of ozone vertical profiles from lidar, SAGE II, HALOE, Aura MLS and ozonesondes at OHP. The data are resolved in 1 km vertical grid.

Ozone profile measurements from instruments such as lidar, ozonesondes, SAGE II, HALOE and Aura MLS are used for investigating the evolution of stratospheric ozone vertical profiles at OHP in 1984–2010. These data sets use various measurement techniques for observing ozone and have different vertical resolutions. Hence, all data sets are interpolated in 1 km vertical resolution for the analysis. Figure 5.15 shows the time series of each data at the reference altitudes of 18, 21, 25, 30, 35 and 40 km, which are obtained by averaging ozone in ±2 km of the reference altitudes. All measurement techniques follow a similar behaviour in the evolution of ozone with respect to time and exhibit clear seasonal variations. Maximum ozone concentration is found at 16–20 and 19–23 km, with highest values in the latter altitude range. The variations in ozone is higher at lower altitudes and decrease with respect to altitude. All observations show relatively large ozone values at 16–20 km in 1999, the details of which are described in the following sections.

5.6.2 Stratospheric ozone anomaly

Figure 5.16 presents the monthly ozone anomaly in % of each measurement technique, interpolated in 1 km vertical interval, and averaged at the altitude bands 16–20, 19–23, 23–27, 28–32, 33–37 and 38–42 km. All measurement techniques exhibit small anomaly, within ±5 % in general at all altitude bands except at 16–20 km, where ozone variability is relatively large. Similarly, ozone anomaly is slightly higher at 38–42 km before the mid-1990s, where a clear decrease in ozone anomaly is found from 1985 to 1996 and a stabilisation afterwards. Not a specific anomalous behaviour is shown by any instrument and all instruments show a similar pattern of ozone anomaly. In 2010, all available data sets show positive anomalies in the lower stratosphere, particularly in 16–20 km, which implies that a major part of the ozone total column in 2010 in the northern mid-latitudes, as described in Sects. 5.4 and 5.5, arise from the lower stratosphere.

5.6.3 Application of multiple regression

Ozone anomaly is used to assess the long-term variability of the vertical distribution of stratospheric ozone at OHP. Similar to the combined data set of total column, the ozone anomalies from lidar, SAGE II, HALOE, Aura MLS and ozonesondes in 1 km vertical grid are averaged to form a single profile in a month. Then, a 5 month running mean is applied to smooth the data. The multiple regression is applied to this smoothed average data having 1 km vertical resolution. Besides, the individual ozone anomaly from lidar and SAGE II, which are also smoothed by 5 month running mean, are analysed using multiple regression. The same regression models, PW and EESC, and the same proxies used for the analysis of ozone total column measurements are used here too. The aerosol proxy data are applied only up to 30 km since no aerosol exists above 30 km. Moreover, aerosol effect on ozone is mostly local through heterogeneous reactions and local heating of stratosphere.

In order to find how well the model is in explaining the observed seasonal variability in the ozone average, R^2 is calculated for each month using the PW regression model and is shown in Fig 5.17 at all altitudes. The smoothing increases R^2 estimate. The model shows generally the best agreement (>0.5) with ozone anomalies in the 18–42 km region in all months except around 25 km in the summer months. The best agreements are found in the winter/spring months, with values greater than 0.5 and reaching to about 0.85 at 22 km in March and April. About 50–60 % of the variability in December–February can be explained using the regression model at 42–45 km. On the other hand, the model can explain only 20–50 % of the variability in 16–18 km at all months, which indicates that, in these regions, the considered proxies are not sufficient to explain the observed variance.

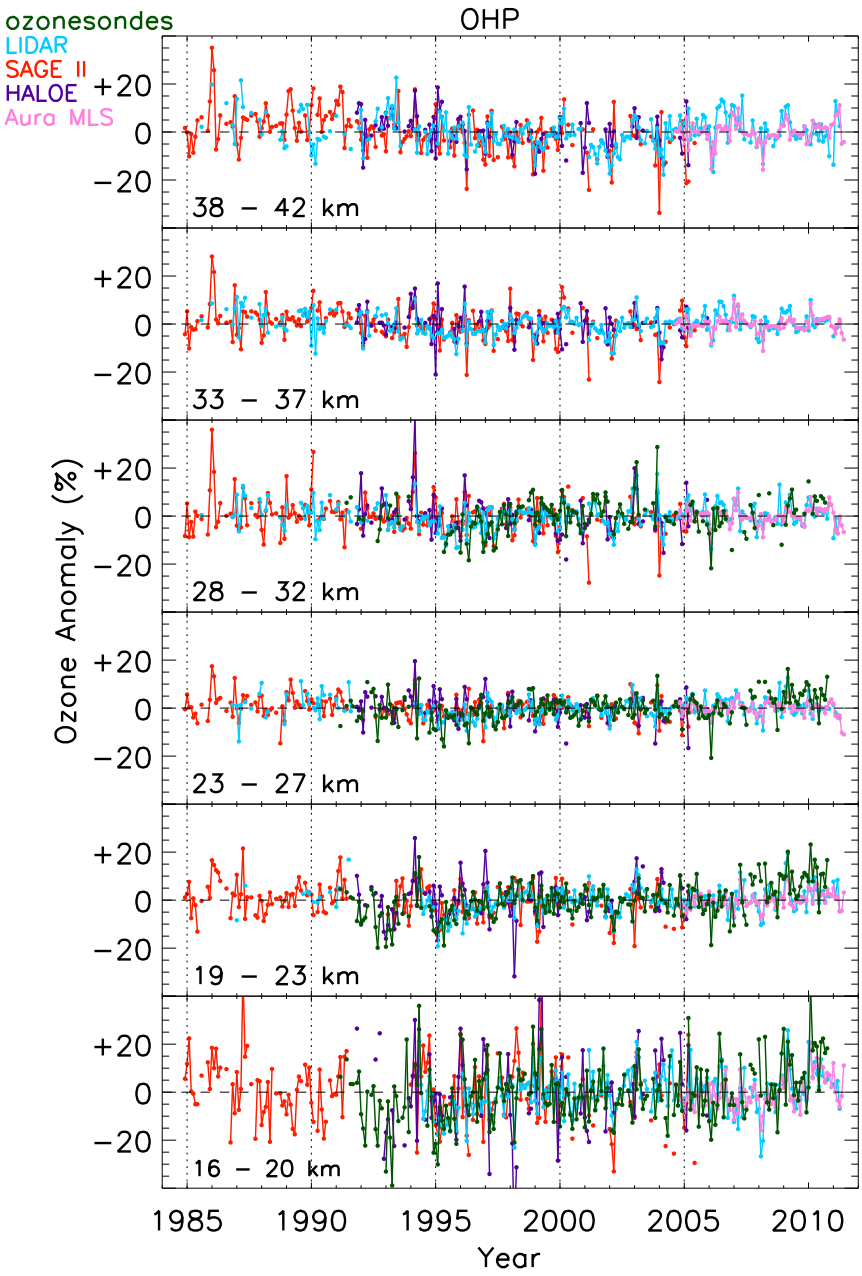

Figure 5.16: Time series of ozone anomaly from lidar, SAGE II, HALOE, Aura MLS and ozonesondes at OHP. The data are resolved in 1 km vertical grid.

The large atmospheric variability in the lower stratosphere makes the proxies difficult to model the observed ozone variations in great detail. The estimate of R^2 is about 0.4 at 25–30 km in July–September and November and at 43–45 km from March to October.

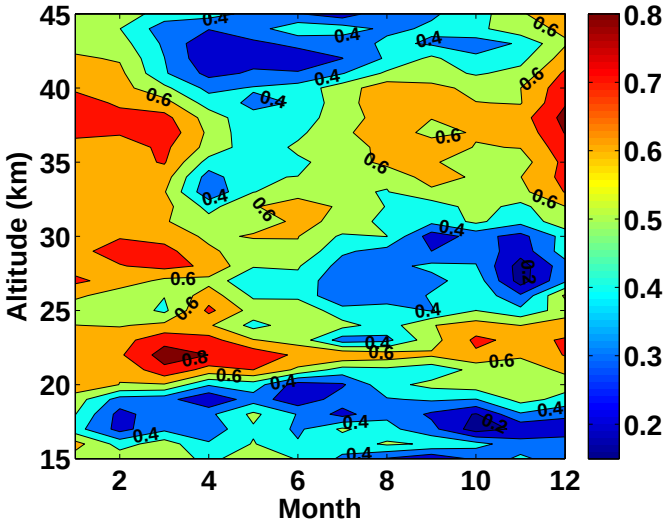

Figure 5.17: Vertical distribution of the monthly R^2 values estimated from the PW regression model for the average data at OHP.

The vertical distribution of R^2, averaged over the period from the monthly estimates of R^2, using both PW and EESC regression models is shown in Fig. 5.18 for the average, lidar and SAGE II data. The R^2 values are similar for both types of regressions. The average and SAGE II data show a similar kind of R^2 variation at all altitudes whereas results from ozone lidar measurements are somewhat different. For example, large R^2 of ∼0.6–0.8 is found in the 20–25 and 35–40 km range for average and SAGE II ozone measurements. In the 25–35 km range, about 50–60% of the variability can be explained by the model for the average and SAGE II data. Below 20 km, the model provides R^2 value of about 0.7 for the ozone lidar measurements and about 0.3–0.5 for the SAGE II and average data. In contrast, R^2 is about 0.5–0.7 for the average and SAGE II data above 40 km while it is less than 0.5 for lidar data because ozone lidar measurements are less sensitive in this altitude range.

Figure 5.19 presents the vertical distribution of the temporal evolution of average ozone anomaly (top panel), the PW regression model (middle panel) and the residual (bottom panel). The observed features in the ozone anomaly are reproduced quite well in the regressed data between 20 and 42 km and the corresponding residuals are nearly zero. Large positive and negative ozone anomalies are found in the whole stratosphere in 1986 and 1995–1997, respectively. The reasons for the observed increase in ozone anomaly in 1986 can be well explained by the regression model in the lower and upper stratosphere whereas in the middle stratosphere the model could not explain completely. In 1995–1997, the decrease in ozone anomaly is clearly replicated in the model. Moreover, large positive anomalies are observed in 1985, 1987, 1999, 2009 and 2010 in the lower stratosphere. The regression model also shows similar values in those years except in 1999. It implies that the very high positive ozone anomaly in the lower stratosphere in 1999 cannot be explained by the considered proxies. Similarly, model could explain only a part of the large ozone

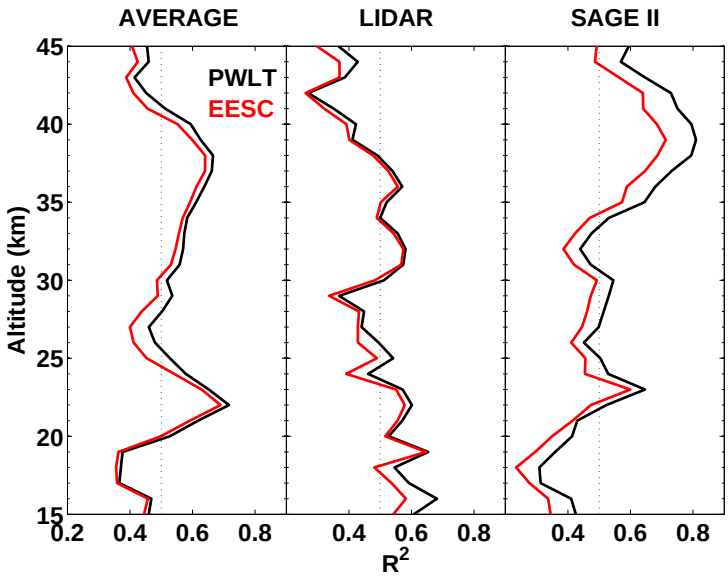

Figure 5.18: Vertical distribution of R^2 estimated over the period for the average, lidar and SAGE II data at OHP.

anomaly in 1987. Also, large positive ozone anomalies are found in the upper stratosphere in 1988, 1991 and 1993, and only a part of which could be seen in the regressed data. Also, slightly larger negative ozone anomaly is observed in 2002, particularly in the lower and upper stratosphere. All these features are very clearly depicted in Fig. 5.20.

The time series of ozone anomaly, the PW regression model and the residuals are drawn at particular altitudes of 18, 21, 25, 30, 35 and 40 km in ±2 km band and is displayed in Fig. 5.20. At 18 km, ozone anomaly is comparatively large of about ±(5–10) % in most years. At 40 km also, ozone anomaly is about ±5 % while other altitudes exhibit smaller anomalies of less than ±4 %. A clear decrease in ozone is visible from 1984 to the mid-1990s at all altitudes. In contrast, an increase in ozone after the mid-1990s is well detectable below 25 and above 35 km only, while at 25–35 km, a stabilisation is detected. In order to investigate the exact reasons for these events, the fitted signals of QBO, NAO, solar flux, heat flux and aerosols to the ozone vertical profile are calculated and are displayed in Fig. 5.21. The Figure shows that the influence of QBO is largest and is present at all altitudes, and that of NAO is also present at all altitudes, but to a lesser extent. On the other hand, heat flux and solar flux contribute reasonably at 18 km, but their influence is smaller at other altitudes.

As mentioned earlier, extremely large ozone anomalies are found in the 1986 winter at all altitude levels and in the 1999 winter at 18 km. From Fig. 5.21, it is found that in 1986, even if solar variation is minimum, moderately large wave activity, easterly phase of QBO and negative NAO index result in large ozone levels in the lower stratosphere. In contrast, no proxies show a notable change in 1999 even though heat flux shows moderately large value, which is not sufficient to explain the observed high ozone level. But the Arctic winter 1999 was characterised by unusually warm polar vortex and the polar vortex filaments were elongated down to southern Europe. These polar filaments were detected above OHP (Heese et al., 2001; Godin et al., 2002), which give rise to large ozone values in the lower stratosphere at OHP. Therefore, an additional proxy combining the position of the station with respect to the vortex and ozone loss within the vortex could provide extra information

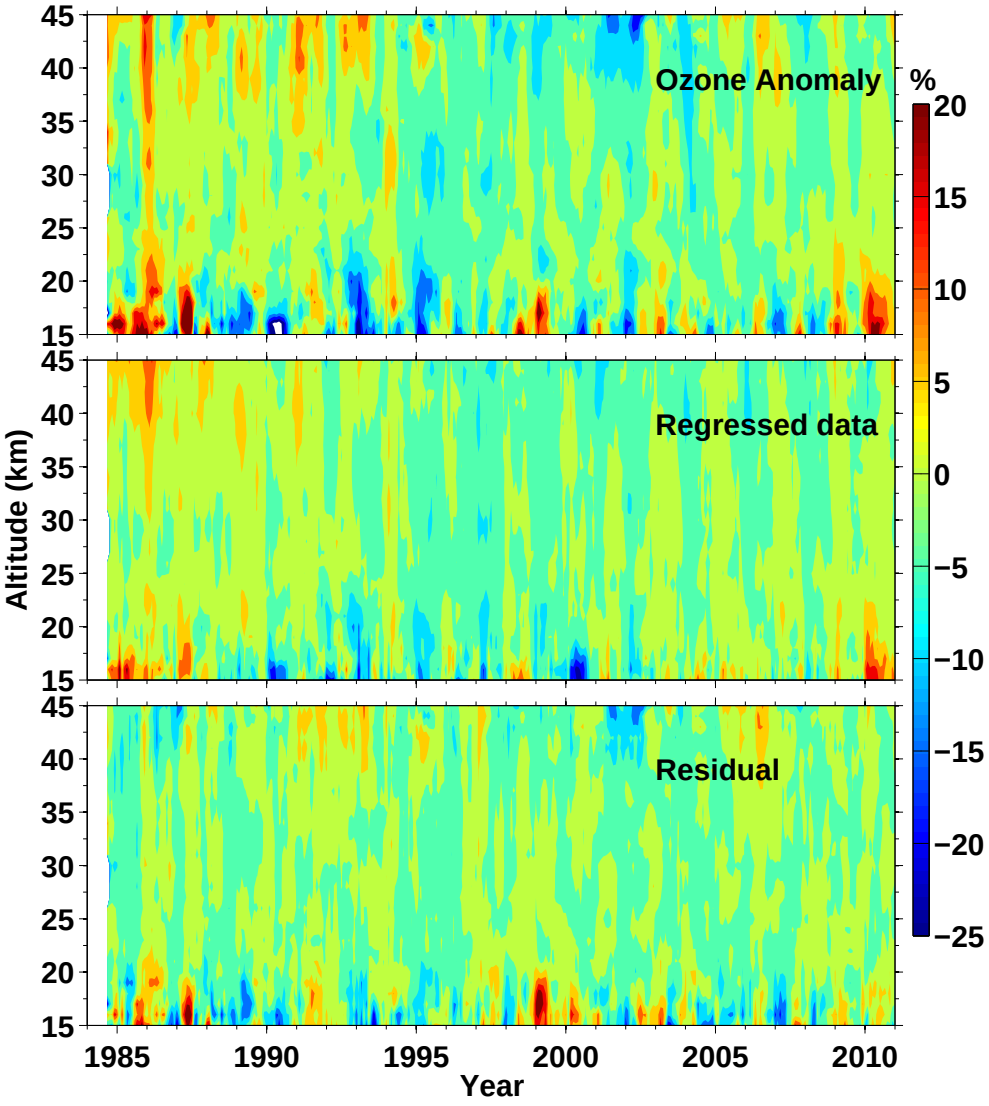

Figure 5.19: Temporal evolution of the vertical distribution of average ozone anomaly (top panel), PW regression model (middle panel) and residual (bottom panel) in 1984–2010 at OHP.

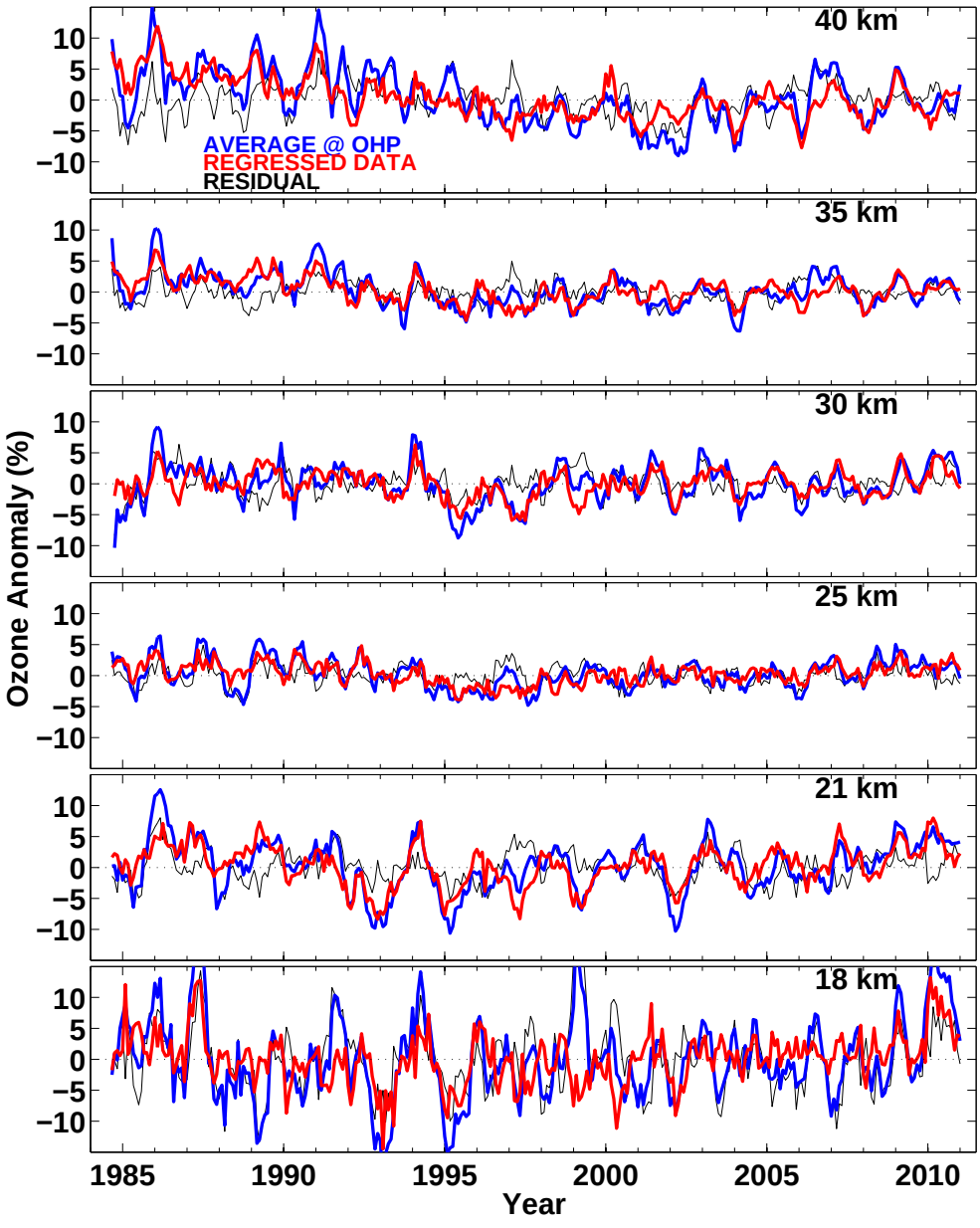

Figure 5.20: Time series of the ozone anomaly, the PW regression model and the residual at 18, 21, 25, 30, 35 and 40 km calculated from the average data at OHP.

of such feature. Position of the station with respect to polar vortex could be modeled by Equivalent latitude (the geometrical latitude enclosing the same area as the PV isoline). Similarly, ozone anomaly is very large at 18 km in 1987 (see Fig. 5.20). It is in part due to the easterly phase of QBO and large negative NAO index. Also, a clear increase in the ozone anomaly is seen in 2009–2010 in the lower stratosphere, with exceptionally large values at 18 km, comparable to that in the ozone total column data at OHP and MOHp during the period. This is due to the large planetary wave activity, as can be seen in the large heat flux, easterly phase of QBO with large values and negative NAO index (see Fig. 5.21). The winters 1986, 1989 and 1991 show much higher ozone values at 40 km. From Fig. 5.21, it is found that only QBO induces slightly large values in its easterly phase in 1986, 1989 and 1991. In addition, ozone anomalies are very low in 1989, 1993, 1995 and 2002 at 18 km and in 1993, 1995 and 2002 at 21 km. This decrease can be well explained using the high positive NAO indices in those years. Additionally, a large reduction of about 15 % in ozone anomaly in 1993 is also associated with the aerosols from the Mount Pinatubo volcanic eruption.

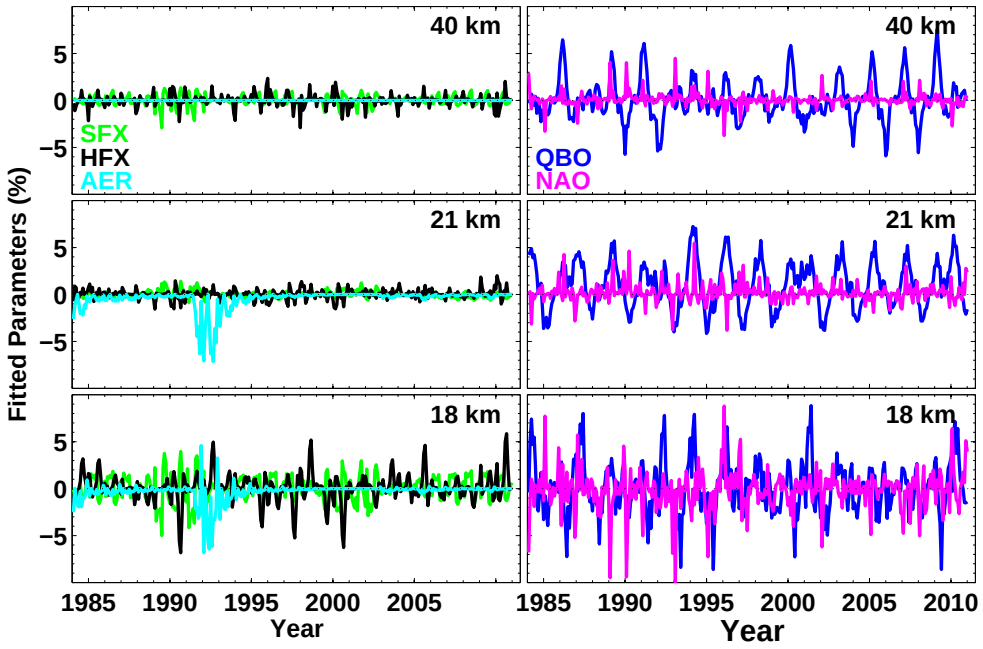

Figure 5.21: Time series of the fitted signals of solar flux, heat flux, aerosols, QBO and NAO at 18, 21 and 40 km computed for the average data at OHP.

5.6.4 Contribution of proxies to the variability of ozone profiles

The contribution of proxies to the variability of ozone vertical distribution is analysed using the average data set at OHP for PW regression and the results are displayed in Fig. 5.22. The study of the influence of proxies at various altitude levels is necessary as the effect of most proxies are limited only to some specific altitude regions in the stratosphere. QBO 30 yields significant contribution at 18–23 and around 30 km. In July–August, it shows a positive correlation influencing significantly the ozone variability at 17 km and is anticorrelated with ozone in March–June in the lower stratosphere. It provides significant contribution to the ozone variability in the upper stratosphere also, in October–February

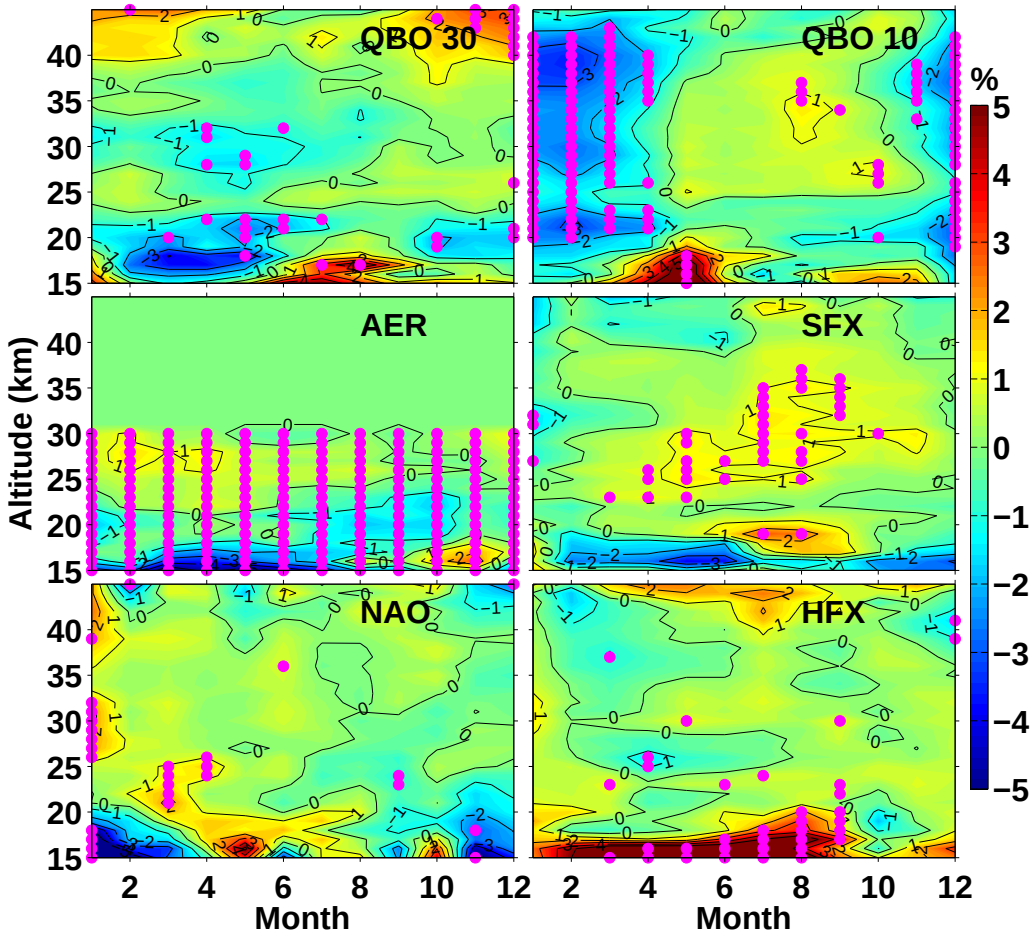

Figure 5.22: The contribution of various proxies to the variability of average ozone profile at OHP.

yielding a positive correlation. The contribution of QBO 10 is significant at all altitudes and in most months, except June–July, with a negative correlation in November–April and a positive correlation in May–October. The contribution of these proxies to ozone variability is maximum in the lower stratosphere and reaches about 10 %. The influence of aerosols to ozone variability is significant in all months with a maximum of 5 %. In the 25–30 km range, aerosols show a positive correlation as found in (Brunner et al., 2006). This change in sign or the increase in ozone above 25 km is caused by the reduced concentration of NO_x that results from the heterogeneous reactions occurring on the surface of aerosols, as described in Chapter 1. Solar flux proxy yields significant contribution only when it has a positive correlation with ozone, in March–November period at 23–37 km, contributing about 2 % ozone variability. Similarly NAO shows a significant contribution in January at all altitudes and in other months particularly in the middle stratosphere, when there is a positive correlation with ozone, contributing to 4 % variability in ozone. Heat flux contributes more to the ozone variability, with about 10 % in the lower stratosphere (15–20 km) and is positively correlated with ozone. A significant contribution is also found in the middle stratosphere at certain altitudes in March–May and December.

5.6.5 Trends in stratospheric ozone vertical profiles

We have seen some significant positive trends indicating ozone recovery in the northern mid-latitudes from the ozone total column measurements. Now we analyse how these trends are reflected in ozone profiles. Trends in the vertical distribution of ozone is calculated from the monthly ozone anomaly in %. Figure 5.23 represents the trends in the vertical distribution of ozone estimated based on PW and EESC fits before 1997 (solid line) and the post-turnaround trend (dashed line) for average (left panel), lidar (middle panel) and SAGE II (right panel) data.

In the case of average data, the year-round pre-turnaround trends estimated using PW and EESC regression models are of the order of -0.4 to $-0.5\,\%\mathrm{yr}^{-1}$ in 18–25 and 34–37 km, $-0.65\,\%\mathrm{yr}^{-1}$ at 16 km and about $-0.8\,\%\mathrm{yr}^{-1}$ in 38–45 km and all are significant at 95% confidence interval. The highest negative trends are found in the 38–45 km region and are similar to those found in Steinbrecht et al. (2009) and Jones et al. (2009). Similarly, statistically significant post-turnaround trend of $0.3\,\%\mathrm{yr}^{-1}$ is computed using PW regression model in the 18–28 km range. Likewise, EESC fit provides statistically significant value of $0.1\,\%\mathrm{yr}^{-1}$ in 15–30 km. In the 31–39 km region both regressions yield similar and significant value of $0.15\,\%\mathrm{yr}^{-1}$. Above 39 km, EESC regression yields statistically significant positive value of $0.3\,\%\mathrm{yr}^{-1}$ while PWLTs are statistically insignificant. It should be noted that the PWLTs in the post-turnaround period are insignificantly small in the upper stratosphere and are larger below 30 km compared to that of EESC, similar to the reports in WMO (2011).

A similar result is achieved from the lidar and SAGE II ozone observations with some discrepancies at certain altitudes. For example, lidar shows statistically significant negative trends (-0.5 to $-0.8\,\%\,\mathrm{yr}^{-1}$) in 18–21 and 35–45 km, except at 25 and 42 km. However, statistically insignificant PW and EESC trends are found below 19 km. Similarly, significant positive trends (0.2–0.4 $\%\,\mathrm{yr}^{-1}$) in 1997–2010 are estimated for PW and EESC regressions in 19–38 and 19–45 km, respectively, except at 25 and 42 km. For SAGE II, significant negative trends are estimated with values varying from -0.4 to $-0.6\,\%\,\mathrm{yr}^{-1}$ in 21–36 km and between -0.75 and $-1\,\%\,\mathrm{yr}^{-1}$ in 37–45 km from both regressions. On the other hand, only EESC regression model provides statistically significant positive trends (0.1–0.3 $\%\,\mathrm{yr}^{-1}$) after 1996 for SAGE II.

As concluded from the ozone total column trends estimated at OHP and MOHp, in the

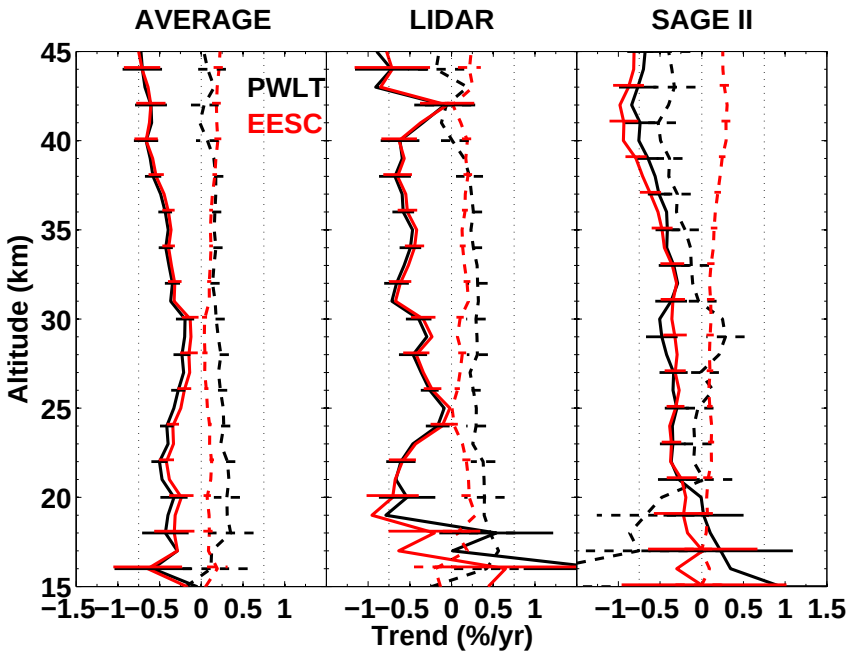

Figure 5.23: Vertical structure of the year-round ozone trends estimated from PW and EESC functions in 15–45 km estimated from the average (left panel), lidar (middle panel) and SAGE II (right panel) data at OHP. The solid lines represent the pre-turnaround trends and the dashed lines represent the post-turnaround trends. The dotted lines represent -0.75, 0 and 0.75 %yr^{-1}.

case of all types of profile measurements also, the PW and EESC based ozone trends show similar values before 1997. On the contrary, positive trends derived from EESC regression model in 1997–2010 are smaller than the PWLTs below 35 km suggesting the influences of other factors in addition to ODSs for the increase in ozone. Above 40 km, significant positive trends can be attributed to EESC only. It reflects the effect of reduced amount of ODSs on the ozone in the upper stratosphere, where the fate of ozone is mainly determined by the processes linked to the homogeneous chemistry.

5.7 Connection between ozone profile and column measurements

To find the altitude range from which the explanatory variables contribute maximum to ozone total column, ozone vertical profiles are analysed by converting them from number density to DU/km and are then integrated in 5 km width. Figure 5.24 shows the contribution of various proxies to the variability of ozone in DU, as measured from the vertical ozone profiles. So this Figure has to be compared with the Fig. 5.10 in order to understand the altitude levels from where the proxies impart maximum contribution to the total ozone.

The contribution of various proxies is distinct at different altitude ranges. For instance, the dynamical parameters QBO 30 and QBO 10 show negative and positive correlations with total ozone from November to April and from May to October (see Fig. 5.10). In comparison to Fig. 5.24, it is found that the maximum contribution (∼3–8 DU) of QBO 30 to the total ozone comes from the lower stratosphere (15–24 km) except in January. The contribution of QBO 10 arise from 15 to 35 km (∼3–13 DU). As expected, influence

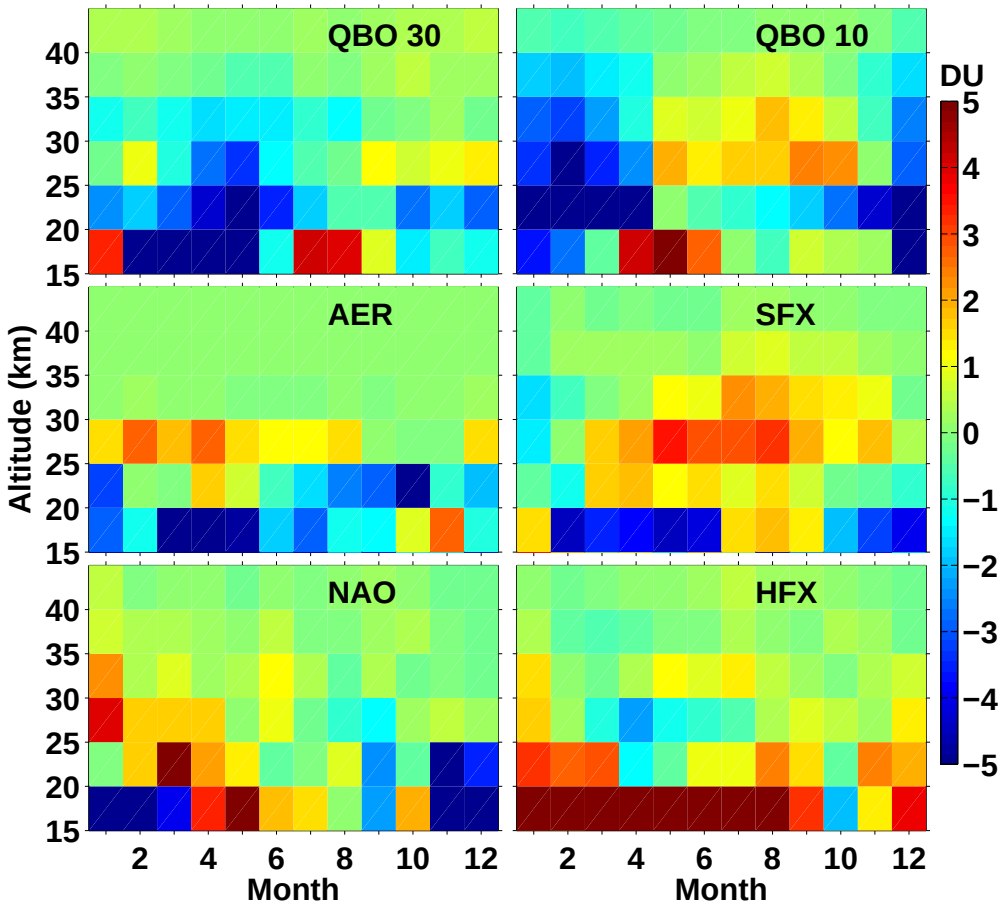

Figure 5.24: Contribution of proxies to the ozone total column in DU, estimated from the average ozone vertical profile at OHP.

of aerosols is mainly in the 15–24 km altitude range.The contribution of solar flux to total ozone in the January–May months corresponds to the values of 2–4 DU in the 20–34 km altitude range. The maximum contribution of about 5 DU in June–September comes from the 15–34 km range and in October–December, from 15–24 km.

The NAO teleconnection pattern provides a maximum contribution of about 5 DU to the total ozone from 15 to 19 km in January–March and in December. The influence of NAO is observed at 15–29 km in April–June and September while at 20–34 km in other months. The influence of another dynamical parameter, heat flux is maximum (∼5–8 DU) in the 15–24 km altitude range in February, March, June and August–December. In January, maximum contribution comes from 15 to 34 km while in April, May and July, the maximum influence of heat flux is present only in the 15–19 km range.

5.8 Summary

Long-term evolution of monthly mean stratospheric ozone measurements in the northern mid-latitude stations, OHP and MOHp, is analysed by using the method of multiple linear regression. The analysis uses ozone total column data from the combined Dobson and SAOZ total column measurements at OHP and the Dobson spectrophotometer at MOHp. In addition, ozone profile observations from lidar, SAGE II and the mean ozone calculated from lidar, SAGE II, HALOE, Aura MLS and ozonesondes are used. In order to analyse the long-term variations in ozone, a multiple regression model is developed including various explanatory parameters such as QBO, solar cycle, aerosols, eddy heat flux and NAO and the PWLT or EESC terms. The regression model could explain well the observed variance of the ozone total column measurements. In the case of ozone vertical profiles, the regression model explained about 60–70 % of the ozone variability in the winter/spring months in the 18–42 km altitude range. The model can explain only about 20–40 % of the variability below 18 and above 42 km. Stratospheric ozone trends are estimated from the residuals obtained by removing the contribution of those proxies using the PW linear and EESC functions. The PWLTs are derived considering 1997 as the turnaround year.

The effect of various proxies on the variability in the ozone total column at OHP is analysed using both PW and EESC regression models. The PW linear and EESC functions are the dominant factors responsible for a large fraction of long-term ozone change. The contribution of aerosols is limited to the periods of volcanic eruptions while influences of QBO, solar flux, eddy heat flux and NAO are found during the whole period with a prominent seasonal variation. The influence of QBO and eddy heat flux is larger in winter/spring whereas solar flux provides a maximum contribution in summer and NAO in winter. We have compared the effect of proxies on the ozone total column measurements at OHP with that at MOHp. Even though the considered stations do not differ much in the latitudinal and longitudinal basis, a slight latitudinal dependency is found for QBO and eddy heat flux and to a lesser extent for solar flux and NAO. The influence of QBO is larger at OHP while that of eddy heat flux, solar flux and NAO are larger at MOHp. So, from OHP to MOHp, the contribution of QBO decreases while that of eddy heat flux, solar flux and NAO increases.

The influence of various proxies at different altitudes is evaluated from the analysis of the vertical distribution of ozone measurements at OHP. Generally, maximum contribution from the proxies to the ozone variability is found in the lower stratosphere. The eddy heat flux influences ozone in the lower stratosphere while QBO contributes at all altitudes in all months. The significant response of ozone to the solar flux and NAO is observed mostly in the middle stratosphere and a small part in the lower and upper stratosphere. The influence

of aerosols is significant at all months.

The estimated ozone total column trends using PW and EESC time series show an obvious decrease before 1997 and an increase afterwards. Both regressions yield similar and significant negative ozone column trends of about $-1.4 \pm 0.29\,\mathrm{DU\,yr^{-1}}$ at OHP and of $-1.5 \pm 0.19\,\mathrm{DU\,yr^{-1}}$ at MOHp. On the other hand, the post-turnaround ozone column trends from both types of regressions are slightly different with the largest value (0.55 ± 0.29 and $0.81\pm0.25\,\mathrm{DU\,yr^{-1}}$ for OHP and MOHp, respectively) in PW regression. Therefore, the analysis reveals an indication of the influence of ODSs in decreasing ozone before the mid-1990s and the influence of other proxies other than the reduced ODS abundance on the increasing tendency of ozone after 1996. For instance, QBO, NAO and heat flux contribute about 20–26 DU to the large total ozone anomaly of 25–30 DU in the winter/spring months in 2010.

The PW and EESC regression analyses on the vertical distribution of stratospheric ozone also yield similar and significant ozone trends in 1984–1996 and are about $-0.5\,\%\mathrm{yr^{-1}}$ in 16–22 and 34–37 km and about $-0.8\,\%\mathrm{yr^{-1}}$ in 38–45 km. Similarly, ozone trends in 1997–2010, estimated based on PW and EESC regressions are of the order of 0.3 and $0.1\,\%\mathrm{yr^{-1}}$, respectively at 18–28 km and about $0.1\,\%\mathrm{yr^{-1}}$ at 31–39 km and are significant too. In the 40–45 km range, EESC provides statistically significant ozone trends of about $0.25\,\%\mathrm{yr^{-1}}$ and are larger than the insignificant PWLTs. This implies that the decline of ozone before 1997 is mainly attributed to the positive ODS trends at all altitudes while the significant increase in ozone after 1996 is only partly attributed to the decrease in ODSs below 40 km. In contrast, the influence of ODS still dominates above 40 km inducing a noteworthy increase in ozone.

Chapter 6

Summary, conclusions and perspectives

Contents

6.1 Summary and conclusions

The primary aim of this thesis is the assessment of ozone trends in the subtropical and mid-latitude regions. To carry out this study, we mainly use the ozone lidar measurements, satellite overpass measurements and other ground-based measurements in these regions. Therefore, we concentrate on the measurements from the stations MOHp, OHP, Tsukuba, TMF, MLO and Lauder. The analysis includes both ozone profile and column measurements in the stratosphere. For instance, we use the ground-based lidar, ozonesondes, Umkehr, Dobson and SAOZ and the space-based occulation measurements from SAGE II, HALOE and GOMOS, nadir observations from SBUV(/2) and limb measurements from UARS MLS and Aura MLS. The profile measurements are characterised by various vertical resolutions, which were retrieved using different measurement techniques.

First of all, as a part of sensitivity and stability diagnosis, ozone lidar measurements are analysed in detail to find out the impact of using different ozone absorption cross-sections and meteorological data on the retrieved ozone number density at different latitudinal regimes. It is found that the switch between BP and BDM ozone cross-section does not have significant influence on the retrieved ozone number density. Because, the relative differences in ozone retrieved from the two cross-sections at Rayleigh (308 nm) and the combined Rayleigh and Raman (308+331.8 nm) wavelengths are very small of the order of ± 0.2 % up to 25 km in the tropics, mid-latitudes and polar regions. Moreover, average ozone difference for the two cross-sections, calculated from the OHP ozone lidar, is negligibly small, ± 0.08 % at 10–50 km. Similarly, the differences in ozone retrieved using CIRA and NCEP temperature shows negligible deviation below 30 km. In contrast, the relative difference in ozone retrieved using these two temperatures is about 0.5% above 30 km. So the ozone lidar retrievals are mostly affected by temperature variations rather than the change in ozone absorption cross-sections.

Then, a number of ground-based and satellite ozone observations are compared with the ozone lidar measurements at different NDACC lidar stations to evaluate the consistency and stability of various ozone measurements in the subtropical and mid-latitude regions. The analysis is done using the collocated measurements and evaluates relative differences and relative drifts of various observations with respect to ozone lidar measurements at the respective stations. All data sets show the best agreement (± 3 %) with the lidars in

20–40 km at the considered lidar sites. SAGE II data behave well ($\pm 0.1\%\mathrm{yr}^{-1}$) with the lidars in the 18–42 km range. The estimated drifts of all profile measurements are within $\pm 0.3\%\mathrm{yr}^{-1}$ in 20–40 km and most of them are not significant at the 2σ confidence interval. To evaluate the stability of ozone lidar measurements, they are compared to the long-term satellite measurements. In addition, stability of long-term ozone measurements are analysed by the cross-comparison of long-term data sets. It is noted that all lidars show negligible drifts of $\pm 0.2\%\mathrm{yr}^{-1}$ with respect to SBUV(/2), SAGE II and HALOE. Among other long-term data sets, SBUV(/2) provides the least drifts of $\pm 0.2\%\mathrm{yr}^{-1}$. SAGE II and HALOE exhibit insignificant drifts of $\pm 0.4\%\,\mathrm{yr}^{-1}$. Aura MLS also shows small and insignificant drift ($\pm 0.2\%\mathrm{yr}^{-1}$) from its 8 years of data record. Therefore, a long-term continuous satellite data set spanning over ∼27 years (1985–2010) is constructed using the terminated SAGE II/ HALOE with Aura MLS ozone observations. The drifts computed for these combined data sets are extremely small ($\pm 0.1\%\mathrm{yr}^{-1}$) and insignificant. It suggests that these combined data sets are highly stable than the individual ozone measurements and thus, they have a great potential to be used in stratospheric ozone trend study; the main goal of making such a long-term data set.

These ozone measurements are then used for the computation of ozone trends, for which a process-oriented multivariate regression model is developed within the framework of this study. The regression model uses different explanatory parameters that describe various natural and anthropogenic processes affecting stratospheric ozone. The key parameters considered in the model are QBO, solar flux, aerosol, NAO, heat flux and the piecewise linear trend (PWLT) or EESC. In order to check the consistency of derived ozone trends, we have applied both PW linear and EESC functions to the same ground-based and satellite data.

The maximum contribution to the total ozone variability is dominated by QBO and heat flux at OHP and MOHp respectively during the northern hemisphere winter months. The influence of QBO decreases while that of heat flux, solar flux and NAO increases with latitude here. The contribution of NAO to the total ozone is maximum during the NH winter months whereas solar flux variation of ozone is maximum in the NH summer months. The high amount of total ozone in 2009–2010 in the northern mid-latitudes is driven by strong planetary wave activity, as can be deduced from the highest heat flux during the period. The computed heat flux is the largest since 1980, indicating the strength of wave drive during this particular winter period.

Ozone trends using both PWLT and EESC functions exhibit significant negative trends of $-1.4 \pm 0.29\,\mathrm{DU\,yr}^{-1}$ at OHP and $-1.5 \pm 0.19\,\mathrm{DU\,yr}^{-1}$ at MOHp prior to 1997. The PWLTs are about $0.55 \pm 0.29\,\mathrm{DU\,yr}^{-1}$ at OHP and $0.81 \pm 0.25\,\mathrm{DU\,yr}^{-1}$ at MOHp in 1997–2010. The EESC based trends are about $0.39 \pm 0.08\,\mathrm{DU\,yr}^{-1}$ at OHP and $0.42 \pm 0.06\,\mathrm{DU\,yr}^{-1}$ at MOHp during the same period. Therefore, the pre-turnaround (before 1997) trends from both regressions are similar, whereas the post-turnaround (after 1996) trends show slight differences, with the highest value derived from PW regression. It implies that the decrease in ozone before 1997 is due to the increase in ODSs in the stratosphere, while reduction in ODS could explain only a part of the increase in ozone after 1996.

The analysis of the influence of explanatory variables at each altitude reveals that heat flux contributes its maximum in the lower stratosphere while the contribution of QBO is more or less the same at all altitudes in the winter months. The influence of solar flux is significant in the middle stratosphere with a positive correlation with ozone. Similarly, NAO shows positive contribution to ozone in the middle stratosphere at all months and in the lower stratosphere in March–July, but are significant only in winter. The maximum and significant contribution of heat flux is present in the lower stratosphere.

Estimation of stratospheric ozone trends in vertical using both PW and EESC regres-

sions shows significant year-round pre-turnaround trends of -0.4 to $-0.5\,\%\mathrm{yr}^{-1}$ in 18–25 and 34–37 km. The largest trends are found at 38–45 km with the value of $-0.8\,\%\mathrm{yr}^{-1}$. Around 30 km, the trends are small of the order of $-0.15\,\%\mathrm{yr}^{-1}$. On the contrary, the year-round post-turnaround trends based on PW and EESC regressions are slightly different below 30 and above 39 km. The PWLT and EESC based trend are of the order of $0.3\,\%\mathrm{yr}^{-1}$ and $0.1\,\%\mathrm{yr}^{-1}$, respectively below 30 km and are significant too. Above 39 km, the ozone trend based on EESC is significant and is about $0.25\,\%\mathrm{yr}^{-1}$ while PWLT is very small and is insignificant. So it can be inferred from the ozone profile trends that the reduction in ODS is still responsible for the increase in ozone above 40 km, while below 30 km, the change in ozone is largely controlled by the dynamical variables like, QBO, NAO and heat flux. Analysis of profile measurements further reveals that the extremely high total ozone found in 2009–2010 in the northern mid-latitude is mainly contributed from the lower stratosphere, below 23 km.

In short, both PW and EESC regressions show significant positive trends after 1996. Previous trend studies showed stabilisation of ozone at 17 km (WMO, 2011) and 35–45 km (Steinbrecht et al., 2006). So this study further extends the previous analysis with a range of measurements for the entire stratosphere. The derived ozone trends are consistent with the results from other studies in the respective regions and confirm their findings of the mid-latitude ozone recovery in the lower and upper stratosphere. More importantly, this study reveals positive ozone trends of about 0.2–$0.4\,\%\mathrm{yr}^{-1}$ in the 18–27 and 40–45 km altitude range. It has been found that most of the recent increase in ozone is not due to the reduction in ODSs in the lower stratosphere (as shown by the difference in ozone trends using PW and EESC regressions) and this conclusion corroborates similar results discussed in Hadjinicolaou and Pyle (2004) and Dhomse et al. (2006). A very similar result was also observed in the Antarctic stratosphere by Salby et al. (2011) who presented a significant positive trend using September–November TOMS/OMI total ozone average, and claimed that Antarctic ozone is recovering. Additionally, much of the increase in ozone in their study is shown to be dominated by the dynamical variables (heat flux and QBO). So the results and discussions given in this thesis confirm some of the results presented in previous works and presents some new and promising results on stratospheric ozone trends that demonstrates clear and significant ozone recovery signals in the mid-latitudes.

6.2 Perspectives

Considering the importance of detecting ozone recovery linked to the implementation of the Montreal Protocol, this thesis opens a path to do some additional works. For instance, in addition to Aura MLS, several satellites have been launched since 2000 and are not validated on the long-term for estimating ozone trends. Therefore, stability of ozone measurements from other satellite instruments such as SCIAMACHY, GOME, GOMOS, SMR, OSIRIS, ACE-FTS and IASI can be evaluated as done in Chapter 4. In addition, the regression analyses could be improved by using additional explanatory variables (e.g., equivalent latitude). The estimation of stratospheric ozone trends can also be extended to other stations (e.g., Tsukuba, TMF, MLO and Lauder etc.), as presented in Chapter 5. Moreover, comparisons and trends evaluated using ozone observations can be compared with the trends deduced from the long-term simulations by Chemical Transport Models (e.g., REPROBUS or SLIMCAT) forced by the ERA-Interim analyses. Similarly, trends estimated from the simulations of Chemistry Climate Models (SPARC, 2010), can be compared with that obtained from observations.

Bibliography

Ancellet, G. and M. Beekmann, 1997: Evidence for changes in the ozone concentrations in the free troposphere over southern France from 1976 to 1995. *Atmos. Environ.*, **31**, 2835–2851. 41

Andersen, S. B. and B. M. Knudsen, 2006: The influence of polar vortex ozone depletion on NH mid-latitude ozone trends in spring. *Atmos. Chem. Phys.*, **6**, 2837–2845. 13

Andrews, D. G., J. R. Holton, and C. B. Leovy, 1987: *Middle atmosphere dynamics*, International geophysics series, Vol. 40. Academic Press. 2, 3, 87, 89

Appenzeller, C., A. K. Weiss, and J. Staehelin, 2000: North Atlantic Oscillation modulates total ozone winter trends. *Geophys. Res. Lett.*, **27(8)**, 1131–1134. 90

Baldwin, M. P., L. Gray, T. Dunkerton, K. Hamilton, and et al., 2001: The quasi-biennial oscillation. *Reviews of Geophys.*, **39(2),doi:10.1029/1999RG000073**, 179–229. 87

Bass, A. M. and R. J. Paur, 1984: The ultraviolet cross-sections of ozone:I: The measurements, II:Results and temperature dependence. *Proc. of the Quadrennial Ozone Symposium, Halkidiki, Greece, D. Reidel, Dordrecht*, 606–615. 29, 32

Bates, D. R. and M. Nicolet, 1950: The photochemistry of atmospheric water vapour. *J. Geophys. Res.*, **55(3), doi:10.1029/JZ055i003p00301**, 301–327. 4

Bhartia, P. K., R. D. McPeters, C. L. Mateer, L. E. Flynn, and C. Wellemeyer, 1996: Algorithm for the estimation of vertical ozone profiles from the backscattered ultraviolet technique. *J. Geophys. Res.*, **101(D13)**, 18 793–18 806. 41

Bhartia, P. K., C. G. Wellemeyer, S. L. Taylor, N. Nath, and A. Gopalan, 2004: Solar backscatter ultraviolet (SBUV) version 8 profile algorithm. *Proc. of the XX Quadrennial Ozone Symposium, edited by: C. S. Zerefos, Int. Ozone Comm., Athens, Greece*, 295–296. 41

Bodeker, G., I. Boyd, and W. Matthews, 1998: Trends and variability in vertical ozone and temperature profiles measured by ozonesondes at Lauder, New Zealand: 1986–1996. *J. Geophys. Res.*, **103(D22)**, 28 661–28 681. 66

Bojkov, R., L. Bishop, W. Hill, G. Reinsel, and G. Tiao, 1990: A statistical trend analysis of revised dobson total ozone data over the Northern Hemisphere. *J. Geophys. Res.*, **95(D7)**, 9785–9807. 86, 87

Boyd, I. S., A. D. Parrish, L. Froidevaux, T. von Clarmann, E. Kyrölä, J. M. R. III, and J. M. Zawodny, 2007: Ground-based microwave ozone radiometer measurements compared with Aura-MLS v2.2 and other instruments at two Network for Detection of Atmospheric Composition Change sites. *J. Geophys. Res.*, **112, D24S33, doi:10.1029/2007JD008720**. 52, 72, 73

Brasseur, G. P., 2008: *Climate Variability and Extremes during the Past 100 years: Creating Knowledge from the Controntation of Observations and Models: The Case of Stratospheric Ozone*, Advances in Global Change Research, Vol. 33, doi: 10.1007/978-1-4020-6766-2_21. Springer, 303–316 pp. 2

Brasseur, G. P., J. J. Orlando, and G. S. Tyndall, 1999: *Atmospheric chemistry and global change*. Oxford university press. xvii, 5, 6, 9, 13

Brewer, A. W., 1949: Evidence for a world circulation provided by the measurements of helium and water vapour distribution in the stratosphere. *Quart. J. Roy. Meteor. Soc.*, **75**, 351–363. 6

Brewer, A. W. and J. R. Milford, 1960: The oxford-kew ozone sonde. *Proc. R. Soc. Lond. A, 256, 1287*, 470–495. 40

Brinksma, E. J., J. B. Bergwerff, G. E. Bodeker, and et al., 2000: Validation of 3 years of ozone measurements over Network for the Detection of Stratospheric Change station Lauder, New Zealand. *J. Geophys. Res.*, **105(D13)**, 17 291–17 306. 29

Brion, J., A. Chakir, J. Charbonnier, D. Daumont, C. Parisse, and J. Malicet, 1998: Absorption spectra measurements for the ozone molecule in the 350–830 nm region. *Journal of Atmospheric Chemistry*, **30**, 291–299. 29

Browell, E. V., et al., 1990: Airborne lidar observations in the wintertime Arctic stratosphere: Polar stratospheric clouds. *Geophys. Res. Lett.*, **17(4), 385–388, doi:10.1029/GL017i004p00385**. 11

Brühl, C., et al., 1996: Halogen occultation experiment ozone channel validation. *J. Geophys. Res.*, **101(D6)**, 10 217–10 240. 42

Brunner, D., J. Staehelin, J. A. Maeder, I. Wohltmann, and G. E. Bodeker, 2006: Variability and trends in total and vertically resolved stratospheric ozone based on the cato ozone data set. *Atmos. Chem. Phys.*, **6**, 4985–5008. 92, 93, 117

Carslaw, K. S., B. P. Luo, S. L. Clegg, T. Peter, P. Brimblecombe, and P. J. Crutzen, 1994: Stratospheric aerosol growth and HNO_3 gas phase depletion from coupled HNO_3 and water uptake by liquid particles. *Geophys. Res. Lett.*, **21(23)**, 2479–2482. 10

Chandra, S., R. McPeters, W. Planet, and R. Nagatani, 1994: The 27 day solar UV response of stratospheric ozone: solar cycle 21 vs. solar cycle 22. *Journal of Atmospheric and Terrestrial Physics*, **56,9**, 1057–1065. 89

Chapman, S., 1930: A theory of upper-atmospheric ozone. *Memoirs of the Royal Meteorological Society*, **3(26)**. 3

Chubachi, S., 1984: Preliminary result of ozone observations at syowa station from february 1982 to january 1983. *Mem. Natl. Inst. Polar Res. Jpn., Spec. Issue*, **34**, 13–20. 7

Crutzen, P. J., 1971: Ozone production rates in an oxygen-hydrogen-nitrogen oxide atmosphere. *J. Geophys. Res.*, **76(30)**, 7311–7327. 4

Cunnold, D., M. Newchurch, L. Flynn, H. Wang, J. Russell, R. McPeters, J. Zawodny, and L. Froidevaux, 2000: Uncertainties in upper stratospheric ozone trends from 1979 to 1996. *J. Geophys. Res.*, **105(D4)**, 4427–4444. 61, 76

Daniel, J. S., S. S. R. W. Portmann, and R. R. Garcia, 1999: Stratospheric ozone destruction: The importance of bromine relative to chlorine. *J. Geophys. Res.*, **104(D19),doi:10.1029/1999JD900381**, 23 871–23 880. 7, 13

Daumont, D., J. Brion, J. Charbonnier, and J. Malicet, 1992: Ozone UV spectroscopy I: Absorption cross-sections at room temperature. *Journal of Atmospheric Chemistry*, **15**, 145–155. 29

DeLand, M. T., L.-K. Huang, S. L. Taylor, C. A. McKay, R. P. Cebula, P. K. Bhartia, and R. D. McPeters, 2004: Long-term SBUV and SBUV/2 instrument calibration for version 8 ozone data. *Proc. of the XX Quadrennial Ozone Symposium, edited by: Zerefos, C., Univ. of Athens, Greece*, 321–322. 41

Deshler, T., J. L. Mercer, H. G. J. Smit, and et al., 2008: Atmospheric comparison of electrochemical cell ozonesondes from different manufacturers, and with different cathode solution strengths: The balloon experiment on standards for ozonesondes. *J. Geophys. Res.*, **113, D04307**. 41

Dhomse, S., M. Weber, I. Wohltmann, M. Rex, and J. P. Burrows, 2006: On the possible causes of recent increases in northern hemispheric total ozone from a statistical analysis of satellite data from 1979 to 2003. *Atmos. Chem. Phys.*, **6, doi:10.5194/acp-6-1165-2006**, 1165–1180. 15, 86, 87, 92, 100, 103, 125

Dobson, G. M. B., 1956: Origin and distribution of polyatomic molecules in the atmosphere. *Proc. Roy. Soc. London.*, The Royal Society, A, Mathematical and Physical Sciences, Vol. 236, 1205, 187–193. 6

Dobson, G. M. B., 1980: Operations handbook ozone observations with a dobson spectrophotometer, edtited by W. D. Komhyr, revised by R. D. Evans, World Meteorological Organization, Global Atmosphere Watch, no. 183. 94

Evans, R., G. McConville, S. Oltmans, I. Petropavlovskikh, and D. Quincy, 2009: Measurement of internal stray light within dobson ozone spectrophotometers. *Int. J. of Remote Sens.*, **30**, 4247–4258. 40

Fahey, D. W., S. R. Kawa, and E. L. Woodbridge, 1993: In situ measurements constraining the role of sulphate aerosols in mid-latitude ozone depletion. *Nature*, **363, doi:10.1038/363509a0**, 509–514. 13

Farman, J. C., B. G. Gardiner, and J. D. Shanklin, 1985: Large losses of total ozone in the Antarctica reveal seasonal ClO_x/NO_x interaction. *Nature*, **315**, 207–210. xv, 7

Felton, M. A., T. A. Kovacs, A. H. Omar, and C. A. Hostetler, 2007: Stratospheric clouds using LIDAR measurements from the SAGE III ozone loss and validation experiment. *Tech. Rep. ARL-TR-4154, U.S. Army Research Laboratory, Adelphi, Md.*, 36. 11

Fioletov, V. E., G. E. Bodeker, A. J. Miller, R. D. McPeters, and R. Stolarski, 2002: Global and zonal total ozone variations estimated from ground-based and satellite measurements: 1964–2000. *J.Geophys.Res.*, **107(D22), 4647, doi:10.1029/2001JD001350**. 14

Fioletov, V. E. and T. G. Shepherd, 2003: Seasonal persistence of midlatitude total ozone anomalies. *Geophys.Res.Lett.*, **30**, 1417,doi:10.1029/2002GL016 739. 90

Fioletov, V. E., D. W. Tarasick, and I. Petropavlovskikh, 2006: Estimating ozone variability and instrument uncertainties from SBUV(/2), ozonesonde, Umkehr, and SAGE II measurements: Short-term variations. *J. Geophys. Res.*, **111, D02305**. 57

Frederick, J. E., 1984: Measurement requirements for the detection of ozone trends. *Ozone Correlative Measurements Workshop, NASA Conf. Publ. 2362*, B1–B19. 49

Froidevaux, L., Y. B. Jiang, A. Lambert, and et al., 2008: Validation of Aura Microwave Limb Sounder stratospheric ozone measurements. *J. Geophys. Res.*, **113, D15S2**. 43, 44, 50, 52

Fujimoto, T., O. Uchino, and T.Nagai, 1996: Four year intercomparison of ozone lidar, ozonesonde and SAGE II data. *Proceedings of the XVIII Quadrennial Ozone Symposium, Edited by: R. Bojkov and G. Visconti, L'Aquila, Italy*, 127–130. 66

Gijsel, J. A. E. V., D. P. J. Swart, J.-L. Baray, and et al., 2009: Global validation of envisat ozone profiles using lidar measurements. *Int. J. Remote Sens.*, **30, doi:10.1080/01431160902821825**, 3987–3994. 52

Godin, S., 1987: Etude experimentale par teledetection laser et modelisation de la distribution verticale d'ozone dans la haute stratosphere. Ph.D. thesis, UPMC. 23

Godin, S., A. I. Carswell, D. P. Donovan, and et al., 1999: Ozone differential absorption lidar algorithm intercomparison. *Appl. Optics*, **38**. 24, 27

Godin, S., M. Marchand, A. Hauchecorne, and F. Lefèvre, 2002: Influence of Arctic polar ozone depletion on lower stratospheric ozone amounts at Haute-Provence Observatory (43.92°N, 5.71°E). *J. Geophys. Res.*, **107, 8272, doi:10.1029/2001JD000516**. 112

Godin, S., G. Mégie, and J. Pelon, 1989: Systematic lidar measurements of the stratospheric ozone vertical distribution. *Geophys. Res. Lett.*, **16(6)**, 547–550. 23

Godin-Beekmann, S. and P. J. Nair, 2012: Sensitivity of stratospheric ozone lidar measurements to a change in ozone absorption cross-sections. 33

Godin-Beekmann, S., J. Porteneuve, and A. Garnier, 2003: Systematic DIAL lidar monitoring of the stratospheric ozone vertical distribution at Observatoire de Haute-Provence (43.92° N, 5.71° E)). *J. Environ. Monit.*, 57–67. xvii, 24, 26, 28, 54

Godin-Beekmann, S., T. Song, P. Keckhut, and J. Porteneuve, 2004: Long-term variability of stratospheric ozone monitored by DIAL measurements at OHP (44°N, 6°E). *Proc. of the International Laser Radar Conference, edited by: Pappalardo, G. and Amodeo, A., ESA SP-561*, 559–562. 55

Griesfeller, A., S. Godin-Beekmann, I. Petropavlovskikh, P. J. Nair, and et al., 2012: Comparison of long-term stratospheric ozone time series from lidar and umkehr measurements at Observatoire de Haute-Provence (OHP), 44° N, 6° E. *in preparation.* 46

Guirlet, M., P. Keckhut, S. Godin, and G. Mégie, 2000: Description of the long-term ozone data series obtained from different instrumental techniques at a single location: the Observatoire de Haute-Provence (43.9° N, 5.7° E). *Ann. Geophys.*, **18**, 1325–1339. 43

Hadjinicolaou, P. and J. A. Pyle, 2004: The impact of arctic ozone depletion on northern middle latitudes: Interannual variability and dynamical control. *Journal of Atmospheric Chemistry*, **47**, 25–43. 13, 125

Harris, N. R. P., E. Kyrö, J. Staehelin, and D. Brunner, 2008: Ozone trends at northern mid- and high latitudes - a European perspective. *Ann. Geophys.*, **26**, 1207–1220. 15, 86, 87

Hauchecorne, A., 1998: Ether, service Arletty, atmospheric model description, ETH-ACR-AR-DM-001,. 22. 70

Hauchecorne, A., J. L. Bertaux, F. Dalaudier, and et al., 2010: Response of tropical stratospheric O_3, NO_2 and NO_3 to the equatorial Quasi-Biennial Oscillation and to temperature as seen from GOMOS/ENVISAT. *Atmos. Chem. Phys.*, **10**, 8873–8879. 43

Hauchecorne, A., M.-L. Chanin, and P. Keckhut, 1991: Climatology and trends of the middle atmospheric temperature (33–87 km) as seen by Rayleigh lidar over the southern France. *J. Geophys. Res*, **96(D8), doi:10.1029/91JD01213**, 15 297–15 309. 49

Haynes, P., 2005: Stratospheric dynamics. *Annu. Rev. Fluid Mech.*, **37**, 263–293. 6

Heese, B., S. Godin, and A. Hauchecorne, 2001: Forecast and simulation of stratospheric ozone filaments: A validation of a high-resolution potential vorticity advection model by airborne ozone lidar measurements in winter 1998/1999. *J. Geophys. Res.*, **106(D17)**, 20 011–20 024. 112

Hendrick, F., et al., 2011: NDACC/SAOZ UV-visible total ozone measurements: improved retrieval and comparison with correlative ground-based and satellite observations. *Atmos. Chem. Phys.*, **11**, 5975–5995. 95

Hofmann, D. and S. Solomon, 1989: Ozone destruction through heterogeneous chemistry following the eruption of El Chichón. *J. Geophys. Res.*, **94(D4)**, 5029–5041. 12

Hofmann, D. J., et al., 1989: Stratospheric clouds and ozone depletion in the arctic during january 1989. *Nature*, **340,doi:10.1038/340117a0**, 117–121. 12

Holton, J. R., P. H. Haynes, M. E. McIntyre, A. R. Douglass, R. B. Rood, and L. Pfister, 1995: Stratosphere-troposphere exchange. *Rev. Geophys.*, **33(4)**, 403–439. xvii, 7

Hood, L. L., 1997: The solar cycle variation of total ozone: Dynamical forcing in the lower stratosphere. *J. Geophys. Res.*, **102(D1)**, 1355–1370. 89

Hurrell, J. W., 1996: Influence of variations in extratropical wintertime teleconnections on northern hemisphere temperature. *Geophys. Res. Lett.*, **23(6)**, 665–668. 90

Hurrell, J. W., Y. Kushnir, G. Ottersen, and M. Visbeck, 2003: *The North Atlantic Oscillation: Climatic Significance and Environmental Impact: An Overview of the North Atlantic Oscillation.* 1962- II, Geophysical monograph 134, American Geophysical Union. 90

Hurst, D. F., S. J. Oltmans, H. Vömel, K. H. Rosenlof, S. M. Davis, E. A. Ray, E. G. Hall, and A. F. Jordann, 2011: Stratospheric water vapor trends over Boulder, Colorado: Analysis of the 30 year Boulder record. *J. Geophys. Res.*, **116, D02306, doi:10.1029/2010JD015065**. 18

Hurwitz, M. M., P. A. Newman, and C. I. Garfinkel, 2011: The Arctic vortex in March 2011: a dynamical perspective. *Atmos. Chem. Phys.*, **11, doi:10.5194/acp-11-11447-2011**, 11 447–11 453. 12

Jiang, Y. B., L. Froidevaux, A. Lambert, and et al., 2007: Validation of aura microwave limb sounder ozone by ozonesonde and lidar measurements. *J. Geophys. Res.*, **112, D24S34**. 52, 72

Johnson, B. J., S. J. Oltmans, H. Vömel, H. G. J. Smit, T. Deshler, and C. Kröger, 2002: Electrochemical concentration cell (ECC) ozonesonde pump efficiency measurements and tests on the sensitivity to ozone of buffered and unbuffered ECC sensor cathode solutions. *J. Geophys. Res.*, **107**, 4393. 41

Jones, A., J. Urban, D. P. Murtagh, and et al., 2009: Evolution of stratospheric ozone and water vapour time series studied with satellite measurements. *Atmos. Chem. Phys.*, **9, doi:10.5194/acp-9-6055-2009**, 6055–6075. 16, 86, 117

Jones, A., J. Urban, D. P. Murtagh, C. Sanchez, K. A. Walker, N. J. Livesey, L. Froidevaux, and M. L. Santee, 2011: Analysis of hcl and clo time series in the upper stratosphere using satellite data sets. *Atmos. Chem. Phys.*, **11**, 5321–5333. xv

Kiesewetter, G., B.-M. Sinnhuber, M. Weber, and J. P. Burrows, 2010: Attribution of stratospheric ozone trends to chemistry and transport: a modelling study. *Atmos. Chem. Phys.*, **10, doi:10.5194/acp-10-12073-2010**, 12 073–12 089. 87

Komhyr, W. D., 1969: Electrochemical concentration cells for gas analysis. *Ann. Geoph.*, **25**, 203–210. 40

Krzyścin, J. W. and B. Rajewska-Wiech, 2009: Trends in the ozone vertical distribution from the umkehr observations at belsk 1963–2007. *Int. J. Remote Sens.*, **30**, 3917–3926. 16

Kuttippurath, J., S. Godin-Beekmann, F. Lefèvre, and F. Goutail, 2010: Spatial, temporal, and vertical variability of polar stratospheric ozone loss in the arctic winters 2004/2005–2009/2010. *Atmos. Chem. Phys.*, **10**, 9915–9930. 10, 90

Kuttippurath, J., S. Godin-Beekmann, F. Lefévre, G. Nikulin, M. L. Santee, and L. Froidevaux, 2012: Record-breaking ozone loss in the Arctic winter 2010/2011: comparison with 1996/1997. *Atmos. Chem. Phys. Discuss.*, **12, doi:10.5194/acpd-12-6877-2012**, 6877–6908. 12

Kuttippurath, J. and G. Nikulin, 2012: The sudden stratospheric warming of the Arctic winter 2009/2010: comparison to other recent warm winters. *Atmos. Chem. Phys. Discuss.*, **12, doi:10.5194/acpd-12-7243-2012**, 7243–7271. 89

Kyrölä, E., J. Tamminen, V. Sofieva, and et al., 2010: Retrieval of atmospheric parameters from gomos data. *Atmos. Chem. Phys.*, **10, doi:10.5194/acp-10-11881-2010**, 11 881–11 903. 42

Lary, D. J., D. W. Waugh, A. R. Douglass, R. S. Stolarski, P. A. Newman, and H. Mussa, 2007: Variations in stratospheric inorganic chlorine between 1991 and 2006. *Geophys. Res. Lett.*, **34, L21811, doi:10.1029/2007GL030053**. 13

Leblanc, T. and I. McDermid, 2000: Stratospheric ozone climatology from lidar measurements at Table Mountain (34.4°N, 117.7°W) and Mauna Loa (19.5°N, 155.6°W). *J. Geophys. Res.*, **105(D11)**, 14 613–14 623. 29

Li, J., D. M. Cunnold, H. J. Wang, E. S. Yang, and M. J. Newchurch, 2002: A discussion of upper stratospheric ozone asymmetries and SAGE trends. *J. Geophys. Res.*, **107(D23), doi:10.1029/2001JD001398**, 4705. 16

Livesey, N. J., W. G. Read, L. Froidevaux, J. W. Waters, and et al., 2003: The UARS Microwave Limb Sounder version 5 data set: Theory, characterization, and validation. *J. Geophys. Res.*, **108(D13), doi:10.1029/2002JD002273**, 4378. 43, 52, 72

Logan, J. A., I. A. Megretskaia, J. Miller, and et al., 1999: Trends in the vertical distribution of ozone: A comparison of two analyses of ozonesonde data. *J. Geophys. Res.*, **104**, 26 373–26 399. 16, 41, 86

Lott, F., J. Kuttippurath, and F. Vial, 2009: A climatology of the gravest waves in the equatorial lower and middle stratosphere: Method and results for the ERA-40 re-analysis and the LMDz GCM. *Journal of the Atmospheric Sciences*, **66, 5, doi: http://dx.doi.org/10.1175/2008JAS2880.1**, 1327–1346. 87

Mäder, J. A., J. Staehelin, D. Brunner, W. A. Stahel, I. Wohltmann, and T. Peter, 2007: Statistical modeling of total ozone: Selection of appropriate explanatory variables. *J. Geophys. Res.*, **112, D11108, doi:10.1029/2006JD007694**. 87

Mäder, J. A., J. Staehelin, T. Peter, D. Brunner, H. E. Rieder, and W. A. Stahel, 2010: Evidence for the effectiveness of the Montreal Protocol to protect the ozone layer. *Atmos. Chem. Phys.*, **10**, 12 161–12 171. xv

Manney, G. L., et al., 2011: Unprecedented Arctic ozone loss in 2011. *Nature*, **478, doi:10.1038/nature10556**, 469–475. xvii, 12

Marchand, M., S. Bekki, A. Pazmino, F. Lefèvre, S. G. Beekmann, and A. Hauchecorne, 2005: Model simulations of the impact of the 2002 antarctic ozone hole on the midlatitudes. *J. Atmos. Sci.*, **62**, 871–884. 10

McCormack, J. P. and L. L. Hood, 1996: Apparent solar cycle variations of upper stratospheric ozone and temperature: Latitude and seasonal dependences. *J. Geophys. Res.*, **101(D15)**, 20 933–20 944. 89

McElroy, M. B., R. J. Salawitch, S. C. Wofsy, and J. A. Logan, 1986: Reductions of antarctic ozone due to synergistic interactions of chlorine and bromine. *Nature*, **321**, 759–762. 9

McGee, T., M. Gross, R. Ferrare, W. Heaps, and U. Singh, 1993: Raman dial measurements of stratospheric ozone in the presence of volcanic aerosols. *Geophys.Res.Lett.*, **10 (20)**, 955–958. 25

McLinden, C. A., S. Tegtmeier, and V. Fioletov, 2009: Technical note: A SAGE-corrected SBUV zonal-mean ozone data set. *Atmos. Chem. Phys*, **9, doi:10.5194/acp-9-7963-2009**, 7963–7972. 41, 70

McPeters, R. D., D. J. Hofmann, and M. Clark, 1999: Results from the 1995 stratospheric ozone profile intercomparison at Mauna Loa. *J. Geophys. Res.*, **104(D23)**, 30 505–30 514. 66

Molina, L. T. and M. J. Molina, 1987: Production of chlorine oxide (Cl_2O_2) from the self-reaction of the chlorine oxide (ClO) radical. *J. Phys. Chem.*, **91(2), DOI: 10.1021/j100286a035**, 433–436. 10

Molina, M. J. and F. S. Rowland, 1974: Stratospheric sink for chlorofluoromethanes, chlorine atom catalysed destruction of ozone. *Nature*, **249**, 810–812. 4

Nardi, B., J. C. Gille, J. J. Barnett, and et al., 2008: Initial validation of ozone measurements from the high resolution dynamics limb sounder. *J. Geophys. Res*, **113, doi:10.1029/2007JD008837**, D16S36. 55

Nazaryan, H. and M. P. McCormick, 2005: Comparisons of Stratospheric Aerosol and Gas Experiment (SAGE II) and Solar Backscatter Ultraviolet Instrument (SBUV/2) ozone profiles and trend estimates. *J. Geophys. Res.*, **110, doi:10.1029/2004JD005483**, D17 302. 57, 61, 76

Nazaryan, H., M. P. McCormick, and J. M. R. III, 2007: Comparative analysis of SBUV/2 and HALOE ozone profiles and trends. *J. Geophys. Res.*, **112, doi:10.1029/2006JD007367**, D10 304. 50, 57, 61, 76

Newchurch, M., L. Bishop, D. Cunnold, and et al., 2000: Upper-stratospheric ozone trends 1979–1998. *J. Geophys. Res.*, **105(D11)**, 14 625–14 636. 16

Newchurch, M. J., E.-S. Yang, D. M. Cunnold, G. C. Reinsel, J. M. Zawodny, and J. M. Russell, 2003: Evidence for slowdown in stratospheric ozone loss: First stage of ozone recovery. *J. Geophys. Res.*, **108(D16), doi:10.1029/2003JD003471**, 4507. 16, 85, 91

Newman, P. A., J. S. Daniel, D. W. Waugh, and E. R. Nash, 2007: A new formulation of equivalent effective stratospheric chlorine (eesc). *Atmos. Chem. Phys.*, **7**, 4537–4552. 13

Newman, P. A., E. R. Nash, S. R. Kawa, S. A. Montzka, and S. M. Schauffler, 2006: When will the Antarctic ozone hole recover? *Geophys. Res. Lett.*, **33, L12814, doi:10.1029/2005GL025232**. 13

Petropavlovskikh, I., P. K. Bhartia, and J. DeLuisi, 2005: New Umkehr ozone profile retrieval algorithm optimized for climatological studies. *Geophys. Res. Lett.*, **32, doi:10.1029/2005GL023323**, L16 808. 40, 46

Petropavlovskikh, I., R. Evans, G. McConville, K. Miyagawa, and S. Oltmans, 2009: Effect of the out-of-band stray light on the retrieval of the Umkehr Dobson ozone profiles. *Int. J. of Remote Sens.*, **30, doi:10.1080/01431160902865806**, 6461–6482. 40

Pommereau, J. P. and F. Goutail, 1988: Stratospheric O_3 and NO_2 observations at the southern polar circle in summer and fall 1988. *Geophys. Res. Lett.*, **15(8)**, 895–897. 95

Press, W. H., B. P. Flannery, S. A. Teukolsky, and W. T. Vetterling, 1989: *Numerical recipes*. Cambridge University Press, Cambridge, UK, 504–508 pp. 49, 93

Ramaswamy, V., M. D. Schwarzkopf, W. J. Randel, B. D. Santer, B. J. Soden, and G. L. Stenchikov, 2006: Anthropogenic and natural influences in the evolution of lower stratospheric cooling. *Science*, **311**, 1138–1141. 18

Randel, W., P. Udelhofen, E. Fleming, and et al., 2003: The sparc intercomparison of middle-atmosphere climatologies. *Journal of Climate*, **17(5)**, 986–1003. 34

Randel, W. J., R. S. Stolarski, D. M. Cunnold, and et al., 1999: Trends in the vertical distribution of ozone. *Science*, **285**, 1689–1692. 15

Randel, W. J., F. Wu, and R. Stolarski, 2002: Changes in column ozone correlated with the stratospheric EP Flux. *J. Meteorol. Soc. Japan*, **80**, 849–862. 89

Reinsel, G., G. Tiao, D. Wuebbles, J. Kerr, A. Miller, R. Nagatani, L. Bishop, and L. Ying, 1994: Seasonal trend analysis of published ground-based and TOMS total ozone data through 1991. *J. Geophys. Res.*, **99(D3)**, 5449–5464. 86, 92, 94

Reinsel, G. C., A. J. Miller, E. C. Weatherhead, L. E. Flynn, R. M. Nagatani, G. C. Tiao, and D. J. Wuebbles, 2005: Trend analysis of total ozone data for turnaround and dynamical contributions. *J. Geophys. Res.*, **110, D16306, doi:10.1029/2004JD004662**. 86, 91

Reinsel, G. C., E. C. Weatherhead, G. C. Tiao, and et al., 2002: On detection of turnaround and recovery in trend for ozone. *J. Geophys. Res.*, **107(D10), doi:10.1029/2001JD000500**, 4078. xx, 86, 91, 94

Remsberg, E. E., 2009: Trends and solar cycle effects in temperature versus altitude from the Halogen Occultation Experiment for the mesosphere and upper stratosphere. *J. Geophys. Res.*, **114, D12303, doi:10.1029/2009JD011897**. 45

Rex, M., et al., 1999: Chemical Ozone Loss in the Arctic Winter 1994/95 as Determined by the Match Technique. *J. Atmos. Chem.*, **32, 1, doi: 10.1023/A:1006093826861**, 35–59. 100

Rinsland, C. P., et al., 2003: Long-term trends of inorganic chlorine from ground-based infrared solar spectra: Past increases and evidence for stabilization. *J. Geophys. Res.*, **108(D8), doi:10.1029/2002JD003001.**, 4252. 13

Rodgers, C. D., 1976: Retrieval of atmospheric temperature and composition from remote measurements of thermal radiation. *Rev. Geophys.*, **14(4), doi:10.1029/RG014i004p00609**, 609–624. 46

Russell, J. M., L. L. Gordley, J. H. Park, and et al., 1993: The Halogen Occultation Experiment. *J. Geophys. Res.*, **98(D6)**, 10 777–10 797. 42

Salby, M., E. Titova, and L. Deschamps, 2011: Rebound of antarctic ozone. *Geophys. Res. Lett.*, **38, L09702, doi:10.1029/2011GL047266**. 125

Sato, M., J. Hansen, M. McCormick, and J. Pollack, 1993: Stratospheric aerosol optical depth, 1850-1990. *J. Geophys. Res.*, **98**, 22 987–22 994. 89

Shepherd, T. G., 2008: Dynamics, stratospheric ozone, and climate change. *Atmos.-Ocean*, **46**, 117–138. 18

Sinnhuber, B.-M., N. Sheode, M. Sinnhuber, M. P. Chipperfield, and W. Feng, 2009: The contribution of anthropogenic bromine emissions to past stratospheric ozone trends: a modelling study. *Atmos. Chem. Phys*, **9**, 2863–2871. 7, 13

Smit, H. G. J., W. Straeter, B. J. Johnson, and et al., 2007: Assessment of the performance of ECC ozonesondes under quasi flight conditions in the environmental simulation chamber: Insights from the Juelich Ozone Sonde Intercomparison Experiment (JOSIE). *J. Geophys. Res*, **112, D19306, doi:10.1029/2006JD007308**. 41

Solomon, S., R. R. Garcia, F. S. Rowland, and D. J. Wuebbles, 1986: On the depletion of Antarctic ozone. *Nature*, **321**, 755–758. 9

Soukharev, B. E. and L. L. Hood, 2006: Solar cycle variation of stratospheric ozone: Multiple regression analysis of long-term satellite data sets and comparisons with models. *J. Geophys. Res.*, **111, D20314, doi:10.1029/2006JD007107**. 89

SPARC, 1998: Stratospheric processes and their role in climate: Assessment of trends in the vertical distribution of ozone, SPARC Report 1, edited by: Harris, N., Hudson, R., and Phillips, C., WMO-Ozone Research and Monitoring Project Report no. 43. 15, 41, 43, 44, 61, 89

SPARC, 2002: Stratospheric processes and their role in climate: SPARC Intercomparison of middle atmosphere climatologies, SPARC Report 3, edited by Randel, W., Chanin, M.-L., and Michaut, C., WMO/TD–No.1142. 34

SPARC, 2010: SPARC CCMVal, SPARC Report on the Evaluation of Chemistry-Climate Models, V. Eyring, T. G. Shepherd, D. W. Waugh (eds.), SPARC Report No. 5, WCRP-132, WMO/TD-No. 1526. 125

Staehelin, J., R. Kegel, and N. Harris, 1998: Trend analysis of the homogenized total ozone series of Arosa (Switzerland), 1926–1996. *J. Geophys. Res.*, **103(D7)**, 8389–8399. 86, 92

Steinbrecht, W., H. Claude, F. Schönenborn, and et al., 2006: Long-term evolution of upper stratospheric ozone at selected stations of the Network for the Detection of Stratospheric Change (NDSC). *J. Geophys. Res.*, **111, D10308, doi:10.1029/2005JD006454**. xv, 16, 86, 125

Steinbrecht, W., H. Claude, F. Schönenborn, and et al., 2009: Ozone and temperature trends in the upper stratosphere at five stations of the network for the detection of atmospheric composition change. *Int. J. Remote Sens.*, **30, doi:10.1080/01431160902821841**, 3875–3886. 17, 117

Steinbrecht, W., B. Hassler, H. Claude, P. Winkler, and R. S. Stolarski, 2003: Global distribution of total ozone and lower stratospheric temperature variations. *Atmos. Chem. Phys.*, **3**, 1421–1438. 87, 100

Steinbrecht, W., U. Köhler, H. Claude, M. Weber, J. P. Burrows, and R. J. van der A, 2011: Very high ozone columns at northern mid-latitudes in 2010. *Geophys. Res. Lett.*, **38, L06803, doi:10.1029/2010GL046634**. 87, 89, 95, 106

Steinbrecht, W., T. J. McGee, L. W. Twigg, and et al., 2009a: Intercomparison of stratospheric ozone and temperature profiles during the october 2005 Hohenpeissenberg ozone profiling experiment (HOPE). *Atmos. Meas. Tech.*, **2**, 125–145. 29, 73

Steinbrecht, W., R. Schwarz, and H. Claude, 1998: New pump correction for the Brewer–Mast ozone sonde: Determination from experiment and instrument intercomparisons. *J. Atmos. Oceanic Technol.*, **15**, 144–156. 66, 73

Stolarski, R. A. and R. J. Cicerone, 1974: Stratospheric chlorine: A possible sink for ozone. *Can. J. Chem.*, **52**, 1610–1615. 4

Stolarski, R. S., A. R. Douglass, S. Steenrod, and S. Pawson, 2006: Trends in stratospheric ozone: Lessons learned from a 3D Chemical Transport Model. *Journal of the Atmospheric Sciences*, **63**, 1028–1041. 14, 92, 94

Storch, H. V. and F. W. Zwiers, 1999: *Statistical analysis in climate Research: Fitting statistical models.* Cambridge University Press. 93

Stübi, R., G. Levrat, B. Hoegger, P. Viatte, J. Staehelin, and F. J. Schmidlin, 2008: In-flight comparison of Brewer-Mast and electrochemical concentration cell ozonesondes. *J. Geophys. Res*, **113, D13302, doi:10.1029/2007JD009091**. 41

Tamminen, J., et al., 2010: GOMOS data characterisation and error estimation. *Atmos. Chem. Phys.*, **10, doi:10.5194/acp-10-9505-2010**, 9505–9519. 58

Tapping, K., 1987: Recent solar radio astronomy at centimeter wavelengths: The temporal variability of the 10.7 cm flux. *J. Geophys. Res.*, **92(D1)**, 829–838. 89

Tatarov, B., H. Nakane, and C. B. Park, 2009: Lidar observation of long-term trends and variations of stratospheric ozone and temperature over Tsukuba. *Int. J. Remote Sens.*, **30**, 3951–3960. 16, 29, 72, 86

Terao, Y. and J. A. Logan, 2007: Consistency of time series and trends of stratospheric ozone as seen by ozonesonde, SAGE II, HALOE, and SBUV(/2). *J. Geophys. Res.*, **112, D06310, doi:10.1029/2006JD007667**. 57

Thompson, D. W. J. and S. Solomon, 2009: Understanding recent stratospheric climate change. *Journal of Climate*, **22, 8**, 1934–1943. 18

Tiao, G. C., G. C. Reinsel, J. H. Pedrick, and et al., 1986: A statistical trend analysis of ozonesonde data. *J. Geophys. Res.*, **91(D12)**, 121–13, 136. 40

Tolbert, M. A., 1996: Polar clouds and sulfate aerosols. *Science*, **272, doi:10.1126/science.272.5268.1597**, 1597. 12

Vigouroux, C., et al., 2008: Evaluation of tropospheric and stratospheric ozone trends over western europe from ground-based ftir network observations. *Atmos. Chem. Phys.*, **8**, 6865–6886. 15

Vömel, H., S. J. Oltmans, F. Hasebe, and et al., 2002: Balloon-borne observations of water vapor and ozone in the tropical upper troposphere and lower stratosphere. *J. Geophys. Res.*, **107, doi:10.1029/2001JD000707**. 41

Vyushin, D. I., V. E. Fioletov, and T. G. Shepherd, 2007: Impact of long-range correlations on trend detection in total ozone. *J. Geophys. Res.*, **112, D14307, doi:10.1029/2006JD008168**. xx, 15, 86, 87, 91, 92, 108

Wang, H. J., D. M. Cunnold, L. W. Thomason, J. M. Zawodny, and G. E. Bodeker, 2002: Assessment of SAGE version 6.1 ozone data quality. *J. Geophys. Res.*, **107, doi:10.1029/2002JD002418**, 4691. 42

Wang, P.-H., D. M. Cunnold, and C. R. Trepte, 2006: Ozone variability in the midlatitude upper troposphere and lower stratosphere diagnosed from a monthly SAGE II climatology relative to the tropopause. *J. Geophys. Res.*, **111, D21304, doi:10.1029/2005JD006108**. 42

Waugh, D. and T. Hall, 2002: Age of stratospheric air: Theory, observations, and models. *Rev. Geophys*, **40(4), 1010, doi:10.1029/2000RG000101**. 13

Weatherhead, E., G. C. Reinsel, G. C. Tiao, and et al., 1998: Factors affecting the detection of trends: Statistical considerations and applications to environmental data. *J. Geophys. Res.*, **103(D14)**, 17 149–17 161. 49, 93

Weber, M., S. Dhomse, F. Wittrock, A. Richter, B.-M. Sinnhuber, and J. P. Burrows, 2003: Dynamical control of NH and SH winter/spring total ozone from GOME observations in 1995–2002. *Geophys. Res. Lett.*, **30(11), 1583, doi:10.1029/2002GL016799.** 100

Weber, M., S. Dikty, J. P. Burrows, H. Garny, M. Dameris, A. Kubin, J. Abalichin, and U. Langematz, 2011: The Brewer-Dobson circulation and total ozone from seasonal to decadal time scales. *Atmos. Chem. Phys.*, **11**, 11 221–11 235. 87

Weiss, A., J. Staehelin, C. Appenzeller, and N. Harris, 2001: Chemical and dynamical contributions to ozone profile trends of the Payerne (Switzerland) balloon soundings. *J. Geophys. Res.*, **106(D19)**, 22 685–22 694. 87

WMO, 1992: World Meteorological Organization: Scientific assesment of ozone depletion: 1991, Global Ozone Research and Monitoring Project-Report No. 25. xv, 12

WMO, 2007: World Meteorological Organization: Scientific assesment of ozone depletion: 2006, Global Ozone Research and Monitoring Project-Report No. 50, 572 pp., geneva, switzerland. xv, 7, 13, 15, 19, 40, 85, 89, 91

WMO, 2011: World Meteorological Organization: Scientific assesment of ozone depletion: 2010, Global Ozone Research and Monitoring Project-Report No. 52, 516 pp., geneva, switzerland. xv, xvii, 7, 14, 15, 16, 17, 18, 19, 86, 92, 108, 117, 125

Wohltmann, I., R. Lehmann, M. Rex, D. Brunner, and J. A. Mäder, 2007: A process-oriented regression model for column ozone. *J. Geophys. Res.*, **112, D12304, doi:10.1029/2006JD007573**. 87, 92, 100

Yang, E.-S., D. M. Cunnold, and R. J. Salawitch, 2006: Attribution of recovery in lower-stratospheric ozone. *J. Geophys. Res.*, **111, D17309, doi:10.1029/2005JD006371**. 15, 87

Yang, S. K., C. S. Long, A. J. Miller, X. He, Y. Yang, D. J. Wuebbles, and G. Tiao, 2009: Modulation of natural variability on a trend analysis of the updated cohesive SBUV(/2) total ozone. *International Journal of Remote Sensing*, **30, 15–16**. 15

Zanis, P., E. Maillard, J. Staehelin, C. Zerefos, E. Kosmidis, K. Tourpali, and I. Wohltmann, 2006: On the turnaround of stratospheric ozone trends deduced from the reevaluated Umkehr record of Arosa, Switzerland. *J. Geophys. Res.*, **111, D22307, doi:10.1029/2005JD006886**. 86, 91